UNIVERSITY OF BIRMINGHAM

Vehicle Speed over Ground Radar

by

Khairul Khaizi Bin Mohd Shariff

A thesis submitted to School of Electronic, Electrical and Computer Engineering of The University of Birmingham for the degree of

DOCTOR OF PHILOSOPHY

2019

Abstract

The non-contact speed measurement over ground (SoG) is a key component of modern vehicle technology since it allows measuring the speed of a vehicle without tapping on the wheels and can be measured without slippage. Applications can be found wherever an accurate measure of speed is needed, i.e., automatic control operations such as anti-lock braking system (ABS), Electronic stability control (ESC) or vehicle intelligent positioning system. The microwave Doppler principle is particularly suitable here because it is the least affected by environmental influences such as rain, snow, fog, temperature, wind, pollution, compared to other contactless measuring systems, i.e., Global Positioning Systems (GPS), ultrasonic, acoustics and optical sensor.

The present work closes a gap in microwave SoG by developing and examining a SoG system based on a four beams radar configuration. Compared to the previous single and dual-beam measuring method, a 4-beam system is capable of estimating the speed vector of the vehicle. Furthermore, this system can minimise the effect of vehicle dynamics on the estimate of vehicle speed. Regarding the Doppler signal processing method, a distinction is made between other known estimation methods. We proposed two types of Doppler processing based on Fourier transform. Theoretical evaluation of these two methods shows that they produce an accurate estimate of mean Doppler frequency. Comparison between these two methods shows that the cross-correlation method produces more accurate estimates and can work at lower input SNR. Finally, evaluation of the developed SoG system with actual road conditions shows that the SoG system can work well on both on-road and off-road conditions with increased speed accuracy when using the cross-correlation method.

Acknowledgment

First and foremost, I would like to express my gratitude to my supervisor Dr. Michail Antoniou for the support and guidance throughout my studies. Secondly, I would like to thank Dr. Edward Hoare and Professor Mikhail Cherniakov for their help and advice.

I would also like to say thank you to Dr. Liam Daniel and Alan Yates of the members in the Microwave Integrated Systems Laboratory (MISL) for the advice and help about the experimental setup and provisions of safety.

I want to thank my grand sponsors, Majlis Amanah Rakyat (MARA) of Malaysia who has provided the financial support throughout my study and make this study possible.

Finally, I would like to thank my wife Rozana for her support and encouragement during this long journey and my children, Arianna and Amelia both who have been patiently supporting their father preoccupation with this thesis.

To my parents,

Mohd Shariff & Kamisah

Table of Contents

Chapter 1. Introduction 1

1.1. Background 1

1.2. Motivation for the Present Work 3

1.3. Thesis Contributions 4

1.4. Thesis Outline 8

Chapter 2. Background 9

2.1. Introduction 9

2.2. Basic Principle of Radar 9

2.2.1. Modes of Operation 10

2.2.2. Basic Range Equations 11

2.2.3. Radar Cross Section (RCS) 13

2.2.4. The Doppler Effect 14

2.2.5. CW Radar Signal Theory 17

2.3. The principle of SoG Radar 20

2.3.1. Consideration of Ground Surface 20

2.3.2. An Ideal Speed Measurement 23

2.3.3. Doppler Spectrum 24

2.3.4. Mean Frequency Estimator 30

2.4. Main Errors in SoG 30

2.4.1.1. Beam Geometry Error 31

2.4.1.2. Fluctuation Error 33
2.5. Literature Review on Mean-Frequency Estimation Methods 35
2.6. Frequency Domain Methods 37
2.6.1. Fourier Transform 37
2.6.2. Methods of Mean frequency estimations 38
2.7. Introduction to Rigid Body Motions 40
2.7.1. References Frames 42
2.7.2. Rotation Matrix 43
2.7.3. Representing Vehicle Attitude 44
2.8. Approximation of Antenna Radiation Pattern for Doppler Spectrum 45
2.9. Summary 46
Chapter 3. Theoretical Overview of SoG Radar and Its Effect on Radar System Parameters 48
3.1. Introduction 48
3.1.1. The principle of Velocity Vector Estimation of a 4-Beam SoG radar 49
3.2. Analysis of Error due to Vehicle Motions 52
3.2.1. Motion Error of a Single-Beam Radar 53
3.2.2. Motion Error of a 4-Beam Radar 58
3.2.3. Comparison of Error Between 4-Beam and Single-Beam Radar 60
3.3. Radar Footprint 62
3.3.1. Model 62
3.3.2. Analysis of Radar Footprint 66

3.4. Modelling Doppler Spectrum 68
3.4.1. Model 68
3.4.1. Analysis of Doppler Spectrum with Values of Radar Parameters 72
3.5. Summary 75
Chapter 4. Derivation of Doppler Shift Estimation Algorithm and Performance Evaluation 76
4.1. Introduction 76
4.1.1. Previous Work 77
4.2. Derivation of Algorithm 79
4.2.1. Conventional Centre-of-Mass 80
4.2.2. Centre-of-Mass with Amplitude Thresholding 83
4.2.3. Centre-of-mass Amplitude Threshold 85
4.2.4. Centre-of-mass Slope Threshold 87
4.2.5. Cross-Correlation Matching 90
4.3. Overview of Performance Evaluation 93
4.3.1. Design goal and signal Processing Performance Requirements 94
4.4. Simulated Doppler signal 96
4.4.1. Principle of Generation 96
4.4.2. Method 97
4.4.3. Example of Generated Signal 99
4.4.4. Test Datasets 102
4.5. Results 104

4.5.1. Effect of Input SNR 104
4.5.2. Effect of Input Sample Length 110
4.5.3. Algorithm Processing Time 116
4.5.4. Discussion and Summary of Results 117
4.6. Summary 118
Chapter 5. Experimental Setup, Procedure, and Preliminary Analysis 120
5.1. Introduction 120
5.2. System Description 120
5.2.1. Hardware and Schematic 121
5.2.2. Installation of Radars on Test Vehicle 124
5.2.3. Recording Software 126
5.3. Data Processing Stages 127
5.4. Description of Test Site 131
5.4.1. Description of Data 132
5.5. Scenarios of Test 135
5.5.1. The trajectory of Test Vehicle and Period of Useful Data 137
5.6. Summary 140
Chapter 6. Experimental Results and Analysis 141
6.1. Introduction 141
6.2. Preliminary Analysis 142
6.2.1. Characteristics of Doppler spectra 142

6.2.2. Variation of Return Power 144
6.2.3. Calibration 146
6.3. Straight-Line Trajectory 148
6.3.1. Asphalt Surface (Test-scenario 1) 148
6.3.2. Elevated Bars (Test-scenario 2) 161
6.3.3. Off-Road Surfaces (Test-scenarios 3-6) 165
6.4. Circle Trajectory 174
6.4.1. Asphalt Road (Test-scenario 7) 175
6.4.2. Off-Roads (Test-scenario 8) 177
6.5. Vehicle Sideslip Angle Measurement 178
6.6. Summary 182
Chapter 7. Conclusion and Future Works 184
7.1. Summary 184
7.2. Conclusion 189
7.3. Future Works 191
Appendix A: Description of radar beam in space 198
Appendix B: SoG radar System Characteristics During No Motion 199
Appendix C: Comparison between low-cost GPS and differential GPS 201
Appendix D: Specification of Radar 203
Appendix F: Explanation of Software 208
Appendix G: Publication 220

List of Figures

Figure 1.1 Illustration of vehicle slipping during off-road conditions.....2

Figure 1.2 Various SRR applications [20].....3

Figure 2.1 A general block diagram of a radar.....10

Figure 2.2 Doppler phenomenon for a moving target.....14

Figure 2.3 Illustration of a radar moving above the ground.....15

Figure 2.4 Diagram of a monostatic CW radar.....17

Figure 2.5 A simple block diagram of a quadrature CW radar and the output waveforms. 19

Figure 2.6 Representation of Doppler signal powers spectrum (a) Single-channel system (b) Quadrature channel system.....20

Figure 2.7 An illustration of scattering of a surface. (a) purely flat and smooth (b) rough surface 21

Figure 2.8 An illustrative definition of parameters in the Rayleigh roughness criterion 22

Figure 2.9 Principle of measuring speed over ground using radar 23

Figure 2.10 A typical setup of SoG radar on a vehicle and the resultant Doppler Spectrum..25

Figure 2.11 An illustration of Doppler spectrum half-power width 26

Figure 2.12 Comparison of radar received power and its parameters 28

Figure 2.13 A typical example of a Doppler power spectrum.....29

Figure 2.14 Radar beam geometry a) On the flat surface. b) On the uneven surface.....31

Figure 2.15 An illustration of Janus configuration principle.....32

Figure 2.16 Comparison of relative error in measuring Doppler shift frequency. Comparison in different value of λ (a) λ = 12.5 mm (b) λ = 3.9 mm.....34

Figure 2.17 Comparison of relative error in measuring Doppler shift frequency. Comparison in different value of t_b (a) t_b = 1s (b) t_b = 0.1s 34

Figure 2.18 Rotational motions along the axis of a vehicle.....42
Figure 2.19 Illustration of the local reference frame and vehicle-body frame 43
Figure 2.20 Comparison between the plots of antenna gain pattern between sinc and Gaussian function 46
Figure 3.1 Geometry of radar beam (a) All of four beams viewed from the front, side, and top of a vehicle. (b) a single-beam at position 1 50
Figure 3.2 An illustration of misalignment angles.....53
Figure 3.3 Comparison of relative error of a single-beam system (a) α/β = 45°/0° (b) α/β = 45°/45° 57
Figure 3.4 Comparison of accuracy of a single-beam system with different values of depression angles 58
Figure 3.5 Comparison of relative error of two kinds of radar beam configuration.....61
Figure 3.6 Geometry of a radar footprint (a) Translation motion of a cone. (b) Illustration of a radar footprint 63
Figure 3.7 Comparison of radar footprint for five different values of depression angle, α. 67
Figure 3.8 The approximation of antenna radiation pattern using Equation (3.50).....69
Figure 3.9 An example of a Doppler spectrum.....71
Figure 3.10 Comparison of Doppler Spectrum for selected vehicle speeds. 72
Figure 3.11 Comparison of Doppler spectrum for selected depression angles.....73
Figure 3.12 Comparison of Doppler spectrum for selected azimuth angles.....73
Figure 3.13 Comparison of Doppler Spectrum at v = 1 mph (a) 24 GHz (b) 77 GHz 74
Figure 4.1 A qualitative illustration of a Doppler spectrum and its parameters.....80
Figure 4.2 An example of Doppler signal spectral density.....81
Figure 4.3 Steps of signal processing for CMA-NS 82

Figure 4.4 An examples of Doppler power spectrum. (a) Before suppression of noise. (b) After suppression of noise. 83
Figure 4.5 Steps of signal processing for CMA-T 84
Figure 4.6 An example of Doppler power spectrum. (a) before the removal of noise. (b) After the removal of noise. 84
Figure 4.7 Examples of algorithms outputs in Step 2 and 3 (a) Input Doppler spectrum (b) Cumulative sum in Step 2. (c) Measured gradient in Step 3. 90
Figure 4.8 Similarity between the Doppler power spectrum and Gaussian curve based on the signal. 91
Figure 4.9 Procedure for evaluating speed estimation algorithm 93
Figure 4.10 Procedure for generating Doppler signal 97
Figure 4.11 Examples of the simulated signal at five stages of the signal processing. (a) Noiseless Gaussian spectrum. (b) White Gaussian noise. (c) The power spectrum of the summation signal in (a) and (b). (d) Discrete samples of the time-domain Doppler signal. (e) The power spectrum of the Doppler signal in dB. (f) Example of actual Doppler signal collected from the experiment with the same radar parameters as in Table 4.2. 101
Figure 4.12 Examples of Doppler signal at different level of SNR 103
Figure 4.13(a) to (f) Comparison of bias and σ for a different level of SNR in Table 4.4. . 107
Figure 4.14 Histogram of 1000 mean frequency estimates for each of the algorithms. 109
Figure 4.15 (a) – (e) Comparison of bias and σ for values of Δf in Table 4.4 113
Figure 4.16 Comparison of relative error for SNR between 0 and 50 dB 115
Figure 4.17 Processing time of the algorithms. 116
Figure 5.1(a) Photograph of the 24 GHz radar transceiver 122
Figure 5.2 Block diagram of a 4-beam SoG radar 123

Figure 5.3 Illustration of X-Janus configuration showing the depression and azimuth angle of the radar sensor (a) top view (b) side view 124
Figure 5.4 Photographs of radar mounting (a) The front radar platforms, also shown is two video cameras mounted on the hood. (b) The rear radar platforms 125
Figure 5.5 A snapshot of the data acquisition software 126
Figure 5.6 Stages of Doppler data processing 127
Figure 5.7 HPF frequency response 129
Figure 5.8 $GPRMC data from the low-cost GPS receiver 130
Figure 5.9 Image of the test site which consists of 1.6-mile straight-track and off-road conditions 132
Figure 5.10 Images showing the condition of the road surface. (a) Asphalt (b) Concrete with elevated bars (c) Grass (d) Bumpy dirt (e) Wet dirt and (f) Water. 134
Figure 5.11 Illustration of the vehicle in the test of straight trajectory 135
Figure 5.12 Illustration of the vehicle in the test of the circular trajectory 137
Figure 5.13 Trajectories of test vehicle during the test. The trajectory for test-scenario 1 to 8 is shown on (a) to (h) respectively 139
Figure 6.1 Power spectra obtained from test-scenario 1 to 8. (a) Spectra from test-scenario 1. (b) Spectra from test scenarios 2 to 6 143
Figure 6.2 Plots of spectra peak power versus samples for data in test-scenario 1. 144
Figure 6.3 Plots of spectra peak power versus samples for data in test scenario 2 to 6 145
Figure 6.4 Radar speed measurement (a) Uncalibrated speed. (b) to (c): Calibrated speed. 146
Figure 6.5 Calibration factor of the SoG system 147
Figure 6.6 Results for v = 10 mph. (a) Radar vs. GPS. Plot of relative error and histogram for each algorithm, (b) CMA-AT (c) CMA-ST (d) XCA 150

Figure 6.7 Results for v = 20 mph. (a) Radar vs. GPS. Plot of relative error and histogram for each algorithm, (b) CMA-AT (c) CMA-ST (d) XCA 151
Figure 6.8 Results for v = 30 mph. (a) Radar vs. GPS. Plot of relative error and histogram for each algorithm, (b) CMA-AT (c) CMA-ST (d) XCA 152
Figure 6.9 Results for v = 40 mph. (a) Radar vs. GPS. Plot of relative error and histogram for each algorithm, (b) CMA-AT (c) CMA-ST (d) XCA 153
Figure 6.10 Results for Run 5 v = 70 mph. (a) Radar vs. GPS. Plot of relative error and histogram for each algorithm, (b) CMA-AT (c) CMA-ST (d) XCA 154
Figure 6.11 Trends of performance across five different speeds 157
Figure 6.12 Results for acceleration phase. (a) Radar vs. GPS Plot of relative error and histogram for each algorithm, (b) CMA-AT (c) CMA-ST (d) XCA 159
Figure 6.13 Results for the deceleration phase. (a) Radar vs. GPS. Plot of relative error and histogram for each algorithm, (b) CMA-AT (c) CMA-ST (d) XCA 160
Figure 6.14 Results for bumps. (a) Radar vs. GPS. Plot of relative error and histogram for each algorithm, (b) CMA-AT (c) CMA-ST (d) XCA 162
Figure 6.15 Results for a smooth surface. (a) Radar vs. GPS. Plot of relative error and histogram for each algorithm, (b) CMA-AT (c) CMA-ST (d) XCA 163
Figure 6.16 Results for Grass. (a) Radar vs. GPS. Plot of relative error and histogram for each algorithm, (b) CMA-AT (c) CMA-ST (d) XCA 166
Figure 6.17 Results for Bumpy dirt. (a) Radar vs. GPS. Plot of relative error and histogram for each algorithm, (b) CMA-AT (c) CMA-ST (d) XCA 167
Figure 6.18 Results for Wet dirt. (a) Radar vs. GPS. Plot of relative error and histogram for each algorithm, (b) CMA-AT (c) CMA-ST (d) XCA 168
Figure 6.19 Water measurements. (a) Radar return power. Plot of radar versus GPS speed estimated by algorithm (a) CMA-AT. (b) CMA-ST and (c) XCA 172

Figure 6.20 The trends of error across four types of off-road surface.....174

Figure 6.21 Results for asphalt road (v = 5 mph). (a) Radar vs. GPS. (b) Plot of relative error and histogram.....175

Figure 6.22 Results for asphalt road (v = 15 mph). (a) Radar vs. GPS. (b) Plot of relative error and histogram.....176

Figure 6.23 Results for Wet dirt. (a) Radar vs. GPS. (b) The measurement of relative error177

Figure 6.24 The velocity component and the side slip of a vehicle.....178

Figure 6.25 The circular track in JLR Gaydon. 180

Figure 6.26 The sideslip angle measurement at v = 5 mph (a) Estimated longitudinal speed, v_l (b) Estimated transverse speed v_t and (c) Estimated sideslip angle.....181

Figure 6.27 The sideslip measurement at v = 15 mph (a) Estimated longitudinal speed, v_l (b) Estimated transverse speed v_t and (c) Estimated sideslip angle.....181

List of Tables

Table 2.1 RMS height of several types of surface 23

Table 3.1 Values of radar parameters used in the analysis 70

Table 4.1 Design goal and performance criteria 94

Table 4.2 The values of radar parameter for the example of Doppler signal 100

Table 4.3 Main dataset and its sub-sets 102

Table 4.4 Relationship between FFT size, frequency, time and speed resolution 110

Table 5.1 Hardware description 121

Table 6.1 Statistical results obtained from Figure 6.6 to Figure 6.10 155

Table 6.2 The statistical results obtained from Figure 6.12 and Figure 6.13 161

Table 6.3 The statistical results obtained from Figure 6.14 and Figure 6.15 164

Table 6.4 The statistical results obtained from Figure 6.16 to Figure 6.18 169

Table 6.5 The statistical results obtained from Figure 6.22 176

Table 6.6 The statistical results obtained from Figure 6.23 177

Table 7.1: Comparison of different mean frequency estimation algorithm during a straight trajectory 188

Glossary of Abbreviations

ABS	Anti Braking System
ADC	Analogue to Digital Converter
AWGN	Additive White Gaussian Noise
BPF	Band Pass Filter
CMA-AT	Centre-of-Mass Amplitude Threshold
CMA-ST	Centre-of-Mass Slope Threshold
CW	Continuous wave
dB	Decibel
DC	Direct Current
DFT	Discrete Fourier Transform
DSP	Digital Signal Processor
DOF	Degree of Freedom
DGPS	Differential Global Positioning System
EM	Electromagnetic Wave
ESP	Electronic Stability Program
FFT	Fast Fourier Transform
F/V	Frequency to Voltage Converter
FMCW	Frequency Modulation Continuous wave
GPS	Global Positioning System
HPF	High Pass Filter
IF	Intermediate Frequency
JLR	Jaguar Land Rover
IMU	Inertial Measurement Unit
LNA	Low Noise Amplifier
MISL	Microwave Integrated System Laboratory
MIX	Mixer
OSC	Oscillator

PLL	Phase Lock Loop
PSD	Power Spectral Density
RCS	Radar Cross Section
RF	Radio Frequency
RMS	Root Mean Square
SNR	Signal to Noise Ratio
SoG	Speed over Ground
SRR	Short Range Radar
TV	Television
USB	Universal Serial Bus
XCA	Cross Correlation

Glossary of Terms

A	Area
a	Amplitude
a_i , a_q	Amplitude of in-phase and quadrature signal
a_{tx}	Transmitter channel amplitude
a_0	CUSUM reference value
a_g	Gaussian function amplitude
a_{rx}	Receiving amplitude in receiving channel
$a(n)$, $b(n)$	Real and Imaginary components of Doppler signal
$avg.\delta_v$	Average speed error
$\{B\}$	Vehicle-body frame
B_{ds}	Doppler spread
B_s	Bandwidth of system
b_m	Block size in CMA-ST algorithm
b_b	Backscattering coefficient
C_S	Cumulative sum
c	Speed of light
d	Distance from source to ground surface
d_1, d_2, d_3	Magnitude of direction cosines
$D(f)$	Digital output of the CMA-AT algorithm
E_{tx} , E_{rx}	Transmitted and received signal
f	Frequency
f_o	Mean Doppler frequency
f_c	Carrier Frequency
f_d	Doppler frequency

$f_{\min}$, $f_{\max}$	Minimum and maximum frequency
f_{start} , f_{stop}	Start and stop frequency
f_s	Sampling frequency
f_{rx}	Received frequency
σ_g	Doppler spectrum spreading at 3-dB
G_t , G_r	Transmitting and receiving antenna gain
g	Centre of gravity
h	Radar height from ground
I_d , Q_d	In-phase and quadrature component of Doppler signal
l,L	Semi-minor and semi-major axis of ellipse
K_{xy}	Cross-correlation between x and y signal
k_B	Boltzmann constant
k_n	SNR scaling factor
$\{L\}$	Local frame
$\max.\delta_v$	Maximum speed error
m	frame length
M , N	Upper limit of summation
N_t	Thermal noise
$\overline{N_r(f)}$	Averaged spectrum noise density
n	the n^{th} sample of a signal
O	Computational complexity
P_i , P_s	Incident and backscattering power
$P_{r_{\min}}$	Minimum detectable power
P_t , P_r	Transmitting and receiving power
p	Point on a ground surface
p_0	Antenna boresight point on a ground surface

$\boldsymbol{R}$	Rotation matrix
R_t	Range between radar and target
$R_{\max}$	Maximum range between radar and target
r	Radius
$\{x, y, z\}$	Cartesian coordinate
$SNR_{\min}$	Minimum SNR for received signal
$S(f)$	Power spectral density
T	Integration time
T_s	System noise temperature
t	Time
t_b	Observation time
$u_x\ u_y, u_z$	The angle between beam axis and velocity vector
v	Velocity
v_l, v_t, v_v	Longitudinal, transverse and vertical velocity
$\overline{v}_l$	Vehicle average longitudinal speed
v_r	Velocity estimated using radar
v_{GPS}	Velocity estimated using GPS receiver
w	Length of window in CMA-AT
$x(t)$	Continuous time-domain doppler signal
$x(n)$	Discrete sample time-domain doppler signal
$X(k)$	Discrete Fourier transform of $x(n)$
Z_1	Threshold 1 in CMA-AT step 2
Z_2	Threshold 2 in CMA-AT step 3
Z_g	Threshold value in CMA-ST step 4
$3\% \mathit{of}\ v_{GPS}$	Percentage of estimate that fell under 3% of GPS speed
Δf	Frequency resolution

Δt	Time resolution
Δv	Speed resolution
α	Depression angle
β	Azimuth angle
λ	Signal wavelength
σ	Standard deviation
σ_0	Radar cross-section
σ_n	Noise floor standard deviation
σ_g	Half-power spectrum standard deviation
σ_v	Vehicle speed standard deviation
$\Omega_S(\theta)$	Antenna radiation pattern using Sinc function
$\Omega_G(\theta)$	Antenna radiation pattern using Gaussian pattern
γ_b	Antenna 3-dB beamwidth
θ	Viewing angle
$\theta_{3dB-V}, \theta_{3dB-H}$	3 dB vertical and horizontal beamwidth of antenna
θ_0	Antenna boresight angle
$\delta_r, \delta_p, \delta_y$	Roll, pitch and yaw angle
φ	Received signal phase
φ_0	Constant phase lag
μ	Mean
Ψ_n	Surface roughness standard deviation
k	Frequency bin
ρ_{xy}	Cross-correlation of x and y signal
η	All constant of a radar system
Γ	Sideslip angle

Chapter 1. Introduction

1.1. Background

One of the essential systems in all modern vehicles are speed measurement system or speedometer system. Such system measures the vehicle's instantaneous speed or vehicle speed-over-ground (SoG). Presently, the vehicle speed is determined by measuring the rotation speed and known size of the wheel [1]. However, both parameters are prone to fault. For example, slippage between the wheel and road surface can happen when driving on the slippery road or off-road as shown in Figure 1.1. In extreme cases, when the wheels are locked, the speedometer will indicate the speed of zero, though the speed of the vehicle above the ground is by no means is zero. Furthermore, the classic speedometer system also assumes the wheel radius or the rolling radius to be constant. However, this is not true since tyre parameters such as pressure and radius can change during operation which causes erroneous measurements of speed.

There is a massive demand for accurate speed estimation system in the automotive industry [2]–[4]. Precise determination of SoG is a critical component of the modern vehicle and driving technology. Its use can be found in the various application including automatic vehicle control operations such as anti-braking system (ABS), electronic stability program (ESP) and for vehicle precise positioning system [5], [6]. Since tapping wheel is prone to slippage and locking of the wheel, a promising solution is to provide contactless speed measurement. Numerous contactless speed sensors have been proposed to replace the conventional speedometer system. These include GPS, Lidar (Laser Radar), Ultrasonic and Acoustics sensors [7]–[10]. Although these sensors can provide an accurate estimate of speed, the reliability of these sensors is less suitable in practice. GPS is known to fail when driving through underground places such as

tunnels and this technology also raises concerns over its long-term availability [11], for example, in the event of satellites failures. A laser can suffer substantial attenuation in the rain, snow and thick foggy conditions [12]. Ultrasonic sensors are susceptible to cross-talk from another ultrasonic sensor [13], and acoustics sensors cannot provide an accurate speed estimate at high speeds [8]. Due to these reasons, another type of sensor that is robust against weather and environment conditions is welcome. The microwave Doppler principle is particularly suitable here because it is the least affected by environmental influences such as temperature, wind, pollution, snow or rain. Furthermore, due to advancements in microwave technology, radar speed sensors have become relatively inexpensive and physically compact and small to be fitted on a vehicle. Because of these reasons, microwave radar has been recognised as a capable sensor for true speed over ground (SoG) system [14]–[17].

Figure 1.1 Illustration of vehicle slipping during off-road conditions

1.2. Motivation for the Present Work

As previously discussed, radar technology used for measuring vehicle speed is considered as one of the critical technologies for developing vehicular safety systems. However, to the best author's knowledge, there is no commercially available SoG radar equipped on passenger cars yet. Several patents in SoG developed in 1970 to 1990s can be found in [18]–[22]. In general, these systems were based on a single or dual-radar system which can estimate speed but cannot estimate the speed vector of the vehicle.

It is crucial to increase the number of radar beams to enable advancements in speed-vector measurements. Multiple radar beams can provide the capability to the SoG system to measure velocity vector in three dimensions. On the application point of view, the use of four-beam radars brings the SoG system consistent with the future development of the vehicular short-range-radar system (SRR) [23]. SRR is any radar for various vehicular application such as lane changing assistant, blind-spot detection, park assistant and others [24]–[26]. Hence, a 4-beam SoG system presents an application opportunity in the SRR area.

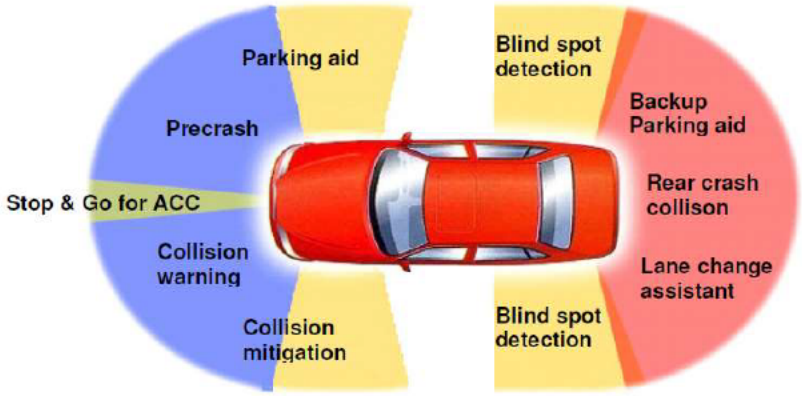

Figure 1.2 Various SRR applications [23]

While the SoG hardware has been developed and optimised in a variety of aspects such as frequency of transmission, antenna type, antenna beamwidth, and safety and health, the improvements in SoG signal processing is minor. Signal processing of Doppler signal has long been limited to techniques such as zero-crossing which is known to have the problem of loss in counting [27]. Recent advances in microprocessor technology have led to the development of inexpensive Fast-Fourier Transform (FFT) processors that enable computationally efficient processing of Fourier Transformation. Recent developments in SoG system signal processing are based on detecting mean frequency in Fourier-domain data [28], [29]. However, we must point out that the proposed processing method is computationally intensive and limited by the processing power. To meet the critical uses of SoG and to have a fast speed-update rate, it is crucial to develop methods that are less computationally extensive and produce accurate and reliable speed estimation.

1.3. Thesis Contributions

This thesis aims to improve the accuracy and reliability of SoG radar for vehicle operating on-road and off-road conditions. In particular, the objective is to introduce a 4-beam radar system and new speed estimation algorithms in dealing with off-road environments. To accomplish this aim, we have performed the following new studies

- Investigation of the influence of vehicle dynamics on the accuracy of speed measurement
- Investigation of the impact of radar parameters on the operation of SoG radar
- Development of new speed estimation algorithms
- Assessment of algorithms performance under simulated Doppler data

- Assessment of SoG performance through long experimental campaigns on a variety of real road conditions

The following points will be described briefly the main objective made in this thesis

Investigation of the influence of vehicle dynamics on the accuracy of speed measurement

SoG radar measures the speed of the ground it points by measuring the frequency change of the returned signal due to the Doppler effect. If the moving ground surface is illuminated at an oblique angle, the Doppler shift frequency is subjected to a reduced frequency given as $f_d = (2v/\lambda)\cos\theta$ where f_d is the Doppler frequency, λ is the carrier wavelength and θ is the oblique angle. A disadvantage of this method is that the measurement is sensitive to the value of the angle. When the vehicle is moving under off-road conditions, the oblique angle can change and therefore, produces an error in the speed measurement.

Improved accuracy can be gained by adding a radar beam in the opposite direction, where the offset angle in one beam can be cancelled out by the offset angle from another beam. This method of using multiple beams leads to improve speed estimation accuracy. In this thesis, the proposed speed estimation procedure is based on four radar beams that aim to reduce the offset angle during vehicle motions. Additionally, we provide the relationship between speed measurement accuracy and vehicle motions. This analysis is discussed in Chapter 3.

Investigation of the influence of radar parameters to the operation of SoG radar

One of the problems of a SoG designer face is providing suitable radar parameters for practical SoG operation. Heuristically, there is a common acceptance about some properties of good radar parameter candidates, for example, narrow beam antenna can provide small radar

footprint and narrow Doppler spectrum. However, this method of quantifying the radar parameters is based on experience and do not provide a deeper insight into the Doppler signal properties. Therefore, this problem creates a question of whether selecting specific values for each parameter can provide the best conditions for the operation of the SoG radar.

In this thesis, the relationship between the radar parameters and the size of the radar footprint on the ground surface is presented. Furthermore, we analysed the effect of radar parameters on the characteristics shape of the Doppler spectrum. A detailed description of this work is given in Chapter 3.

Development of new speed estimation method

An important aspect of speed accuracy enhancement is the development of speed estimation algorithm. Over the past decades, the speed estimation methods were based on time-domain processing. This method is quite attractive because the approach is relatively simple. For example, they can be realised by using a few electronic components. However, this method is not reliable when the Doppler signal is noisy and weak. Recently, due to the advancement of microprocessor technology, speed estimation can be performed in the frequency domain. Methods based on frequency domain offer more advantages in reducing the effects of noise in speed estimation and hence, produce more accurate speed estimation results.

This thesis proposes speed estimation methods based on the frequency domain. The proposed procedure is based on spectral centre-of-mass, where the emphasis is given to ensure accurate speed estimation results. Furthermore, for a weak return signal from the ground, a method based on correlation is proposed. The detail description of the algorithms is presented in Chapter 4.

Assessment of algorithm performance under simulated Doppler data

As been stated earlier, this thesis introduces three new speed estimation algorithms. However, it is not clear that what is the strength and weakness of each algorithm, and which algorithm should be preferred under a given vehicle operational condition, i.e., when operating under off-road environments. This thesis formulates a design goal and criteria that describes the algorithm suitability for speed estimation. The algorithms bias and variance are evaluated with simulated Doppler signal. Furthermore, the computational complexity of the algorithms is also presented. The detail descriptions of each algorithm performance are described in Chapter 4.

Assessment of SoG performance using Doppler signal collected through long experimental campaigns on a variety of real road conditions

The emphasis of this thesis was to contribute to the enhancement of SoG speed estimation accuracy. However, contribution via theoretical study is thought not enough. A practical assessment of the proposed SoG system presents additional challenges that need to be addressed. Therefore, it is necessary to perform testing of the 4-beam radar system and new algorithms under actual environments.

To verify the performance of the SoG radar system. A 4-beam radar is developed and mounted on an all-wheeled drive vehicle. The test vehicle was driven at different values of speed and various types of off-road ground surfaces to collect Doppler signals. Finally, the performance of the proposed speed estimation algorithm and the SoG itself were verified. More detail on the development of SoG radar system is presented in Chapter 5, and the results of the performance evaluation are presented in Chapter 6.

1.4. Thesis Outline

We divide this thesis into seven chapters. The following points describe the general content of each chapter

- Chapter 2 covers two parts of the theoretical review of radar. The first part of this chapter reviews the necessary knowledge in radar technology related to this work. The second part of this chapter describes the speed-over-ground radar system regarding the principle of measurement, errors and signal processing. This part also reviews the previous work in SoG radar.
- Chapter 3 describes the theoretical work of the proposed 4-beam radar system. The work includes the analysis of error due to vehicle motions and comparison to a single beam system. This chapter also theoretically investigates the size of radar footprint on the ground and the effect of radar parameters to the shape of the Doppler spectrum.
- Chapter 4 concerned with the speed estimation algorithms. The chapter begins with the introduction of the proposed algorithm, followed by modelling of artificial Doppler signal and the results of evaluation using synthetic Doppler signal.
- Chapter 5 describes in detail the SoG experimental setup and the procedure of testing the system.
- Chapter 6 presents the results of the performance assessment of the developed system under real-world conditions.
- Finally, Chapter 7 conclude the work in this thesis.

Chapter 2. Background

2.1. Introduction

This chapter provides a general overview of basic radar principles used in this thesis, as well as a more specific background investigation of speed over ground (SoG) radar. It does not cover in details of all aspects in speed over ground (SoG) radar, but to give the reader of this thesis a proper introduction of some knowledge is SoG radar that is needed for the following chapters. In the first part of this chapter, we review the fundamentals of radar technology which include the types of radar, radar range and radar cross-section equations, and the signal theory of CW radar. In the second part of this chapter, we discuss the concept of measuring speed using CW radar and the issues of accurate speed estimation. We review some previous research related to the improvement of speed estimation techniques. In the third part of this chapter, we discuss some basic theory of rigid body motions which is used to analyse the speed accuracy of moving the vehicle on uneven surfaces in the following chapter. Finally, we discuss some of the available methods or algorithms for estimating vehicle speed.

2.2. Basic Principle of Radar

The word RADAR is an acronym for Radio Detection and Ranging. A radar system functions to radiates electromagnetic waves (EM) to detect the presence of reflecting object in its searched area. Figure 2.1 shows the high-level representation of a radar system. The function of the transmitter is to generate a signal with a specific waveform and radiates it in the form of EM waves in the environment. If an object is present in that volume of space, the object will

reflect some amount of the transmitted energy to the receiver part of the radar system. This radar system determines the presence of the object and extracts the information about the object range, velocity and position in space [30]. In most cases, the received echo is weak and contaminated with some level of noise which can limit the accuracy of the range, velocity, and position estimation. The purpose of the signal processing block is to improve the accuracy of information extracted from the received signal.

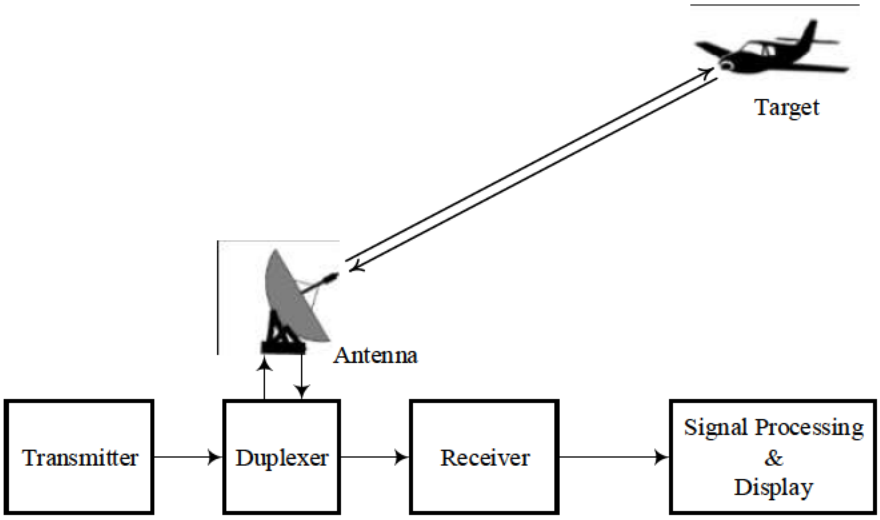

Figure 2.1 A general block diagram of a radar

2.2.1. Modes of Operation

Radar systems can be classified in several ways. Firstly, by its operation. Radar can be active or passive. An active radar owns its transmitter channel. In contrary to an active radar, a passive radar is primarily a receiver only radar. It collects signal from a target that is illuminated by one or multiple transmitters that do not cooperate with the receiver. This non-cooperative transmitter in the environment could be a TV broadcasting antenna or navigation system satellites such as GPS [31], [32].

Secondly, radar can also be categorised as monostatic or bistatic. Monostatic radar has its transmitter and receiver antenna located in the same place. Often, it shares the same antenna for signal transmission and echo reception. Radar is also considered as monostatic if the transmitter and receiver antennas are placed very close to each other. On the other hand, a bistatic radar has its transmitter and receiver spatially separated.

Thirdly, radar can be classified according to its waveform. A variety of radar waveforms can be found in the literature [30], but in general, it can be classified into continuous wave (CW) or pulses radar. The CW radar can be unmodulated CW or frequency modulated CW (FMCW). In contrast to continuous transmission, a pulsed waveform consists of a train of short pulses. The type of waveform defines the ability of the radar. CW radar can only measure the speed of a target; on the contrary, FMCW, and pulses radar can measure both speed and range of the target. The main disadvantage of CW radar is that it cannot measure the range of the target. Furthermore, sufficient isolation is needed between the transmitter and the receiver channel to keep high sensitivity detection [33].

2.2.2. Basic Range Equations

The radar range equation, often directly called the radar equation, is one of the crucial aspects in radar theory. It defines the relationship between the parameters that influence the radar signal when propagating from the transmitter antenna to the target, and from the target back to the receiver antenna. The received power by the radar is given as [30]

$$P_r = \frac{P_t G_t G_r \lambda^2 \sigma_0}{(4\pi)^3 R_t^4} \tag{2.1}$$

where P_r and P_t are the averaged received power and transmitted power in Watts, G_t and G_r is the directivity or antenna gain for transmitting and receiving antenna. λ is the carrier

wavelength, σ_0 is the radar cross-section (RCS), and R_t is the distance from the radar to the point target.

The theoretical maximum operational range of radar can be determined by rearranging Equation (2.1).

$$R_{\max} = \sqrt[4]{\frac{P_t G_t G_r \lambda^2 \sigma_0}{(4\pi)^3 P_{r_{\min}}}} \tag{2.2}$$

where $R_{\max}$ is the maximum distance in meters (m) of a target and $P_{r_{\min}}$ is the minimum detectable power at the receiver antenna. It can be predicted that if the range is required to double, the increase factor of P_t is 16-fold. In practical condition, the received echo from the target is corrupted by noise and therefore it best to describe the target range by using signal-to-noise ratio (SNR) at the receiver.

$$R_{\max} = \sqrt[4]{\frac{P_t G_t G_r \lambda^2 \sigma_0}{(4\pi)^3 N_t SNR_{\min}}} \tag{2.3}$$

where N_t is the thermal noise and is given as [30]

$$N_t = k_b T_s B_s \tag{2.4}$$

where k_b is the Boltzmann constant, T_s is the system noise temperature in Kelvin and B_s is the bandwidth of the system. Equation (2.3) assumes that the transmission medium is lossless. Factor such as water vapours along the propagation path can affect the received signal at the receiver. However, the description of this factor is beyond the subject of this thesis.

2.2.3. Radar Cross Section (RCS)

An object illuminated with EM waves will disperse the incident wave in all directions. This energy distribution in space is called scattering. Specifically, the energy reflected in the monostatic radar is called the backscattered wave. We quantify the intensity of the backscattering from the object by using the radar cross section (RCS).

RCS is a measure of the efficiency of a target in reflecting incident wave to the radar. The reflecting efficiency relies on many factors such as the size, shape, material composition of the object and the angular position of the object to the radar [34]. To make a useful comparison from one target to another, it is much more precise to compare the efficiency of each object in terms of cross-sectional area of an equivalent conducting sphere that would reflect the same amount of backscatter energy to the radar. The formal definition of RCS is given by [35]

$$\sigma_0 = \lim_{r\to\infty} 4\pi r^2 \frac{P_s}{P_i} \tag{2.5}$$

where P_s is power per unit solid angle of the backscattered wave and P_i is the incident power of transmitted wave impinging on the object. The RCS has a unit of m^2.

The theoretical RCS of some individual target such as a conducting sphere, cylinder or rectangular plates can be computed by electromagnetic theory [36]. However, many realistic targets of the human-made or natural object are too complicated to be represented by an equation. Nevertheless, some example of RCS measurements of an isolated object such as human, car, and aircraft can be found in [37].

RCS of a road surface

Unlike the individual objects such as a sphere or rectangular plate, a road surface is an extensive object, which means that the RCS depends on the amount of energy scattered by a spread of

area, in this case, the area corresponds to the footprint of the radar. The RCS of a road surface is given by [38]

$$\sigma_0 = b_b A \tag{2.6}$$

where σ_0 is RCS, A is the actual area on the road surface and b_b is the backscattering coefficient. The backscattering coefficient is a measure of the ratio between the transmitted power and received power by the radar, and it is unitless.

2.2.4. The Doppler Effect

Doppler effect or also known as Doppler shift is defined as the effective change of frequency of waves occurred when the transmitter of the wave is in relative motion with the target. An example of a Doppler effect that we probably have encountered is the sound of a police siren. As the siren comes close to us, the pitch sound of the siren becomes higher, and as it goes away from us, the sound becomes low-pitched. An illustration of this description is shown in Figure 2.2.

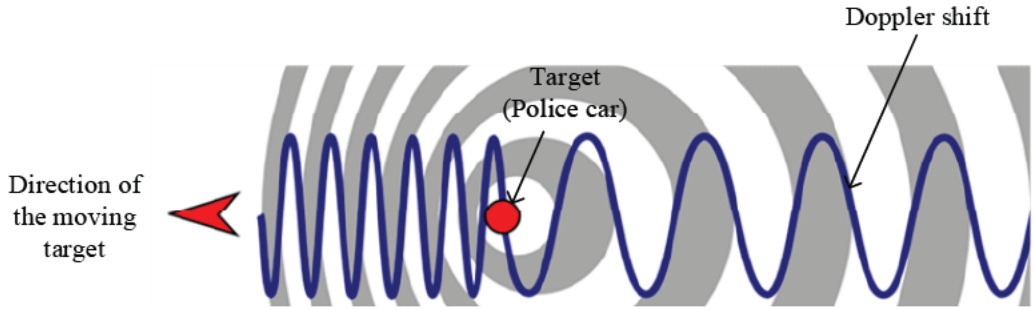

Figure 2.2 Doppler phenomenon for a moving target

Doppler effect has been utilised in speed measuring systems. Figure 2.3 [39] illustrates a moving radar with a speed of v relative to the ground surface. The electromagnetic wave is propagated to point p on the ground. Some small energy of the wave is reflected to the receiver of the radar. Quantitively, we can estimate the Doppler frequency due to the moving radar.

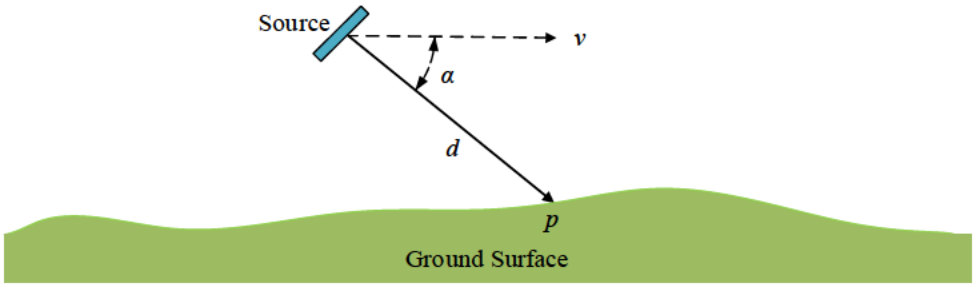

Figure 2.3 Illustration of a radar moving above the ground

The continuous wave emitted from the transmitter is a pure sine wave and can be given by

$$E_{tx}(t) = a_{tx}\sin(2\pi f_c t) \tag{2.7}$$

When the transmitted signal is reflected from a ground surface and returned to the radar, the received signal can be defined as

$$E_{rx}(t) = a_{rx}\sin(2\pi f_c t - \varphi) \tag{2.8}$$

where a_{tx} and a_{rx} are the signal amplitude, f_c *is* the carrier frequency, and φ is the phase lag of the received signal with respect to the transmitted signal. The phase lag is given by

$$\varphi = 2\pi\frac{2d}{\lambda} \tag{2.9}$$

where d is the distance between the radar and point p on the ground surface and λ is the carrier frequency wavelength. Over a short period of time the distance d can be presented by

$$d(t) = d_0 - vt\cos\alpha \tag{2.10}$$

where d_0 is the distance at $t = 0$ and α is the angle between the velocity, v, and the radar beam. By replacing φ and d in Equation (2.8) with the ones in Equation (2.9) and (2.10), the received signal can be written as

$$E_{rx}(t) = a_{rx}\sin\left[2\pi\left(f_c + \frac{2v}{\lambda}\cos\alpha\right)t - \frac{4\pi d_0}{\lambda}\right] \tag{2.11}$$

By comparing the received signal to the transmitted signal, the received signal differs by amplitude, frequency and constant phase lag ($\varphi_0 = (4\pi d_0)/\lambda$). However, the significant change is in the received frequency, f_{rx} where the frequency term is dependent on the velocity of the moving radar.

$$f_{rx} = f_c + \frac{2v}{\lambda}\cos\alpha \tag{2.12}$$

Thus, the change in frequency is given as

$$f_d = f_{rx} - f_c = \frac{2v}{\lambda}\cos\alpha \tag{2.13}$$

where f_d is Doppler shift frequency. A positive sign in Equation (2.13) indicates that the target is approaching the radar. On the other hand, Doppler frequency with a negative sign shows that the target is receding from the radar.

2.2.5. CW Radar Signal Theory

The type of radar employed in this work is classified as monostatic CW radar. Thus, it is worth to discuss the signal theory behind it. Two cases of CW radar system are shown here; single channel and quadrature (I/Q) channel. They are distinguished only by the down conversion mixer and the intermediate frequency (IF) circuitry. Later, it will be shown why the quadrature system is preferred for this project. Figure 2.4 Illustrates a single-channel CW radar consisting a pair of transmitting (Tx) and receiving (Rx) antennas, mixer (Mix), a frequency oscillator (Osc), a band-pass filter (BPF) and a Low Noise Amplifier (LNA) [30]. The CW radar output is indicated with I_d.

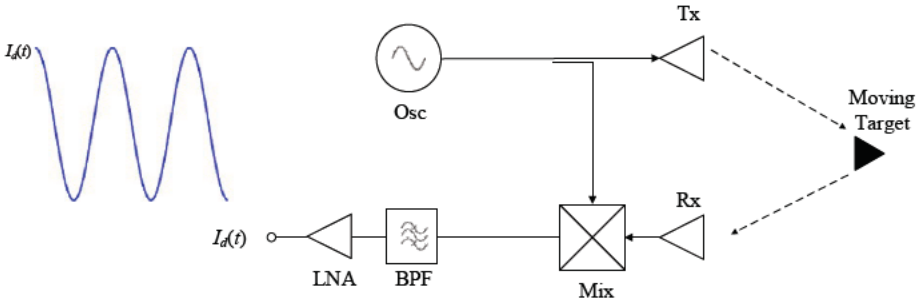

Figure 2.4 Diagram of a monostatic CW radar

The transmitted RF signal is generated by an RF oscillator and the waveform is a constant sine wave of

$$a_{tx}\cos 2\pi f_c t \tag{2.14}$$

This wave is radiated by the transmitter antenna (Tx). Let a moving target is present in the illuminated area, and some of the energy is reflected to the receiver antenna (Rx). The received signal can be represented as

$$a_{rx}\cos\left[2\pi(f_c+f_d)\right]t \tag{2.15}$$

The received echo is mixed with the transmitted signal ($a_{tx}\cos 2\pi f_c t$) in the mixer (Mix) as shown in Equation (2.16)

$$a_{rx}\cos\left[2\pi(f_c+f_d)\right]t \bullet a_{tx}(\cos 2\pi f_c t)=\frac{a_{tx}a_{rx}}{2}\cos\left[2\pi(2f_c+f_d)t\right]+\frac{a_{tx}a_{rx}}{2}\cos 2\pi f_d t \tag{2.16}$$

A BPF is coupled to the mixer to remove unwanted frequencies components. The filter selects only the Doppler signal but removes the DC and the RF components, leaving only Doppler signal at the output of the BPF. Finally, the LNA amplifies the Doppler signal that is suitable for further processing. The Doppler signal at the output of the LNA is given by

$$I_d(t)=a\cos 2\pi f_d t \tag{2.17}$$

where *a* is the amplitude of the Doppler signal which is determined by the received power and gain in the receiving channel.

Quadrature CW radar

Figure 2.5 illustrates a simplified block diagram of a quadrature CW radar. The received signal is divided into two channels known as In-phase, I_d and Quadrature, Q_d (these channels are also known as I/Q pair). The in-phase channel is like the one in the single channel system, hence producing the same output signal. The difference is the quadrature channel where the received signal is mixed with the transmitted signal that is phase shifted by 90°.

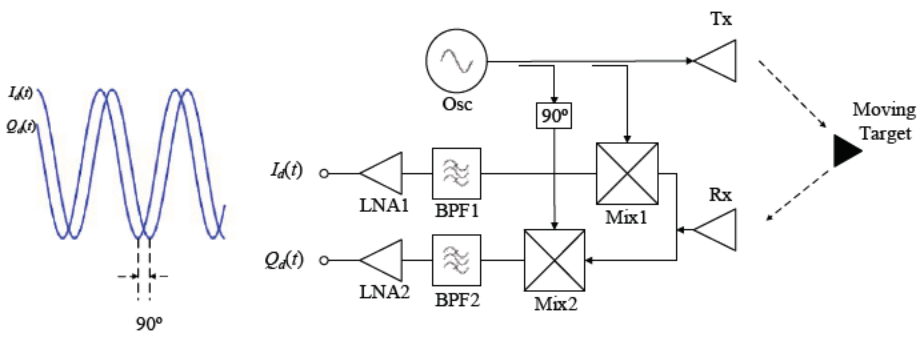

Figure 2.5 A simple block diagram of a quadrature CW radar and the output waveforms.

The comparison of power spectral density between a single channel and quadrature channel is shown in Figure 2.6. For a single-channel system in Figure 2.6(a), the spectral density is observed on both positive and negative halve of the spectrum. The existence of negative frequency is because of the nature of Fourier transforms which 'mirrored' the real signal into positive and negative halve of the spectrum. Therefore, it is not possible to determine the direction of the target's velocity. However, by combining the outputs of the in-phase and quadrature channels, we can estimate the target if moving towards or away from the radar. The outputs of the demodulator can be defined as

$$I_d(t) = a_i \cos 2\pi f_d t \tag{2.18}$$

$$Q_d(t) = a_q \sin 2\pi f_d t \tag{2.19}$$

We can formulate a complex Doppler signal from Equation (2.18) and (2.19)

$$a_i \cos(2\pi f_d t) + j a_q \sin(2\pi f_d t) = a e^{j 2\pi f_d t} \tag{2.20}$$

We can determine the power spectral density by squaring the magnitude of the Fourier transform of the complex signal. Figure 2.6(b) illustrates the power spectral density of the complex signal. Note that, the details of Fourier transform will be given in Section 2.6.1.

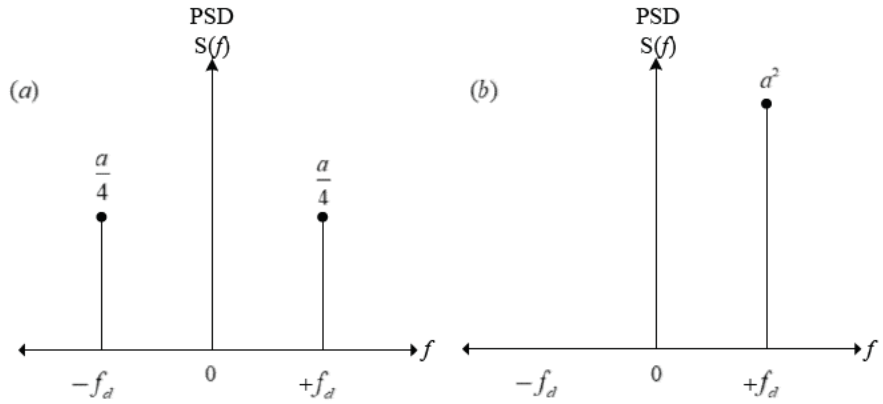

Figure 2.6 Representation of Doppler signal powers spectrum (a) Single-channel system (b) Quadrature channel system

From Figure 2.6(b) we can see that the power spectrum of the quadrature channel system has a single peak at $+f_d$. Thus, the direction of the target can be determined using the power spectral density of the Doppler signal.

2.3. The principle of SoG Radar

2.3.1. Consideration of Ground Surface

One of the essential pre-requisites in the operation of a SoG radar is the roughness of the ground surface. Although many types of surface are visually identical, their backscattering characteristics are different.

The magnitude of backscatter-wave from any types of the surface depends upon the roughness of the surface. This condition can be explained by comparing the scattering between a purely smooth and random surface in Figure 2.7(a) and (b) respectively. In (a), because the surface is smooth, all the incident energy is forward-reflected, and no energy is backscattered. Contrary to (b), the increase in surface roughness produces a scattering which is quasi-Lambertian, which means that most of the scattering is random, but still, some of the energy is coherent in the forward-reflection. A pure Lambertian reflection would scatter the incident-wave randomly in all direction [15].

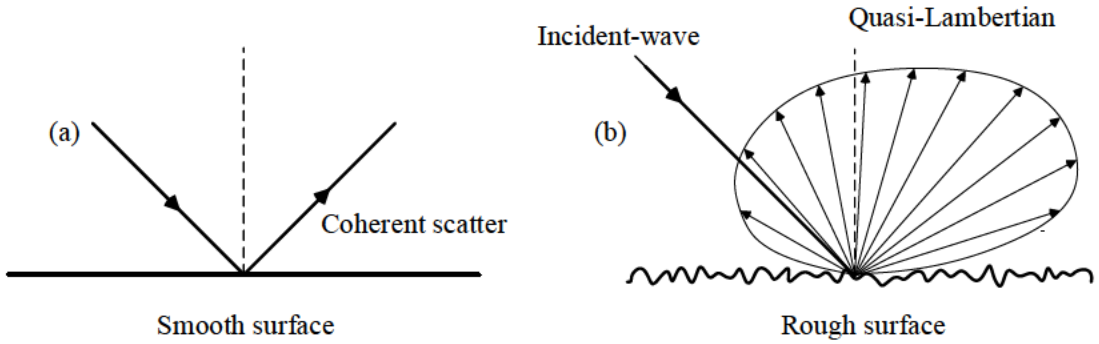

Figure 2.7 An illustration of scattering of a surface. (a) purely flat and smooth (b) rough surface

Theoretically, the Rayleigh roughness criterion is used to estimate the degree of roughness of a surface [42]. This criterion is used as a guideline whether the surface is rough or smooth according to the wavelength and incidence angle of the waves. The Rayleigh criterion is given as

$$\psi_n \geq \frac{\lambda}{8\sin\alpha}\,[cm] \tag{2.21}$$

where Ψ_n is the standard deviation of the surface roughness in centimetre, λ is the wavelength and α is the incidence angle of the incident waves. Figure 2.8 shows the geometry for discussion of the criterion. The surface is considered rough if $\psi_n \geq \lambda / 8 \sin \alpha$ or smooth if $\psi_n \leq \lambda / 8 \sin \alpha$. Equation (2.21) also tells us that the surface roughness is dependent on three parameters; Ψ_n , λ and α. Radar operating at a higher frequency can work on the smoother ground surfaces. For example, if a CW radar is transmitting 24 GHz wave at α = 45°, the minimum surface roughness, Ψ_n must be 0.02 mm. For radar operating at a higher frequency such as 77 GHz, the minimum surface roughness is 0.006 mm.

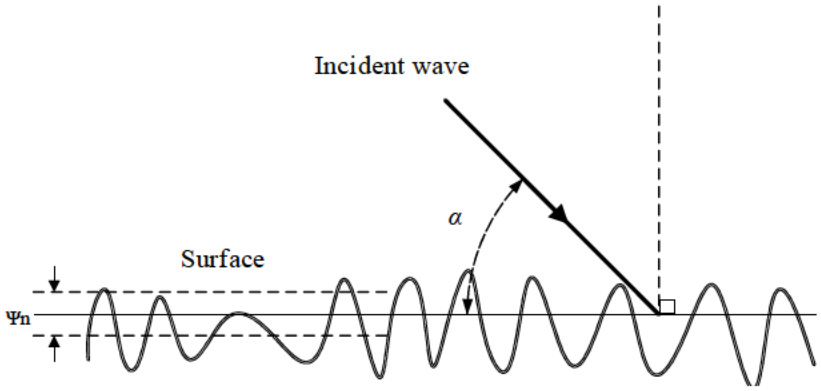

Figure 2.8 An illustrative definition of parameters in the Rayleigh roughness criterion

Due to the difficulty in measuring the exact roughness of surfaces, the RMS height of the ground surface is generally used as the roughness representation [43]. Table 2.1 below shows measurements of RMS height for some surfaces obtained from [44], [45], [46]. The present analysis shows that the for radar operating at high frequency, i.e., 24 GHz, the backscattering signal can be obtained for asphalt and dirt or soil surfaces.

Table 2.1 RMS height of several types of surface

Surface types	RMS Height (mm)	Surface types	RMS Height (mm)
Smooth concrete	0.2	Harrowed agricultural soil	16
1-year old (smooth) asphalt	0.34	Ploughed agricultural soil	27
Rough asphalt	0.9	Grass covered field	90
Agricultural seedbed	6		

2.3.2. An Ideal Speed Measurement

Figure 2.9 depicts a conventional setup of SoG radar for estimation of vehicle speed. The non-contact speed measurement is based on the back-scattering of the electromagnetic wave from the ground surface. Hence, the transmitting and receiving antenna of the Doppler radar must be fixed at an oblique angle, α. The rough surface diffuses the incident-waves, and accordingly, beams are collected on the receiver antenna. The Doppler effect causes the reflected signal frequency to be shifted. This return echo is mixed with the transmitter signal to produce a Doppler shift frequency, f_d that is proportional to the speed of the moving vehicle.

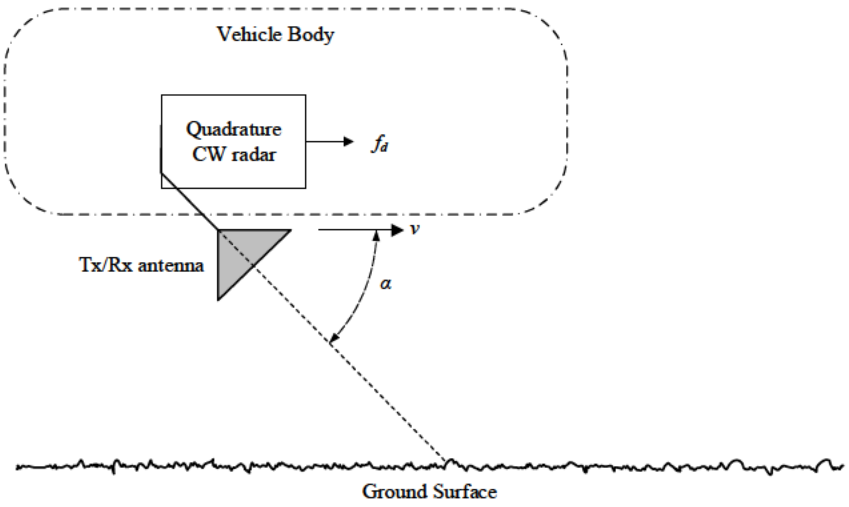

Figure 2.9 Principle of measuring speed over ground using radar

In an ideal condition, the output of the Doppler radar produces a single frequency that is directly proportional to the speed of the moving vehicle above the ground. Hence, the speed of the moving vehicle can be determined by only using the classic Doppler equation

$$v = \frac{f_d \lambda}{2 \cos \alpha} \tag{2.22}$$

2.3.3. Doppler Spectrum

In the previous discussion, the radar beam is considered very narrow and drawn as a single line as in Figure 2.9. However, a practical SoG radar has an antenna with considerable beamwidth. Because the radar echo comes from an antenna with finite beamwidth, the resultant echo cannot be a single Doppler frequency but constitute of spread frequencies that is described by a frequency spectrum.

For this discussion, consider a typical SoG configuration presented in Figure 2.10. Let a radar with antenna beamwidth of γ_b mounted on the vehicle with a viewing angle of α moving with a constant velocity in the direction of travel. For simplicity of explanation, let us consider the setup is 1-dimensional. In this case, the radar illuminates a strip of line on the ground bounded by the antenna beamwidth. Let the illuminated strip consist of many point scatterers with a point p as an illustration of a point scatterer on the line.

The lower portion of Figure 2.10 illustrates the Doppler power spectral density from all scatterers under the illuminated area. Most of the spectral power is concentrated in the shaded region, which defined as the main lobe of the spectrum. The power of the spectrum reaches a maximum when the boresight of the radar antenna directly illuminates the point p_0. The location of the peak amplitude is the mean frequency of the Doppler spectrum [27], [39].

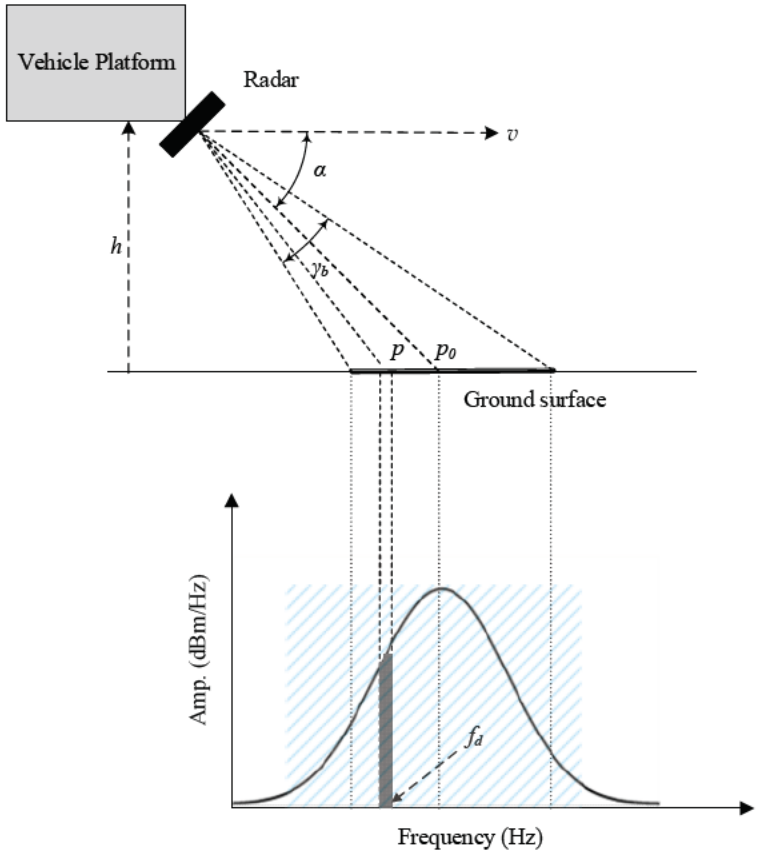

Figure 2.10 A typical setup of SoG radar on a vehicle and the resultant Doppler Spectrum

Some approximation about the statistical properties of the Doppler spectrum has been given by [27], [39]. In general, the shape of Doppler power spectral density is assumed like the characteristics of a probability density function. Specifically, it is assumed that the half-power width of a Doppler spectrum is equal to the standard deviation of the Doppler frequency about its mean value. Figure 2.11 shows the spectral half-power width and the standard deviation of a Doppler power spectral density.

$$\sigma_{ds} = \frac{B_{ds}}{2} \tag{2.23}$$

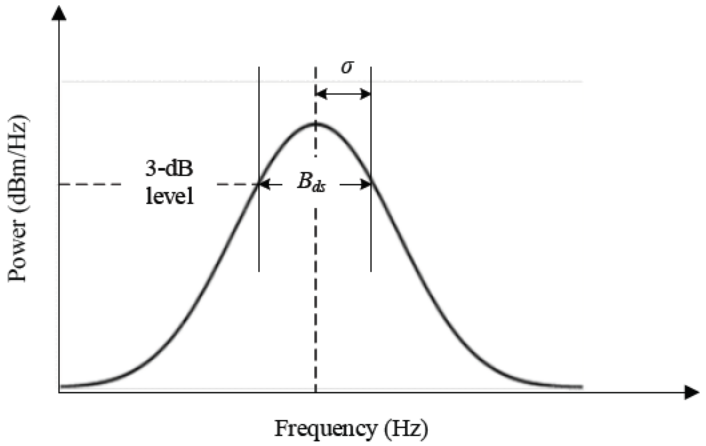

Figure 2.11 An illustration of Doppler spectrum half-power width

From Figure 2.11, the half-power bandwidth of a Doppler spectrum can be defined using the 3-dB beamwidth of the radar antenna [39]

$$B_{ds} = \frac{2v}{\lambda}\left[\cos\left(\alpha - \frac{\gamma_b}{2}\right) - \cos\left(\alpha + \frac{\gamma_b}{2}\right)\right] \tag{2.24}$$

$$B_{ds} \approx \frac{2v}{\lambda}\gamma_b \sin\alpha \tag{2.25}$$

The standard deviation of the Doppler spectrum half-power width is approximately

$$\sigma_{ds} \approx \frac{v}{\lambda}\gamma_b \sin\alpha \tag{2.26}$$

One conclusion that can be made from Equation (2.25) is that the spread of the Doppler spectrum is a function of the speed v, depression angle, α, and the beamwidth, γ_b of the antenna. As the value of these parameters (v, α and γ_b) increases, the spread of the Doppler spectrum will also increase.

A meaningful interpretation of Doppler spectrum requires an understanding of the effects of radar parameters on the shape of the Doppler spectrum. Particularly the amplitude at a specific frequency in the spectrum is related to the echo power when viewed from a certain angle from the antenna boresight, θ_0. Assuming the scatterers on the ground surface is uniform, the power distribution of the return echo around the antenna boresight can be evaluated using the radar received power equation [8]

$$P_{\mathrm{r}}(\theta) = \eta \frac{\sigma_0(\theta)\Omega_s^{\,2}(\theta-\alpha)}{R_t^{\,4}(\theta)} \tag{2.27}$$

here θ is the angle with respect to the horizontal plane and η is all the constant of the radar system, σ_0 is the radar cross section (RCS) of the ground surface, Ω_s is the antenna gain pattern which is given by a sinc function, and R_t is a range. Figure 2.12 shows a qualitative plot of radar received power when viewed around boresight of the radar beam. For comparison purpose, radar parameters including RCS, Ω_s and R_t of different values across the viewing angle are also plotted. As can be seen, the shape of the received power is influenced mainly by the antenna gain pattern, Ω_s. A careful examination of this figure shows that the Doppler mean frequency is slightly biased to the left side when compared to the peak of Ω_s. This condition is due to range bias, cosine angle bias and the roughness of the surface.

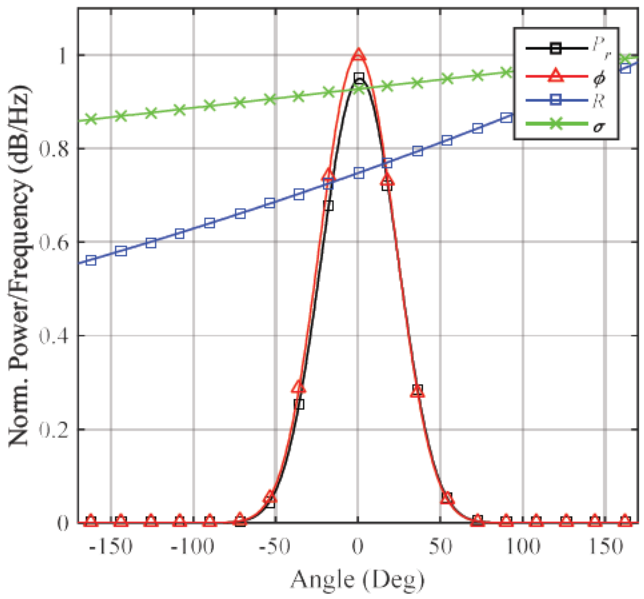

Figure 2.12 Comparison of radar received power and its parameters

The influence of surface roughness on the shape of the Doppler spectrum have been investigated by several researchers. In [47], they show that the Doppler spectrum from a rough surface observed at a viewing angle of 45° is characterised by a normal distribution around the mean Doppler frequency. In comparison, a relatively smooth surface generates a Doppler spectrum that is skewed, which causes a shift in the peak of the power spectrum in the direction of lower frequency. This effect is known as 'terrain bias,' and it is known to reduce the accuracy of the estimated speed in aircraft Doppler navigation systems [48]. A compensation method for water surface is proposed to reduce the error when traveling across oceans. However, for land vehicles, the effect of terrain bias is not dominant [49]. Nonetheless, a theoretical analysis of wave scattering from a rough surface by [50], [51] shows that the shape of the spectrum asymmetrical around its mean frequency. As the surface roughness increases, the width of the

spectrum lobe also increases, on the other hand, for decreasing roughness, the width of the main lobe become more narrow [47].

The nature of amplitude fluctuations of Doppler signal

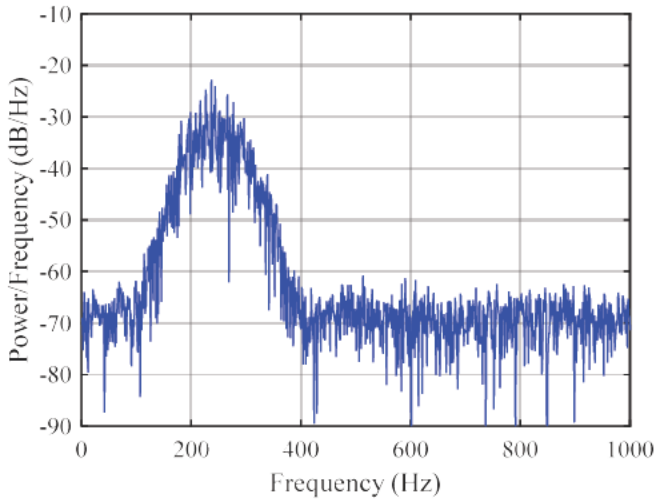

Figure 2.13 A typical example of a Doppler power spectrum

Figure 2.13 shows a typical example of the random nature of the Doppler signal. The random intensity of the main lobe is due to the combinations of many backscatter returns from the ground surface. Each backscatter signal has slightly different amplitude and phase from another backscatter signal which may interfere constructively or destructively, creating random variations in amplitude.

2.3.4. Mean Frequency Estimator

A critical characteristic of a SoG radar system is its ability to estimate the average instantaneous frequency over a short interval of time, or we called simply the mean frequency of the Doppler signal. In general, there are two ways of estimating the mean frequency of the Doppler signal; the primary method is outlined below:

- Time-domain estimator
- Frequency-domain estimator

In time-domain, the estimation of mean Doppler frequency is direct because the Doppler signal is already in time-domain. Measurement of mean frequency is performed by counting the zero-crossing of the Doppler signal over an interval of time [52]. A simple version of a time-domain estimator can be developed using inexpensive electronics components [47].

On the other hand, a frequency-domain estimator is based on spectral analysis. In this method, the Doppler signal is decomposed into its fundamental frequency components. This method requires the use of a microprocessor and can be more expensive than the time-domain method. Nonetheless, the use of a microprocessor can further improve the quality of estimate by implementing algorithms that can suppress or evade noises in the signal.

2.4. Main Errors in SoG

Error in velocity measurement arises from differences between the measured velocity (speed and direction) and the true velocity of the vehicle. Kees et al. [49] listed several errors in SoG speed measurement. However, the main errors can be classified into two main types of error, that is a systematic error (Beam geometry error) and signal fluctuation error.

2.4.1.1. Beam Geometry Error

Figure 2.14(a) illustrates an ideal operation of SOG radar. The ground is drawn ideally flat, and vehicle velocity is parallel to the ground surface for all time. However, in a practical scenario, the vehicle velocity is not always parallel to the ground. This condition is particularly true in the circumstance of driving on off-road conditions where the road surface is not flat as illustrated in Figure 2.14(b). The front end of the vehicle moves upwards, effectively changing the radar viewing angle and thus the velocity vector of the vehicle. The radar itself has no way to know the degree of the offset angle unless an inertial measurement unit (IMU) is equipped to the radar system. This situation produced an erroneous speed measurement. The extent of this problem depends on the severity of the road condition and the wheels' suspension system of the vehicle. The error angles can be several degrees when moving on off-road conditions [53].

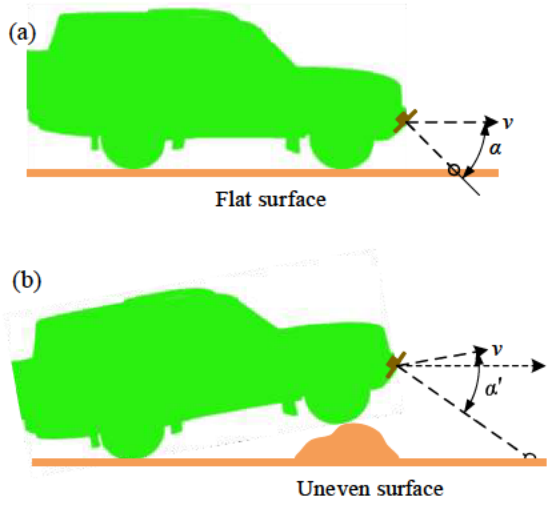

Figure 2.14 Radar beam geometry a) On the flat surface. b) On the uneven surface.

Many works in SoG proposed the use of dual-beam radar to minimise the impact of uneven surface on the accuracy velocity estimation [19], [20], [54]. This configuration has a much

lower sensitivity of error due to the perturbation of the vehicle. This principle behind this approach is called the Janus configuration [55] (Janus is a mythical Roman God who faces both past and future), which places two transducers to produce forward and backward beam to cancel the misalignment error introduced by the angular motions of the vehicle. Figure 2.15 shows the depiction of dual-Janus Configuration.

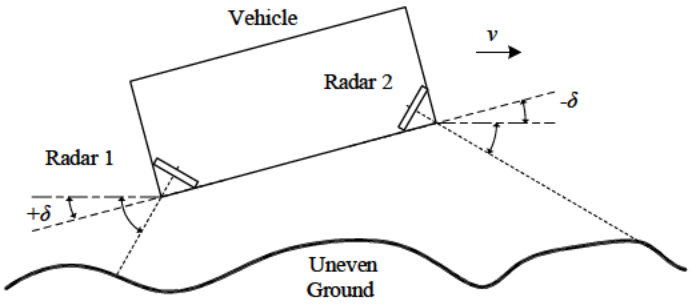

Figure 2.15 An illustration of Janus configuration principle

Let assume that the vehicle in Figure 2.15 experiences an angular motion. This motion changes the viewing angle of Radar 1 and Radar 2 by the amount of angle -δ and +δ respectively. The difference of Doppler frequency between the two radar beams can be described as

$$f_{\Delta} = f_{radar\,1} - f_{radar\,2} \tag{2.28}$$

$$f_{\Delta} = \frac{2v}{\lambda}\left[\cos(\alpha+\delta)+\cos(\alpha-\delta)\right] = \frac{2v}{\lambda}\left[\cos(\alpha)\cos(\delta)\right] \tag{2.29}$$

where f_{Δ} is the difference in Doppler frequency between Radar 1 and Radar 2. As can be seen in Equation (2.29), this technique minimises the error to cos(δ). For a small cosine angle of less than 10°, the cosine value is near to unity. Hence Equation (2.29) is reduced to

$$f_{\Delta} \approx \frac{2v}{\lambda}\cos\alpha \tag{2.30}$$

2.4.1.2. Fluctuation Error

Fluctuation error defined as the random fluctuations in the spectral density of a Doppler spectrum. The fluctuation error in SoG radar is a result of two factors; one is due to the finite bandwidth of the practical antenna, and another is due to the characteristics of the ground surface. Combination of these elements produce fluctuations in the amplitude of the Doppler spectrum as illustrated in Figure 2.13. The fluctuation error is measured by finding a ratio between the standard deviation of the spectrum main lobe to the mean frequency of the Doppler spectrum and is given by [47]

$$\frac{\sigma_{ds}}{f_d} = \frac{1}{2}\frac{\sqrt{\lambda\gamma_b}}{\sqrt{vt_b}}\frac{\sqrt{\sin\alpha}}{\cos\alpha} \tag{2.31}$$

where σ_{ds} is the standard deviation of the 3-dB bandwidth of the Doppler spectrum and t_b is the observation time. The relative error is calculated as, Relative error = $\left(1-\sigma_{ds}/f_d\right)100$.

It is essential to understand the effect of radar system parameters – λ, α, γ_b and t_b to the accuracy of measuring speed from a noisy spectrum. Equation (2.31) can be used to estimate the effect of the radar parameters. Figure 2.16 compares the relative error of measuring the speed of a 24 GHz (λ = 12.45 mm) and 77 GHz (λ = 3.9 mm) radar. As can be seen from the two plots, higher transmitter frequency produces a lower relative error. However, the difference is not significant for example, at nominal viewing angle and antenna beamwidth of $\alpha = 45°$ and $\gamma_b = 13°$, the difference in error is just 2%.

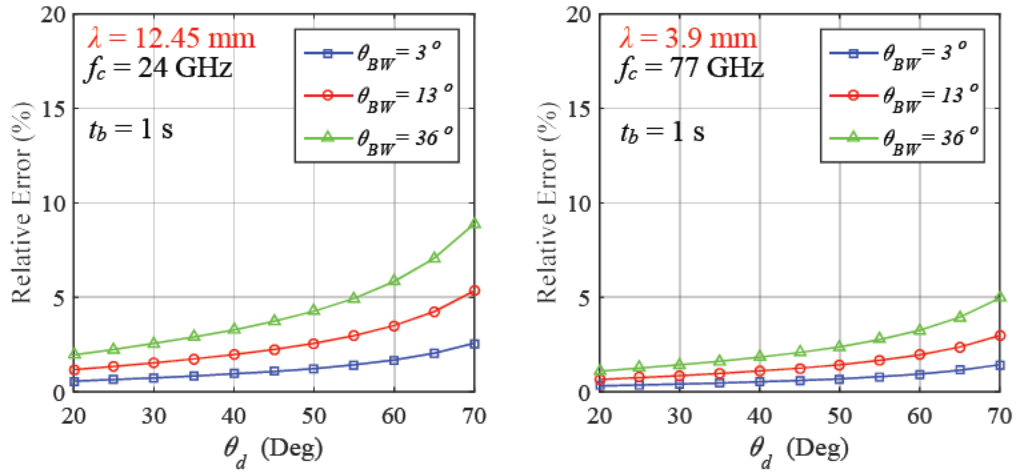

Figure 2.16 Comparison of relative error in measuring Doppler shift frequency. Comparison in different value of λ (a) λ = 12.5 mm (b) λ = 3.9 mm

Likewise, Figure 2.17 compares the relative error of measuring speed with two different observation period. Evidently, from the plots, shorter observation period (t_b = 0.1 s) increases the relative error. For a long observation period (t_b = 1 s), the error in measuring Doppler shift frequency is significantly lower. For example, at a nominal viewing angle of α = 45° and antenna beamwidth, γ_b = 13°, the difference in error is 5%.

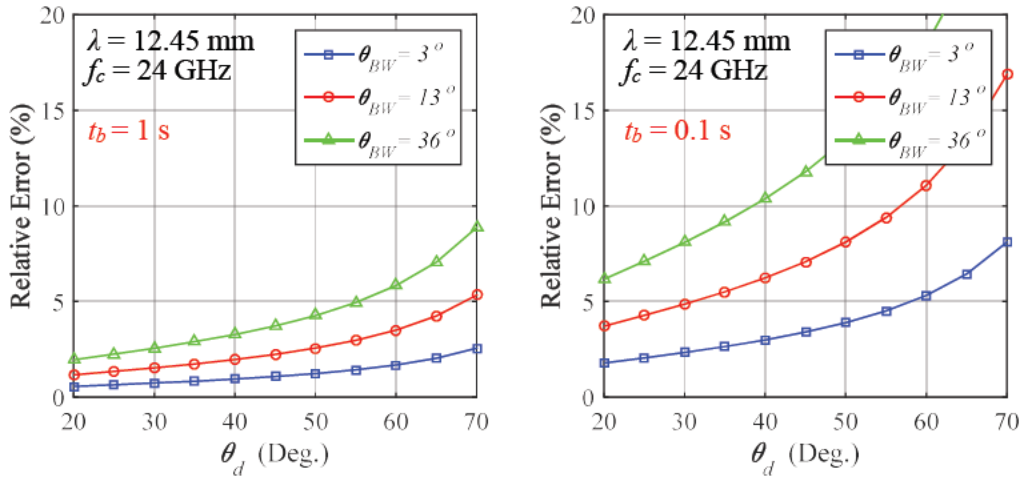

Figure 2.17 Comparison of relative error in measuring Doppler shift frequency. Comparison in different value of t_b (a) t_b = 1s (b) t_b = 0.1s

Two conclusions can be derived from the four plots. Firstly, the relative error in measuring frequency becomes smaller for an antenna with narrower beamwidth, and secondly, the steeper angle of the antenna viewing angle produces a higher relative error. The antenna viewing angle presents a compromise between speed measurement error and the strength of return echo.

2.5. Literature Review on Mean-Frequency Estimation Methods

In the early nineties, when microprocessors were mostly unavailable, almost all patents in SoG were based on the time-domain zero-crossing method [19]–[21], [56]. This method is based on measuring the zero-crossing rate of the Doppler signal. The zero-crossing rate is defined by [52], [57]

$$z_c(n) = \sum_{m=-M}^{M} \left|\text{sgn}\left[x(m)\right] - \text{sgn}\left[x(m-1)\right]\right| w(n-m) \tag{2.32}$$

where

$$\text{sgn}\left[x(n)\right] = \begin{cases} 1, & for\ x(n) \geq 0 \\ -1, & otherwise \end{cases} \tag{2.33}$$

and

$$w(n) = \begin{cases} 1/(2M) & for\ 0 \leq n \leq M-1 \\ 0 & otherwise \end{cases} \tag{2.34}$$

where z_c is the zero-crossing and m is the frame length and M is the limit of summation. One of the advantages of this method is the simplicity of operation and can be implemented using inexpensive frequency to voltage (F/V) converter circuit. However, this method relies on very high SNR and sensitive to noise. Hyltlin et al. [27] explain that random amplitude modulation

can generate a return echo that is too weak and hence undetectable by the zero-crossing circuit. Due to this reason, the speed estimation error based on this method could not be sustained lower than 1%. The Doppler mean frequency can also be estimated using Phase-lock-loop (PLL) [27]. In general, PLL is a servo system that tracks one signal using a reference signal in frequency and phase. It keeps two signals almost synchronising by adjusting the phase of the reference signal and monitoring the phase error between the two signals. For more details of PLL, the reader is advised to read [58]. Like the zero-crossing, this method can be implemented using analogue circuits. Furthermore, this method is low-cost and can provide real-time speed measurement. However, the main disadvantage of this method is that it requires high SNR to estimate speed accurately. Also, designing the loop filter can be complicated because the locking width of the PLL usually is narrow which can be a problem with the spreading of the Doppler signal. Due to this reason, the accuracy of PLL cannot be sustained lower than 1% at high speed (i.e., 60 mph).

Many researchers use spectral-based estimation [28], [29], [59]. This motivation is mainly due to the availability of optimised DSP systems which permits frequency analysis in a small but powerful microprocessor. Furthermore, it is much easier for SoG designers to minimise or evade the impact of noise in the frequency domain.

In general, processing via frequency domain is divided into three main steps which are (1) digitising the time-domain signal, (2) Fourier transformation of time-domain signal and (3) finding the mean-frequency of the Doppler signal. For the signal digitisation, it is necessary to use the analogue-to-digital converter (ADC). Furthermore, to avoid aliasing, the sampling frequency must be at least twice the maximum Doppler frequency of the SoG system.

2.6. Frequency Domain Methods

In this section, we review some principles theory of FFT and the basic principle behind the mean frequency estimation from a Doppler spectrum.

2.6.1. Fourier Transform

The mapping of a time-varying signal to its frequency distribution can be performed using the Fourier Transform. Fourier Transform decomposes the time-varying signal to the sum of basic sinusoids signals of different frequencies. The Fourier transform for a continuous signal, $x(t)$ with infinite length is defined as [60]

$$X(f) = \int_{-\infty}^{+\infty} x(t) e^{-j2\pi ft} dt \tag{2.35}$$

For discrete Fourier transform, the sequence of a complex number $x(n)$ is transformed into a sequence of frequency X(k). The value of each frequency bin, k is determined by the sampling frequency. In the real world, the signal has a finite length. Hence, X(k) can be defined for the discrete finite waveform.

$$DFT(k) = X(k) = \sum_{n=0}^{N-1} x(n) e^{-j\frac{2\pi}{N}kn} \tag{2.36}$$

For N-point DFT, the frequency resolution of DFT is given by f_s/N. Each bin of DFT output corresponds to a frequency. In particular, the frequency of the kth bin is given by $f = k$ (f_s/N). The energy spectral density of the DFT can be computed by squaring the magnitude of DFT, $|X(k)|^2$. We can call the squared magnitude as the power spectral density or simply PSD. Whereas, the magnitude of DFT is related to the magnitude spectrum. In practice, the PSD is usually represented using a log scale with the decibel unit.

$$dB(|X(k)|) = 20\log_{10}(|X(k)|) = 10\log_{10}(|X(k)|^2) \quad (2.37)$$

DFT has a computational complexity of $O[N^2]$. Because of this reason, the operation of DFT requires a powerful computer for an increased size of N [60]. The requirement for powerful computer has made DFT to be useless for many practical engineering problems. An efficient version of DFT is called Fast Fourier Transform (FFT). This method breaks the computation of DFT into two or more shorter DFTs and merges the results appropriately. Compared to DFT, FFT significantly reduces the computational complexity to $O[N\log_2(N)]$. This efficient method of computing DFT makes it's popular in many fields of engineering. For details on how FFT is performed, the reader is suggested to read [60].

However, DFT has two main disadvantages. Firstly, the fundamental trade-off between resolution in time and resolution in frequency. To obtain a good frequency resolution, we need to have more samples in time-domain. Hence, good frequency resolution implies poor time resolution. The second one is due to the spectral leakage in DFT. DFT assumes that time domain signal is periodic and infinite. However, if the time-domain input is not an integer multiple of the period, this causes a spectral leakage in the frequency domain. This leakage is due to the windowing process which selects only a limited number of samples from a time-domain signal.

2.6.2. Methods of Mean frequency estimations

There are two methods used to estimate the mean frequency of the Doppler signal in this thesis. The first one is based on centroid or centre-of-mass of the spectrum and the second is based on cross-correlation.

Centre-of-mass

Mathematically, the mean frequency of the Doppler signal is associated with the first spectral moment or the centre-of-mass of the power spectrum. The first spectral moment of a spectrum is defined by [52]

$$f_0 = \frac{\sum_{f=1}^{M} fS(f)}{\sum_{f=1}^{M} S(f)} \tag{2.38}$$

where f_0 is the mean frequency of the Doppler signal f is the frequency, $S(f)$ is the power spectral density and M is the upper limit of the summation. The DC component ($(f = 0)$ is not included in the computation.

Cross-correlation

Cross-correlation of two signal is a well-known method for feature detection in many engineering fields. Cross-correlation is computed by shifting the reference signal across the length of the tested signal and integrating the inner product on each sample across the signal length. For a given two discrete signals $x(n)$ and $y(n)$, the cross-correlation function is defined by [61]

$$\mathrm{K}_{xy}(\iota) = \sum_{n=-\infty}^{\infty} x(n)y(n-\iota) \tag{2.39}$$

where K_{xy} is the cross-correlation coefficient and parameter ι is any integer between $-\infty < \iota < \infty$. K_{xy} is a measure of linear interdependence between the $x(n)$ and $y(n)$. A cross-correlation coefficient value is between -1 and 1. If both signals are identical, the cross-correlation output

will produce a coefficient of 1 and vice-versa for dissimilar signals. Furthermore, the coefficient of the correlation will be largest at the position where both signals are maximally correlated.

2.7. Introduction to Rigid Body Motions

In the following chapter 3, the analysis of vehicle vibrations impact in the uncertainty in velocity measurement is dealt with. Therefore, this section gives the introduction to rigid motions of a vehicle.

A body is considered 'rigid' if the distance between any of its two particles remains equal under considerable forces acting on it. Mathematically a rigid body is defined as

$$\|p_1(0)\| - \|p_2(0)\| = \|p_1(t)\| - \|p_2(t)\| \tag{2.40}$$

for all $t \neq 0$ [62]

where p_1 and p_2 represent two particles randomly picked from a rigid body. In practice, real object or body may deform. However, the deformation is considered small and negligible that the object can still be approximated as a rigid body.

The motion of the rigid body is categorised into two ways; it can translate and rotate. Translational motion specifies the position quantity, and rotational motion determines the attitude quantity of a rigid body. These motions are independent of each other, the general motion of a rigid body can be purely translational or rotational, or a combination of the two motions.

Both motions are different in a fundamental way. For rotational movements, every particle moves in the purely circular path by the same amount of angle about a chosen point in space. On the other hand, for translational motion, every particle in the body moves with the same amount of distance and always remains parallel to its previous position. Both motions create six degrees of freedom (DOF) in 3D space in which, three DOF in translation and three DOF in the rotation. A classic example of six DOF is the motion of a passenger car; the three translational motions are surging forward and backward, heaving up and down, and swaying left, and right and the three rotational motions around the vehicle's centre of gravity are tilting forward and backward, pivoting side to side and swivelling left and right. These rotational motions are also known as pitch, roll and yaw motions, and each motion has its rotation axis. Figure 2.18 illustrates the three rotational motions of a vehicle. The pitch motion is around the longitudinal direction, the roll motion is around the transverse direction, and the yaw is around the vertical direction of the vehicle.

Note that throughout this thesis, the coordinate system used for vehicle motions is according to the Cartesian coordinate as shown in Figure 2.18. The *x*-axis represents the longitudinal direction, the *y*-axis represents the transverse direction and positive when it points to the left of the driver and the *z*-axis represents the vertical direction of the vehicle.

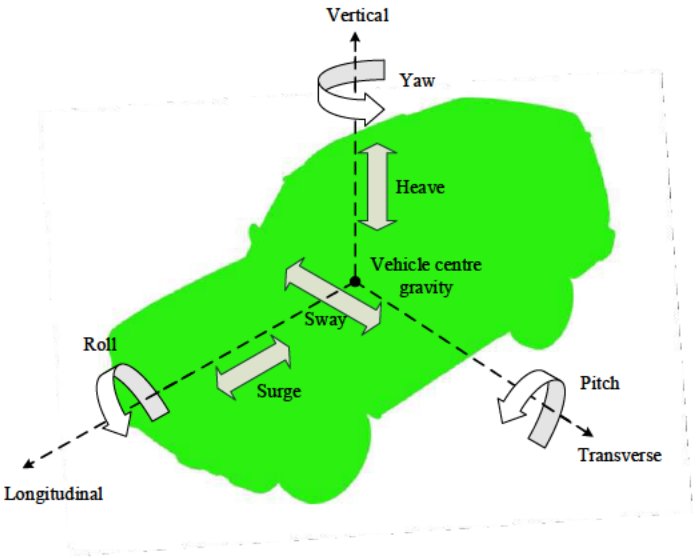

Figure 2.18 Rotational motions along the axis of a vehicle

2.7.1. Reference Frames

Reference frames provide the reference to build the equations of motions of a rigid body. A reference frame can be divided into the inertial and non-inertial frame. An inertial frame is a primary frame that is fixed and non-rotating for all time. Conversely, the frame that is fixed to a rigid body is called the non-inertial frame. This frame can rotate freely with time, and there can be some multiple numbers of non-inertial frames depending on the number of a rigid body in space. In this work, two reference frames are defined. The points below described each frame:

- **Local reference frame**

Denoted $\{L\}$ and axis components indicated with $\{x_L, y_L, z_L\}$, this is an inertial reference frame or observer frame. In the case of land vehicles, this can be assumed to be an earth-fixed frame. The x_L-y_L plane sits on the horizontal plane and perfectly perpendicular to the direction of gravity. The z_L-axis points vertically upward and positive.

- **Vehicle body frame**

Denoted $\{B\}$ and axis component indicated with $\{x_B, y_B, z_B\}$, this frame has its position and alignment fixed to the vehicle. The x_B-axis lies in the vehicle longitudinal movement direction, and the y_B-axis points to the side of the vehicle with positive in the direction of right-hand rule. The z_B-axis is let tangential to the x_B-y_B plane. This frame can rotate freely in the 3D space. In this work, we assumed that the radar is rigidly attached to the body of the vehicle and therefore, the orientation of the radar follows the same orientation of the vehicle body frame. Figure 2.19 illustrates the local and vehicle-body frames. The local reference frame is indicated with $\{x_L, y_L, z_L\}$ and solid line and vehicle body-frame is indicated with $\{x_B, y_B, z_B\}$ and dashed line.

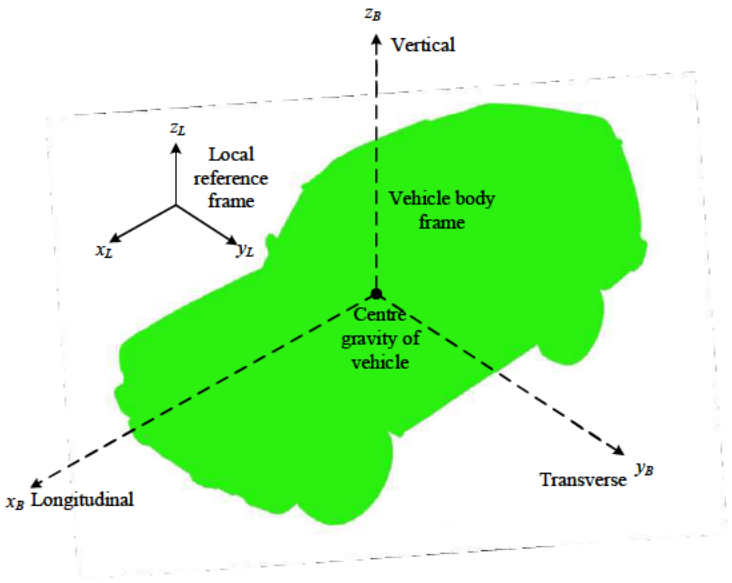

Figure 2.19 Illustration of the local reference frame and vehicle-body frame

2.7.2. Rotation Matrix

The orientation of the vehicle is given by the rotation matrix, $\boldsymbol{R}$. This matrix maps the vectors expressed using the $\{B\}$-frame coordinates to the $\{L\}$-frame coordinates, given that both

frames share the same point of rotation which in this case is the centre gravity of the vehicle. For example, consider a point p^B in the frame $\{B\}$ is rotated and aligned with the Local frame $\{L\}$. The rotated point, p^L in the $\{L\}$-frame is given by [62]

$$p^L = {}^L_B\boldsymbol{R}p^B \tag{2.41}$$

where ${}^L_B\boldsymbol{R}$ represents the rotation matrix from $\{B\}$ to $\{L\}$ frame. Note that a rotation matrix must satisfy two conditions; det($\boldsymbol{R}$) = 1 and $\boldsymbol{R}^T\boldsymbol{R} = I$.

2.7.3. Representing Vehicle Attitude

An intuitive way to model the orientation of a rigid body using a set of angles is called Euler angles. These angles measure how much rotation needed for each axis in the $\{B\}$-frame to align with the $\{L\}$-frame. Overall, Euler angles are measured through three necessary rotations, with each rotates around one axis. The rotations can be done in any sequence of the axis. However, conventionally the sequence of rotation follows the x_B-y_B-z_B-order.

The transformation process from the vehicle-body frame, $\{B\}$ to local-frame $\{L\}$ using Euler angles can be summarised as follows:

1. Rotation by an angle ψ around z_B-axis, yielding to x_B', y_B', z_B'
2. Rotation by an angle υ around y_B'-axis, yielding to x_B'', y_B'', z_B''
3. Rotation by an angle ω around x_B''-axis, yielding to x_B, y_B, z_B

All rotations are assumed in a positive direction. These three successive rotations produce rotation matrix which constitutes of three rotation matrices [62]

$$ {}^{L}_{\mathrm{B}}\mathbf{R} = \boldsymbol{R}_x(\omega)\boldsymbol{R}_y(\upsilon)\boldsymbol{R}_z(\psi) \tag{2.42} $$

where

$$ \boldsymbol{R}_z(\omega) = \begin{bmatrix} \cos\omega & \sin\omega & 0 \\ -\sin\omega & \cos\omega & 0 \\ 0 & 0 & 1 \end{bmatrix} \tag{2.43} $$

$$ \boldsymbol{R}_y(\upsilon) = \begin{bmatrix} \cos\upsilon & 0 & -\sin\upsilon \\ 0 & 1 & 0 \\ \sin\upsilon & 0 & \cos\upsilon \end{bmatrix} \tag{2.44} $$

$$ \boldsymbol{R}_y(\psi) = \begin{bmatrix} 1 & 0 & 0 \\ 0 & \cos\psi & \sin\psi \\ 0 & -\sin\psi & \cos\psi \end{bmatrix} \tag{2.45} $$

2.8. Approximation of Antenna Radiation Pattern for Doppler Spectrum

In the following chapters, readers will find that the antenna radiation pattern for the Doppler spectrum model is approximated by using sinc and Gaussian function. In this section, we explain the rationale of using these two functions.

In the case of Chapter 2 and 3, We analysed the effects of radar parameters to the characteristics of the Doppler spectrum. Here, we consider the typical attributes of a practical antenna like the main lobes and sides lobes. Therefore, the solution to this problem is to use the sinc function as antenna pattern because the main-lobe/side-lobe characteristics can be easily modelled using a sinc function.

In Chapter 4, we used a set of Doppler spectra to evaluate the proposed SoG algorithms. The Gaussian function is chosen in this chapter because it can be used to model the Doppler spectra effectively. Recall that Equation (2.22) and (2.25) can be used to transform the vehicle speed and antenna beamwidth to values of centre frequency and standard deviation of a Gaussian

distribution. Therefore, the use of Gaussian function simplifies the generation of Doppler spectra with good accuracy.

The characteristics shape of the sinc and Gaussian function on the first half-power is approximately the same. Figure 2.20 shows the comparison of radiation pattern between a sinc function and a Gaussian function. We can see that the profile of the first 3-dB gain for both functions is relatively identical. Therefore, both functions are judged to be adequate for modelling of Doppler spectrum in this thesis.

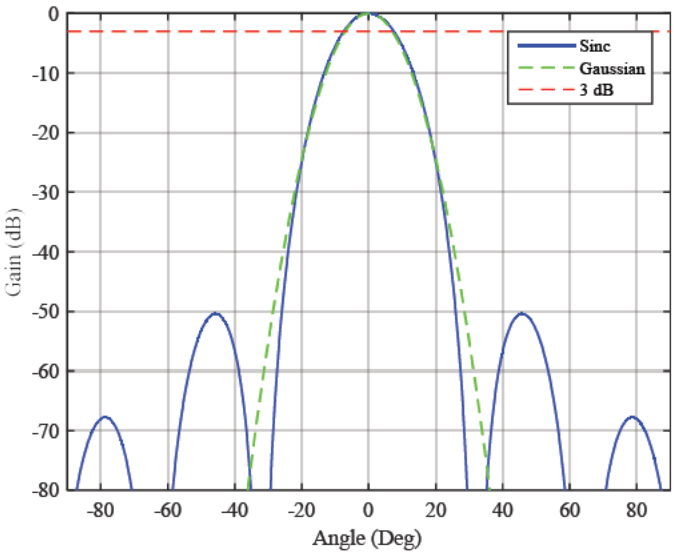

Figure 2.20 Comparison between the plots of antenna gain pattern between sinc and Gaussian function

2.9. Summary

In the first part of this chapter, we reviewed the basic concepts of radar. These include the definition of radar, basic radar equations, Doppler effect and introduction to quadrature CW radar system. In the second part of this chapter, we introduced the fundamentals concepts of SoG radar system that includes the method of measurement and the signal processing of

Doppler signals. In short, it has been shown that radar can be practically adapted for vehicle speed measurement. However, the uncertainty in the speed measurement depends on two main issues. This uncertainty is firstly due to the random fluctuations in power spectral density of the received signal and secondly, is due to the changes in angle at which the antenna faces the ground when moving on an uneven surface. The suppression of these two issues is therefore, the most important task to improve the speed measurement accuracy of the SoG radar. To increase the accuracy as well as the reliability of speed measurement with regards to the two problems, the following conclusion can be drawn:

- Speed measurement can be uncertain when a vehicle is moving on an uneven ground surface. Due to this reason, the possibility of using 4-beam radar arranged as Janus configuration can be used to minimise the speed measurement error.
- Practical Doppler signal is masked by noise, the estimation of mean Doppler frequency especially in the case of low SNR can lead to inaccuracy estimate of speed. Therefore, the development of new algorithms for speed estimation is critical for improving the reliability and accuracy of speed measurement.

In the following parts of this thesis, these proposed methods are examined.

Chapter 3. Theoretical Overview of SoG Radar and Its Effect on Radar System Parameters

3.1. Introduction

This chapter aims to investigate the effects of radar parameters to the operations of SoG radar. This chapter provides the theoretical analysis of three critical elements of SoG radar that are the accuracy of speed measurement, shape, and size of radar footprint on the ground and analysis of the Doppler spectrum. Accordingly, this chapter is divided into three main parts.

The first part analyses the speed estimation accuracy of the proposed 4-beam radar system. We begin by introducing the concept of a 4-beam radar and how speed is estimated from the system. Subsequently, we provide the accuracy analysis when operating under roll, pitch and yaw motions.

In the second part of this chapter, we investigate the effects of radar parameters such as radar antenna beamwidth, height and viewing angle to the shape and size of the radar footprint. The geometry of the antenna beam is used to estimate the size of the footprint on the ground.

Finally, the third part of this chapter investigates the impact of different values of radar parameters on the Doppler spectrum characteristics. In this work, the radar parameters including radar viewing angle, transmitter frequency and also vehicle speed are analysed concerning the shape of the Doppler spectrum.

3.1.1. The principle of Velocity Vector Estimation of a 4-Beam SoG radar

Although the 4-beam radar system has been used since the mid-70s in avionics navigation system [63], [64] and acoustic Doppler Current Profilers (ADCP) for maritime systems [65], [66], its application for ground vehicles is not fully explored. Here we introduced the concept of a 4-beam radar system for SoG radar. Figure 3.1(a) illustrates the 4-beam radar system viewed from the front, side, and top of a passenger car. The system consists of four radars, and each radar is indicated by a blue rectangular. The position of the radars is indicated with Radar 1, Radar 2, Radar 3 and Radar 4. For this analysis, we assumed that the radar produces a narrow beam. This assumption is made to simplify this analysis. A red line indicates this narrow beam. The velocity components along the car are referred to the longitudinal velocity v_l, transverse velocity v_t, and vertical velocity v_z and intersect the centre gravity of the vehicle. The four beams are arranged to be pairwise-symmetric with respect to the vertical axis so that each beam will measure the same magnitude of speed when the vehicle is moving along the longitudinal direction. Figure 3.1(b) shows an example of beam geometry in position 1. The location of the beam in space is described using two angles; depression angle, α, and azimuth angle, β. The angles between the velocity vector and the beam axis are defined as u_x, u_y and u_z for x_B, y_B and z_B-axis respectively.

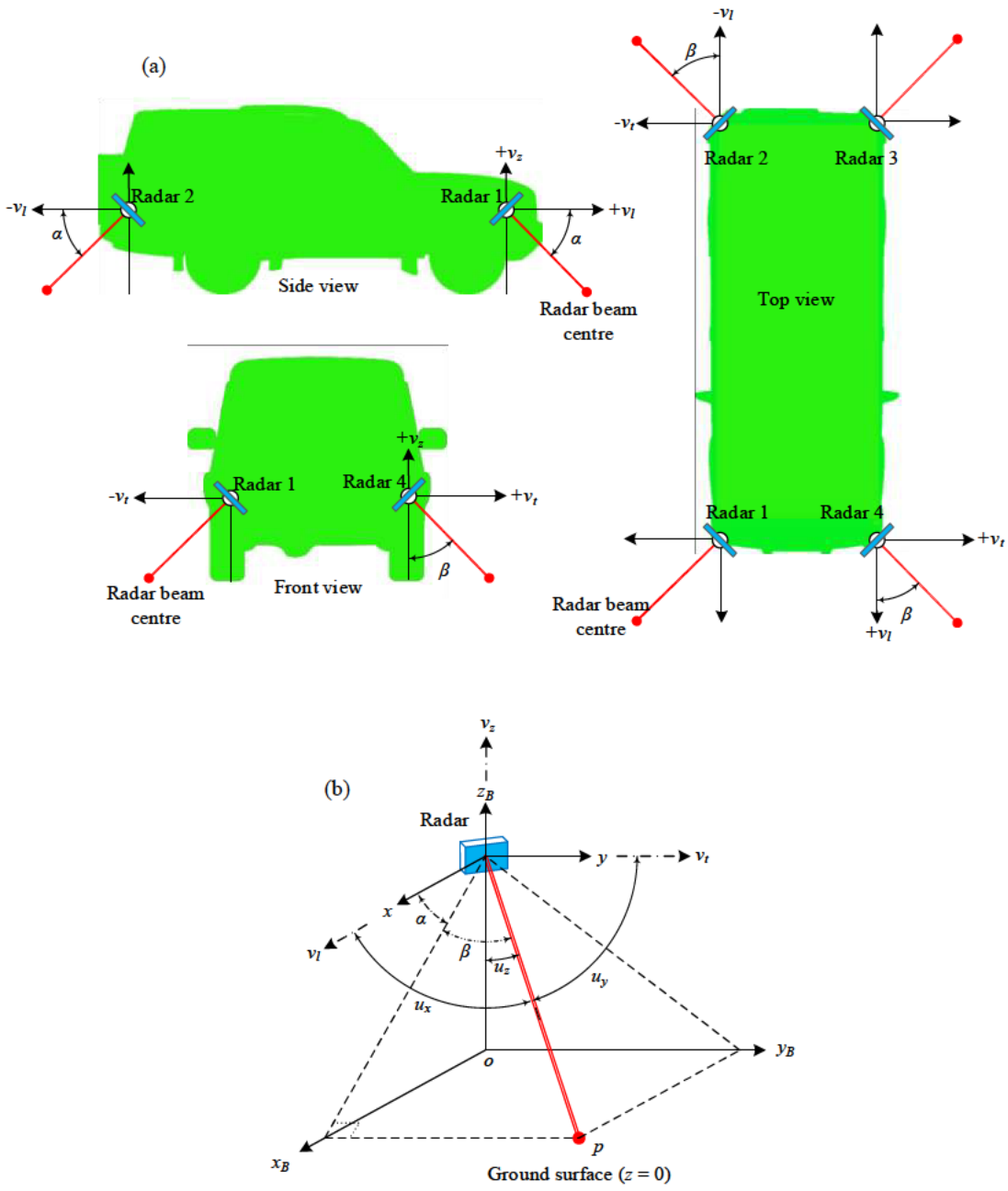

Figure 3.1 Geometry of radar beam (a) All of four beams viewed from the front, side, and top of a vehicle. (b) a single-beam at position 1

Let us assume that the vehicle in Figure 3.1(a) is moving straight with forward motion in the direction along x_B. Assumed that the road on which the vehicle travelling is ideally flat, and no angular motions induced on the vehicle, the Doppler shift along beam at position 1 can be defined as [48]

$$f_{d1} = \frac{2}{\lambda}\left(v_l \cos u_x + v_t \cos u_y + v_z \cos u_z\right) \tag{3.1}$$

Each radar beam measures the same magnitude of speed. Therefore, the Doppler frequency from beam 1 to 4 are given by

$$f_{d1} = \frac{2}{\lambda}\left(+d_1 v_l + d_2 v_t + d_3 v_v\right) \tag{3.2}$$

$$f_{d2} = \frac{2}{\lambda}\left(-d_1 v_l + d_2 v_t + d_3 v_v\right) \tag{3.3}$$

$$f_{d3} = \frac{2}{\lambda}\left(-d_1 v_l - d_2 v_t + d_3 v_v\right) \tag{3.4}$$

$$f_{d4} = \frac{2}{\lambda}\left(+d_1 v_l - d_2 v_t + d_3 v_v\right) \tag{3.5}$$

where d_1, d_2, and d_3 are the magnitudes of the beam direction cosines. Thus, the desired velocity component along the vehicle direction can be computed as a function of Doppler shift frequency

$$v_l = \frac{1}{4d_1\lambda}\left(+f_1 - f_2 - f_3 + f_4\right) \tag{3.6}$$

$$v_t = \frac{1}{4d_2\lambda}\left(+f_1 + f_2 - f_3 - f_4\right) \tag{3.7}$$

$$v_v = \frac{1}{4d_3\lambda}\left(+f_1 + f_2 + f_3 + f_4\right) \tag{3.8}$$

The magnitude of d_1, d_2, and d_3 as a function of α and β is defined as

$$d_1 = \cos\alpha \cos\beta \tag{3.9}$$

$$d_2 = \sin\beta \tag{3.10}$$

$$d_3 = -\sin\alpha \cos\beta \tag{3.11}$$

Further detail how d_1, d_2, and d_3 are obtained is given in Appendix A. Finally, the true velocity of the vehicle v_r can be computed as

$$v_r = \sqrt{v_l^2 + v_t^2 + v_z^2} \tag{3.12}$$

3.2. Analysis of Error due to Vehicle Motions

As discussed in Section 2.4, one of the primary sources of error is due to the vehicle motions when operating on uneven surfaces such as in off-road conditions. This error comes from the changes of the cosine angle: $\cos\theta$ of the Doppler equation $f_d = (2v/\lambda)\cos\theta$.

We describe the analysis in this section in two parts. The first part describes the error analysis on a single-beam radar and the second part describes the error analysis on a 4-beam radar. Finally, we compare the performance of both systems in measuring velocity under the influence of vehicle motions.

3.2.1. Motion Error of a Single-Beam Radar

Recall from the geometry of a single-beam radar in Figure 3.1(b), under perturbation-free conditions, the cosine angles along v_l, v_t and v_z are similar as in Equation (3.9) through (3.11). However, when the radar system in under pitch, roll and yaw motions, the cosine angles along each direction can change and therefore produces miss-alignment angles. Figure 3.2(a) to (c) show the illustration of the angular motions; pitch, roll, and yaw attributed to a passenger car. We used two axes to indicate these angular movements in the vehicle-body frame $\{B\}$. The axes marked with solid lines show the original vehicle position in the vehicle-body frame $\{B\}$ and the dashed axes indicate the new position of the vehicle under the respective angular motions. We define the miss-alignment angle as δ_p, δ_r, δ_y for pitch, roll, and yaw motions respectively.

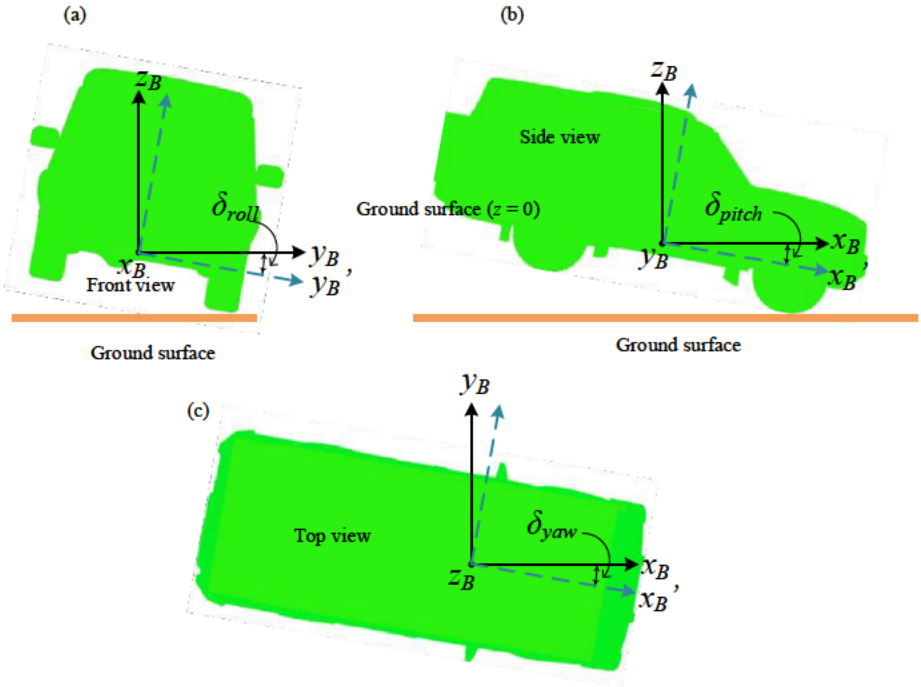

Figure 3.2 An illustration of misalignment angles

These angular motions can exist simultaneously and known as composite angular motion. The composite of yaw, pitch, and roll in the observer-frame $\{L\}$ can be presented using a composition rotation matrix $\boldsymbol{R}$ [67].

$$\{L\} = \boldsymbol{R}\{B\} \tag{3.13}$$

where $\boldsymbol{R}$ is composed of individual rotation matrix as in Equation (2.43) to (2.45). $\boldsymbol{R}$ can be given as

$$\boldsymbol{R}(\delta_y, \delta_p, \delta_r) = \begin{bmatrix} \cos\delta_y & \sin\delta_y & 0 \\ -\sin\delta_y & \cos\delta_y & 0 \\ 0 & 0 & 1 \end{bmatrix} \begin{bmatrix} \cos\delta_p & 0 & -\sin\delta_p \\ 0 & 1 & 0 \\ \sin\delta_p & 0 & \cos\delta_p \end{bmatrix} \begin{bmatrix} 1 & 0 & 0 \\ 0 & \cos\delta_r & \sin\delta_r \\ 0 & -\sin\delta_r & \cos\delta_r \end{bmatrix} \tag{3.14}$$

The three matrices from left to right represents the rotation whose angles are δ_y, δ_p, and δ_r. For the general case of land vehicles such as passenger car, the motion error is mostly attributed by roll and pitch motions when moving along a straight track. By comparison, yaw motion is typically minimal and has no significant impact on the accuracy of velocity estimation. Here we assumed that $\delta_y = 0$ Therefore, Equation (3.15) is reduced to

$$\boldsymbol{R}(\delta_y, \delta_p, \delta_r) = \begin{bmatrix} 1 & 0 & 0 \\ 0 & 1 & 0 \\ 0 & 0 & 1 \end{bmatrix} \begin{bmatrix} \cos\delta_p & 0 & -\sin\delta_p \\ 0 & 1 & 0 \\ \sin\delta_p & 0 & \cos\delta_p \end{bmatrix} \begin{bmatrix} 1 & 0 & 0 \\ 0 & \cos\delta_r & \sin\delta_r \\ 0 & -\sin\delta_r & \cos\delta_r \end{bmatrix} \tag{3.15}$$

The angular motions which in this case, pitch and roll motions can give rise to an error in velocity measurement. The error in the velocity measurement can directly be estimated by multiplying the error-free velocities in Equation (3.9) to (3.11) with the rotation matrix, $\boldsymbol{R}$.

$$\hat{v} = {}^{L}_{B}\boldsymbol{R} v^{B} \tag{3.16}$$

where $\hat{v}$ the error-weighted velocity components, and v^B is the error-free velocity components. Replacing v^B with Equation (3.9) to Equation (3.12) yields the solution

$${}^{L}\hat{v} = \begin{bmatrix} \cos\delta_p & \sin\delta_r \sin\delta_p & -\cos\delta_r \sin\delta_p \\ 0 & \cos\delta_r & \sin\delta_r \\ \sin\delta_p & -\cos\delta_p \sin\delta_r & \cos\delta_p \cos\delta_r \end{bmatrix} \begin{bmatrix} \cos\alpha\cos\beta \\ \sin\beta \\ -\sin\alpha\cos\beta \end{bmatrix} \tag{3.17}$$

We can simplify Equation (3.17) into three velocity components

$$\hat{v}_l = \cos\alpha\cos\beta\cos\delta_p + \sin\delta_p(\sin\beta\sin\delta_r - \sin\alpha\cos\beta\cos\delta_r) \tag{3.18}$$

$$\hat{v}_t = \sin\beta\cos\delta_p + \sin\alpha\cos\beta\sin\delta_p \tag{3.19}$$

$$\hat{v}_v = -\sin\alpha\cos\beta\sin\delta_p + \cos\delta_p(\sin\beta\sin\delta_r - \sin\alpha\cos\beta\cos\delta_r) \tag{3.20}$$

We can estimate the impact of misalignment angles to velocity measurement by finding the ratio between the velocity components with misalignment angles to the velocity components with no misalignment angles

$$\frac{\hat{v}_l}{v_l} = \cos\delta_p + \sin\delta_p\left(\frac{\tan\beta}{\cos\alpha}\sin\delta_r - \tan\alpha\cos\delta_r\right) \tag{3.21}$$

$$\frac{\hat{v}_t}{v_t} = \cos\delta_r + \frac{\sin\alpha}{\tan\beta}\sin\delta_r \tag{3.22}$$

Finally, we can compute the relative error of velocity by using the corresponding error equation

$$\textit{Relative error}\ (\%) = \left(1 - \left\|\frac{\hat{v}_u}{v_u}\right\|\right)100 \tag{3.23}$$

where the subscript *u* specifies the axis of the velocity components. It is evident from Equations (3.21) and (3.22) that the relative error is a function of viewing angles, α, and β, and pitch and roll angles δ_p and δ_r .

We now evaluate the relative error of estimating velocity under the influence of roll and pitch motions on a vehicle. Depending on the configuration of viewing angles used to estimate the vehicle velocity, different values of depression angle α, and azimuth angle β can be used. For this analysis, we considered two configurations, the first one is based on a conventional single-beam radar system with viewing angles of $\alpha = 45°$and $\beta = 0°$ and second one with viewing angles of $\alpha = 45°$and $\beta = 45°$ Figure 3.3(a) and (b) show the plot relative error versus pitch. Note that, to limit the dimension of the plot, we only used three selected roll angles of 0°, 4°, and 8°.

From the two figures, both plots indicate that the velocity error increases with the increase in pitch angle. However, the increase in roll angle did not increase error in the conventional single-beam system. As can be seen in Figure 3.3(a), the selected roll-angles, 0°, 4°, and 8°, are very close to each other. It can be said that the conventional single-beam system is insensitive to roll motions. On the other hand, the configuration of viewing angle with $\beta \neq 0°$ increases the error. Figure 3.3(b) shows an example of a relative error plot using $\alpha = 45°$and $\beta = 45°$. If we compare this result to the earlier one, this configuration produces a higher error for the same value of roll angles.

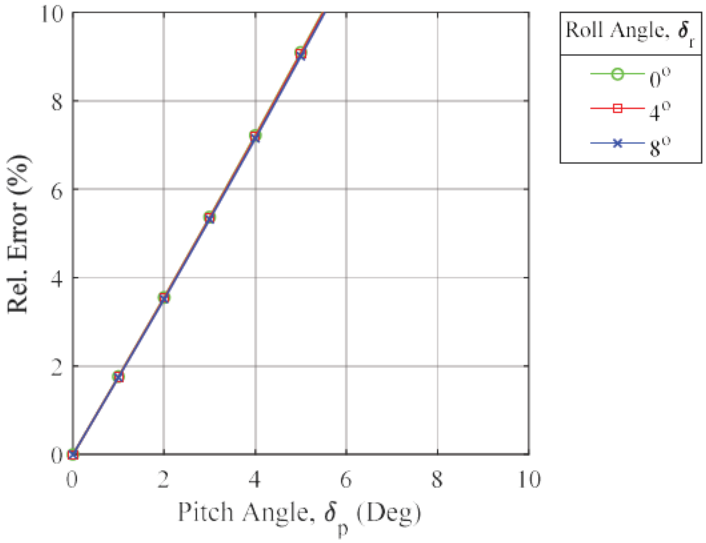

(a)

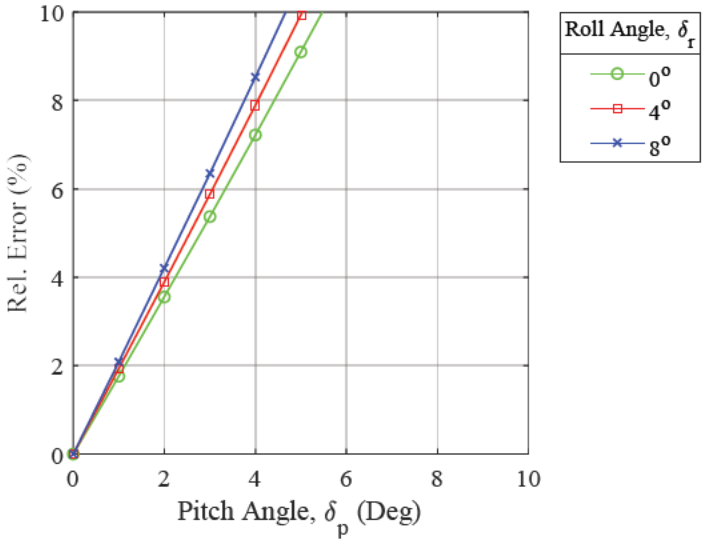

(b)

Figure 3.3 Comparison of relative error of a single-beam system (a) $\alpha/\beta = 45°/0°$ (b) $\alpha/\beta = 45°/45°$

Additionally, the choice of depression angle, α also influences the accuracy of velocity estimation. Figure 3.4 shows a comparison of relative error of a conventional single-beam system for $\alpha = 30°$, 45°, and 60°. The plot shows that the relative error increases two-fold when α changes from 30° to 60°. The results obtained here is also in agreement with the results in [68] although they used a different approach to estimate the impact of radar depression angle on the accuracy of velocity estimation.

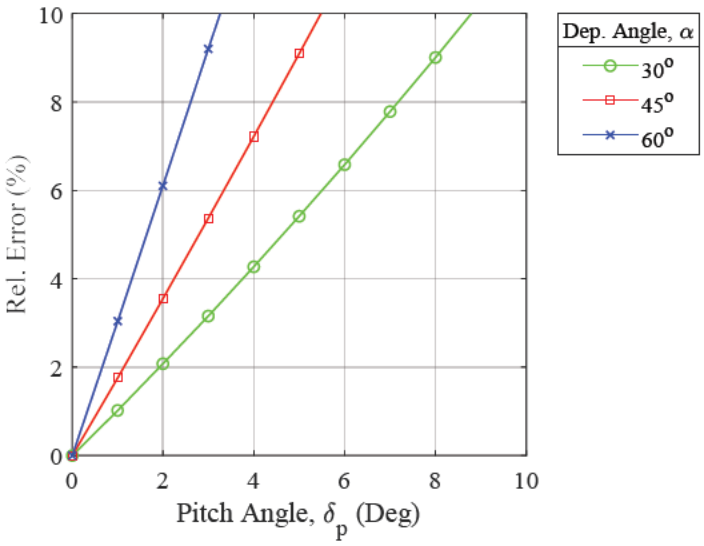

Figure 3.4 Comparison of accuracy of a single-beam system with different values of depression angles

3.2.2. Motion Error of a 4-Beam Radar

Equations (3.2) to (3.5) show that radar beam at position 1,2,3 and 4 measure the same magnitude of speed but in different directions. Therefore, one can use Equation (3.21) and Equation (3.22) (ratio between velocity vector with misalignment error to the velocity vector with no error) for each of the four beams.

$$\frac{\hat{v}_{l1}}{v_{l1}} = \cos\delta_p - \sin\delta_p \left[\frac{\tan\beta}{\cos\alpha} \sin\delta_r + \tan\alpha \cos\delta_r \right] \tag{3.24}$$

$$\frac{\hat{v}_{l2}}{v_{l2}} = \cos\delta_p + \sin\delta_p \left[\frac{\tan\beta}{\cos\alpha} \sin\delta_r + \tan\alpha \cos\delta_r \right] \tag{3.25}$$

$$\frac{\hat{v}_{l3}}{v_{l3}} = \cos\delta_p + \sin\delta_p \left[\frac{\tan\beta}{\cos\alpha} \sin\delta_r - \tan\alpha \cos\delta_r \right] \tag{3.26}$$

$$\frac{\hat{v}_{l4}}{v_{l4}} = \cos\delta_p - \sin\delta_p \left[\frac{\tan\beta}{\cos\alpha} \sin\delta_r - \tan\alpha \cos\delta_r \right] \tag{3.27}$$

And for the lateral velocity, the ratio is given as

$$\frac{\hat{v}_{t1}}{v_{t1}} = \cos\delta_r + \frac{\sin\alpha}{\tan\beta} \sin\delta_r \tag{3.28}$$

$$\frac{\hat{v}_{t2}}{v_{t2}} = \cos\delta_r + \frac{\sin\alpha}{\tan\beta} \sin\delta_r \tag{3.29}$$

$$\frac{\hat{v}_{t3}}{v_{t3}} = \cos\delta_r - \frac{\sin\alpha}{\tan\beta} \sin\delta_r \tag{3.30}$$

$$\frac{\hat{v}_{t4}}{v_{t4}} = \cos\delta_r - \frac{\sin\alpha}{\tan\beta} \sin\delta_r \tag{3.31}$$

Note that for each of the expressions, different sign conforms with the direction of the angular rotations. Each of the beams contributes some amount of error in the final velocity computation depending on the misalignment angles occurred on each beam. By averaging the contribution of error from each beam, we can compute the average ratio between velocity components with misalignment error to the velocity components with no error from all four beams.

$$\frac{\hat{v}_l}{v_l} = \frac{\hat{v}_{l1} + \hat{v}_{l2} + \hat{v}_{l3} + \hat{v}_{l4}}{4 v_l} = \cos\delta_p \tag{3.32}$$

$$\frac{\hat{v}_t}{v_t} = \frac{\hat{v}_{t1} + \hat{v}_{t2} + \hat{v}_{t3} + \hat{v}_{t4}}{4v_t} = \cos\delta_r \tag{3.33}$$

Hence, the average relative error in estimating velocity from a 4-beam radar system can be given as

$$relative\ error\ (\%) = \left(1 - \cos\delta_p\right)100 \tag{3.34}$$

$$relative\ error\ (\%) = \left(1 - \cos\delta_r\right)100 \tag{3.35}$$

where Equation (3.34) and (3.35) are for longitudinal velocity and lateral velocity respectively. It is evident from both Equations (3.32) and (3.33) that the 4-beam system reduces the sum of error to just $\cos\delta_p$ and $\cos\delta_r$. Also, the error is independent of the viewing angles. Any combination of viewing angles (α/β) that form a Janus configuration would have the same amount of relative error as presented here.

3.2.3. Comparison of Error Between 4-Beam and Single-Beam Radar

The equation (3.34) and (3.21) are used to compute the relative error for a 4-beam radar and a single beam radar respectively. We set the viewing angle for radar beam to $\alpha = 45°$and $\beta = 45°$ for Radar 1, Radar 2, Radar 3 and Radar 4 as in Figure 3.1(a). For conventional single-beam radar system, the viewing angle is set similar is set to $\alpha = 45°$and $\beta = 0°$. Figure 3.5 shows the comparison of relative error between the two methods.

As can be seen, a 4-beam radar configuration produces a significantly lower error in the presence of pitch and roll motions compared to the single-beam radar. As an example, for a combination of 1° pitch and 1° roll, the relative error of a single-beam radar reach 1.8% while

a 4-beam radar only produces an error of 0.1%. Even as the combination of pitch and roll error reaches 5°, the relative error of a 4-beam configuration is still under 0.4%.

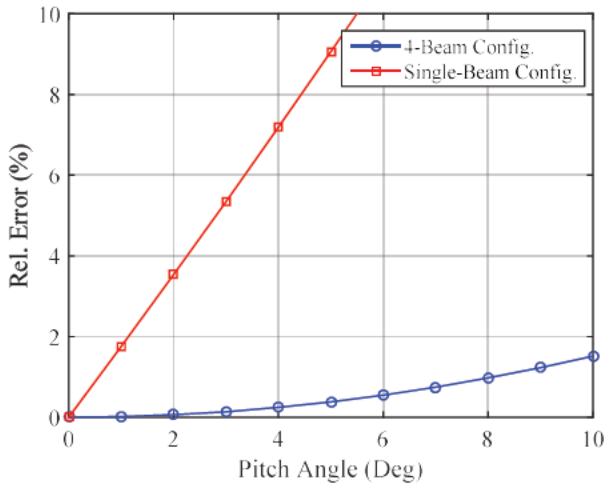

Figure 3.5 Comparison of relative error of two kinds of radar beam configuration

3.3. Radar Footprint

This section presents an analysis of radar footprint for given radar parameters. We define the radar footprint as the intersection between a radar beam and the ground plane. The actual shape of the radar footprint is complicated to estimate. In the research by [54], using small perturbation model, they showed that an antenna with canonical beam produces a footprint with a shape that is close to an ellipse.

It is not enough to know the presence of radar footprint is somewhere on the ground. If its location is unknown, there is a risk that the beam may illuminate the shoulder of the road during SoG operation. Therefore, it is essential to determine the size and distance of the radar footprint on the ground.

3.3.1. Model

In the following analysis, we assumed that the radar antenna produces a conical beam. The basic structure of a radar footprint model is shown in Figure 3.6. The upper figure illustrates a cone undergoing two motions that are rotation motion and vertical motion. Let the base of the cone has a radius of r and opening angle of 2ϕ. The cone, C is indicated as C' after a rotation (Rot) and C'' after a vertical motion (Vert). The observation point of cone C, C' and C'' are represented using Cartesian coordinates as $\{x_B,y_B,z_B\}$, $\{x_B',y_B',z_B'\}$ and $\{x_B'',y_B'',z_B''\}$ respectively. The lower figure illustrates the footprint of the radar beam as an intersection between the projected cone and the ground plane. The intersection of the cone and the ground plane forms a shape of an ellipse with the semi-minor axis and the major axis of l and L respectively.

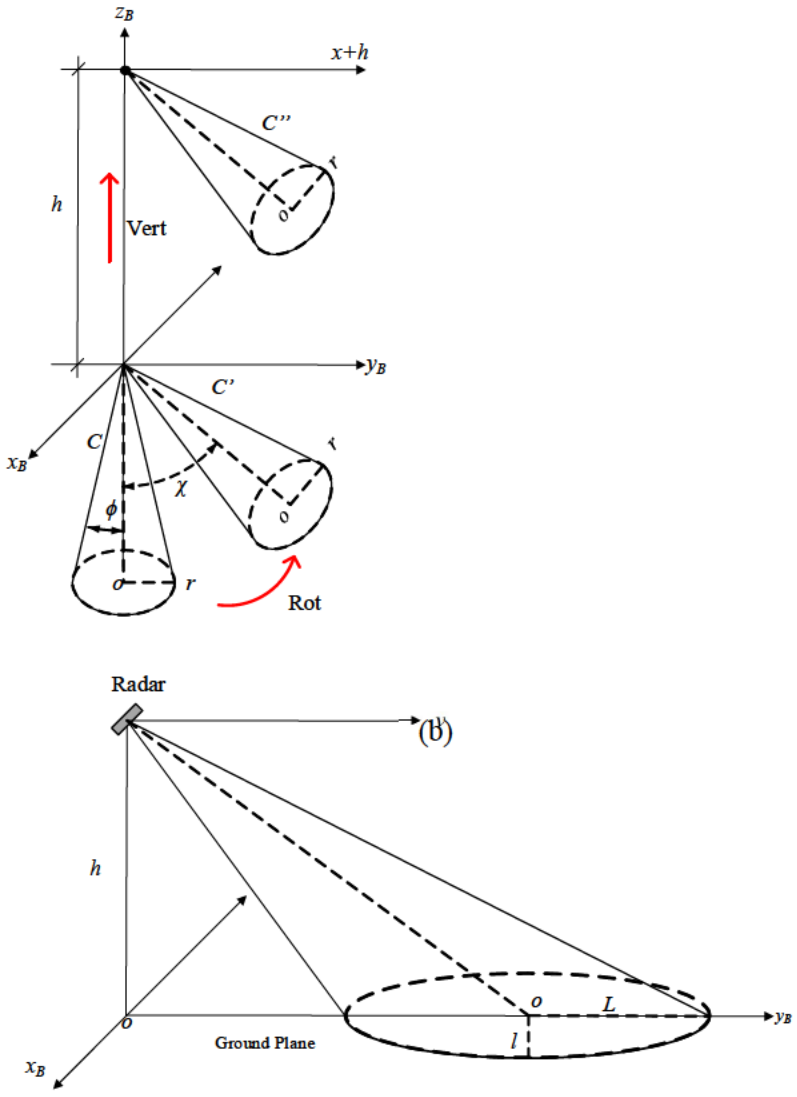

Figure 3.6 Geometry of a radar footprint (a) Translation motion of a cone. (b) Illustration of a radar footprint

Referring to Figure 3.6(a), the base of the cone C is an ellipse of equal semi-minor and semi-major axis. An ellipse equation for the base of the cone C can be defined as

$$x^2 + y^2 = (z\tan\phi)^2 \tag{3.36}$$

The mapping of cone C to C'' is defined by two motions; a rotational motion around x_B-axis plus a vertical motion along the z_B-axis. Following the two motions of the cone C, we derive the relationship between the antenna parameter and the size of the ellipse on the ground surface. The relationship between the cone C, C' and C'' is given as

$$\begin{bmatrix} x_B'' \\ y_B'' \\ z_B'' \end{bmatrix} = \begin{bmatrix} x_B' \\ y_B' \\ z_B' \end{bmatrix} + \begin{bmatrix} 0 \\ 0 \\ h \end{bmatrix} \tag{3.37}$$

where $\{x_B', y_B', z_B'\}$ is the observation point of cone C' after a rotational motion of cone C, $\{x_B'', y_B'', z_B''\}$ is the observation point of cone C'' after a vertical motion of cone C', and h is the height of radar from the ground plane. From Figure 3.6, the rotational motion from coordinate $\{x_B, y_B, z_B\}$ to $\{x_B', y_B', z_B'\}$ along the x_B-axis can be represented using Euler matrix.

$$\begin{bmatrix} x_B' \\ y_B' \\ z_B' \end{bmatrix} = \begin{bmatrix} 1 & 0 & 0 \\ 0 & \cos\chi & \sin\chi \\ 0 & -\sin\chi & \cos\chi \end{bmatrix} \begin{bmatrix} x_B \\ y_B \\ z_B \end{bmatrix} \tag{3.38}$$

The above Equation (3.38) can be further simplified as

$$\begin{bmatrix} x_B' \\ y_B' \\ z_B' \end{bmatrix} = \begin{bmatrix} x_B \\ y_B\cos\chi + z_B\sin\chi \\ -y_B\sin\chi + z_B\cos\chi \end{bmatrix} \tag{3.39}$$

The cone C' is vertically displaced by distance h to arrive at the position C''. Therefore, the total displacement along the z_B-axis is equal to $z_B - h$. Therefore, the cone C'' can be given as

$$\begin{bmatrix} x_B'' \\ y_B'' \\ z_B'' \end{bmatrix} = \begin{bmatrix} x_B \\ y_B\cos\chi + (z_B - h)\sin\chi \\ (z_B - h)\cos\chi - y_B\sin\chi \end{bmatrix} \tag{3.40}$$

For convenience, we can express $x_B = x_B''$, $y_B = y_B''$ and $z_B = z_B''$. Equation (3.40) can be substituted into Equation (3.36) as

$$x_B^{\,2} + \left(y_B \cos\chi + (z_B - h)\sin\chi\right)^2 = \left((z_B - h)\cos\chi - y_B \sin\chi\right)^2 \tan^2\phi \tag{3.41}$$

The ground plane is at $z_B = 0$. Therefore, we can further simplify Equation (3.41) as

$$x_B^{\,2} + (y_B \cos\chi - h\sin\chi)^2 = (h\cos\chi + y_B \sin\chi)^2 \tan^2\phi \tag{3.42}$$

We can re-arrange Equation (3.42) so that it appears as an ellipse equation

$$\frac{x_B^{\,2}}{l} + \frac{y_B^{\,2}}{L} = 1 \tag{3.43}$$

After the re-arrangement, Equation (3.41) becomes

$$\frac{x_B^{\,2}}{h\sqrt{(\tan^2\phi - \tan^2\chi)\cos^2\chi + \dfrac{\sin^2\chi(1+\tan^2\phi)}{1-\tan^2\chi\tan^2\phi}}} + \frac{\left(y_B - h\dfrac{\tan\chi(1+\tan^2\phi)}{1-\tan^2\chi\tan^2\phi}\right)^2}{h\sqrt{\dfrac{(\tan^2\phi - \tan^2\chi)(1-\tan^2\chi\tan^2\phi) + \tan^2\chi(1+\tan^2\phi)^2}{(1-\tan^2\chi\tan^2\phi)^2}}} = 1 \tag{3.44}$$

Equation (3.44), shows that the ellipse centre has offsets along the y_B-axis. Therefore, the semi-minor and semi-major axis of the ellipse is given by

$$l = h\sqrt{(\tan^2\phi - \tan^2\chi)\cos^2\chi + \frac{\sin^2\chi(1+\tan^2\phi)}{1-\tan^2\chi\tan^2\phi}} \tag{3.45}$$

$$L = h\sqrt{\frac{(\tan^2\phi - \tan^2\chi)(1-\tan^2\chi\tan^2\phi) + \tan^2\chi(1+\tan^2\phi)^2}{(1-\tan^2\chi\tan^2\phi)^2}} \tag{3.46}$$

From Figure 3.6(a), the viewing angle α has a relationship with angle χ . Additionally, the antenna beamwidth is twice the angle of ϕ. The following equations described the relationship

$$\alpha = 90° - \chi \tag{3.47}$$

$$\gamma_b = 2\phi \tag{3.48}$$

3.3.2. Analysis of Radar Footprint

Equation (3.45) through (3.48) are used to determine the size and distance of radar footprint using radar parameters of γ_b , α, and h. In this work, the radar footprint is analysed using non-symmetrical antenna beamwidth. The vertical and horizontal beamwidth is not equal in size. The size for vertical and horizontal beamwidth is 13° and 24° respectively. These values are selected to replicate the actual 3-dB beamwidth of the radar which we used in the experimental setup in Chapter 5.

Figure 3.7 shows the radar footprint shape and size. The difference between the figure in (a) and (b) is how the antenna is mounted on the vehicle. The figure in (a) shows the radar footprint when the vertical plane of the antenna is vertically oriented with respect to the ground plane. Contrarily, figure in (b) shows the footprint of radar when the horizontal plane of the antenna is vertically oriented with respect to the ground plane. For comparison purpose, we plotted five footprints of different depression angle values with α = [20º, 30º, 45º, 50º, 60º]. The height of radar from the ground is h = 0.5 m and is similar for all plots. The star marker (*) indicates the centre of the beam on the ground plane

Few conclusions can be made from Figure 3.7(a) and (b). Firstly, the footprints are elliptical with the ellipticity and size varies with different values of depression angle, α. As α becomes

shallower, the footprint becomes more eccentric. Also, the eccentricity of the ellipse becomes more critical when considering the orientation of the antenna. When the horizontal plane is mounted vertically with respect to the ground plane, the major axis of the ellipse footprint stretches further with the shallower depression angles.

Therefore, it is desirable to have the vertical beamwidth is vertically mounted with respect to the ground plane like in figure (a) because it produces smaller radar footprint compared to the configuration shown in figure (b). Additionally, it is shown that in figure (a) that depression angle $\alpha = 45^{\circ}$ is desirable since it provides a small size of the footprint at a distance of 0.5 m from the radar.

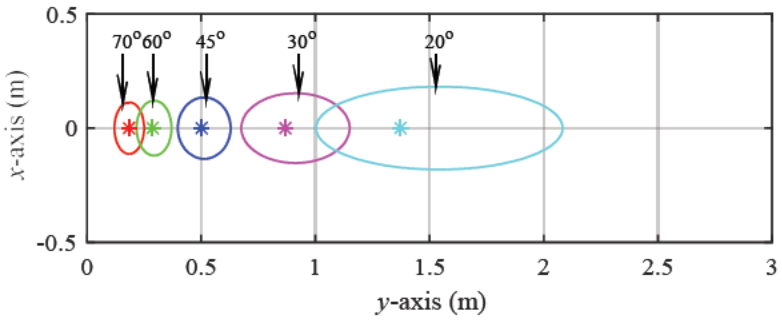

(a)

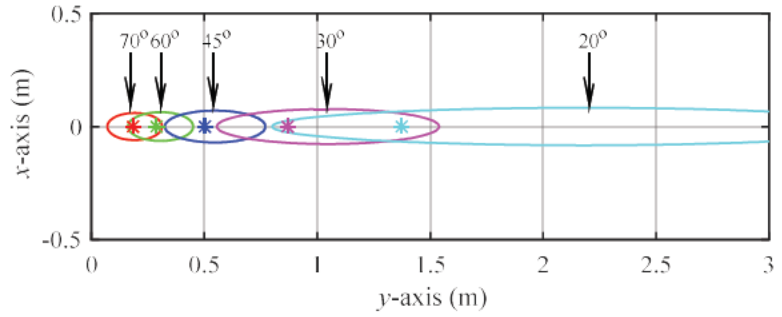

(b)

Figure 3.7 Comparison of radar footprint for five different values of depression angle, α.

3.4. Modelling Doppler Spectrum

It is essential to understand the influence of radar parameters on the shape of the Doppler spectrum. One way to understand is by collecting Doppler signal using SoG radar moving on actual roads. However, the Doppler signal from an experimental source is without the absence of noise and clutter. Also, the imperfection of the experimental setup can also affect the quality of the collected Doppler signal. An alternative way is to estimate its characteristics by modelling. This section investigates the effect of the radar parameters to the shape of the Doppler spectrum.

3.4.1. Model

Consider the typical radar setup as in Figure 3.6. We can the radar power receive equation to model the Doppler spectrum. Equation (2.26) gives an estimate of received power as a function of angle

$$P_r(\theta) = \eta \frac{\sigma_0(\theta)\Omega_S{}^2(\theta - \theta_0)}{R_t(\theta)^4} \tag{3.49}$$

The range, R_t can be derived from the radar geometry shown in Figure 3.6. However, for ground surface RCS and antenna radiation pattern, the actual values for these parameters depend on so many factors as explained in Section 2.2.3. Therefore, for simplicity of the modelling, two assumptions were made. Firstly, the RCS of the ground target is 1 m^2. Secondly, the radar has a rectangular antenna aperture. For this aperture, the antenna radiation pattern can be modelled using a sinc function as shown in Equation (3.50).

$$\Omega_S(\theta) = \text{sinc}\left(\frac{\theta}{30}\right)^{3\,72} \tag{3.50}$$

where θ is the width of the main lobe. Figure 3.8 shows the two-dimensional appearance of the antenna pattern generated by Equation (3.50). Note that, the value of 30 and 3.72 in Equation (3.50) are chosen arbitrarily to get a the 3-dB beamwidth of $\gamma_b = 13°$ with power drops rapidly as the beam moves away from the main lobe. The sidelobe power is relatively low, at 49.6 dB below the main lobe.

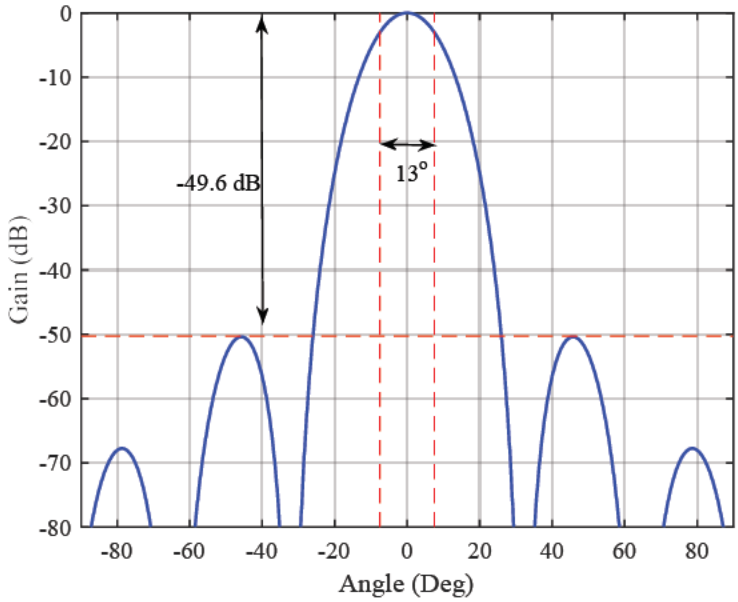

Figure 3.8 The approximation of antenna radiation pattern using Equation (3.50)

We can determine the respective antenna pattern at any of the point scatterers by measuring the angle between the point scatterer in the illuminated area and the antenna beam centre. The angle can be measured using a dot product and can be given as

$$\theta = \cos^{-1}\left(\frac{\mathrm{Re}(\vec{p}\ .\vec{p}_0)}{\|\vec{p}\ \|\|\vec{p}_0\|}\right) \tag{3.51}$$

where $\vec{p} = a_n\vec{x}_B + b_n\vec{y}_B$ is a point scatterer on the x_B-y_B plane and $\vec{p}_0 = a_0\vec{x}_B + b_0\vec{y}_B + c_0\vec{z}_B$ is the location of the radar beam centre on the ground plane. Finally, we can estimate the power

spectral density by replacing the θ with Doppler frequency, f_d from the Doppler equation as in Equation (2.22).

$$P\left(\cos^{-1}\left(\frac{f_d\lambda}{2v}\right)\right)=\frac{\sigma_0\left(\cos^{-1}\left(\frac{f_d\lambda}{2v}\right)\right)\Omega_S{}^2\left(\cos^{-1}\left(\frac{f_d\lambda}{2v}\right)\right)}{R^4\left(\cos^{-1}\left(\frac{f_d\lambda}{2v}\right)\right)} \tag{3.52}$$

where $\theta=\cos^{-1}\left(\frac{f_d\lambda}{2v}\right)$.

Figure 3.9 shows an example of a Doppler spectrum is generated using radar parameters in Table 3.1 and Equation (3.52).

Table 3.1 Values of radar parameters used in the analysis

Parameters	Value
Vehicle velocity, v	20 mph
Expected Doppler, f_d	1.01 kHz
3dB Radiation Beamwidth, γ_b	13°
Carrier frequency, f_c	24.0 GHz
Radar height from ground, h	0.5 m
Depression angle, α	45°
Azimuth angle, β	0°

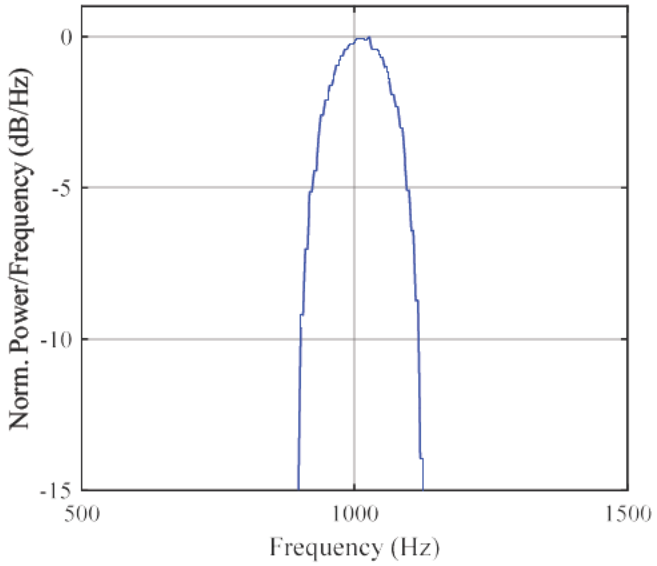

Figure 3.9 An example of a Doppler spectrum

As can be expected, the shape of the Doppler spectrum follows the shape of the antenna radiation pattern. The rugged construction near the peak of the spectrum is due to the number of scatterers used in the modelling. For this spectrum we used 5000 scatterers on the ground target. Less rugged peak can be achieved by adding more scatterers on the ground target. The peak of the spectrum is broad and somewhat blunt. For any Doppler shift algorithm in spectrum domain, this blunt peak causes some uncertainty in the estimation of mean Doppler frequency. In the following sub-section, we analyse the effect of radar parameters to the shape and summit of the Doppler spectrum.

3.4.1. Analysis of Doppler Spectrum with Values of Radar Parameters

In this sub-section, we use Equation (3.52) to analyse the effect of several SoG operational parameters; this includes the velocity of the vehicle, v viewing angles α/β and carrier frequency, f_c. Note that, other values of radar parameters are stated in Table 3.1.

Effect of vehicle velocity, v

Figure 3.10 shows the comparison of five Doppler spectra at different value of velocities, v = [1, 5, 10, 20, 30, 50 and 90] mph. As can be seen, the bandwidth of the spectra increases with the increase in speed. This observation can be explained using in Equation (2.25) where the bandwidth of the Doppler spectrum is proportional to the speed of the vehicle. Furthermore, the increase in speed also reduces the peak amplitude of the Doppler spectrum. For example, at v = 90 mph, the peak of the spectrum is nearly 40 dB lower than that in v = 5 mph. Lower peak power at higher vehicle speed is due to the spreading of power to a large number of spectral components.

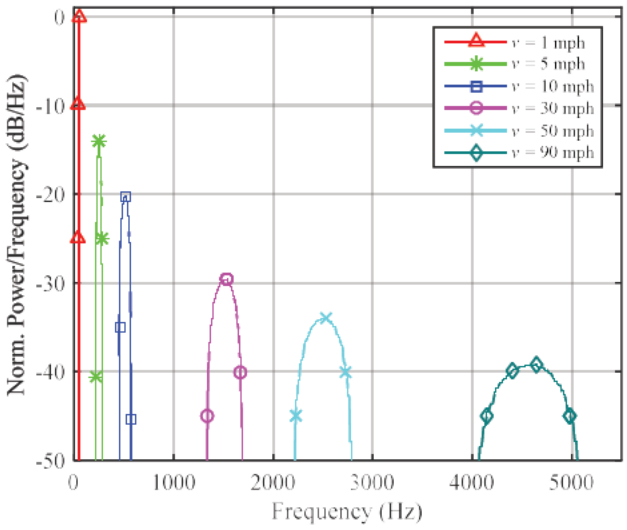

Figure 3.10 Comparison of Doppler Spectrum for selected vehicle speeds.

Effect of depression angle α and azimuth angle, β

Figure 3.11 shows the comparison of five spectra of different value of depression angles α = [15°, 30°, 45°, 60°, 70°]. Similarly, Figure 3.12 shows the comparison of six spectra of different values of azimuth angles β = [0°, 20°, 30°, 45°, 60°, 70°].

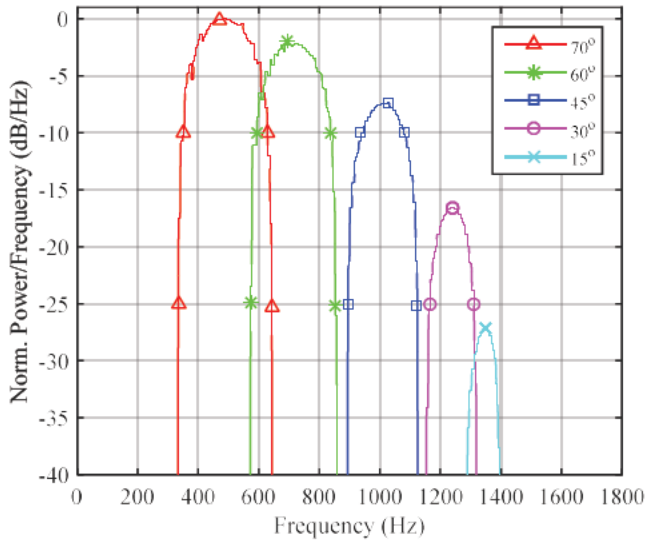

Figure 3.11 Comparison of Doppler spectrum for selected depression angles

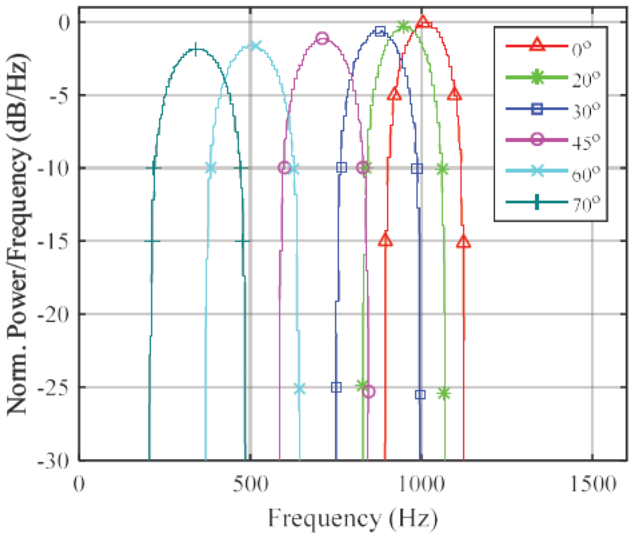

Figure 3.12 Comparison of Doppler spectrum for selected azimuth angles

As shown in Figure 3.11, the shallow values of α resulted in narrower spectral widths and sharper peaks. On the other hand, steep values of α produce Doppler spectrum with a broader width and rounded peak. Furthermore, the spectrum peak power reduces significantly with a smaller value of α. This result supports the result shown in Figure 3.4, where we showed that radar with low α has a smaller relative error than the steeper ones.

By comparison to Figure 3.12, the change in β has no significant effect on the shape of the spectrum peak. Between β values of 0° and 70°, the width and summit of the spectrum are approximately the same. Furthermore, the reduction in peak power is small which is less than 3 dB between β values of 0° and 70°.

Effect of the carrier frequency, f_c

Figure 3.13 shows the comparison of two different transmitter frequency of f_c = [24.0, 77.0] GHz. Note that, these two values re-present the standard frequencies that are used for vehicular radar in EU and USA.

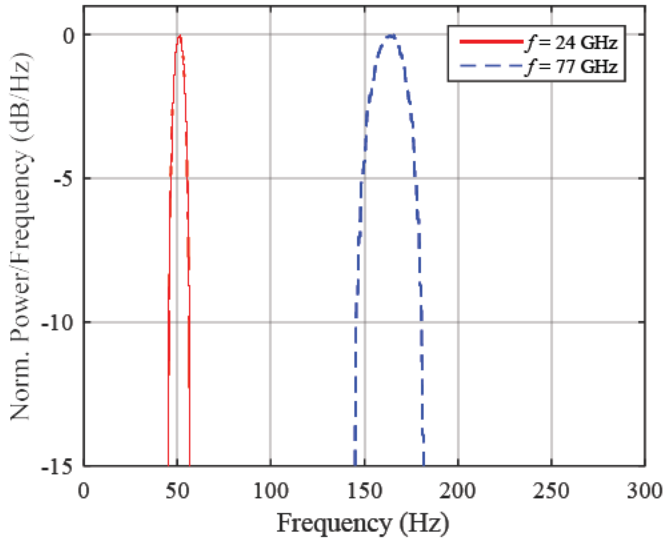

Figure 3.13 Comparison of Doppler Spectrum at v = 1 mph (a) 24 GHz (b) 77 GHz

In term of practical SoG application, it is much preferable to have a Doppler signal far from the 0 Hz because of the existence of low-frequency noises. Furthermore, employing HPF that is very close to 0 Hz can be challenging to implement. On the contrary, the 77 GHz radar produces a Doppler spectrum that is three times broader than the spectrum at 24 GHz. This effect is due to the relative spread of the Doppler spectrum. Such characteristics can be explained by Doppler frequency spread. A Doppler frequency spread can be defined as the ratio between the 3-dB bandwidth of the Doppler spectrum to the mean frequency of that Doppler spectrum. Using Equation (2.13) and (2.25), the Doppler spectrum spread can be given by

$$\frac{B_{ds}}{f_d} = \gamma_b \tan\alpha \tag{3.53}$$

The above equation shows that the Doppler spectrum spread is a function of antenna beamwidth and the radar depression angle. In other words, the bandwidth size of the Doppler spectrum is a constant scale of its mean frequency. As the radar carrier frequency goes higher, the Doppler spectrum bandwidth will also increase by a factor of $\gamma_b \tan\alpha$.

3.5. Summary

The theoretical analysis in this chapter has proved that some values of radar parameters can produce desirable effects on SoG operations. We have shown the 4-beam radar configuration has a much lower sensitivity to the vehicle roll and pitch motions when compared to a single-beam radar system. From the analysis in Section 3.3 and 3.4, we observed that the combination $\alpha = 45°$and $\beta = 45°$ produces the appropriate size of the ground footprint and sufficiently sharp and narrow Doppler spectrum. In the following Chapter 5, we implemented these configurations on the actual experimental setup.

Chapter 4. Derivation of Doppler Shift Estimation Algorithm and Performance Evaluation

4.1. Introduction

Estimating a mean frequency from Doppler signal remains a challenge in signal processing of SoG radar. As explained in Section 2.3.3, the radar echo from the ground surface is noisy. The complete suppression of this noise is difficult to realise without affecting the quality of mean frequency estimates. For example, the main lobe of the Doppler signal can be discriminated from the noise floor using amplitude threshold. However, in practice, Doppler signal SNR can vary and can go below the threshold level. Because of this reason, there is a need for algorithms that can track the main lobe of the Doppler signal. Therefore, the purpose of this chapter is to design algorithms that are capable of estimating the Doppler mean frequency accurately under varying SNR conditions.

In this chapter, two techniques are used to estimate the mean frequency of the Doppler signal. The first method is based on centre-of-mass of a Doppler spectrum and the second method is based on correlating the Doppler spectrum with a pre-determined spectrum template. A total of three algorithms are proposed in this chapter in which two of the algorithms are based on the centre-of-mass, and one algorithm is based on the cross-correlation. The detail of these approaches can be found in Section 2.4. Subsequently, these new algorithms are tested with artificial Doppler signal to evaluate its performance. Additionally, the performance of the proposed algorithms is also compared with two simple algorithms.

4.1.1. Previous Work

Many different mean frequency estimation algorithms for SoG radar has been proposed. The common objective of these algorithms is to estimate the mean frequency of Doppler signal with high accuracy. Despite their common aim, the approaches to determine the mean frequency are different. The earliest investigation in SoG radar signal processing was performed by Hyltin et al. in 1975 [47]. They proposed the use of the time-domain zero-crossing technique with a Schmitt trigger circuit to prevent low-amplitude noises from generating false zero crossings. Despite their effort, this method cannot achieve a consistent relative error of less than 1% due to the large amplitude fluctuations that occur on the Doppler signal.

Over the last decade, the research efforts are focused in frequency-domain. The generation of power spectral density of the Doppler signal is performed by using spectral analysis methods. Most researchers proposed the use of Fast-Fourier Transforms (FFT). [29] suggested using the computationally-efficient periodogram power spectrum and [59] introduced the use of the Welch method to reduce the variance in the spectral estimate. One issue with the FFT method it is poor frequency resolution for short samples (< 20 ms) of Doppler signal. To increase the frequency resolution, an alternative approach using autoregressive (AR) model-based methods based on Yule-Walker and Burg method have been investigated by [69] and [70]. The AR methods can produce a spectrum with high resolution but with higher computational complexity. Estimation using eigenvalue decomposition based on MUSIC algorithm has also been proposed by [71] and [69] to estimate the spectral density of Doppler signal.

Several algorithms have been proposed to estimate the mean-frequency from Doppler power spectral density. The simplest of these algorithms rely on finding the frequency component with the strongest amplitude [72], [59]. Theoretically, the strongest frequency component is simply the mean frequency of the Doppler signal. While this method is simple and

computationally inexpensive, the frequency shift with the highest intensity isn't always the mean frequency. Therefore, this method produces speed measurement with high variance.

Another approach is based on spectrum centre-of-mass. This method was proposed a decade ago by [71] in 1992. Later, [29] enhanced this method by implementing a pre-processing which captures the useful Doppler bandwidth and removes the spectral components with higher variance. The resulting spectrum is expected to have a lower incidence of frequency components with high variance and therefore reducing the variance in the estimation of mean frequency. While the pre-processing is proposed to enhance the estimation accuracy, the stability aspects of the pre-processing remain unclear and can directly impact the accuracy of the speed estimation. Their pre-processing captures the useful bandwidth by detecting critical changes in the spectral slope. However, the substantial variations in spectral amplitude may influence on the slope measurement and hence, affect the accuracy of the mean frequency estimation.

Cross-correlation has also been used to estimate the mean frequency of the Doppler signal. This method was first introduced by [28] and further developed by [59]. Both studies proposed cross-correlating the actual spectra against an assumed template of Doppler spectra. In this approach, the proposed algorithm computes the cross-correlation of the observed spectrum against a possible set of spectra and determine a pair of cross-correlation with the maximum correlation coefficient (refer Section 2.6.2 for cross-correlation coefficient). Hence, the location of mean frequency corresponds to a pair of cross-correlation with maximum correlation. This technique was shown to provide an estimate of the mean frequency with high accuracy [73]. However, its implementation would require a high cost of computation which takes too much time to update speed in a short time, i.e. 10 ms. Furthermore, the generation of simulated spectra is complex and may not represent the true spectra obtained in practice.

4.2. Derivation of Algorithm

The previous section shows that estimating a mean Doppler frequency with high accuracy and reliability is still an open challenge. This section derives the new method in an attempt to solve the problem. For the convenience of the reader, we will first describe two simple algorithms which we called centre-of-mass noise subtraction (CMA-NS) and centre-of-mass level-threshold (CMA-T). It is important to mention here that these two algorithms serve as a comparison to the three algorithms that are proposed in the second part of this chapter.

In the second part of this chapter, we proposed three new algorithms. The reason for introducing these algorithms is to handle the issues found in practice such as varying SNR, significant sidelobes and the random peak of high amplitudes. The first two of the proposed algorithms based on centre-of-mass. We called these algorithms as centre-of-mass amplitude threshold (CMA-AT) and centre-of-mass slope threshold (CMA-ST). These two algorithms can adaptively find the main lobe of the spectrum before the computation of the mean frequency. The main difference between them lies in the filtering process; a process that distinguishes the main lobe from the spectral noise. As the name suggests, CMA-AT uses the spectral amplitude to filter the spectral noise, while CMA-ST uses the slope of the main lobe to estimate the position of the spectrum main lobe. On the other hand, the third algorithm is based on the cross-correlation method. We named this algorithm as the cross-correlation algorithm (XCA).

Figure 4.1 illustrates a Doppler spectrum with its fundamental parameters. This figure is aimed to help readers to understand the spectrum key parameters used in the following sub-sections. The spectrum can be characterised by the signal power $S(f)$, noise power $N_r(f)$, standard

deviation of noise power σ_n, main lobe start frequency f_{start} and stop frequency f_{stop} of the main lobe and mean Doppler frequency f_0 .

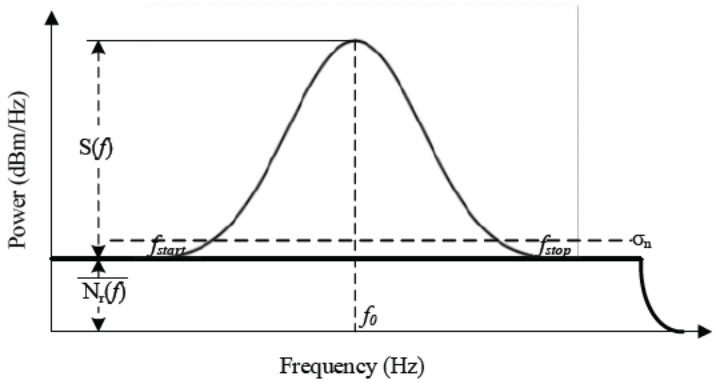

Figure 4.1 A qualitative illustration of a Doppler spectrum and its parameters

4.2.1. Centre-of-Mass with Noise Suppression

As been described in Chapter 2, the basic CMA method corresponds to the sum of spectral power. If the spectrum has considerable noise power such as in Figure 4.2, the estimation of mean frequency will result in significant bias. Note that the green dashed line indicates the region of the main lobe and the red point-line indicates the noise spectral density.

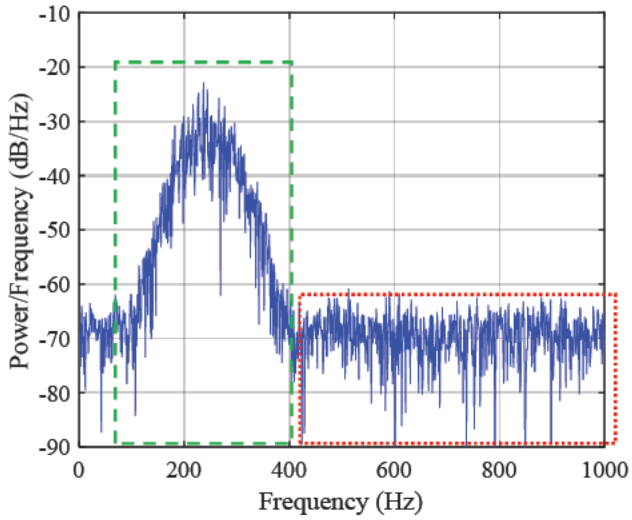

Figure 4.2 An example of Doppler signal spectral density.

In the frequency domain, one of the simplest ways to minimise the effect of noise is by subtracting the noise density from the main lobe. This method has been applied in the field of speech processing [74] [75] and can be applied in this work. The mean frequency of the noise-subtracted spectrum is given by

$$f_0 = \frac{\sum_{f=1}^{M} f\left[S(f) - \overline{N_r(f)}\right]}{\sum_{f=1}^{M}\left[S(f) - \overline{N_r(f)}\right]} \tag{4.1}$$

where f and f_0 are the frequency and mean frequency of the spectrum, $S(f)$ is the spectral density, $\overline{N_r(f)}$ is the average noise density and M is the upper limit of summation. Figure 4.3 shows the detail signal processing of the algorithm. It consists of four steps: FFT, noise density level measurement, noise subtraction, and centre-of-mass computation. The noise level is measured when the vehicle is at rest or no motion, and we assumed that the noise density is stationary. Figure 4.3(a) and (b) show a Doppler spectrum before and after the noise subtraction respectively. It can be seen that the subtracted spectrum has a lesser random variation of noise

density. The distorted distribution of noise is due to the algorithm process. Due to the random variation of noise density in Figure 4.3(a), the spectral subtraction produces negative values of power spectral density. These negatives values are mapped to a non-negative value which distorts the new distribution of noise density and this distortion is more noticeable at lower SNR. For reference hereafter, this technique is called CMA-NS.

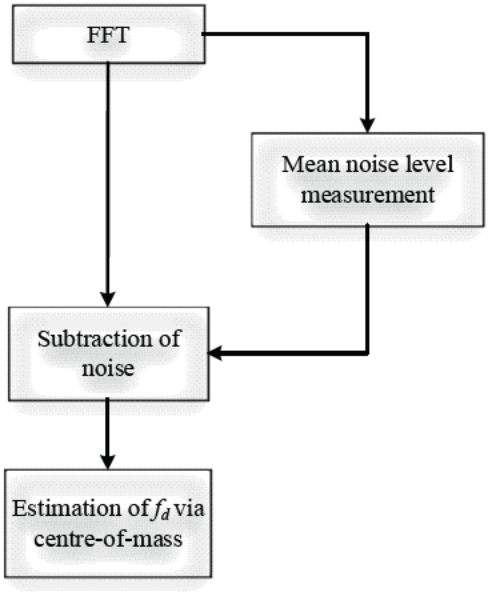

Figure 4.3 Steps of signal processing for CMA-NS

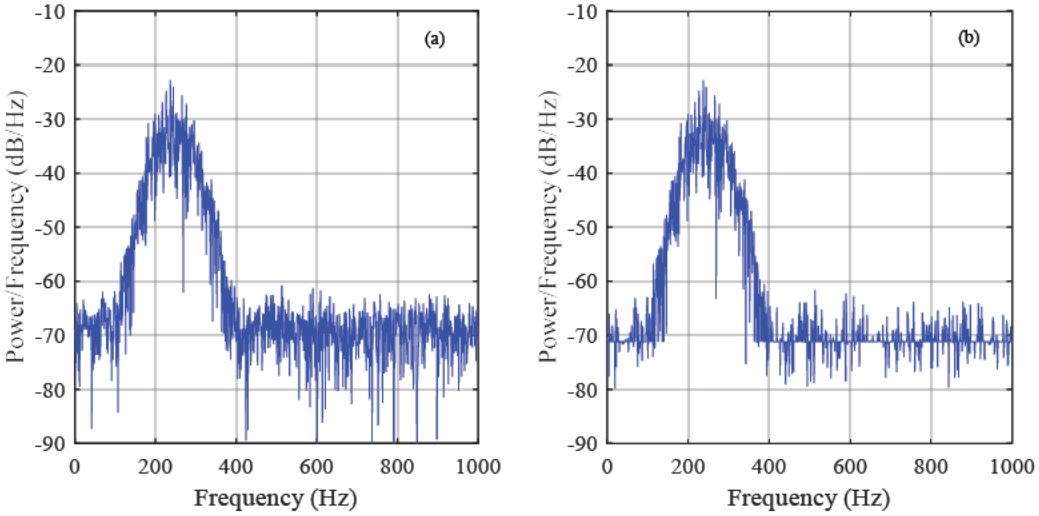

Figure 4.4 An examples of Doppler power spectrum. (a) Before suppression of noise. (b) After suppression of noise.

4.2.2. Centre-of-Mass with Amplitude Thresholding

The basic idea of this method is to discard the noise density from the total mass of the spectra. This method is performed by setting an amplitude threshold to separate the spectral components to useful signal and noise [76]. The processing approach is as follows: The first three steps of processing are similar to CMA-NS. In the fourth step, the algorithm removes any signal below the threshold. The final step is the computation of CMA. The rule of thresholding the noise is given by

$$S(f) = \begin{cases} S(f) & for \quad S(f) \geq threshold \\ 0 & Otherwise \end{cases} \tag{4.2}$$

where $S(f)$ is the amplitude of the power spectra. In this work, we set the threshold value to 10 dB from the mean noise density $\overline{N_r(f)}$. The value of 10 dB is chosen so that the algorithm can still function when processing Doppler signal with weak SNR between 10 to 20 dB. An

example of a Doppler spectrum before and after the noise cut-off in Equation (4.2) is shown in Figure 4.6. For reference hereafter, this technique is called CMA-T.

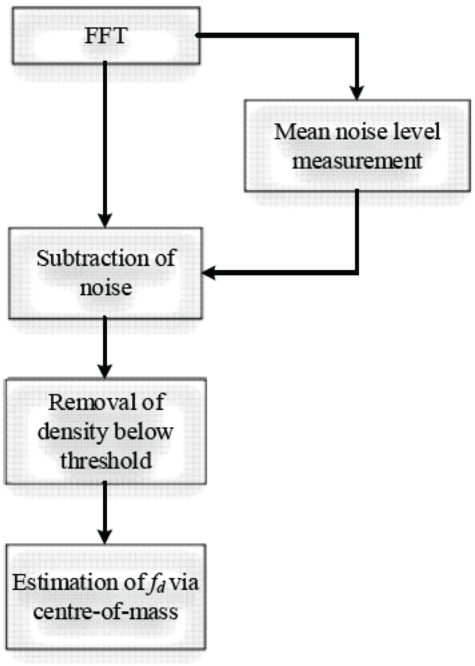

Figure 4.5 Steps of signal processing for CMA-T

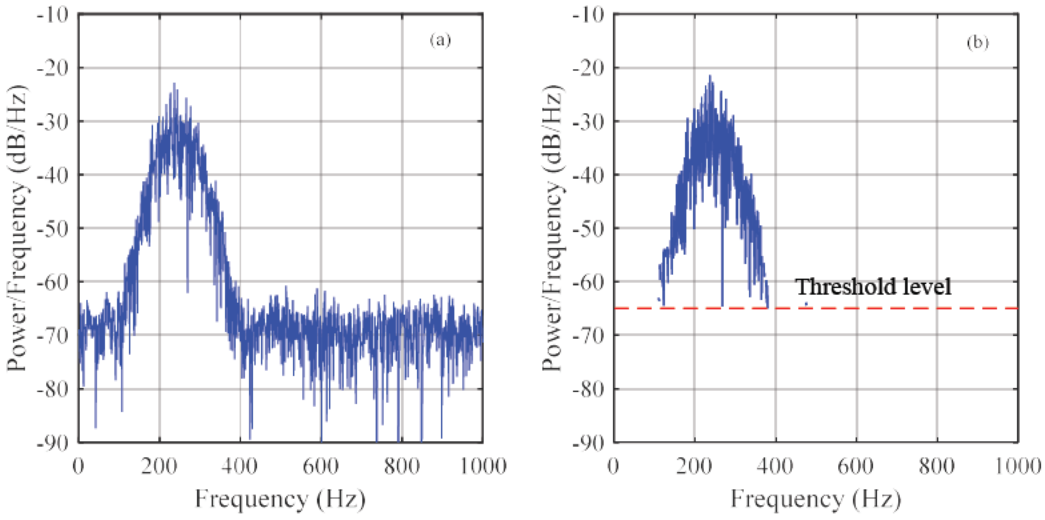

Figure 4.6 An example of Doppler power spectrum. (a) Original. (b) After the removal of spectral density below threshold.

4.2.3. Centre-of-mass Amplitude Threshold

The motivation of this algorithm stems from the nature of the Doppler signal. In practice, the Doppler signal may have random spurious peaks and low-frequency noise surrounding the main lobe. This unwanted noise can be rejected from CMA computation by setting the limits of the computation only to the useful bandwidth of the spectrum main lobe.

In general, the algorithm consists of two stages with a different purpose. The first stage is pre-processing, and the second stage is the computation of CMA. The function of pre-processing is to determine the start and stop frequency of the main lobe. Here, we summarise the pre-processing operation. At first, the algorithm estimates the noise level density in the spectrum and classify each of the spectral components by their power level into binary values of 1 and 0. Next, the algorithm finds the minimum and maximum frequency of the main lobe. This technique is performed by sliding a window of finite length along the spectral length. For each sliding step, the algorithm sums the binary content within the window and compares to a pre-determined threshold value. If the sum exceeds the threshold, the algorithm assumes a start/stop frequency of the main lobe is found. Finally, in the second stage, the algorithm computes the centre-of-mass via Equation (2.38).

The following steps summarise the signal processing of the algorithm:

Step 1: Estimate the DFT of the Doppler signal via the FFT algorithm

Step 2: Compares the power of each spectral component to a pre-determined threshold value. If the amplitude of the frequency component is above the threshold level, the frequency location is set to 1 and 0 for vice-versa. The digital output of the comparison process is given as

$$D(f) = \begin{cases} 1 & for \quad S(f) \geq Z_1 \\ \\ 0 & for \quad S(f) \leq Z_1 \end{cases} \tag{4.3}$$

where D(*f*) is the digital output, Z_1 is the threshold of the algorithm which roughly differentiates between signal and noise power. Here, we assumed that the SNR of the Doppler signal is relatively high but given the distance of radar from the ground is sufficiently short (less than a meter), this assumption is acceptable. The value Z_1 is associated with the noise floor of the spectrum.

$$Z_1 = \overline{N_r(f)} + 3\sigma_n \tag{4.4}$$

where $\overline{N_r(f)}$ and σ_n is the mean and standard deviation of the noise density. In this work, the $3\sigma_n$ represents 99.7% of the noise density level.

Step 3: Find the lower bound frequency of the main lobe. The search process is performed by sliding a window of length *w* from the left to the right of the spectrum. For each movement, the algorithm computes the sum of ones within the window length and compares the sum to a pre-determined threshold, Z_2. If the sum of the binary is below the threshold, $\sum_{n}^{n+w} D(f) < Z_2$ the search will continue until the algorithm founds a location which the binary sum exceeds the threshold, $\sum_{n}^{n+w} D(f) > Z_2$. If this condition is satisfied, the algorithm assumed a start frequency of the main lobe is found.

Step 4: Find the upper bound frequency of the main lobe. The process is similar as in Step 3, but the search begins from right to left of the spectrum. Here, it is essential to set the size of the window length, *w.* To distinguish between a right start/stop frequency of the main lobe and

a random noise peak, the size of *w* must be bigger than the width of a typical spurious peak. On the other hand, a large size of *w* is not suitable when the main lobe is narrow. For the algorithm to properly work on both narrow and broad spectrum, we have determined two values of *w* for two range of mean Doppler frequency.

$$w = \begin{cases} 5 & for \quad f_d < 1000\,Hz \\ 10 & for \quad f_d \geq 1000\,Hz \end{cases} \tag{4.5}$$

where f_d is the mean Doppler frequency that is roughly estimated from the peak of the Doppler spectrum after a simple smoothing process on *f*(*n*). This rough estimate of f_d does not introduce deficiency in determining the mean Doppler frequency.

Step 5: Compute the mean Doppler frequency by estimating the CMA of the spectrum energy between f_{start} and f_{stop}.

Step 6: Finally, compute the vehicle speed using the Doppler equation, $v = \frac{f_d \lambda}{2\cos\theta}$

For reference hereafter, this technique is called CMA-AT.

4.2.4. Centre-of-mass Slope Threshold

Like the previous method, the centre-of-mass slope threshold uses CMA to determine the mean Doppler frequency. But instead of using the sliding window to estimate the location of the main lobe, it measures the change in slope of the spectral data. This algorithm makes use of the cumulative sum (CUSUM) algorithm [77]. CUSUM is a well-known change detection technique which has been widely used in the fields of signal processing [78], [79]. This algorithm functions to detect small changes that depart from its mean value by cumulating the

sum of the difference between the present value and the previous average. The cumulative-sum control-chart can be defined as

$$C_S(1) = 0 \tag{4.6}$$

$$C_S(n) = \max[o, S(f) - (\overline{N_r(f)} + a_0\sigma_n) + C_S(n-1)] \tag{4.7}$$

where $\overline{N_r(f)}$ and σ_n are the mean and standard deviation of noise floor density, a_0 is the reference value which is used to detect a drift from the control values. $C_S(n)$ is the cumulative sum of deviation from the target at the observation sample. It is apparent from the equation that if a negative change is found, the cumulative-sum is reset to zero. Thus, only positive change is counted. $C_S(n)$ will point upward if the sample values are out of the control values $S(f) > a_0\sigma_n$. The slope of the cumulative sum would be steeper or shallower depending on how large the sample deviates from the control value.

The following steps summarise the signal processing of this method.

Step 1: Estimate the DFT of the Doppler signal via FFT algorithm.

Step 2: Compute the cumulative-sum, $C_S(n)$ of the spectral data. Here, the noise floor is defined as the stationary process of the cumulative sum. Hence, the value of $\overline{N_r(f)}$, and σ_n of Equation (4.7) are measured from the noise floor of the spectrum. We set a_0 = 3 which represents three standard deviations.

Step 3: Divide the cumulative-sum into blocks of fixed size, b_m. In this work, we define the size of each block, m = 5. For each block, we estimate the spectral amplitude pattern by

estimating the gradient (in degrees) between the first and last spectral values of each block. The algorithm saves the gradient values for all blocks.

Step 4: Compare the gradient value of each block to a predetermined gradient threshold, Z_g. Our preliminary analysis of the value of Z_g indicates that $Z_g = 0.05°$ is suitable to distinguish the noise floor from the main lobe.

Step 5: Search for the start frequency of the main lobe. Perform a search on the blocks until two consecutive blocks with slope values above the Z_g is found ($b_m(n) \& b_m(n+1) > Z_g$). If this outcome is found, the algorithm determines the location of the $b_m(n)$ on the spectrum and assume this location as the start frequency of the main lobe. Note that the search is performed from left-most block to the right.

Step 6: Search for the stop frequency of the main lobe. The process is similar to Step 5. However, the search is performed from the right-most block to the left.

Step 7: Compute the mean Doppler frequency by estimating the CMA of the spectrum between the start and stop frequency.

Step 8: Finally, compute the speed of the vehicle using the Doppler equation, $v = \frac{f_d \lambda}{2\cos\theta}$,

Figure 4.7(a) to (c) show the outputs of the algorithm after FFT, cumulative sum, and slope measurement. The red line indicates the start and stop frequency of the main lobe. As can be seen from (b), a relatively flat cumulative sum implies that there is no significant increase in from the noise floor. However, the cumulative sum produces a jump when spectral data has a substantial change from the mean noise spectral density.

For reference hereafter, this technique is called CMA-ST

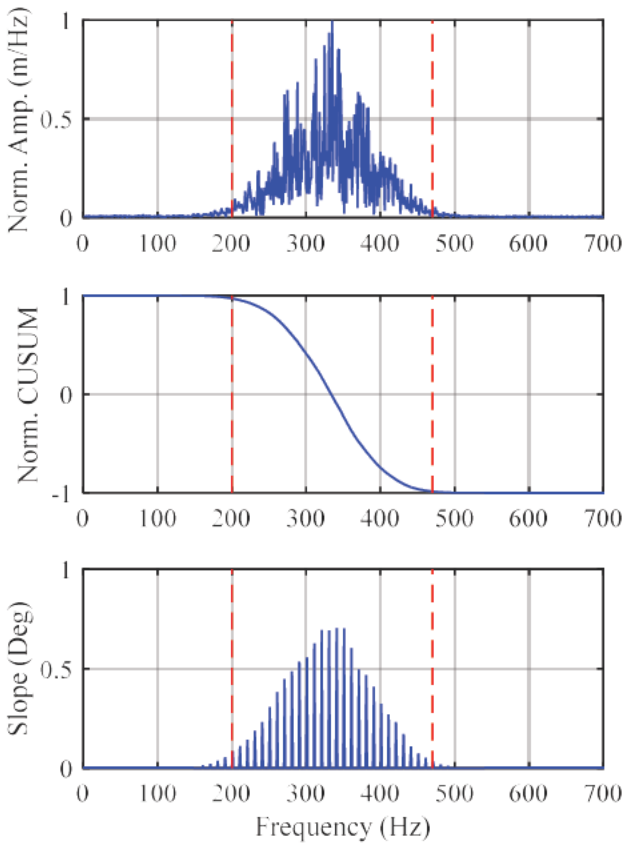

Figure 4.7 Examples of algorithms outputs in Step 2 and 3 (a) Input Doppler spectrum (b) Cumulative sum in Step 2. (c) Measured gradient in Step 3.

4.2.5. Cross-Correlation Matching

As discussed in Section 4.1.1, the cross-correlation method proposed by [28], [59] has two application problems when they are used for practice. These problems are firstly due to the multiple cross-correlations require large computational power which can be expensive to implement and may limit the possibility of real-time processing. Secondly, the reference template is complex to generate and may not represent the actual spectra in practice.

In this work, we proposed two modifications to the technique. Firstly, we aimed to reduce the computational complexity by reducing the number of cross-correlation from multiple to one.

Secondly, for the benefits of practicality and ease of implementation, we proposed the use of Gaussian function as the reference template. The assumption of the Gaussian pattern is based on the theoretical work and actual data collected from the experiments. Furthermore, the Gaussian curve is easy to generate and simple to work with. Figure 4.8 shows an example of this template matching using a Gaussian curve. The Doppler spectrum is shown as the solid blue line, and the Gaussian pattern is indicated with a dashed red line. It can be said that the Gaussian curve can be used to approximate the main lobe of the spectrum.

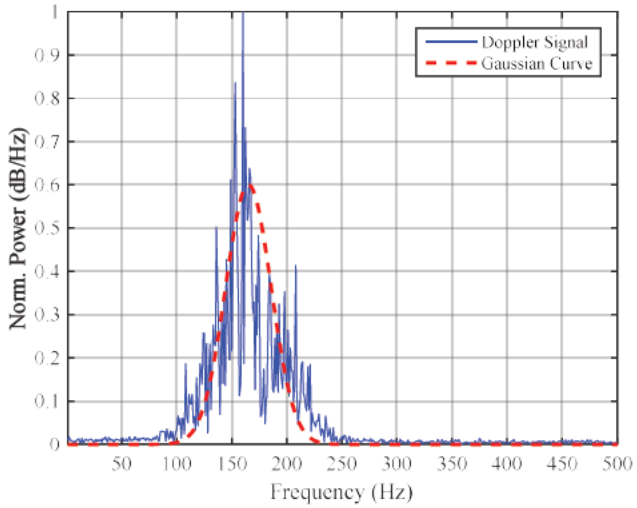

Figure 4.8 Similarity between the Doppler power spectrum and Gaussian curve based on the signal.

One drawback of this approach is that it requires an antenna with a radiation pattern shaped like a Gaussian curve. Any antenna pattern which departs from the Gaussian shape especially on the first 3-dB power is not suitable for this approach.

The following steps summarise the signal processing of the algorithm.

Step 1: Estimate the power spectrum of the Doppler signal via FFT algorithm.

Step 2: Smooth the spectrum using a simple moving averaging filter and locate the largest amplitude in the spectrum. At this stage, we assume the location of the peak as the mean Doppler frequency f_d'. This rough estimation provides information for the algorithm to compute the speed parameter, v and hence compute the standard deviation of the Gaussian pattern that enables the generation of Gaussian shape. Nevertheless, this is a rough estimate of a mean Doppler frequency. The following step 3 and 4, will shift f_d' to arrive on a position which best matches the Gaussian shape and the Doppler spectrum.

Step 3: Generate the Gaussian curve by the following relationship

$$v = \frac{f_d' \lambda}{2\cos\alpha} \tag{4.8}$$

$$\sigma_{ds} \approx \frac{v}{\lambda} \gamma_b \sin\alpha \tag{4.9}$$

$$\Omega_G(f) = a_g \exp\left[\frac{(f - f_d')^2}{2\sigma_g^{\,2}}\right] + b_g \tag{4.10}$$

where $\Omega_G(f)$ is the Gaussian curve, a_g is the peak amplitude of the Gaussian curve.

Step 4: Cross-correlate the generated Gaussian curve with the Doppler spectrum and determined the location of which the coefficient of cross-correlation is largest.

Step 5: Finally, compute the speed of the vehicle using the Doppler equation, $v = \frac{f_d \lambda}{2\cos\theta}$

4.3. Overview of Performance Evaluation

In this section we provide, an overview of the evaluation procedure for the proposed algorithms and followed by the description of the design goal and performance criteria. Figure 4.9 shows the flowchart of the evaluation procedure. Each algorithm is provided with a set of simulated Doppler signal with known mean frequencies. The algorithms transform the signal into power spectral density via the FFT algorithm and estimate the mean frequency of the Doppler signal. The results are recorded, and the measurement of bias and the standard deviation is performed. Finally, a comparison of accuracy between the algorithms is performed.

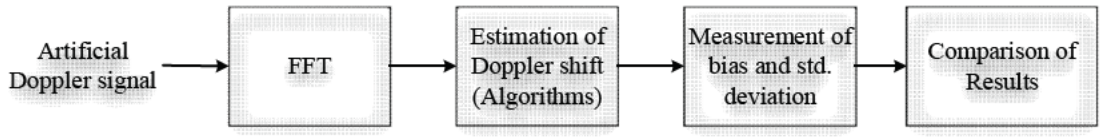

Figure 4.9 Procedure for evaluating speed estimation algorithm

The bias of an algorithm is defined as a consistent deviation of results from its true value. This value can be under or over-estimate from the true value. Bias is defined as [80]

$$Bias = \hat{f}(n) - f(n) \tag{4.11}$$

where $\hat{f}(n)$ is the expected value of the observed data or the average of the observation data and $f(n)$ is the true value. On the other hand, the standard deviation is used to measure the precision of the algorithm. A standard deviation of a measure is defined as [80]

$$\sigma = \sqrt{\frac{1}{N}\sum_{n=1}^{N}\left(\hat{f}(n) - f(n)\right)^2} \tag{4.12}$$

where μ is the average of mean frequency and N is the number of trials or number of mean Doppler frequency measurement. In the following sub-section, we describe in detail on the generation of the simulated Doppler signal and the datasets which are used to test the algorithms.

4.3.1. Design goal and signal Processing Performance Requirements

This sub-section discusses the specific design objectives and performance requirements of the signal processing. The points are summarised in Table 4.1, followed by the reasoning behind them.

Table 4.1 Design goal and performance criteria

No	Design objectives	Requirements
1	Detection velocities range	1 to 110 mph
2	Maximum relative error	< 3%
3	Noise sensitivity	SNR > 10 dB
4	The possibility of real-time processing	Yes, at least 100 ms with relative error < 3%
5	Cost of Algorithm	low-cost

Criterion 1: Speed Detection range. The speed detection range is expected to be broad. This need is to ensure that the algorithm can work for the standard range of vehicle speedometer. The lower limit of the range is influenced by HPF which function to suppress low-frequency noise [81] [82]. In this work, we set the minimum detectable speed to 1 mph. For the SoG system with f_c = 24 GHz and α = 45°, the resulting Doppler shift of 1 mph is 70 Hz. For

maximum detectable speed, this value is limited by the received power of the radar. However, for this evaluation, we define the maximum measured speed of 110 mph.

Criterion 2: Maximum relative error. The error in estimating mean frequency is expected to be lower than 3% over the range of measured speed. This expected value is constructed from the previous study of SoG radar [83].

Criterion 3: Noise sensitivity. The algorithm must be able to work under weak signal and noisy conditions. As discussed in Chapter 3, the Doppler signal in practice does not have a constant SNR. The SNR varies with radar mounting configuration and speed of the vehicle. The value of SNR can be further reduced due to the condition of the ground surface. The challenge of each algorithm is to minimise the effect of the noise on the accuracy of the estimated speed.

Criterion 4: Real-time processing. Technically speaking, almost none of the algorithm can produce the output at the same time as the input. In the actual case, this is impossible to do since there will be some delay due to the processing of the input signal. It is preferable that algorithms have low computational complexity so that it could work in real time. For this work, we set the speed update rate to a minimum of 100 ms to match with the requirement of vehicle safety system such as ABS or ASC [84] [54], [85].

Criterion 5: Cost of Algorithm. For SoG radar to be successful in practical applications, the cost implementation of the algorithm must be minimum. The algorithm itself must be efficient computationally inexpensive. Additionally, it can be implemented using low-cost hardware. Furthermore, the algorithm must also be flexible for future trend in vehicular radar so that it can be performed with minimum cost — for example, a software upgrade rather than hardware upgrade [81], [86].

Note that these design objectives and performance criteria are limited to the evaluation in this chapter.

4.4. Simulated Doppler signal

Simulated Doppler signal provides many advantages which overcome the main limitation of an actual Doppler signal. Mainly, it makes it possible to generate a set of Doppler signals with known mean frequency, SNR and bandwidth. This section describes the mathematical background of the Doppler signal modelling and the examples of an artificial Doppler signal.

4.4.1. Principle of Generation

Before we discuss the principle of Doppler signal generation, it is worth noting that the main lobe of the Doppler spectrum is primarily influenced by the antenna radiation pattern as discussed in Section 2.3.3. Additionally, in Section 2.8 we stated that both sinc and gaussian antenna pattern could be used for the antenna pattern approximation. For this chapter, we assumed that the antenna radiation pattern follows the Gaussian function. The use of Gaussian model enables the estimate of Doppler spectrum bandwidth using vehicle speed as presented in Equation (2.25).

Consider a typical characteristic of the Doppler spectrum; the spectral density of the main lobe is not smooth but randomly varies from one spectral component to another. Mathematically, a simulated Doppler spectrum can be obtained by generating a population of spectral densities and adding the spectral densities with white noise. Figure 4.10 illustrates the procedure of creating an artificial Doppler signal.

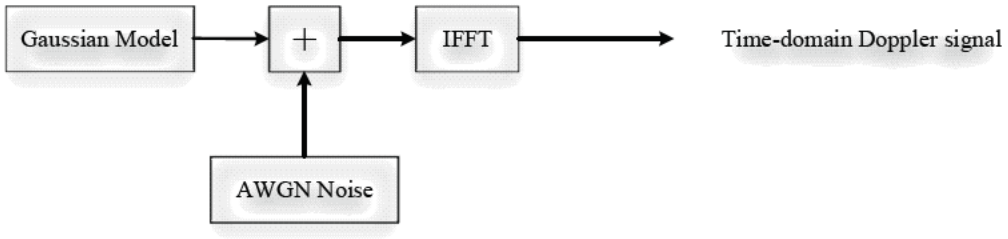

Figure 4.10 Procedure for generating Doppler signal

4.4.2. Method

This work uses the technique introduced by Zrnic et al. [87]. Initially, this method was designed to generate an arbitrary shape power spectrum for meteorological study. Nevertheless, their approach can be used in this study.

The simulated Doppler signal is formed according to the following steps: Firstly, the population density of the spectrum is generated using a Gaussian function. A Gaussian curve is defined by [88]

$$\Omega_G(f) = \frac{1}{\sigma_g\sqrt{2\pi}} \exp\left[\frac{(f-f_0)^2}{2\sigma_g{}^2}\right] \tag{4.13}$$

where $\Omega_G(f)$ is the spectrum coefficient, σ_g is the standard deviation of the distribution, f and f_0 are the frequency and mean frequency of the Doppler spectrum respectively. The value of f_0 and σ_g is associated with the vehicle speed and the parameter of radar which determined by classic Doppler and Doppler spectrum equations. In this case, the mean frequency is a Doppler frequency.

$$v = \frac{f_d \lambda}{2\cos\alpha} \tag{4.14}$$

$$\sigma_g \approx \frac{v}{\lambda}\theta_{bw}\sin\alpha \tag{4.15}$$

In the next step, noise is added into the spectral distribution. Noise is normally distributed to replicate the noise distribution of an actual Doppler signal. This step is accomplished by generating the composite spectral density [87]

$$S(f) = -\ln(\rho(n))\left[k_n \Omega_G(f) + \frac{1}{n}\right] \tag{4.16}$$

where $S(f)$ is the Doppler spectrum plus noise, ρ is a number that is uniformly distributed between the value of 0 and 1 ($0 < \rho < 1$) and k_n is the signal-to-noise (SNR) scaling factor which is used to improve or worsen the condition of the Doppler signal against noise. The average SNR in the spectrum is given as

$$SNR = \frac{1}{nN_f}\sum_{f=1}^{N}\Omega_G(f) \tag{4.17}$$

where N_f is the noise power per discrete frequency, and nN_f is the total noise power in the spectrum. k_n is given by

$$k_n = \frac{10^{\frac{SNR}{10}}}{\sum_{f=1}^{N}\Omega_G(f)} \tag{4.18}$$

The SNR is expressed in dB. The final stage of signal generation is to convert the power spectrum to time-series samples using the inverse FFT (IFFT). The decomposition of the power spectrum into real and imaginary components of a time-domain signal is given by

$$a(n) = \sqrt{S(n)}\cos(2\pi\rho) \tag{4.19}$$

$$b(n) = \sqrt{S(n)}\cos(2\pi\rho) \tag{4.20}$$

where $a(n)$ and b(n) are the real and imaginary components of the signal and ρ is a value that is uniformly distributed between 0 and 1. We assumed that the phase is uniformly distributed to rebuild the Doppler signal. The final step is to perform IFFT on the complex signal. The computation of IFFT is accomplished via the MATLAB IFFT function. The complex Doppler signal is given by

$$I_d(n) + jQ_d(n) = \sum_{n=0}^{N-1}(a(n) + jb(n))\exp\left(j\frac{2\pi}{N}km\right) \tag{4.21}$$

4.4.3. Example of Generated Signal

As explained in the previous section, the generation process of the Doppler signal consists of three stages; the generation of the main lobe, the addition of white Gaussian noise and transformation from frequency-domain to time-domain. This sub-section shows an example of a Doppler signal generated using Equation (2.1) through (4.21). The input parameters of the Doppler signal is shown in Table 4.2.

Table 4.2 The values of radar parameter for the example of Doppler signal

Radar Parameters	Value
Mean Doppler frequency, f_0	718 Hz
Transmitter frequency, f_c	24.0125 GHz
Sampling Frequency, f_s	15.0 kHz
3-dB Antenna beamwidth, γ_b	13.0°
SNR	40.0 dB
Observation time, T (Update rate)	1 second

Figure 4.11(a)–(f) illustrate the signal at several stages of the signal generation. The noiseless Doppler spectrum is shown in (a), (b) shows the white Gaussian noise and (c) shows the summation of the signal in (a) and (b). As can be seen in (b), the shape of the power spectrum reflects the shape of the Gaussian curve in (a). The mean noise density level is -87 dB and SNR is approximately 40 dB which is expected.

An inverse Fourier transform of the spectrum in (c) produces a time-domain signal in (d). The bold blue line indicates the in-phase, I_d signal and dashed red-line indicates the quadrature signal Q_d. As specified in the evaluation procedure, the time-domain signal is transformed back to the frequency domain. The power spectrum in dB is shown in (e). For comparison purpose, an actual power spectrum which was collected using the same parameter in Table 4.2 is shown in (f). Clearly, the modelled signal in (e) is very similar to the actual signal. The small difference in the shape of the spectrum is due to the assumption of Gaussian shape spectrum. Nevertheless, the first half power of the artificial spectrum is very close to the shape of the actual Doppler spectrum. The modelled spectrum demonstrates that the Doppler signal can be well-represented using the modelling procedure in Section 4.4.2.

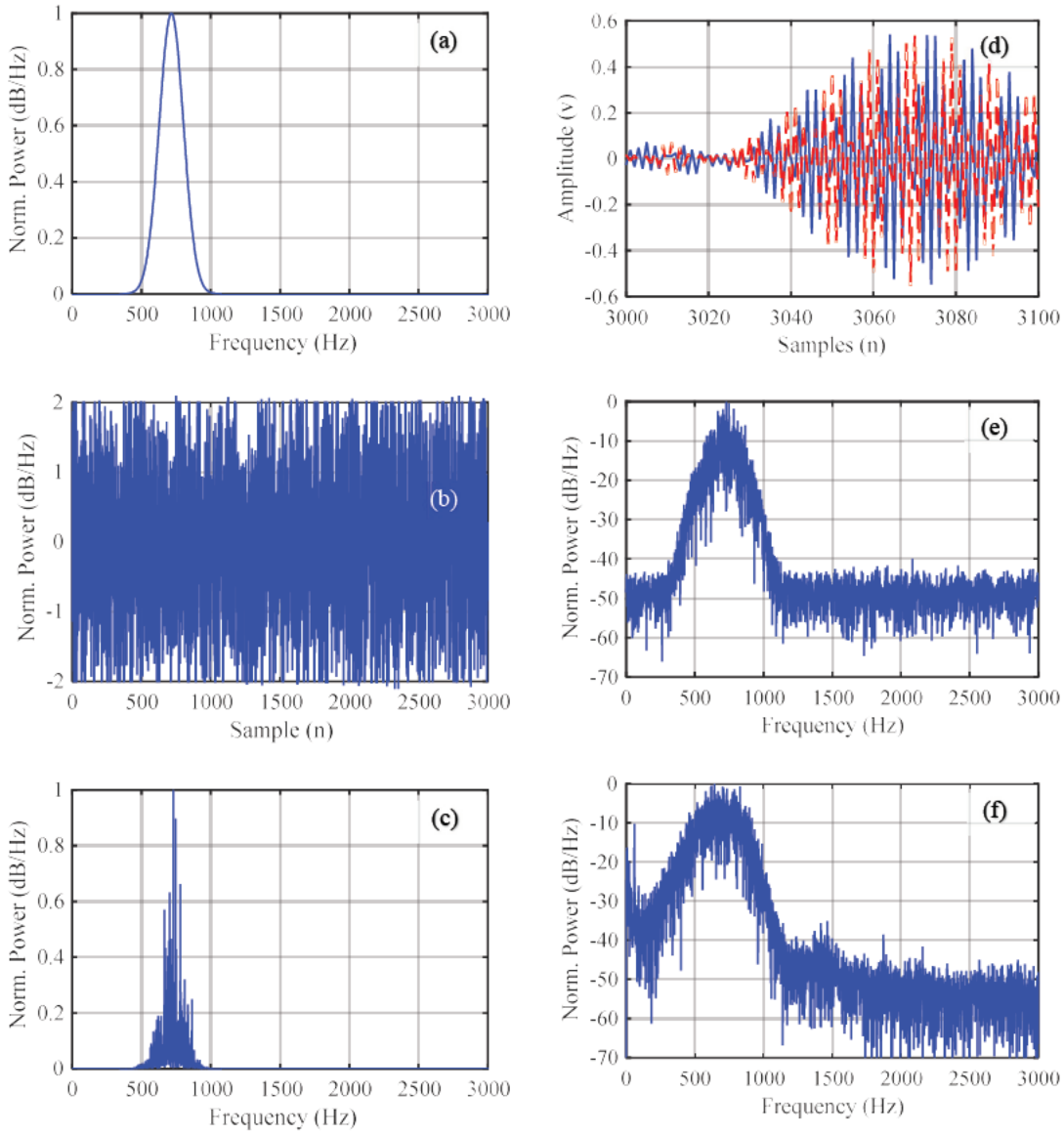

Figure 4.11 Examples of the simulated signal at five stages of the signal processing. (a) Noiseless Gaussian spectrum. (b) White Gaussian noise. (c) The power spectrum of the summation signal in (a) and (b). (d) Discrete samples of the time-domain Doppler signal. (e) The power spectrum of the Doppler signal in dB. (f) Example of actual Doppler signal collected from the experiment with the same radar parameters as in Table 4.2.

4.4.4. Test Datasets

The method in Section 4.4.2 is used to generate artificial Doppler signals. In summary, we created five datasets consisting of 100,000 Doppler signals of different SNR values. Each dataset contains 40 sub-sets of different values of mean frequency. Finally, each of the 40 sub-sets includes 500 Doppler signals which have the same mean frequency but having random amplitude fluctuations around the spectrum main lobe. Table 4.3 below summarises the data in each level of sets

Table 4.3 Main dataset and its sub-sets

Main dataset	5 Sets of Doppler signals with different SNR values: [SET0 SET1 … SET5] = [SNR_1 = 0, SNR_2 = 10… SNR_5 = 50 dB].
Sub-dataset-1	40 sets of Doppler signals with different mean frequency: [Subset-1, Subset-2… Subset-3] = [f_{d1} = 100 Hz, f_{d2} = 200 Hz… f_{d40} = 4 kHz].
Sub-dataset-2	500 of 1-second samples of time-domain Doppler signals. Each sample is randomly generated according to the method in Section 4.4.2.

An example of a Doppler signal from the database is plotted in Figure 4.12(a) to (e). These plots show Doppler signals with the same mean frequency of 1 kHz but with a different value of SNR. Based on our observation, SNR values between 50 and 30 dB represents the typical strength of radar echo found in practice. On the other hand, SNR lower than 20 dB represents the presence of a signal but with insignificant power. SNR lower than 10 dB represents an extreme case of signal strength.

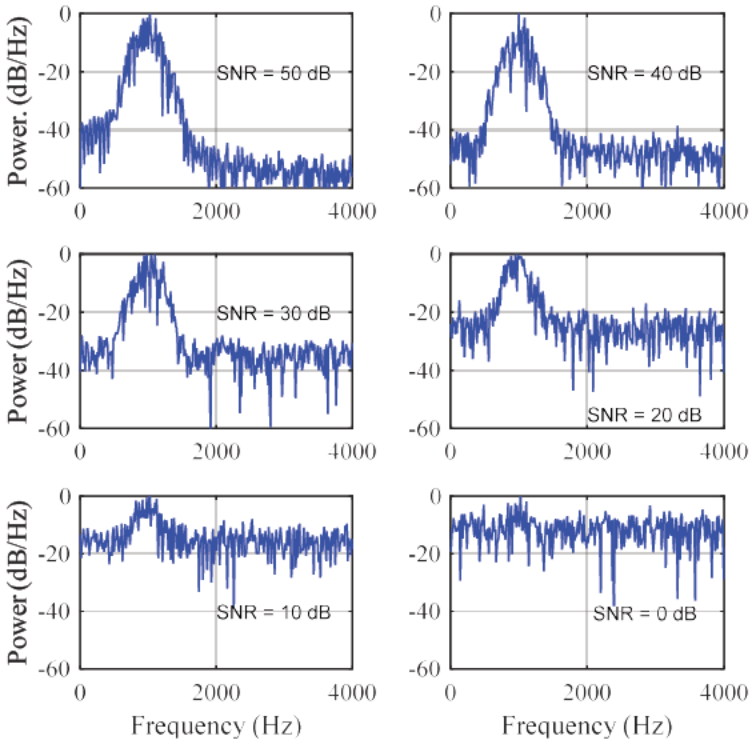

Figure 4.12 Examples of Doppler signal at different level of SNR

The other input parameters for simulating the Doppler signal is shown in the following statement:

Transmitter frequency, f_c	:	24.0125 GHz
Antenna viewing angle, α	:	45.0°
Antenna beamwidth, γ_b	:	13°
Sampling Rate, f_s	:	25 kHz
FFT size, NFFT	:	2048 samples

4.5. Results

The algorithms were tested using the datasets created in section 4.4.4. The evaluation was performed using MATLAB and results are presented by comparing the algorithms with different level of SNR, FFT length and processing time.

4.5.1. Effect of Input SNR

Figure 4.13(a) to (f) show the measurement bias and standard deviation for SNR values of 0, 20, 30, 40 and 50 dB respectively. For each SNR results, the left-hand plot shows the normalised bias measurement, and the right-hand plot shows the normalised standard deviation of the estimate. The true mean frequency, f_T on the x-axis for both bias and standard deviation plots is normalised to the value of the maximum true mean frequency of $f_{max,}$ = 4000 Hz. The result of each point in the plot is an average of 500 estimated mean frequency. Note that for SNR = 0 dB, CMA-T is not computed.

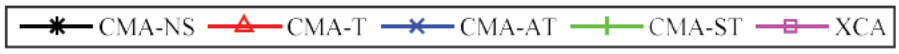

SNR = 50 dB

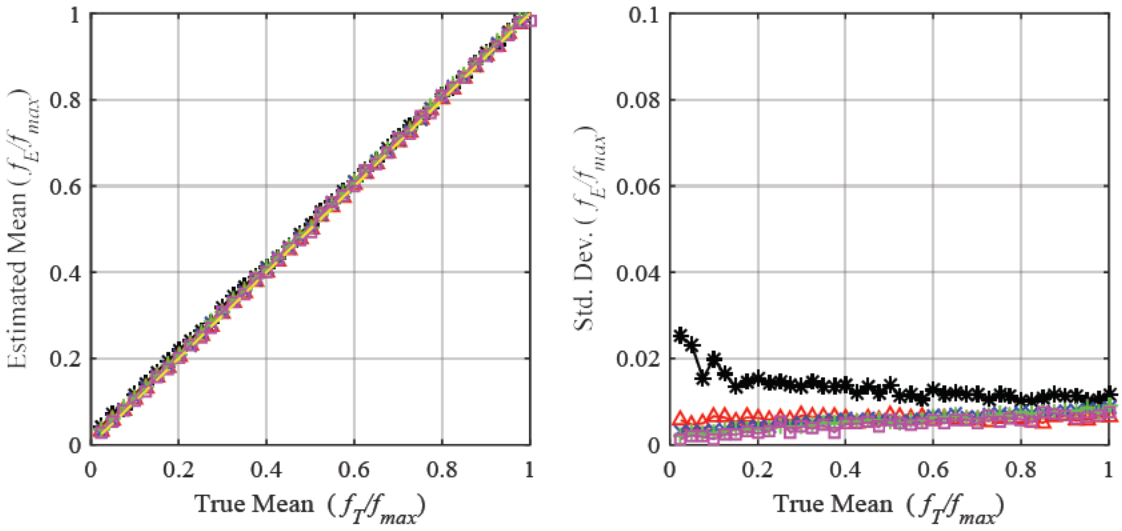

(a)

SNR = 40 dB

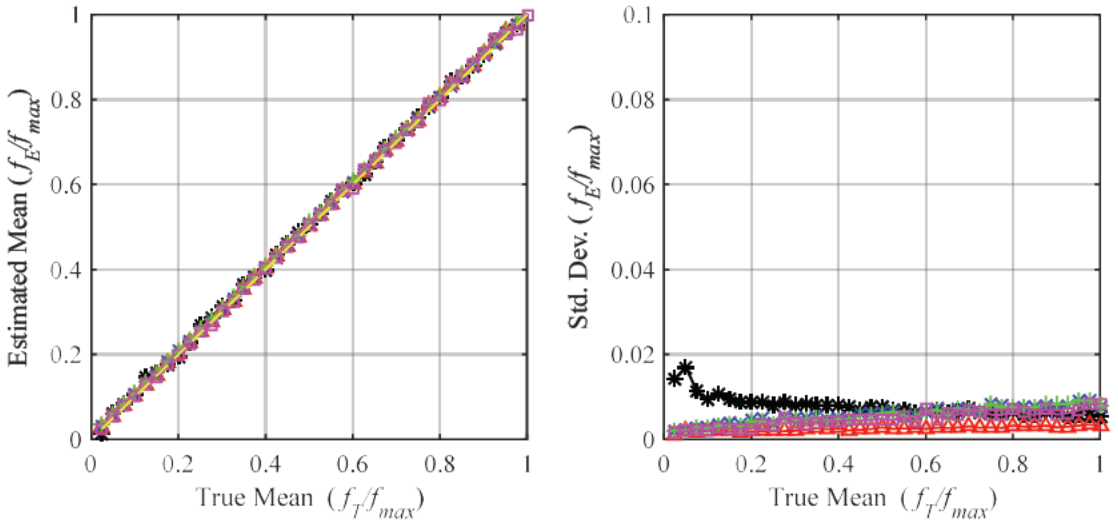

(b)

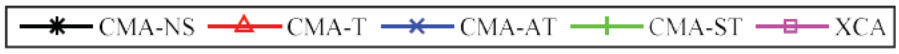

SNR = 30 dB

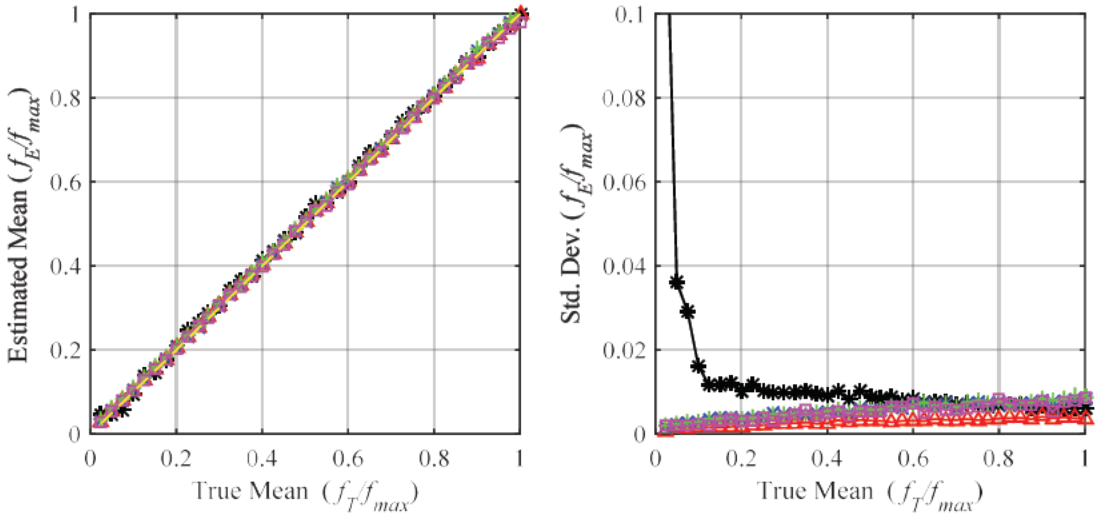

(c)

SNR = 20 dB

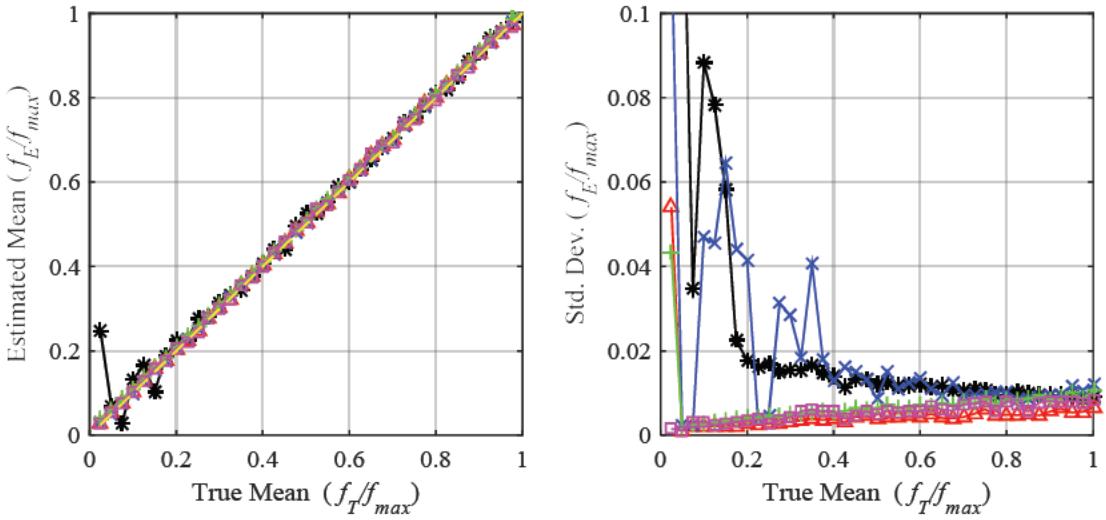

(d)

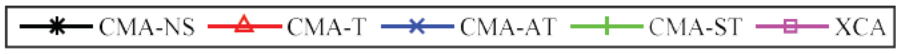

SNR = 10 dB

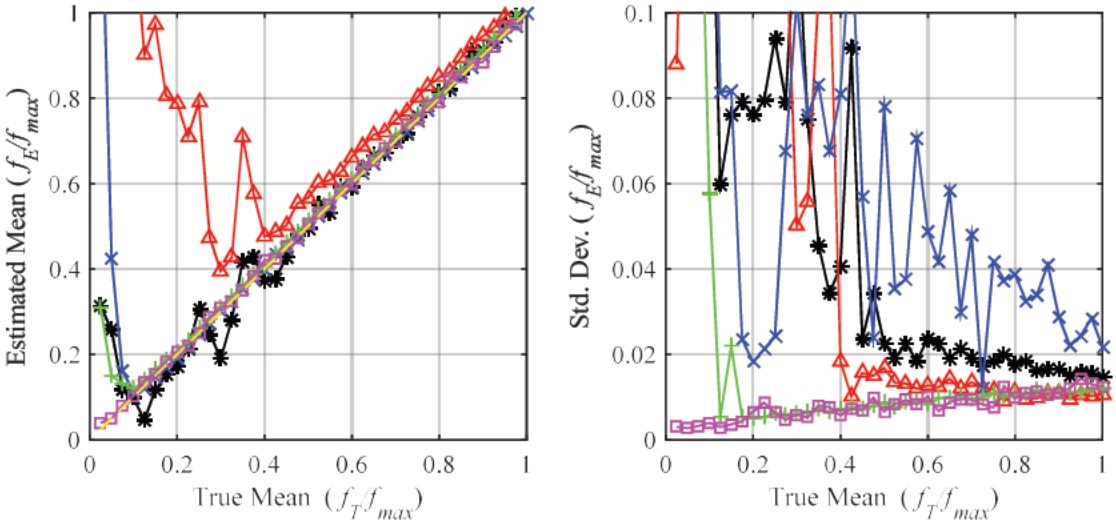

(e)

SNR = 0 dB

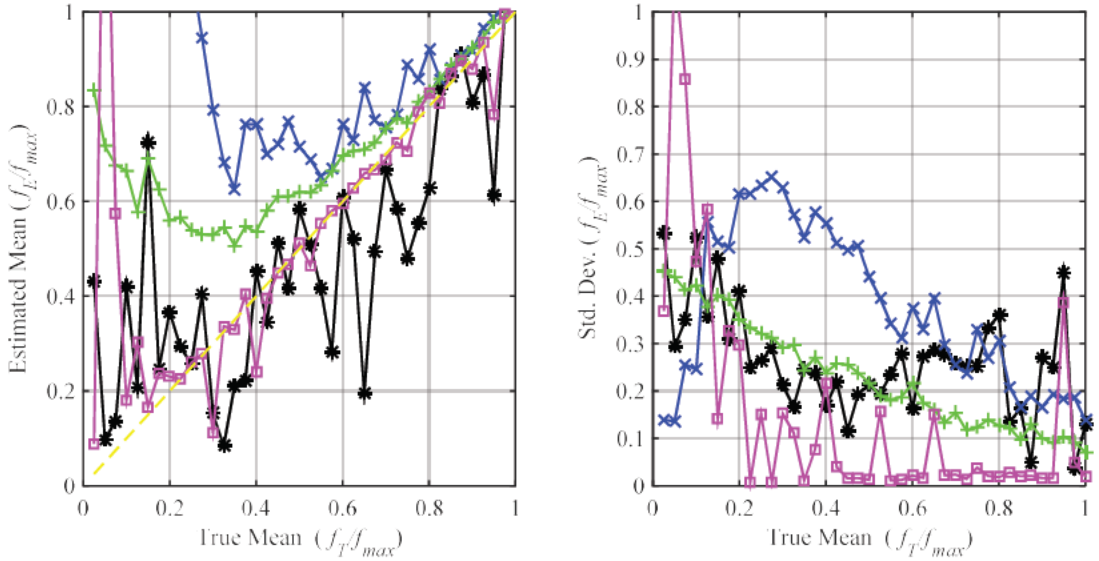

(f)

Figure 4.13(a) to (f) Comparison of bias and σ for a different level of SNR in Table 4.4.

.

Figure 4.13(a) to (f) shows that the performance of all algorithms deteriorates with decreasing SNR values. For all plots, higher bias and standard deviation are observed on lower mean frequency compared to higher mean frequencies. This characteristic is due to the Doppler spectrum bandwidth. As discussed in Chapter 3, the value of Doppler mean frequency is proportional to its bandwidth. At low relative mean frequency between 0 to 0.4 however, the spectrum bandwidth is narrow, and therefore, the number of spectral components that represents the main lobe is small. Hence, this condition increases the bias and variance in the mean frequency measurement.

Between SNR of 30 and 20 dB, CMA-AT produces larger variance than other proposed algorithms. Investigation on this method reveals that the algorithm cannot effectively locate the start and stop frequency of the spectrum main lobe when the relative mean frequency is between 0 to 0.4. This is due to the presence of high amplitude spikes near the start or stop frequency of the main lobe.

At very low SNR (SNR = 10 dB), the two of the proposed methods; CMA-ST and XCA demonstrate lower standard deviation than the two simple algorithms. This performance shows that the proposed algorithms produce more accurate mean frequency estimation. The only algorithm that works well in this SNR is the XCA algorithm. This algorithm shows low bias and standard deviation that is relatively unchanged from SNR = 30 dB.

At the lowest SNR (SNR = 0 dB), all algorithm shows very large uncertainty in measurement. None of the algorithms can estimate mean Doppler frequency with high accuracy.

Histogram of 1000 estimates of mean frequency

Figure 4.14 shows the histograms of 1000 mean frequency estimates for each algorithm. The figures in column (a), (b) and (c) shows the histogram of estimating mean frequency at three selected frequencies of 0.5, 1 and 3 kHz respectively. The vertical blue line in each histogram indicates the location of true mean frequency.

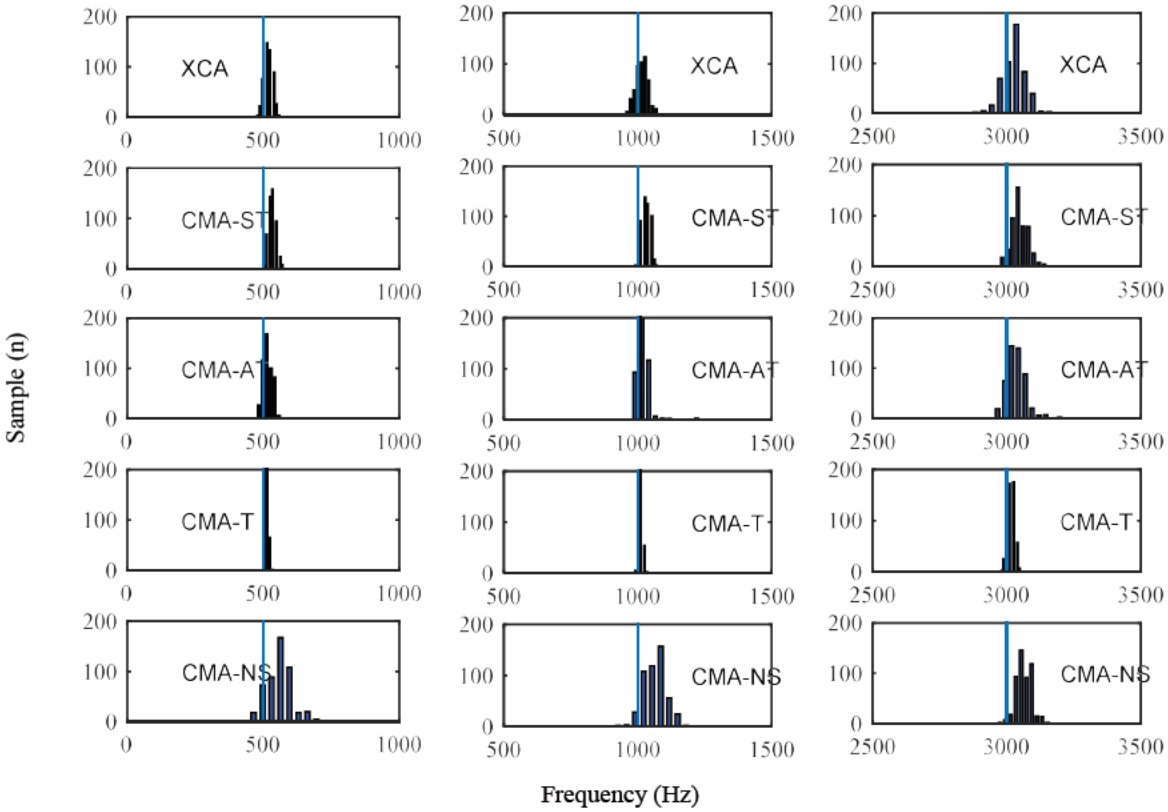

Figure 4.14 Histogram of 1000 mean frequency estimates for each of the algorithms.

From the above figure, all algorithms produce estimates that are normally distributed. An increase in standard deviation at higher mean frequency estimate is observed. This increase is due to the larger main lobe of the Doppler spectrum at higher speed.

All estimator yielded an over-estimating bias. In particular, the largest overestimates occur in CMA-NS with the bias of nearly 100 Hz (the equivalent vehicle speed, v = 1.7 mph). For the proposed algorithms, the average of over-estimation is 30 Hz (0.5 mph). This condition is firstly due to the settings of threshold values in the algorithms. In the presence of noise, the threshold induces bias in the estimate of mean frequency. The second cause is due to coarse frequency sampling in FFT. In this case, the Doppler signal is sampled at 25 kHz and evaluated using 2048 FFT points. Therefore, this also introduces bias in the frequency estimates [88]. In the following section, we assess the impact of different FFT length on the bias and standard deviation in estimating mean Doppler frequency.

4.5.2. Effect of Input Sample Length

The algorithms are evaluated with different length of FFT. Table 4.4 shows the FFT size used in the evaluation. Data from SET3 (SNR = 30 dB) in Table 4.3 is used.

Table 4.4 Relationship between FFT size, frequency, time and speed resolution

FFT size 2^n (n)	Frequency resolution Δf (Hz)	Time resolution Δt (ms)	Equivalent speed resolution Δv (mph)
8092	3.1	320	0.05
4096	6.1	163	0.12
2048	12.2	80	0.24
1024	24.4	40	0.48
512	48.8	20	0.96

Note that for CMA-AT, the width function, w (described in Section 4.2.3) are change to 3, 4, 5, 8 and 15 for FFT size of 512, 1024, 2048, 4096 and 8092 respectively. This change is needed to prevent the algorithm from ceasing to work because of the logical functions. The level threshold, Z_1 remain the same.

The performance of the proposed algorithms is presented in Figure 4.15(a) – (e). The left-hand plots show the bias estimate, and the right-hand side of the plot shows the standard deviation of the estimate.

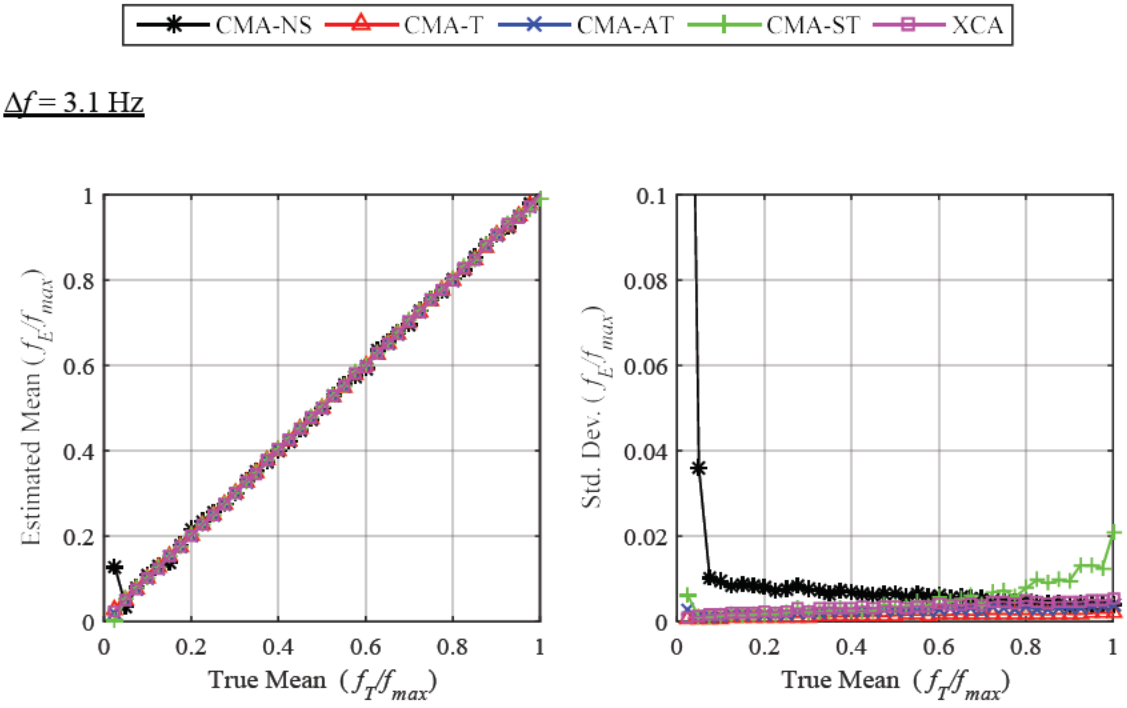

(a)

Δf = 6.1 Hz

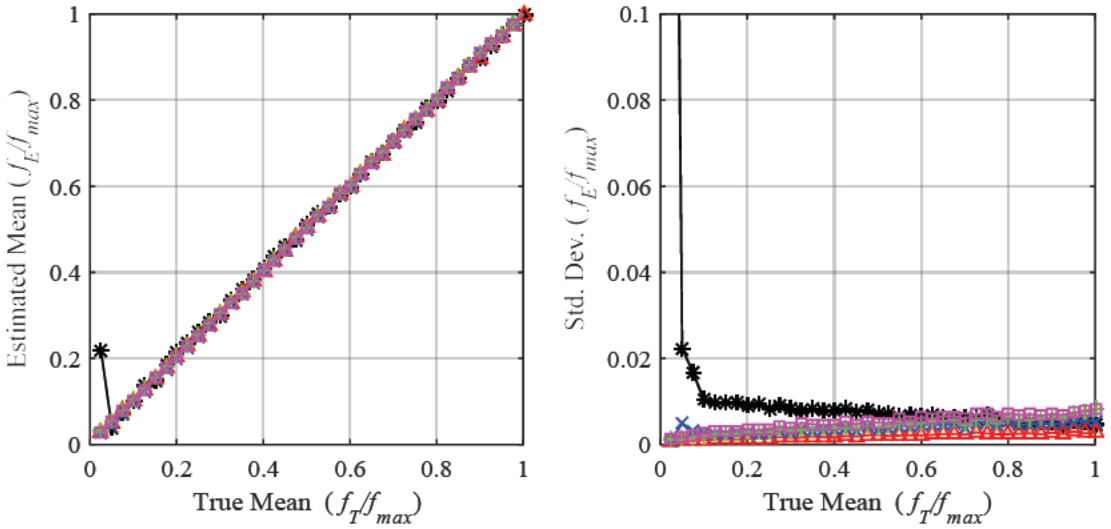

(b)

Δf = 12.2 Hz

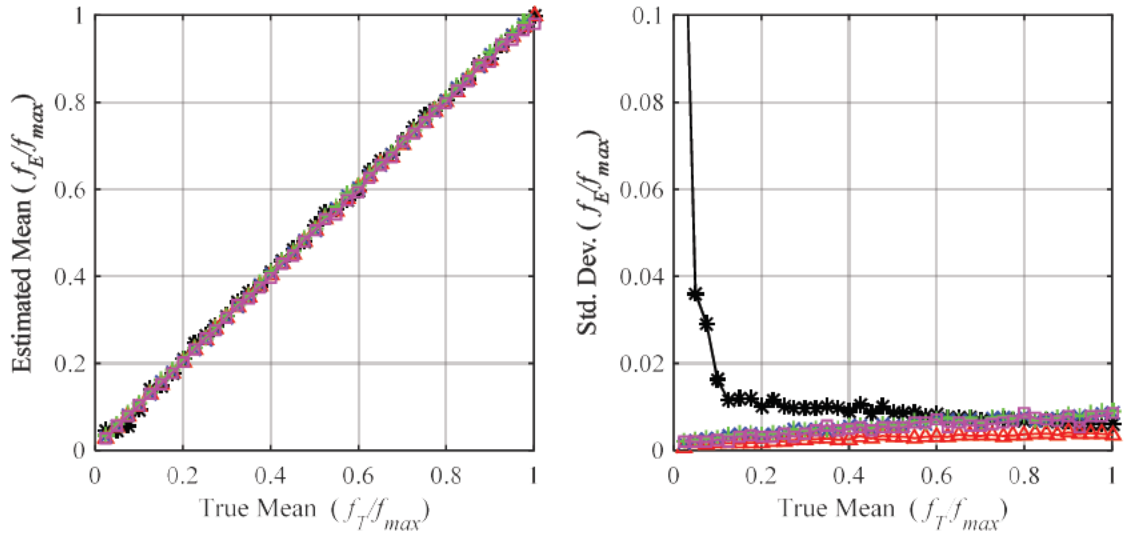

(c)

Δf = 24.4 Hz

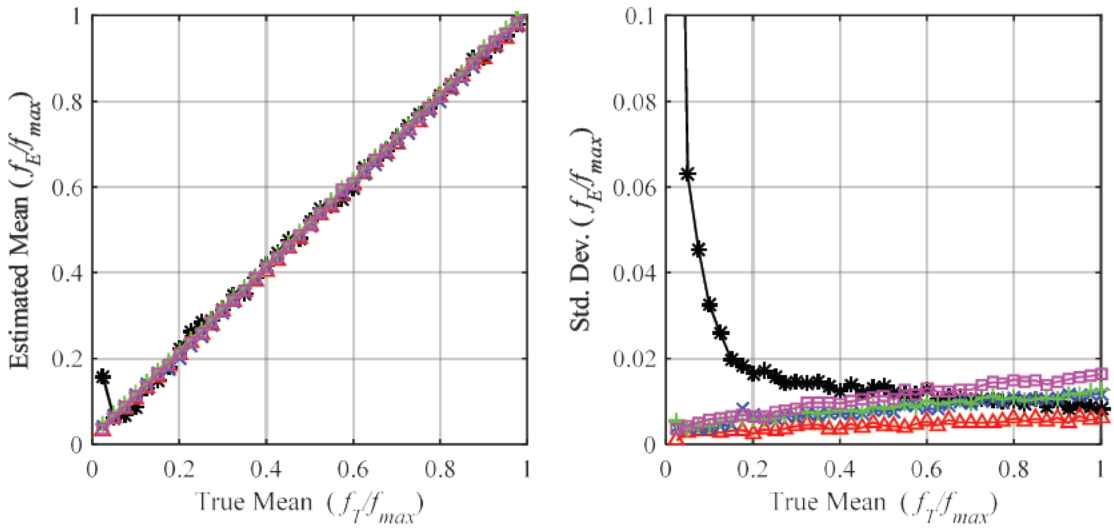

(d)

Δf = 48.8 Hz

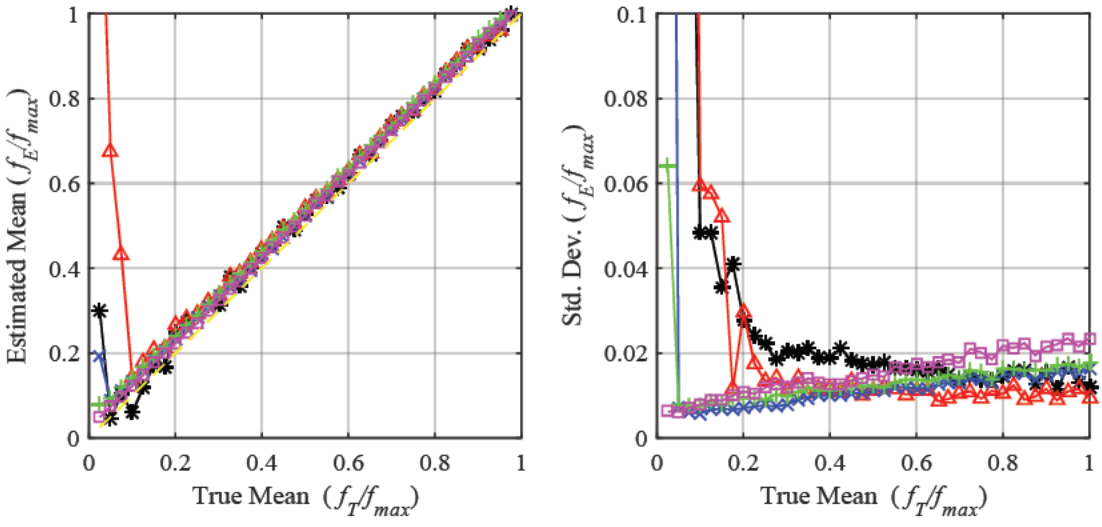

(e)

Figure 4.15 (a) – (e) Comparison of bias and σ for values of Δf in Table 4.4

As can be seen from Figure 4.15(a) to (f), high-resolution input produces lower bias and smaller standard deviation compared to the coarse one. For all algorithms with an exception of CMA-NS, we observe no significant difference in terms of bias and standard deviation when the input resolution is decreased from 3.1 to 12.2 Hz.

At coarse input resolution of Δf = 48.8 Hz, a significant difference can be observed between the proposed and simple algorithms. Under true mean frequency of 0.3, the simple algorithms produce larger uncertainty than the three proposed algorithms. Notably, the XCA algorithm demonstrates low standard deviation for the whole range of mean frequency.

Nonetheless, the choice of frequency resolution in spectral processing will be a trade-off between resolution and accuracy, in our view, input resolution of Δf = 12.2 Hz is suitable for the proposed algorithms because it provides appropriate speed update rate (time resolution of 80 ms) with low bias and standard deviation.

Section 4.3.1, describes the algorithm design goals. Criterion 2 states that the relative error for measuring speed must be under 3%. For this purpose, we investigate the relative error in estimating mean Doppler frequency at different SNR levels. Figure 4.16 plots the percentage relative error of the algorithms for SNR = 10, 20, 30, 40 and 50 dB. The frequency resolution used the test is Δf = 12.2 Hz. The horizontal yellow line indicates 3% relative error.

From the figure, we can see that the relative error for all algorithms with an exception of CMA-NS is under 3% for SNR above 20 dB and true mean frequency above 2 kHz. However, all algorithm shows error larger than 3% for mean frequency under 2 kHz. This behaviour is due to spectral estimation. As the Doppler frequency gets lower, its main lobe bandwidth becomes narrower. The spectrum main lobe cannot be properly estimated using Doppler signal with low-frequency resolution. One method to improve this problem is to increase the frequency

resolution. Nevertheless, this is a trade-off between the estimation accuracy and the speed update rate. For practice, one can use FFT with higher frequency resolution when the vehicle moving at low speed and changes for lower frequency resolution when the vehicle travelling at high speed.

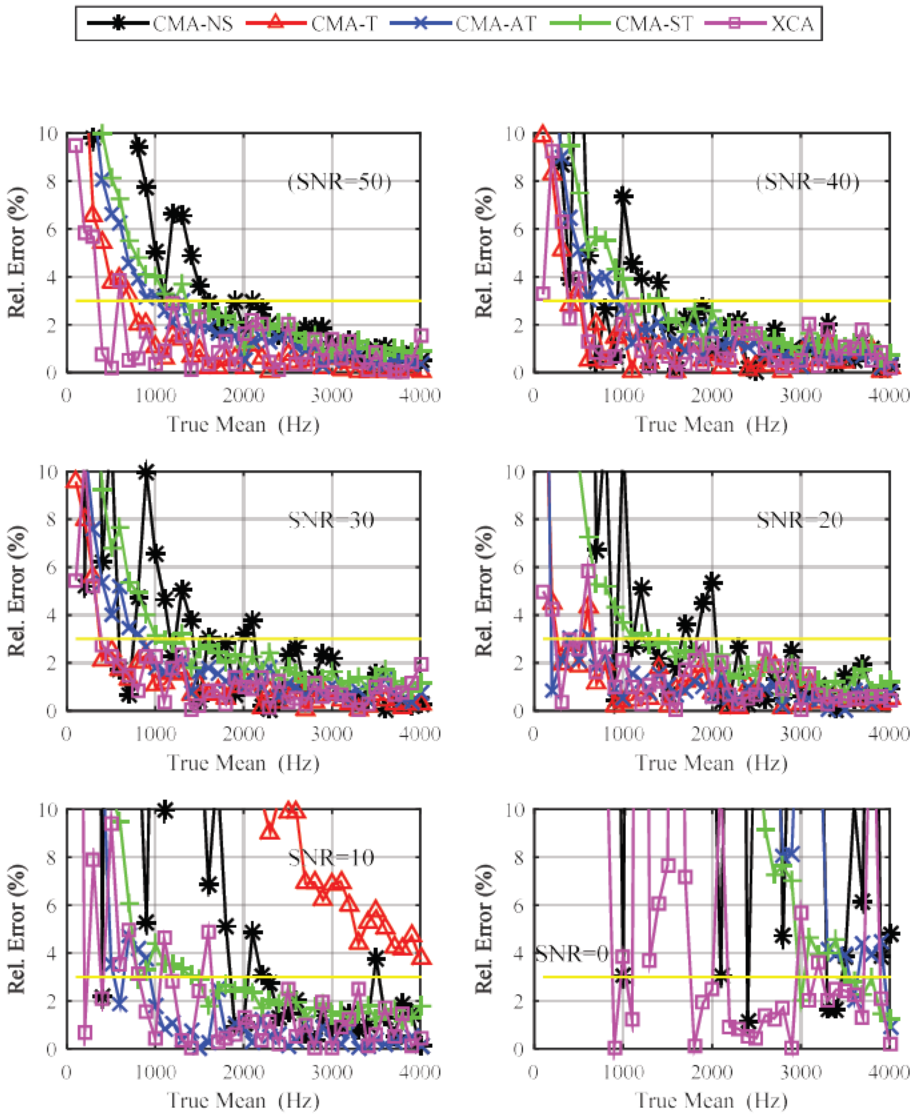

Figure 4.16 Comparison of relative error for SNR between 0 and 50 dB

4.5.3. Algorithm Processing Time

The average processing time to estimate a single mean Doppler frequency is analysed by recording the period of mean frequency estimation of 2000 Doppler signal in dataset 3 (SET 3). The measurement was performed using a computer with a microprocessor speed of 2.3 GHz (Intel i5, 2013) and 8 GB of memory. The MATLAB start-stopwatch timer operands of *tic* and *toc* are located at the first and completion of the algorithm process. Figure 4.17 shows results of 500-average processing time in for FFT lengths of 512, 1024, 2048, 4096 and 8192. The blue line with circle marker represents the period of the FFT size according to the 25 kHz sampling rate. In other words, the blue line is used as a rough approximation of the speed update rate.

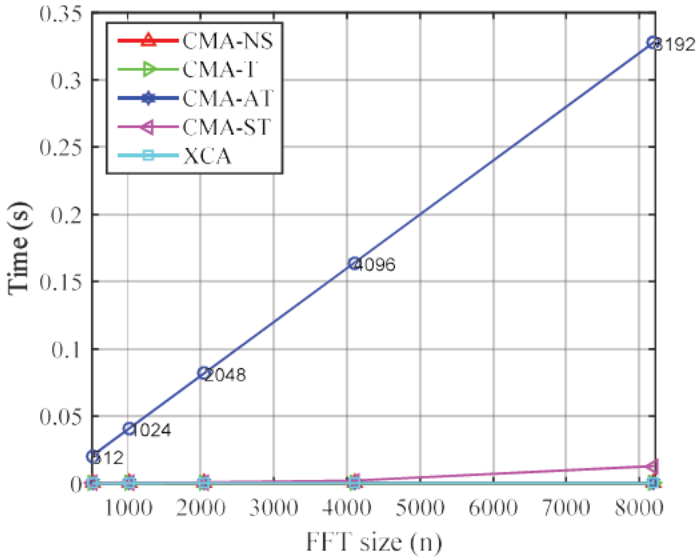

Figure 4.17 Processing time of the algorithms.

As can be seen from the figure, the processing time for all algorithms is much smaller than the speed update rate. At the most extended FFT length of 8192 samples, the average processing time for algorithms is 0.03, 0.02, 0.29, 12.9 and 0.31 ms for CMA-NS, CMA_T, CMA_AT,

CMA-ST, and XCA respectively. CMA-ST shows the slowest processing time; upon investigation, the processing time is slowed by the computation of CUSUM. Nevertheless, the overall processing time is still 20 times smaller than the speed update rate.

4.5.4. Discussion and Summary of Results

The first two algorithms; CMA-NS and CMA-T are purposely used as a comparison to the proposed algorithms which are more complex. Nevertheless, the CMA-T shows good performance and can work well if the SNR is above 30 dB. Furthermore, this method produces one of the lowest computational complexity between the five algorithms.

CMA-AT and CMA-ST are based on the centre-of-mass method and has adaptive pre-processing to find the spectrum main lobe in the presence of noise. The AT version depends on thresholding the signal amplitude level and finding the limits of the spectrum main lobe. On the other hand, the ST version finds the start and stop frequency by thresholding the slope of the signal. The simulation results show that these two methods show better performance in both bias and standard deviation when compared to the simple method of CMA-NS.

Comparison between CMA-AT and CMA-ST shows that the earlier produces higher bias and standard deviation. For SNR below 30 dB, the influence of noise is significant in the AT method which leads to the obscure determination of start and stop frequency of the spectrum main lobe. At lower SNR (SNR = 0 to 20 dB), it is more difficult to separate between signal and noise power using amplitude threshold. If amplitude threshold, Z_1 (refer to Section 4.2.3) is set too low, the algorithm may count random peak as start or stop frequency, and if the Z_1 is set too high, the algorithm may not find the start and stop frequency.

The third algorithm namely XCA is based on cross-correlation. Simulation results show that the XCA algorithm outperforms the centre-of-mass methods under severe SNR condition. One main factor that contributes to its robustness is that the correlation does not require the knowledge of the signal to be detected. This method is an advantage when the SNR level is severe. i.e. SNR = 10 dB. Hence, this method shows higher accuracy at low SNR.

Here, it is important to realise that there is no optimum algorithm in the sense of accuracy and computational cost. The CMA-AT is computationally efficient, but the performance is limited by the signal-to-noise ratio. On the other hand, XCA and CMA-ST can work well under limited SNR but are computationally more expensive. Nevertheless, it can be said that the performance of the three proposed algorithms is more accurate than the simple algorithms in the case of low SNR and low input resolution.

One main factor that limits the accuracy of the algorithms is the frequency resolution of the Doppler signal. Lowering the sampling frequency can minimise the bias and variability of the estimation but with the cost of slower speed update rate. For practical SoG operations, we suggest a dynamic sampling rate to improve the overall performance of these algorithms.

4.6. Summary

In this chapter, three new speed estimation algorithms were proposed. Two of the methods namely CMA-AT and CMA-ST are based on the centre-of-mass and one method is based on cross-correlation is named XCA. Based on design goal and performance objective, the proposed algorithms are evaluated with an extensive database of artificial Doppler signal of different frequency range, SNR and frequency resolution. Results show that, compared to

simple algorithms, these algorithms perform better under low SNR and coarse frequency resolution. Additionally, a comparison between the three proposed algorithm shows that the XCA method performs better than the CMA methods. Nevertheless, the evaluation results show that these three algorithms are qualified for effective SoG operations.

The results in this chapter are however limited to the simulated signal. In the next chapter, these three algorithms are tested with actual Doppler data collected from the experimental campaign.

Chapter 5. Experimental Setup, Procedure, and Preliminary Analysis

5.1. Introduction

This chapter describes the experimental 4-beam SoG radar system that was developed at the University of Birmingham. The development aims to evaluate the performance of a 4-beam SoG radar system under on-road and off-road conditions and also to evaluate the proposed algorithms in Chapter 4.

This chapter is divided into two parts. The first part of this chapter explains the experimental SoG radar system. These include the description of hardware and software, installation of radar on a test vehicle and signal processing of Doppler signal collected from the actual ground surface. The second part of this chapter describes the experimental sites and the procedure of collecting data from the test sites.

5.2. System Description

An Experimental SoG radar system was designed by Edward Hoare and developed by the author and Liam Daniel in the MISL lab. We used low-cost hardware as well as existing hardware available from the lab. In general, the system consists of hardware, software and a test vehicle.

5.2.1. Hardware and Schematic

The 4-beam SoG radar system consists of five main components. Table 5.1 below describes each of the items including the model number and some brief description about its specification.

Table 5.1 Hardware description

No	Item	Model and Manufacturer	Description
1	4 x Radar	RFbeam Microwave GmbH. Model: K-MC1 (Appendix D)	A 24 GHz quadrature radar transceiver with antenna beamwidth of 12° in the vertical plane and 25° in the horizontal plane. The nominal output power is +18 dBm. Figure 5.1 shows the antenna radiation pattern.
2	GPS Module	L80 Quectel (Appendix E)	A compact, low-cost GPS module integrated with the patch antenna. The accuracy for positioning, acceleration and speed are < 2.5 m, < 0.1 ms^{-2} and 0.1 ms^{-1}. This device reports speed information every one second
3	ADC	USB-2537 Measurement Computing	A 16-bit data acquisition board with 1 M S/s and 64 single-ended input.
4	Computer	Latitude E6420 Laptop	A standard computer with Pentium Core i5 processor and 4 GB of RAM.
5	Power Supply	12V Yuasa	A 1.2 Ah Battery
6	Video Camera	GoPro	A small and compact video camera for video recording during the experimentation

Figure 5.1(a) shows the picture of the radar module. The dimension of the radar module is 55 mm x 65 mm with a thickness of 5 mm. Additionally, Figure 5.1(b) shows the antenna radiation pattern. The radiation pattern is obtained from the radar datasheet as shown in Appendix D. For the illustration in this chapter. A software named GetData Graph Digitizer 2.24 was used to read the data from the radiation pattern plots in the datasheet.

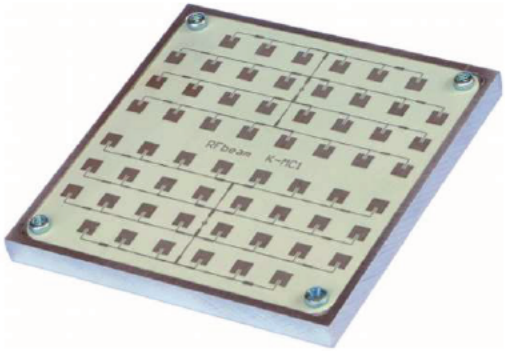

Figure 5.1(a) Photograph of the 24 GHz radar transceiver

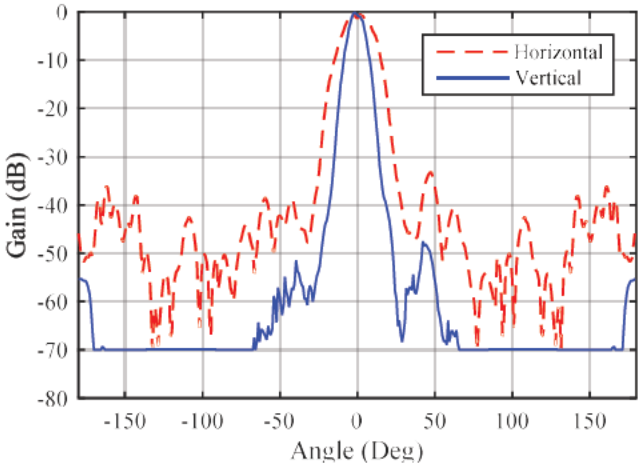

Figure 5.1(b) K-MC1 antenna gain in both vertical and horizontal direction.

Figure 5.2 illustrates the data collection setup. The system consists of four radars operating at the same transmitting frequency of 24.0125 GHz. Each radar produces a pair of in-phase and quadrature Doppler signals. In total, four in-phase and four quadrature Doppler signals are generated at any time during the experiment process. An ADC is used to digitise the Doppler signals. Each of the Doppler signals from the radar is sampled at a rate of 15 kHz. A laptop computer is equipped with data acquisition software which controls the acquisition process. Except for radar modules, the ADC, computer, and battery are located at the back seat of the test vehicle. The ADC is connected to the radars using screened cables and DIN connectors.

Note that the GPS receiver has no direct needs in the SoG radar system but rather implemented in this project to collect speed and location information obtained from GPS satellites.

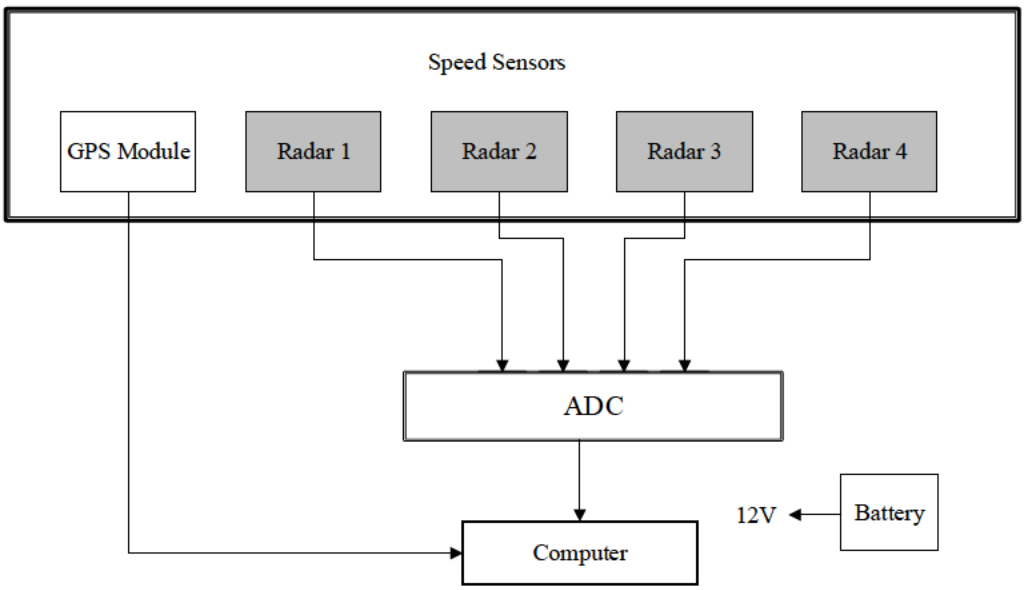

Figure 5.2 Block diagram of a 4-beam SoG radar

5.2.2. Installation of Radars on Test Vehicle

An illustration of the four radars installed on the test vehicle is shown in Figure 5.4. The theoretical analysis in Chapter 3 provides the knowledge of mounting the radar on the test vehicle. The four radars are arranged to form an X-Janus configuration as described in Section 3.1.1. In this setup, two radars were mounted at the front bumper, and another two radars were attached at the rear bumper. The radars were set up to point the road surface at 45° from the longitudinal and lateral direction ($\alpha/\beta = 45°/45°$) at height, h of 0.5 meters from the surface. To obtain narrow Doppler spectrum, the vertical plane of the radar antenna is vertically aligned to the ground surface.

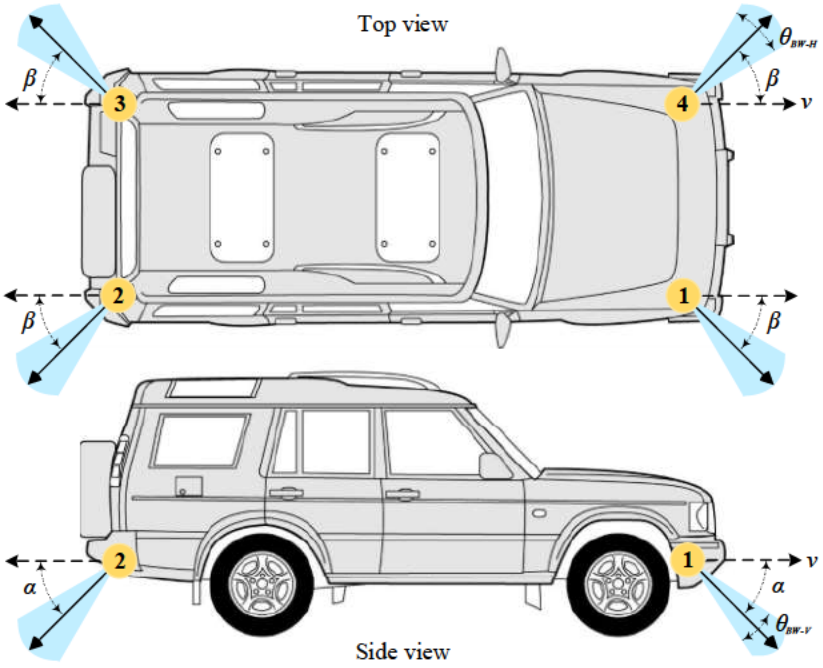

Figure 5.3 Illustration of X-Janus configuration showing the depression and azimuth angle of the radar sensor (a) top view (b) side view

Figure 5.4 shows the actual installation of the radar on the test vehicle. Each radar is placed in a polycarbonate plastic enclosure necessary to protect the radar from dirt and water.

Subsequently, the enclosure is fixed to a sturdy multi-axis camera arm mount. Angular markings on the arms help to position the beam of the radar in space with high precision. These camera arms are mounted sturdily on the bumpers using 17 mm bolt and nuts.

Figure 5.4 Photographs of radar mounting (a) The front radar platforms, also shown is two video cameras mounted on the hood. (b) The rear radar platforms

Test Vehicle

For this present study, we used a 4x4 vehicle provided by Jaguar Land Rover. The vehicle is capable is moving under various conditions including on off-road environments.

5.2.3. Recording Software

A software written in MATLAB was used to collect speed data from radar and GPS simultaneously during the experiment. The software also hosts several other functions as listed below

- The setting of ADC sampling rate
- Assigning filename for the collected data
- Real-time observation of Doppler signal collected during experimentation
- Data collection start and stop control

The speed data from the four radars are recorded into a MATLAB readable format of .daq, and the GPS data is stored in a text format of .txt. Each data is named according to the naming convention that consists of a test name, the location of test, date and time of the test. Figure 5.5 shows the snapshot of the software graphical user interface (GUI). As seen in the below figure, the four small windows show the in-phase and quadrature Doppler signal of each radar during the data collection process. The small window in the figure shows the period of data collection.

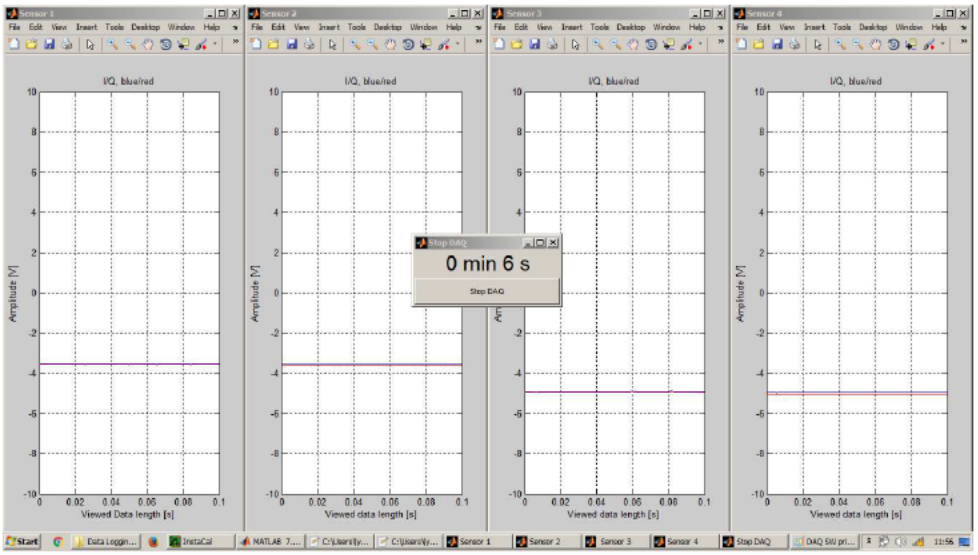

Figure 5.5 A snapshot of the data acquisition software

5.3. Data Processing Stages

Figure 5.6 shows the complete processing steps of the Doppler signal. In general, the process is divided into three stages. The first stage covers the steps from (1) to (6), the second stage includes the steps from (7) to (8), and the third stage comprises the steps from (9) to (10).

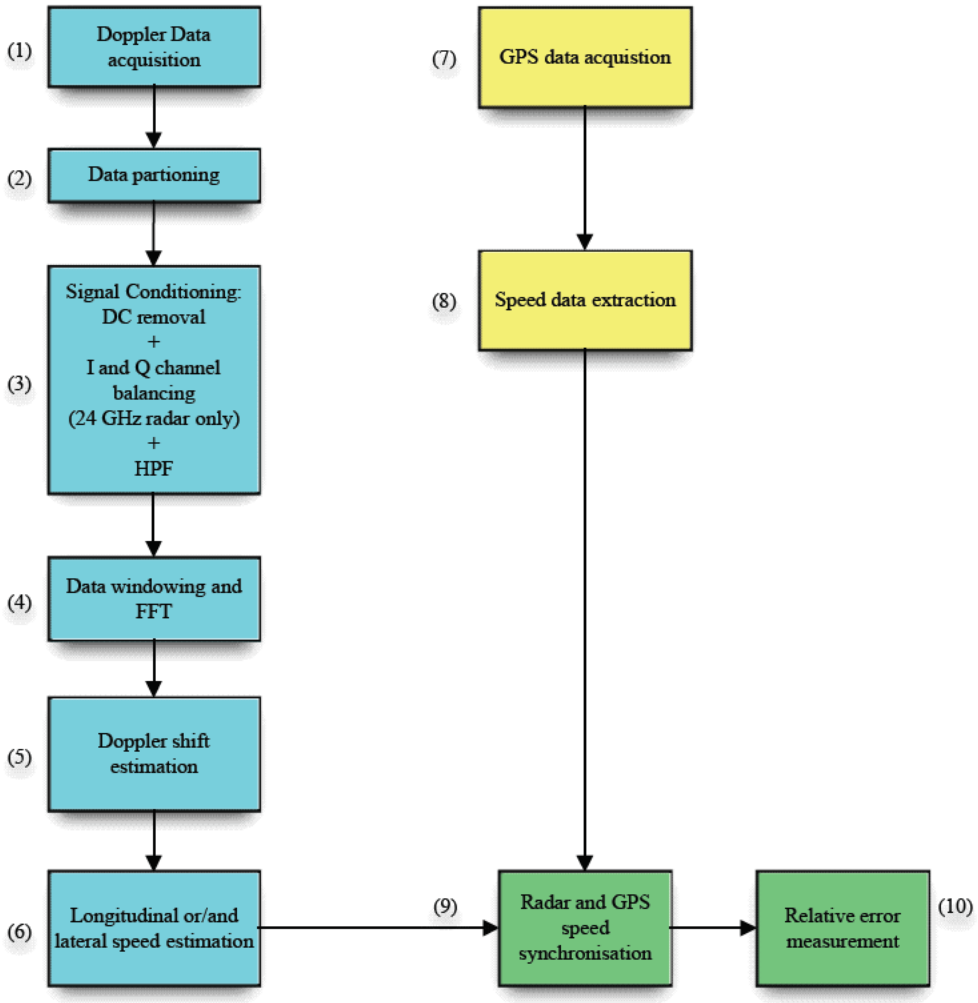

Figure 5.6 Stages of Doppler data processing

Stage 1

The Doppler signal used for spectral processing is digitised using an ADC. Based on the design goal described in Section 4.3.1, the digitised Doppler signal is divided into small blocks with a size of 100 ms. Next, the DC component of the signal is removed by finding the mean value of the 100 ms signal and subtracting this average out of the signal; this can be given by [89]

$$x'(n) = x(n) - \frac{1}{n}\sum_{n=0}^{N} x(n) \tag{5.1}$$

where $x(n)$ is the Doppler signal and $x'(n)$ is the Doppler signal with no DC offset. In this work, we assumed that $x(n)$ is stationary and has a mean value of zero. Next, we minimised the gain imbalance between the in-phase and quadrature Doppler signals. The gain balancing between the two signals is performed by finding the ratio between the amplitude of the two signals and multiplying the gain with the amplitude of the signal. The signal gain is determined by

$$Gain = \frac{Var(I_d)}{Var(Q_d)} \tag{5.2}$$

where *var* is the variance of the signal, following the gain balancing, we suppressed the low-frequency noise using a built-in HPF in MATLAB. Figure 5.7 shows the frequency response of the HPF indicated with a blue line.

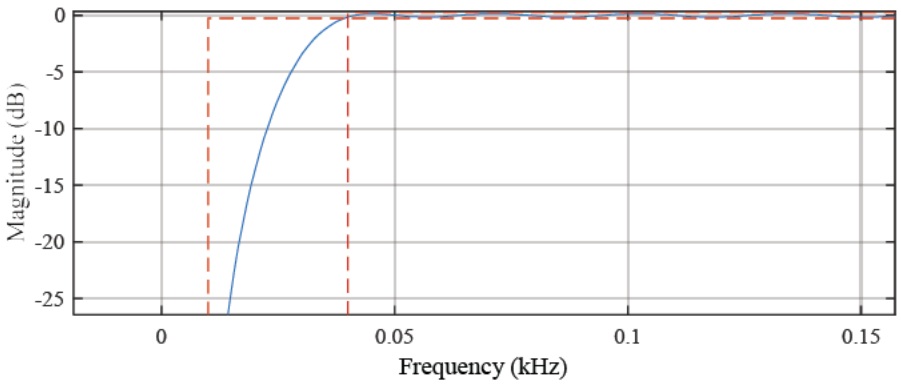

Figure 5.7 HPF frequency response

Next, we estimate the mean Doppler frequency from the 100 ms Doppler signal using the proposed algorithms.

The above process from the stage (1) to (6) is repeated for each of the four radars. Finally, we compute the speed along the longitudinal and transverse direction of the vehicle using Equation (3.18) to (3.19) in Chapter 3.

Stage 2

Stage two consists of collecting and extracting ground speed data from the GPS receiver. The speed and location data from GPS receiver are formatted in the National Marine Electronics Association (NMEA) sentences. We developed a MATLAB script to extract the speed data from the NMEA sentences. In particular, the vehicle speed is obtained from the $GPRMC data. Figure 5.8 shows an example of a $GPRMC data which contains the date and time in universal time coordinated (UTC), geographical latitude and longitude of the collected speed data and speed measurement in knots.

File Edit Format View Help

```
2012 7 12 16 27 28.046 $GPRMC 112812.000 A 5210.5578 N 00130.3919 W 15.90 51.66 120712 NaN NaN D
2012 7 12 16 27 28.980 $GPRMC 112813.000 A 5210.5605 N 00130.3862 W 15.87 51.57 120712 NaN NaN D
2012 7 12 16 27 29.787 $GPRMC 112814.000 A 5210.5633 N 00130.3806 W 15.89 51.86 120712 NaN NaN D
2012 7 12 16 27 30.713 $GPRMC 112815.000 A 5210.5660 N 00130.3749 W 15.90 52.12 120712 NaN NaN D
2012 7 12 16 27 31.630 $GPRMC 112816.000 A 5210.5687 N 00130.3692 W 15.88 52.35 120712 NaN NaN D
2012 7 12 16 27 32.622 $GPRMC 112817.000 A 5210.5715 N 00130.3635 W 15.89 52.31 120712 NaN NaN D
```

Figure 5.8 $GPRMC data from the low-cost GPS receiver

Stage 3

This stage prepares the radar and GPS speed for speed estimation accuracy analysis. A few processing needs to be done before a comparison can be made between the radar and GPS speed; the following points describe the reason for the processing:

- As discussed in Section 5.2.1, Radar and GPS data are recorded at a different sampling rate. For radar, the ADC sampling is made at 15 kHz while the GPS data is sampled at a rate of 1 Hz. Therefore, radar and GPS do not have a matching number of speed data.
- Radars and GPS have different data recording connection path as shown in Figure 5.2. Therefore, the recorded speed from radar and GPS and is not synchronised.
- Precise mounting of radars on the test vehicle is difficult to achieve. A small misalignment angle in the setup can generate a constant bias in the speed obtained by the radars.

The following steps are taken to minimise the impact of the unmatched sampling rate, unsynchronised radar, and GPS speed and imprecise mounting of radar on the test vehicle.

- We increase the number of samples in GPS data by using the interpolation function in MATLAB by a factor of 10. This interpolation provides a matching number of samples between the radar and GPS speed data.

- We estimate the time-displacement between GPS and radar by cross-correlating the speed of radar to the speed of GPS and finding the period of displacement.
- We estimate the scale factor between the radar and GPS speed. This scale estimation is performed by fitting a straight line on a constant speed phase on both radar and GPS and measuring the difference between the radar and GPS speed.

Once the speed data is synchronised and scaled, we can estimate the relative error in the speed estimation by radar. The relative error can be defined by

$$\text{Relative error } (\%) = \left(\frac{v_r - v_{GPS}}{v_{GPS}} \right) 100 \tag{5.3}$$

where v_r is the speed estimated by radar and v_{GPS} is the speed measured by GPS receiver.

5.4. Description of Test Site

Experiments were conducted in the Jaguar Land Rover (JLR) proving grounds in Gaydon, Warwickshire. Figure 5.9 shows the layout of the JLR test track obtained from Google Earth. The lower part of the image shows the 1.6-mile-long straight-track made of asphalt, and the upper-right of the image shows the off-road surfaces. These test sites are chosen because they provide different surface characteristics.

Figure 5.9 Image of the test site which consists of 1.6-mile straight-track and off-road conditions

5.4.1. Description of Data

Data were collected on several types of surface available on the proving grounds. The classification of the ground surfaces is based on on-site inspection and video-camera observation. Nonetheless, it must be said that the description is only accurate for a large proportion of the surface. Some small part of the road may not be accurate as per description. Examples of surface images used in this work are shown in Figure 5.10. A total of six surfaces were selected. The following points provide the name of each surface and a brief description of the surface:

- *Long straight-track* – 1.6 miles of flat road made of asphalt. The surface was dry during the data collection process. The asphalt surface image is shown in Figure 5.10(a).
- *Elevated bars* – 50 m of the road made of concrete with elevated bars which are laterally placed to provide a bumpy motion to the vehicle when traversing across it. The elevated bars image is shown in Figure 5.10(b).

- *Grass* – Grass covered surface with grass height approximately between 1 and 7 cm. The surface is rigid and relatively flat. The grass surface image is shown in Figure 5.10(c).
- *Bumpy* dirt– Road with many potholes filled with rainwater. The depth of potholes is approximately 5 to 7 cm. The road is made of a mix of gravel and dirt. The bumpy dirt surface image is shown in Figure 5.10(d).
- *Wet Dirt* – Road with many potholes filled with rainwater. The depth of potholes is approximately 3 to 5 cm. The road is mostly made of dirt and some gravels. The wet dirt surface is shown in Figure 5.10(e).
- *Water* – An approximately 10 meters long dirt road completely submerged in rainwater. The depth of water is about 3 to 5 cm. The water surface is shown in Figure 5.10(f). Note that, when the picture was taken, the volume of rainwater has reduced to potholes of rainwater. However, when the test was conducted, the 10 meters long dirt road was wholly submerged in rainwater.
- *Circle* – A circle track with a diameter of 25 m. The surface is made of asphalt. The image of the surface is similar to the one in Figure 5.10(a).
- *Curve* – A curve track with a diameter of 5 m. The surface is made of dirt and gravels. The image of the surface is similar to the one in Figure 5.10(d).

Figure 5.10 Images showing the condition of the road surface. (a) Asphalt (b) Concrete with elevated bars (c) Grass (d) Bumpy dirt (e) Wet dirt and (f) Water.

5.5. Scenarios of Test

This section explains how the test is carried out on the proving ground. In general, the test is classified in terms of the trajectory of the test vehicle. Two trajectories were used; straight and circular motion. These simple trajectories ensure that data obtained from the test can be used to explain the accuracy and reliability of the proposed SoG radar system.

Figure 5.11 illustrates the straight-line motion of the test vehicle. The disconnected line shows the straight trajectory of the test vehicle and the symbol v_l and v_t represents the longitudinal and transverse speed of the test vehicle. Doppler signal is collected between the start point and end point. Depending on the test, the test car may move with constant or variable speed.

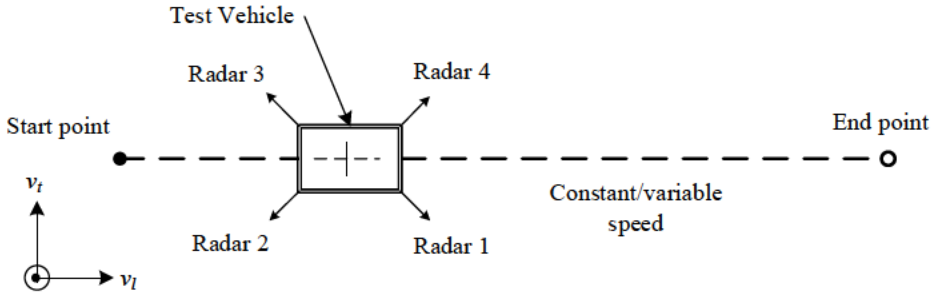

Figure 5.11 Illustration of the vehicle in the test of straight trajectory

To measure the ability of the system with different speed and types of surface, we divided the test into six test scenarios which are described in the following points:

- *Test-scenario 1*: Performing a straight-line motion on the 1.6-mile straight track in Figure 5.10(a). Straight motion is performed at five constant speed of v = 10, 20, 30, 40 and 70 mph.

- *Test-scenario 2*: Performing a straight-line motion on the elevated bars in Figure 5.10(b) for one time with a vehicle speed of $v = 5$ mph.
- *Scenario 3*: Performing straight-line motion on the grass surface as in Figure 5.10(c) for one time with a vehicle speed of $v \approx 5$-10 mph.
- *Scenario 4*: Performing straight-line motion on the wet dirt surface as in Figure 5.10(e) for one time with a vehicle speed of $v \approx 5$-10 mph.
- *Scenario 5*: Performing straight-line motion on the bumpy dirt road as in Figure 5.10(d) for one time with a vehicle speed of $v \approx 5$-10 mph.
- *Scenario 6*: Performing straight-line motion on the water covered road as in Figure 5.10(f) for one time with a vehicle speed of $v \approx 5$ mph.

On the other hand, Figure 5.12 shows the circular trajectory test. In this test, the test vehicle is driven in a circular-line motion. The procedure of the test is similar to one in a straight trajectory. However, due to the difficulty in driving in a circular path. We limit the speed of the test vehicle to a maximum speed of 15 mph. This low-speed driving is to ensure that the driver of the test vehicle is safe during the test. For the circular driving, we divided the test into two test scenarios which are described in the following points:

- *Test-scenario 7*: Performing circular motion on a circle track. Circular driving is performed at two constant vehicle speeds of $v = 5$ and $v = 15$ mph.
- *Test-scenario 8*: Performing a curve motion on the wet dirt surface for one time with a vehicle speed of $v \approx 5$ mph.

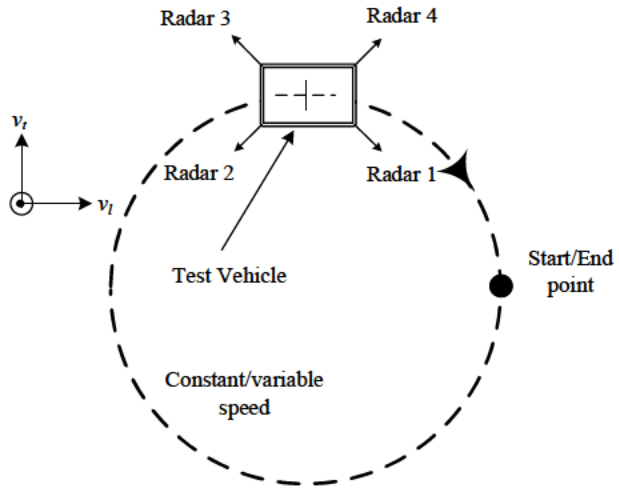

Figure 5.12 Illustration of the vehicle in the test of the circular trajectory

5.5.1. The trajectory of Test Vehicle and Period of Useful Data

Data collection work was performed by Dr. Liam Daniel and Dr. Edward Hoare and the author on the test site. A total of eight tests were performed according to the eight test-scenarios. Figure 5.13(a) to (h) shows the trajectory of the test vehicle for each test scenario. The image is obtained by plotting the GPS position of the vehicle during the test on Google Earth. The trajectory is indicated with the blue line, and the yellow dots show the start and stop time of recording.

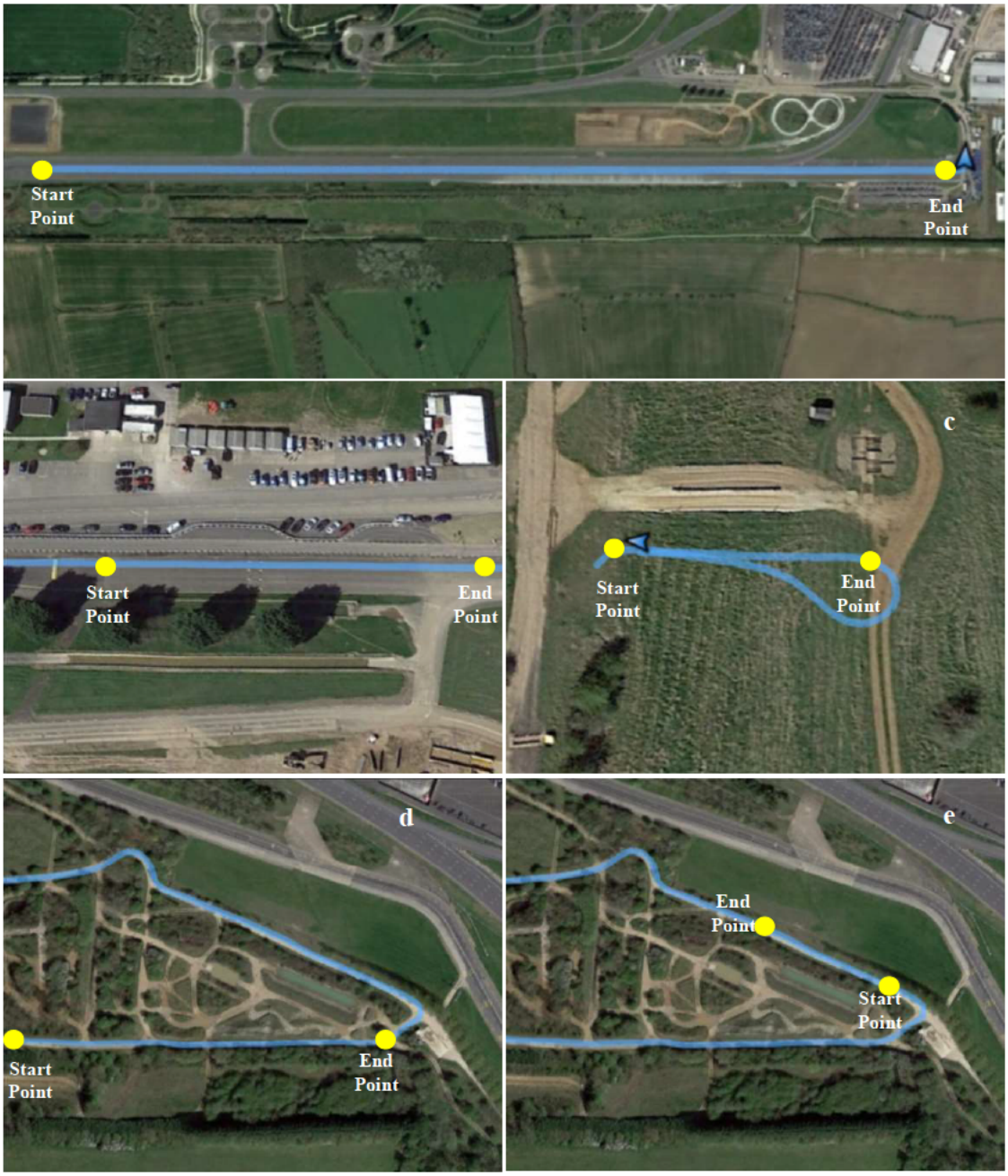
Start Point
End Point
Start Point
End Point
c
Start Point
End Point
d
Start Point
End Point
e
End Point
Start Point

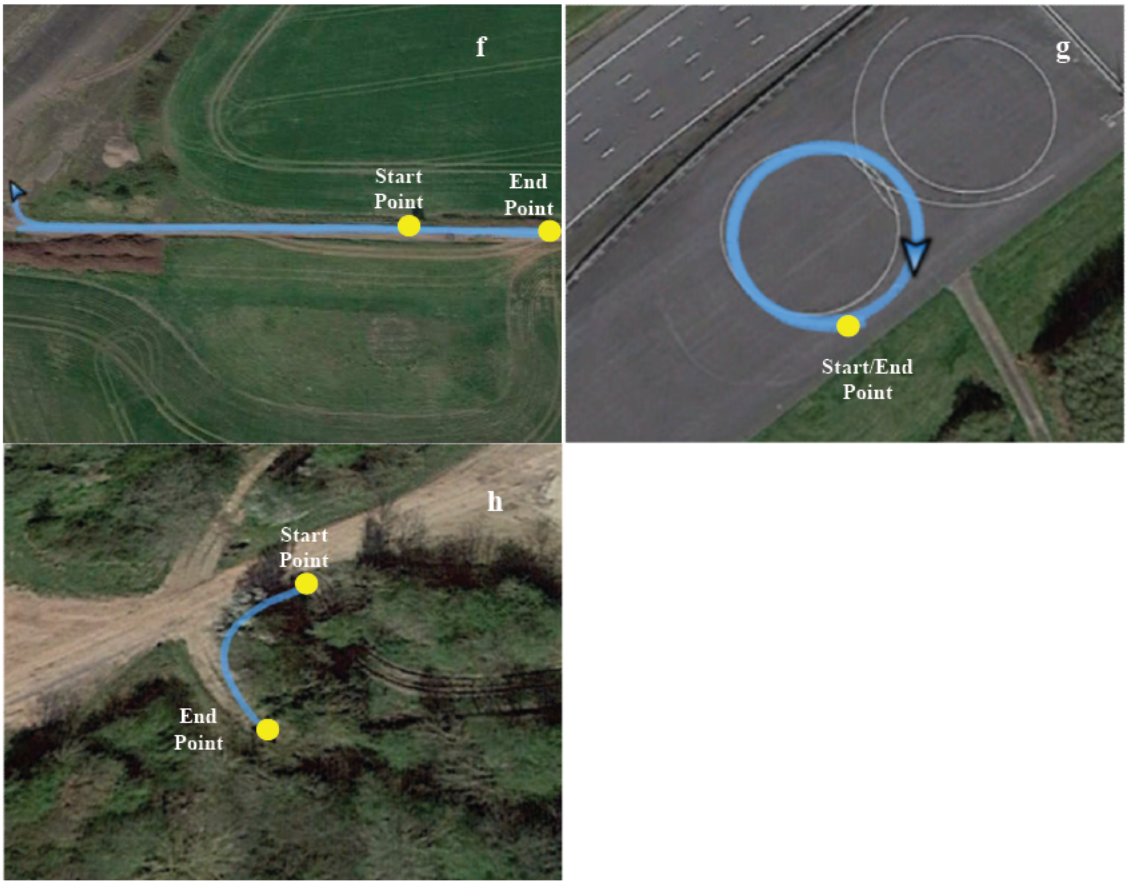

Figure 5.13 Trajectories of test vehicle during the test. The trajectory for test-scenario 1 to 8 is shown on (a) to (h) respectively

During the straight-line trajectories on off-road surfaces, the test vehicle was driven in a straight-path regardless if there are any potholes on the ground. However, for safety reason, the vehicle was driven at low speed about 2 to 16 mph depending on the road conditions. In some of the test, the data collection was performed even before the vehicle enters the target road surface.

5.6. Summary

This chapter described the radar system used in the experimental campaign and how experiments are executed. The system namely 4-beam SoG radar consists of four CW radars operating at a frequency of 24 GHz. These radars were mounted on a 4x4 vehicle and positioned in a Janus configuration. For analysis purposes, A GPS receiver is used to estimate vehicle speed during the experiment process. A MATLAB code is written to record the Doppler signal and GPS data simultaneously.

We collected a sufficiently large database of speed data using the SoG radar. Speed data were collected under six different types of road surfaces and two kinds of vehicle trajectories. In summary, speed data from eight test-scenarios were collected to verify the performance of the SoG radar system.

Chapter 6. Experimental Results and Analysis

6.1. Introduction

This chapter presents the performance evaluation of the developed 4-beam SoG radar system based on experimental data. Eight series of test-scenarios were performed, and they described in detail in Section 5.5. For each test, the statistical differences between the estimated speed and GPS speed (reference speed) are measured. These statistics are used as the basis for the performance assessment in this chapter. It is worth mentioning here that we do not take the GPS speed as 100% accurate but rather as a relative comparison of speed.

The performance analysis of this chapter is divided into five sections. Section 6.2 presents the results of the preliminary examination on the spectra collected from the test-scenarios and the results algorithm's calibration factor. Section 6.3 and 6.4 show the results of the performance assessment based on straight and circular trajectories. Finally, in section 6.5 we demonstrate the result of vehicle sideslip estimation using the developed SoG radar system.

6.2. Preliminary Analysis

Doppler signals collected from test-scenarios 1 to 8 were used in the preliminary analysis. The following subsections describe in detail on each of the preliminary analysis.

6.2.1. Characteristics of Doppler spectra

Figure 6.1(a) and (b) show the examples of measured Doppler spectra. Each of the spectra is computed from a 100 ms samples of Doppler signal of different test-scenarios. The amplitude of the spectra was smooth with n = 20 to show its main shape.

The spectra in (a) are obtained from the dry asphalt road surface when the test vehicle is moving at different constant speeds of v = 10, 20, 30, 40 and 70 mph (test-scenario 1). As can be seen from the plots, the shape of each spectrum looks like a bell-shaped or Gaussian curve which due to the shape of the antenna radiation pattern. The width of the spectra increases with the increase in vehicle speed. This observation agrees with the theoretical analysis in Section 3.4.1.

The spectra in (b) were obtained from the other types of surfaces which are concrete, grass, bumpy-dirt, wet dirt and water (test-scenarios 2 to 6). Comparatively speaking, the spectra obtained from the off-road surfaces is much narrower than the one in asphalt road. This narrow main lobe is because the vehicle was driven at a low speed between 2 to 5 mph. Notably, the spectrum from water is weaker than the ones obtained from other surfaces. This is due to the low surface roughness of the water surface.

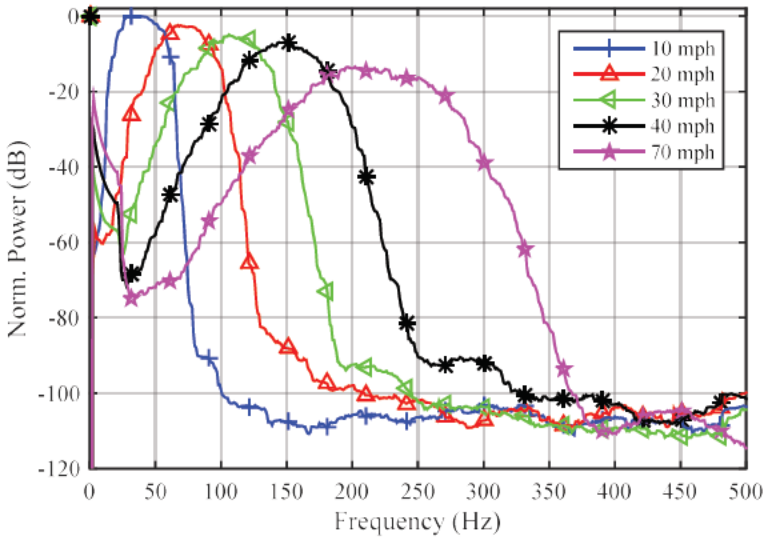

(a)

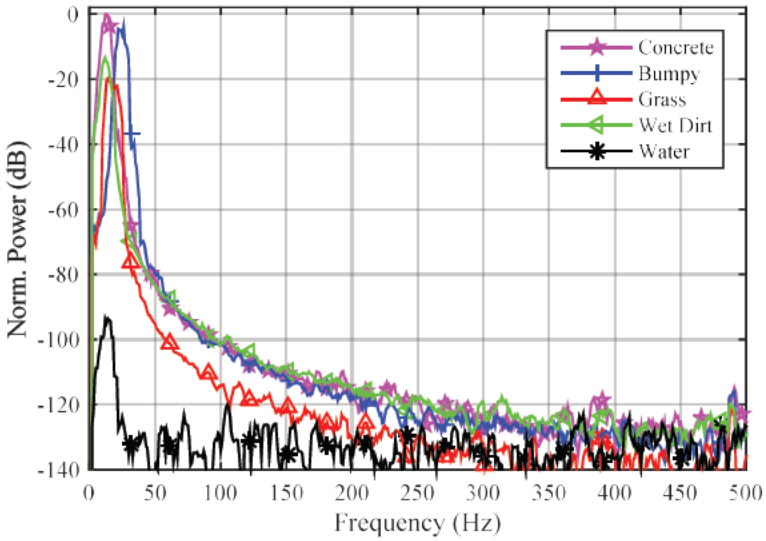

(b)

Figure 6.1 Power spectra obtained from test-scenario 1 to 8. (a) Spectra from test-scenario 1. (b) Spectra from test scenarios 2 to 6.

6.2.2. Variation of Return Power

As discussed in Chapter 4, a low radar return power may influence the accuracy of the proposed algorithm. For this reason, we analyse the variation of radar return power with six different surfaces. The variation of return power is examined by estimating the peak power density from each 100 ms spectra. Figure 6.2(a) to (e) shows the measured peak power density obtained from dry asphalt surface when the test vehicle was moving at different speeds of v = 10, 20, 30, 40 and 70 mph (test-scenario 1). Comparatively, Figure 6.3(a) to (e) shows the measured power density obtained from other surfaces that are concrete, grass, bumpy dirt, wet dirt and water (test-scenarios 2 to 6). Note that, for grass surface, the Doppler signal is only collected for 16 seconds and therefore, the length of the plot is shorter than other surfaces.

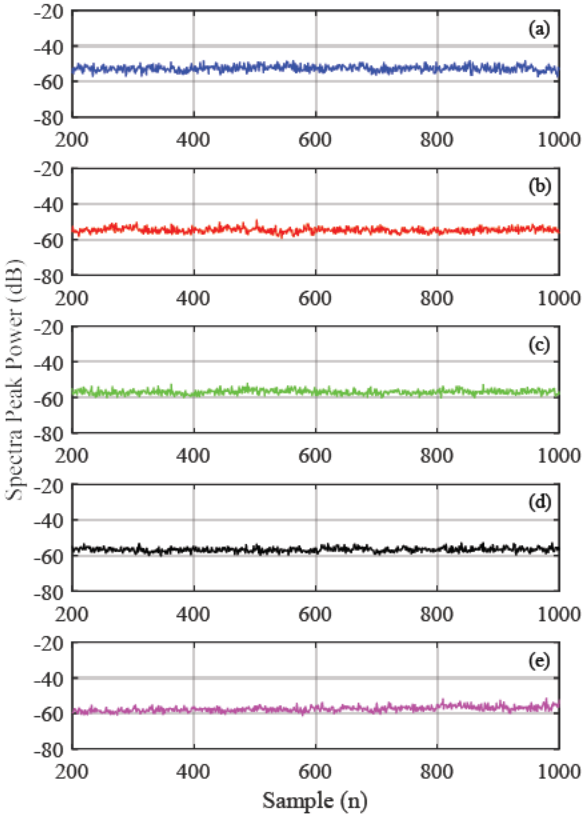

Figure 6.2 Plots of spectra peak power versus samples for data in test-scenario 1.

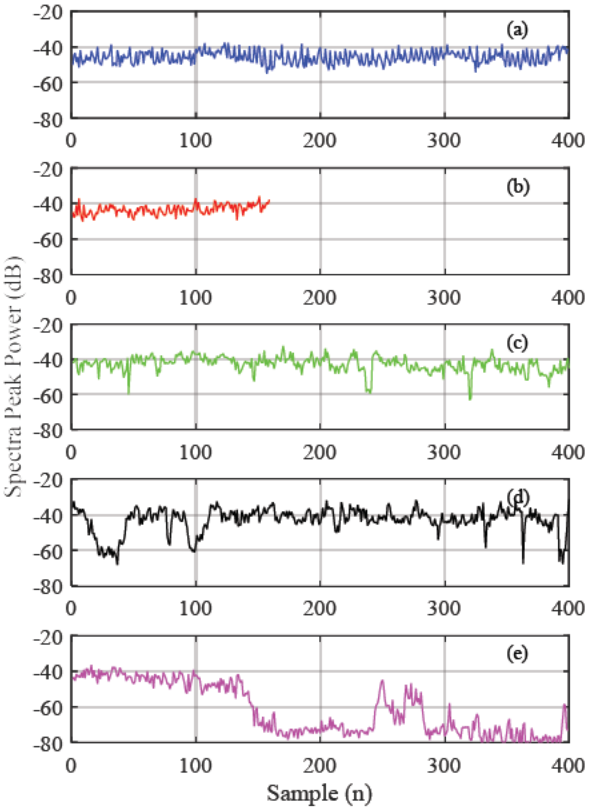

Figure 6.3 Plots of spectra peak power versus samples for data in test scenario 2 to 6

From both Figure 6.2 and Figure 6.3, it appears that the variation of power on the asphalt road is relatively smaller than the off-road surfaces. The standard deviations of peak power from the asphalt road for v = 10, 20, 30, 40 and 70 mph are 1.7, 1.5, 1.3, 1,3 and 1.0 dB respectively. For off-road surfaces, the standard deviations are higher. The standard deviation of 3.5, 2.7, 4.4, 7.1 and 13.2 dB for concrete grass, bumpy dirt, wet dirt, and water respectively were recorded. Higher power variation from off-road surfaces is expected because of the surface itself. For bumpy dirt and wet dirt, the surfaces have a lot of water potholes. As discussed in Chapter 2, water on potholes can reduce the return echo of the Doppler signal. For water surface, we found that large power drop between samples number 150 and 400. This large power drop happened when the radar beam completely illuminates the surface of the water.

In summary, it can be said that the recorded Doppler signal has small power fluctuations between 1 and 7 dB for all types of surfaces with an exception for the water surface. This little variation is still within the processing capability of the proposed algorithms.

6.2.3. Calibration

The imprecise mounting of radar during the setup can produce a constant bias in the estimate of speed. Fortunately, this bias can be minimised by finding the radar mounting calibration factor as described in Section 5.3. Figure 6.4(a) to (b) compares the estimate of speed before and after the calibration process. The unscaled speed is shown in (a), and the scaled speed is shown in (b). From Figure 6.4(b), the mean difference between the speed of radars and GPS are -1.8, +4.8, -9.9 and +2.9 mph for Radar 1, Radar 2, Radar 3 and Radar 4 respectively.

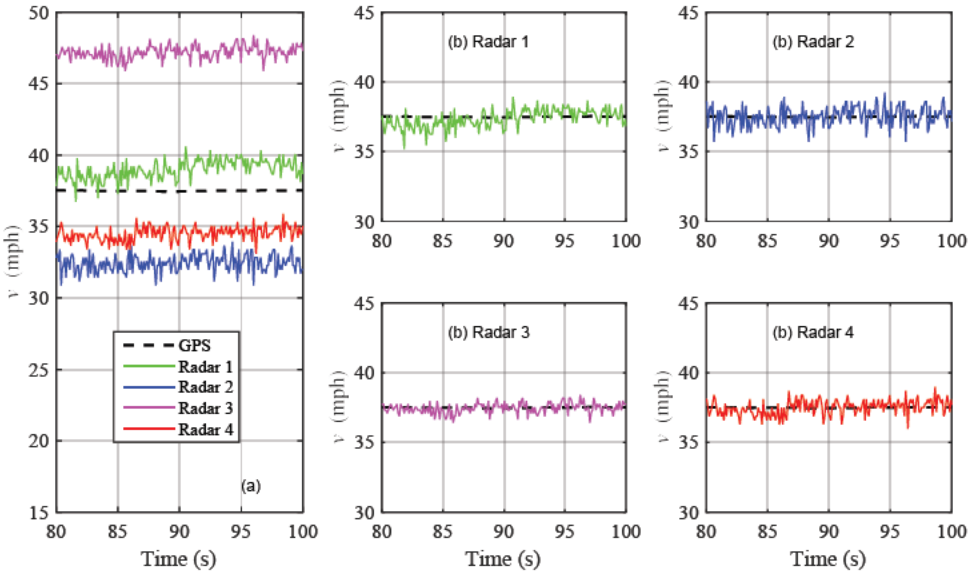

Figure 6.4 Radar speed measurement (a) Uncalibrated speed. (b) to (c): Calibrated speed

As described in Chapter 4, the bias is also dependent on the type of algorithm used. Figure 6.5 shows the results of the calibration factor based on the CMA-AT, CMA-ST, and XCA algorithms.

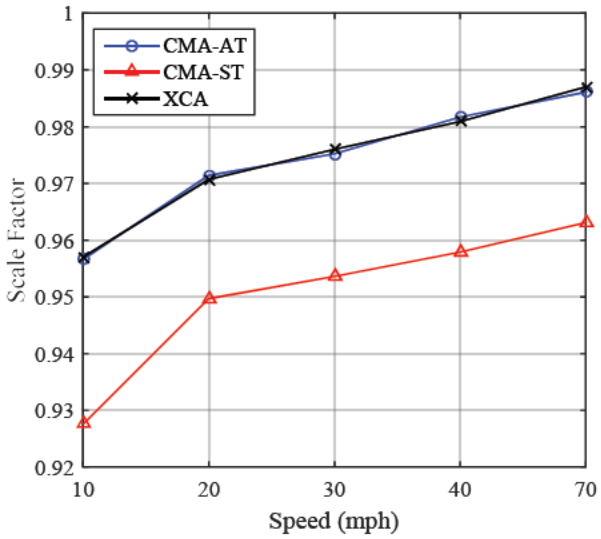

Figure 6.5 Calibration factor of the SoG system

Few deductions can be made from the graph. Firstly, the calibration factor for all algorithms are less than 1; this indicates that the raw speed measurement is over-estimated. Secondly, the scale factor is not linear. The three algorithms produce more over-estimate at $v = 10$ mph than speed above 20 mph. Thirdly, the difference in calibration factor between each algorithm is constant at every speed. This constant scaling factor shows that bias from the imprecise mounting of radar viewing angles is constant. In other words, the viewing angle of each radar did not change when the test was performed.

6.3. Straight-Line Trajectory

This section evaluates the performance of the SoG radar in test-scenarios 1 to 6. In total, the test-scenarios 1 to 6 are comprised of ten linear motions: five linear motions on a dry asphalt road at different vehicle speeds, one linear motion on the concrete road with elevated bars and four linear motions on off-road roads surfaces which we called grass, bumpy dirt, and water. The results presented in the following sub-sections are based on the three proposed algorithms.

6.3.1. Asphalt Surface (Test-scenario 1)

For the asphalt surface, the evaluation is divided into two parts: phase of constant speed and phase of acceleration and deceleration.

Constant Speed

Figure 6.6 through Figure 6.10 show the comparison of speed estimation between radar and GPS for test-scenario 1 which consist of five test-runs with speed of v = 10, 20, 30, 40 and 70 mph. For every figure, the top figure indicated with (a) shows the plot of speed between radar and GPS. The bottom plots indicated with (b), (c) and (d) show the corresponding relative error of speed estimation for each algorithm. The distribution of relative error is plotted with time series and histogram.

From the plots of radar versus GPS speed, we observed that the speed estimated by the radar is very close to the speed determined by the GPS over the five test scenarios. Similarly, all plots of relative error versus time show a small variation of error. The standard deviation of relative error is less than 3%. This indicates good long-term accuracy of the proposed SoG radar system regardless of which algorithm is used. In like manner, the distribution of the relative error from all figures shows that the error is normally distributed. Furthermore, the

error distributions found in this experimental work are consistent with the simulated error distribution shown in Section (4.5.1) of Chapter 4.

As mentioned in Chapter 4, the proposed algorithms aim to estimate speed with a specified relative error. Therefore, we investigate the results using five statistical indicators. They are mean, standard deviation, average relative error, maximum relative error and percentage of the estimate that fell under 3% from the GPS speed. Note that the 3% error is based on the performance criteria described in Chapter 4. We shall denote these parameters as $\bar{v}$ σ_v, avg. δ_v, Max. δ_v and 3% of $v_{GPS}(\%)$ respectively.

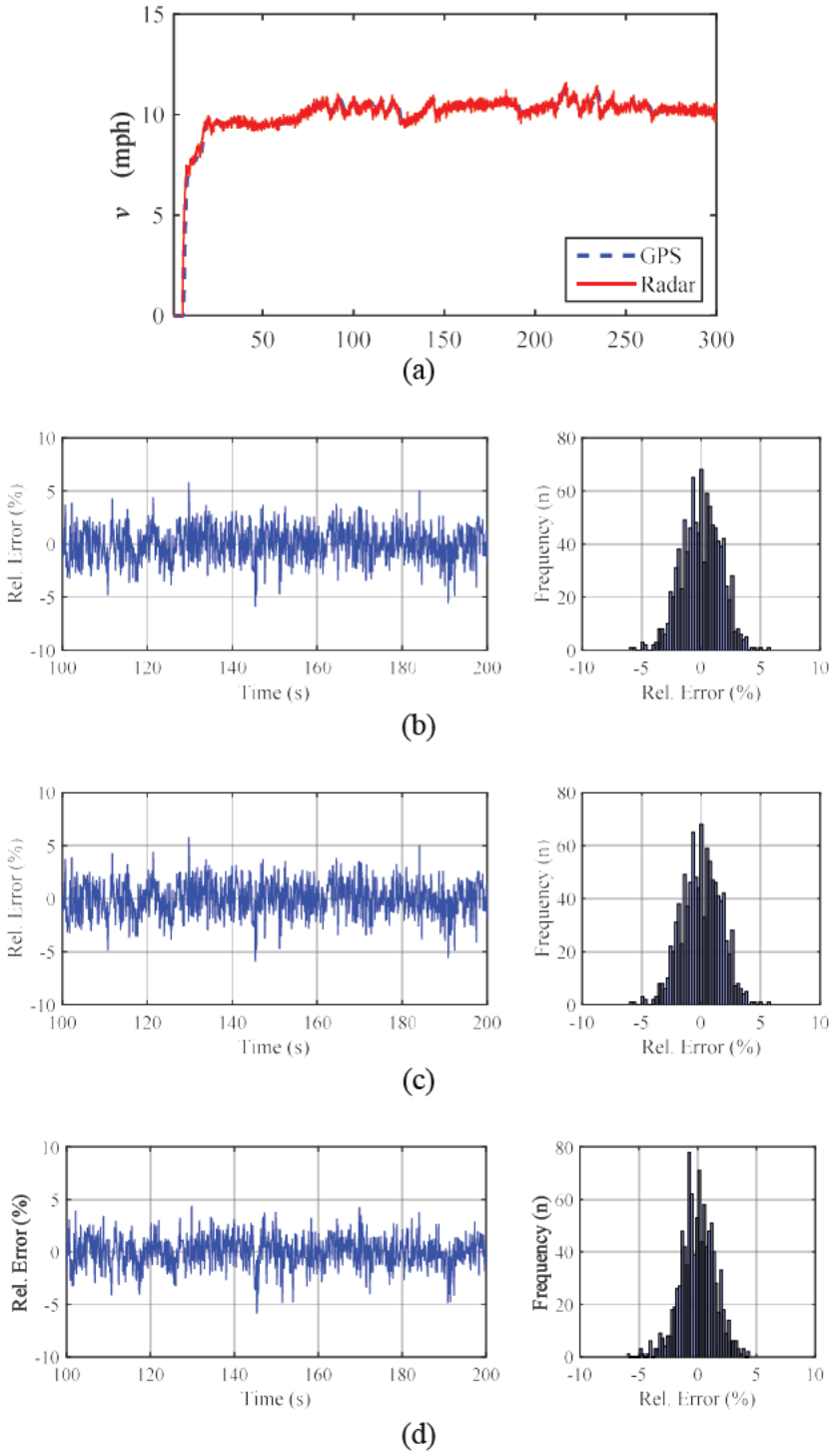

Figure 6.6 Results for v = 10 mph. (a) Radar vs. GPS. Plot of relative error and histogram for each algorithm, (b) CMA-AT (c) CMA-ST (d) XCA

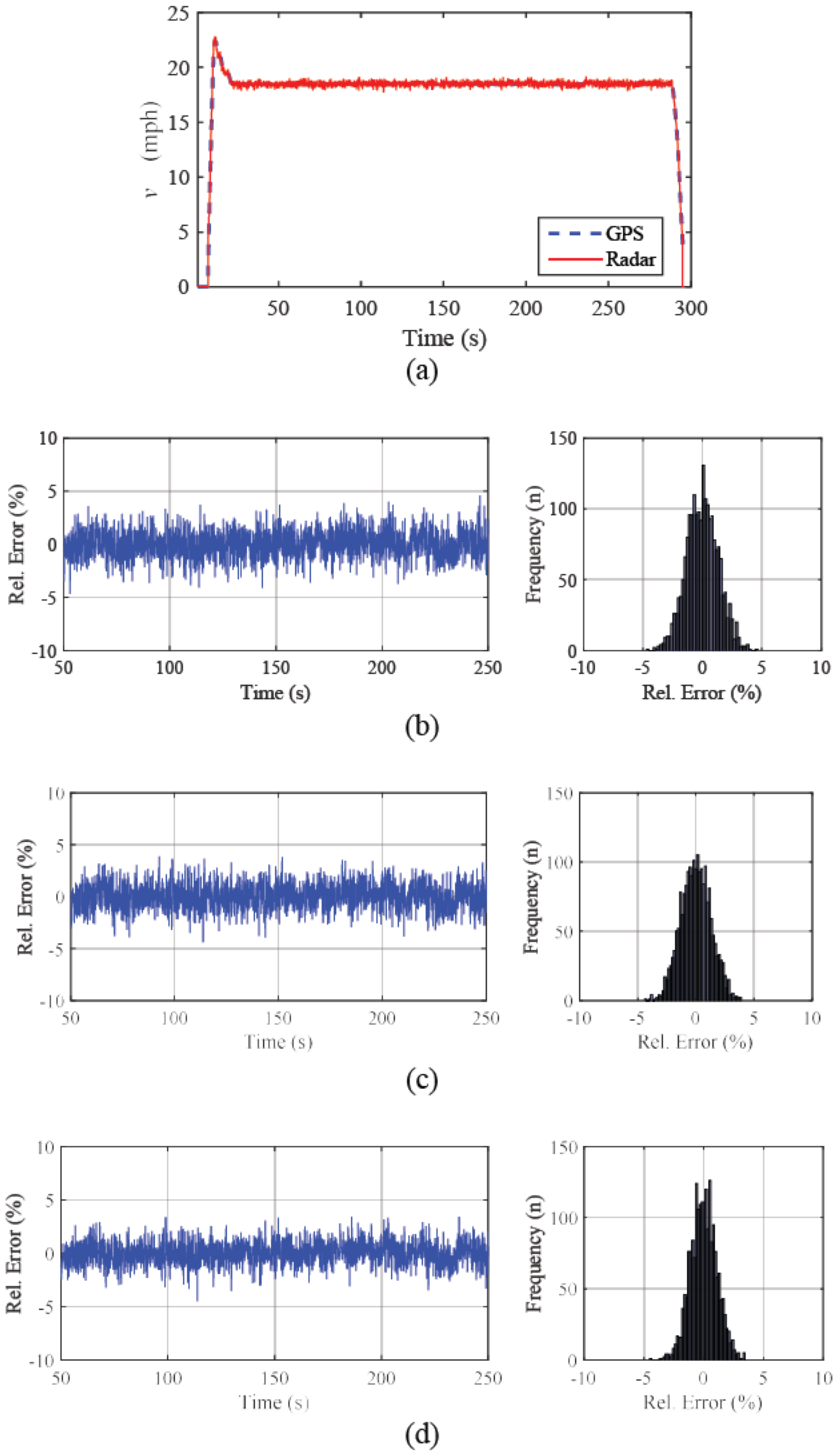

Figure 6.7 Results for $v = 20$ mph. (a) Radar vs. GPS. Plot of relative error and histogram for each algorithm, (b) CMA-AT (c) CMA-ST (d) XCA

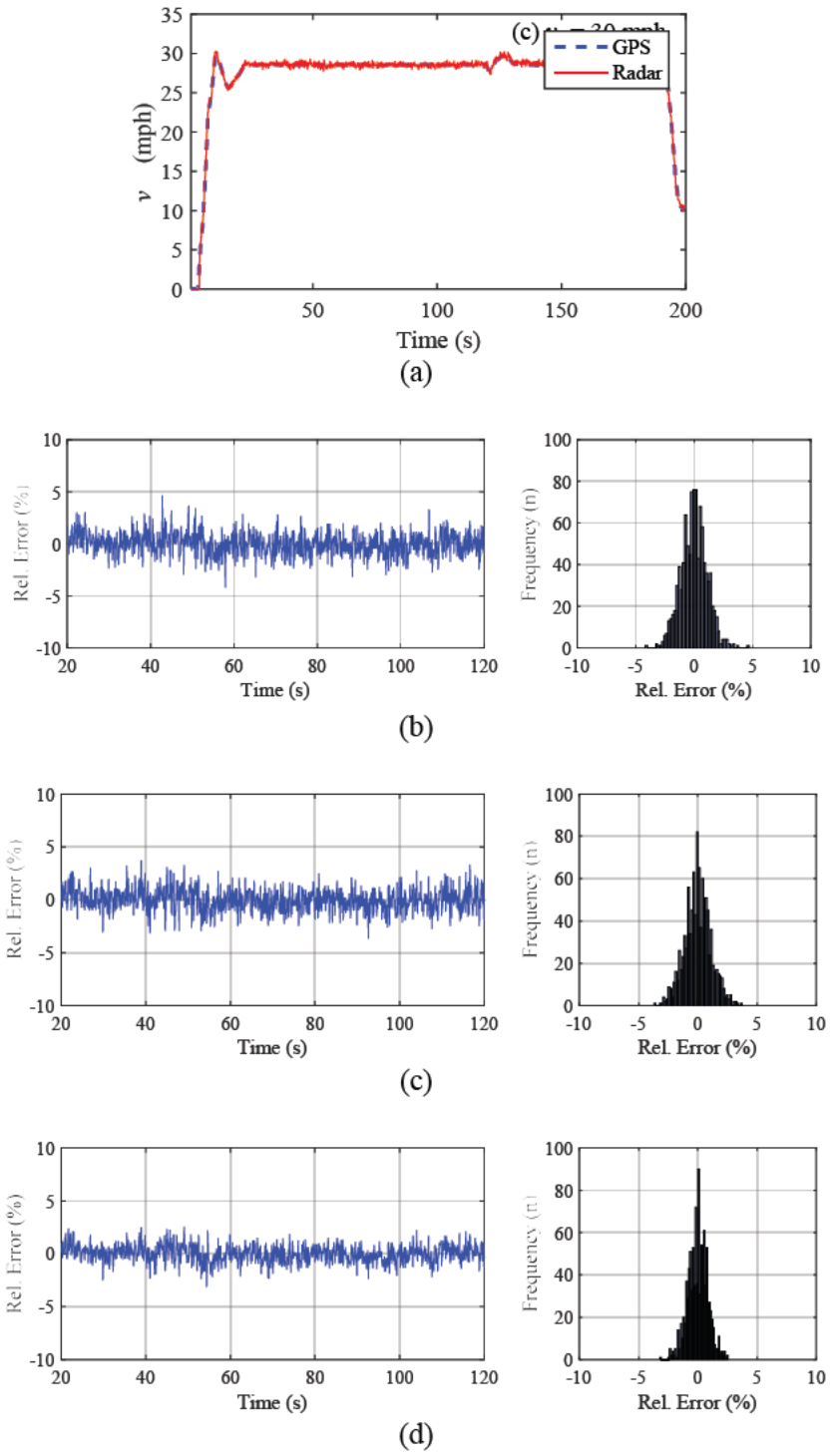

Figure 6.8 Results for v = 30 mph. (a) Radar vs. GPS. Plot of relative error and histogram for each algorithm, (b) CMA-AT (c) CMA-ST (d) XCA

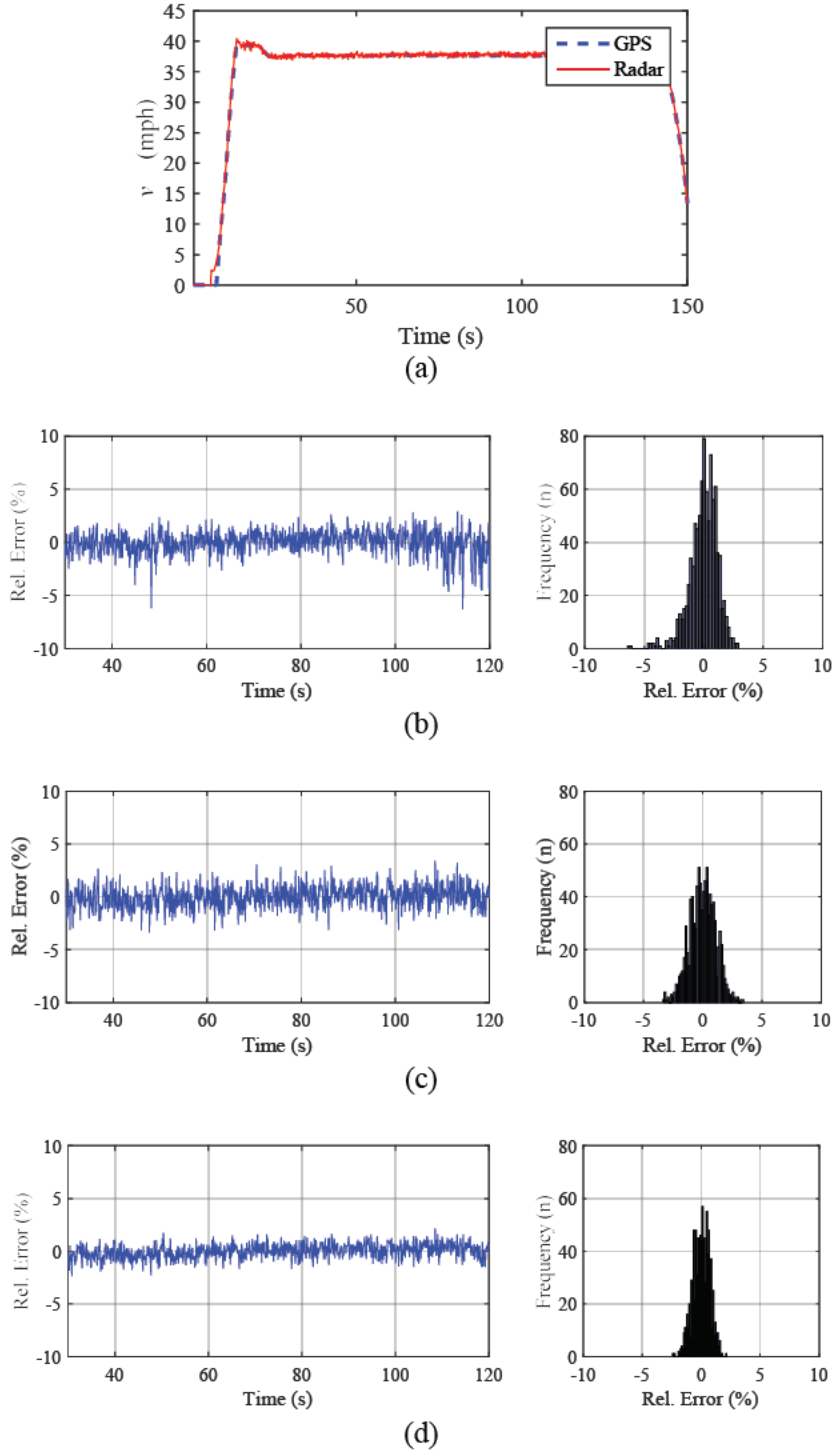

Figure 6.9 Results for v = 40 mph. (a) Radar vs. GPS. Plot of relative error and histogram for each algorithm, (b) CMA-AT (c) CMA-ST (d) XCA

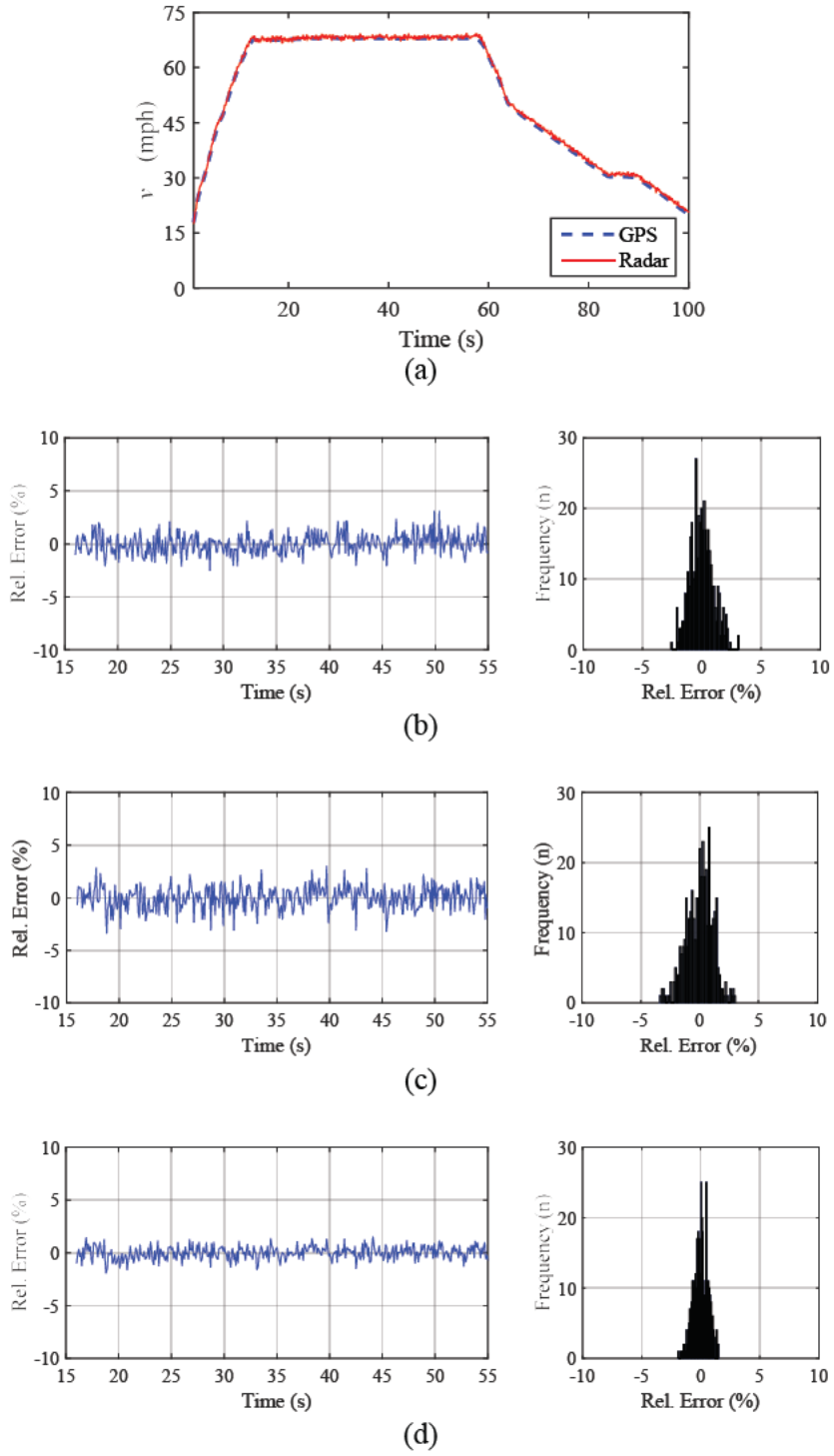

Figure 6.10 Results for Run 5 $v = 70$ mph. (a) Radar vs. GPS. Plot of relative error and histogram for each algorithm, (b) CMA-AT (c) CMA-ST (d) XCA

The statistical results for each of the five test-run are tabulated in Table 6.1.

Table 6.1 Statistical results obtained from Figure 6.6 to Figure 6.10

(a) v = 10 mph

	$\bar{v}$ (mph)	σ_v (mph)	Avg. δ_v (%)	Max. δ_v (%)	in 3% of v_{GPS} (%)
GPS (*Reference*)	9.90	0.35			
CMA-AT	10.3	0.38	1.37	6.27	92.5
CMA-ST	10.6	0.37	1.35	6.32	92.8
XCA	10.3	0.38	1.21	6.03	94.9

(b) v = 20 mph

	$\bar{v}$ (mph)	σ_v (mph)	Avg. δ_v (%)	Max. δ_v (%)	in 3% of v_{GPS} (%)
GPS (*Reference*)	18.3	0.02			
CMA-AT	18.5	0.24	1.07	4.60	97.6
CMA-ST	18.9	0.23	1.03	4.38	98.5
XCA	18.5	0.20	0.87	4.48	99.2

(c) v = 30 mph

	$\bar{v}$ (mph)	σ_v (mph)	Avg. δ_v (%)	Max. δ_v (%)	in 3% of v_{GPS} (%)
GPS (*Reference*)	27.8	0.15			
CMA-AT	27.6	0.34	0.88	4.65	99.0
CMA-ST	27.0	0.33	0.86	3.74	99.1
XCA	27.5	0.27	0.67	3.10	99.9

(d) v = 40 mph

	$\bar{v}$ (mph)	σ_v (mph)	Avg. δ_v (%)	Max. δ_v (%)	in 3% of v_{GPS} (%)
GPS (*Reference*)	37.6	0.02			
CMA-AT	37.3	0.44	0.87	6.31	98.1
CMA-ST	37.2	0.41	0.87	3.41	99.0
XCA	37.3	0.27	0.57	2.40	100.0

(e) v = 70 mph

	$\bar{v}$ (mph)	σ_v (mph)	Avg. δ_v (%)	Max. δ_v (%)	in 3% of v_{GPS} (%)
GPS (*Reference*)	66.7	0.13			
CMA-AT	66.3	0.65	0.77	3.12	99.4
CMA-ST	66.5	0.76	0.90	3.40	99.5
XCA	66.3	0.44	0.50	1.91	100

Table 6.1. provides the error analysis for each algorithm. The results show good speed estimation accuracy for all three algorithms. The percentage of the estimate that fell under 3% from the GPS speed is more than 90%. The average relative error is small between 0.5% to 1.3%. Furthermore, the maximum relative error is also small at 6%. This low error in the estimated speed shows the long-term accuracy of the SoG system regardless of the algorithm used. However, the increase in standard deviation with the increase of vehicle speed can be seen. This trend is also found in the simulation results presented in Chapter 4 which mainly due to the spreading of the Doppler spectrum at high speed. Through the five test-runs, the XCA algorithm always produces lower error than the CMA algorithms.

Figure 6.11 plots the average, maximum and the percentage of the estimate that fell under 3% from the GPS speed. It can be seen that the accuracy of speed estimation increases with the increase in vehicle speed. It can be said that all three algorithms perform better at high speed between 40 to 70 mph. Large measurement variance at low speed is related to the frequency resolution of the Fourier transform. When a vehicle is moving with low speed, the resultant Doppler spectrum has a narrow bandwidth. Consequently, the detail of the spectrum cannot be properly captured using FFT with low resolution. One method to improve this problem is by using FFT with higher points.

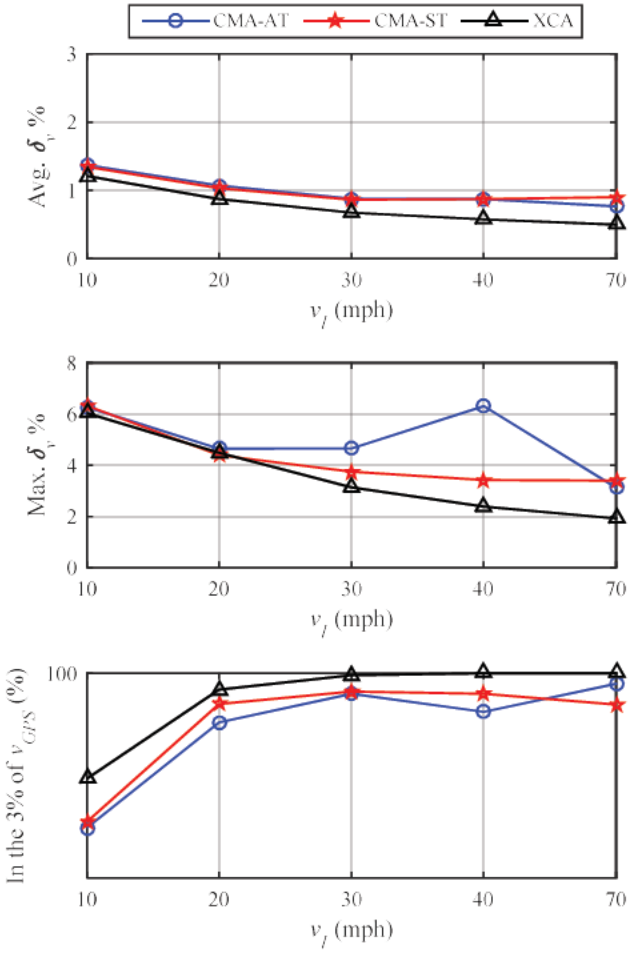

Figure 6.11 Trends of performance across five different speeds

One conclusion drawn from the first test-scenario is that the SoG radar system works well under constant speed and relatively flat-surface road condition. Emphasis is given to the XCA algorithm as this technique consistently produces more accurate estimates and achieve lower average relative error compared to both CMA methods. The observed performance here confirms the observation in the simulation given in Chapter 4.

The XCA algorithm benefits from two characteristics of Doppler spectra obtained from the dry asphalt road. The first one is due to the shape of the spectra which closely follow the shape of

a Gaussian antenna pattern. The second one is due to the amplitude variation in the spectra which have the characteristics of white Gaussian noise. When these two characteristics exist, the XCA algorithm with produce accurate results.

Acceleration & Deceleration phase

Comparison of relative error between the algorithms was made with acceleration and deceleration data in test-scenario 1 at v = 70 mph. The value of acceleration/deceleration rate are 4.1 mph/s^2 and 1.0 mph/s^2 respectively. The following plots present the results of the analysis.

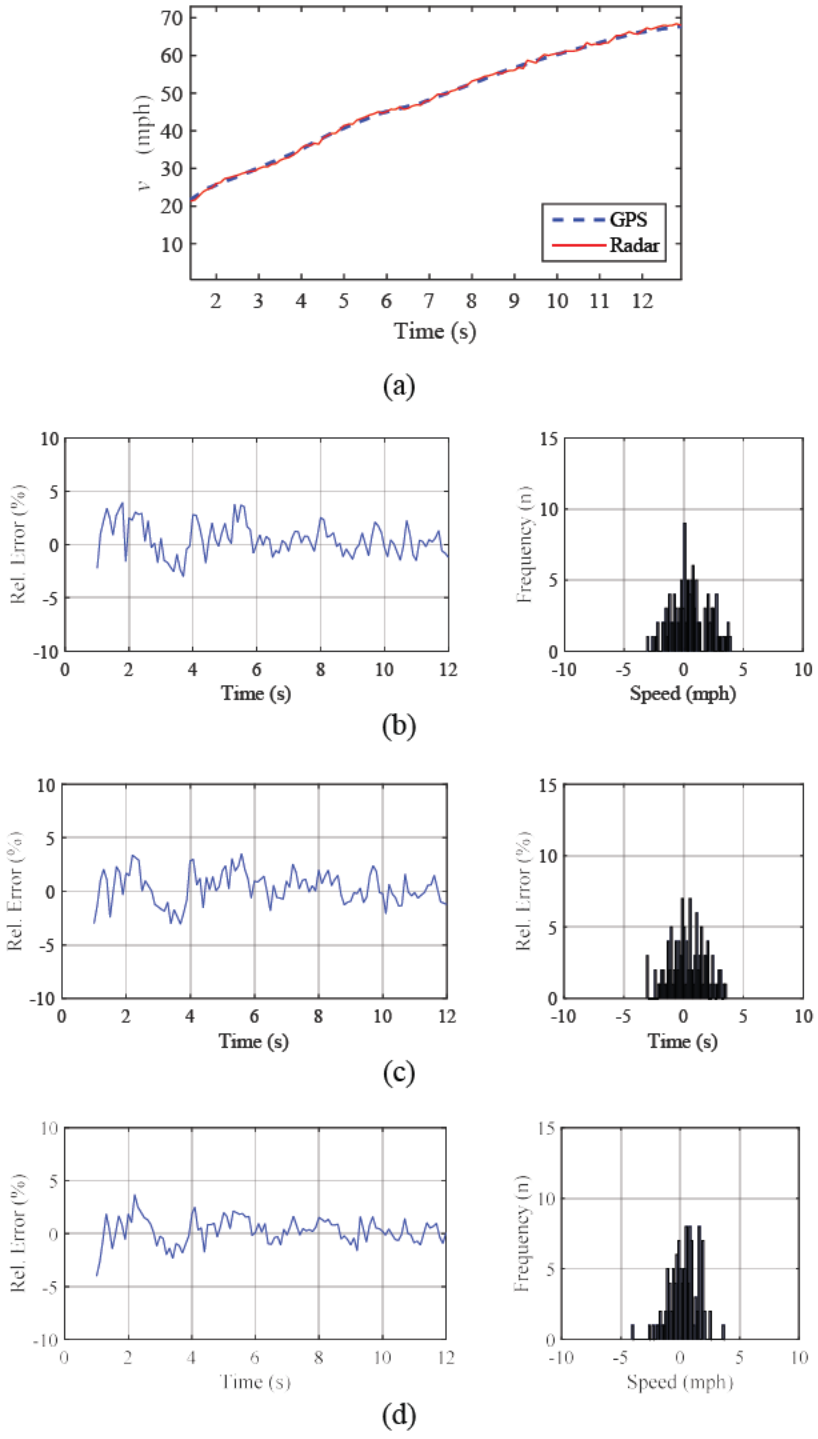

Figure 6.12 Results for acceleration phase. (a) Radar vs. GPS Plot of relative error and histogram for each algorithm, (b) CMA-AT (c) CMA-ST (d) XCA

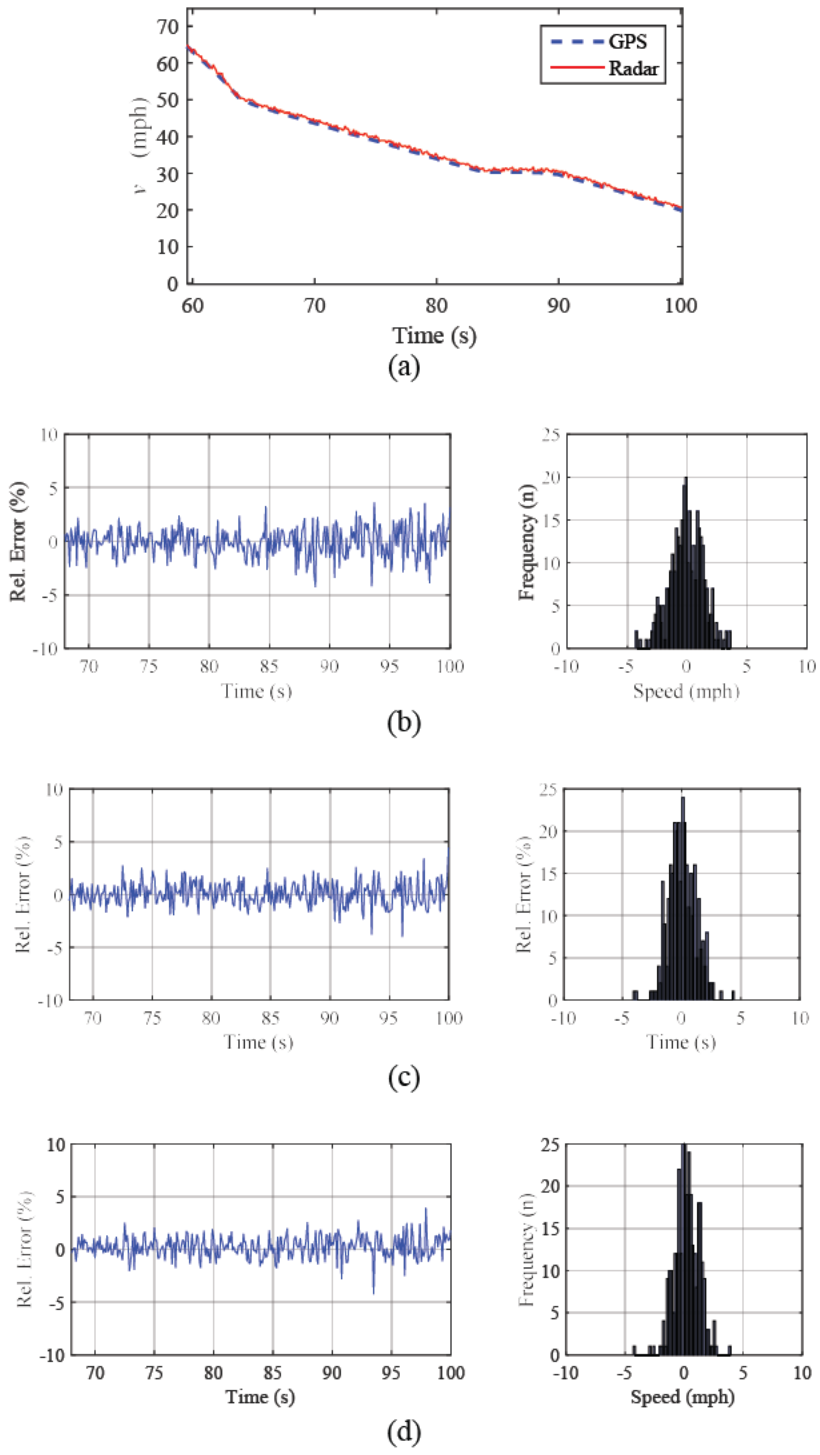

Figure 6.13 Results for the deceleration phase. (a) Radar vs. GPS. Plot of relative error and histogram for each algorithm, (b) CMA-AT (c) CMA-ST (d) XCA

The statistical parameters for both acceleration and deceleration phases are presented in Table 6.2(a) to (b)

Table 6.2 The statistical results obtained from Figure 6.12 and Figure 6.13

(a) Phase: acceleration

	Avg. δ_v (%)	Max. δ_v (%)	in 3% of v_{GPS} (%)
CMA-AT	1.24	3.90	92.7
CMA-ST	1.24	3.52	94.6
XCA	0.97	4.00	98.2

(b) Phase: deceleration

	Avg. δ_v (%)	Max. δ_v (%)	in 3% of v_{GPS} (%)
CMA-AT	1.11	4.20	96.9
CMA-ST	0.91	4.40	98.8
XCA	0.80	4.00	99.4

In both acceleration and deceleration phase, the relative error of speed estimate is comparable to the one found on a constant speed. The maximum relative error measured in both phases is less than 4%. This evaluation shows that all algorithms have good accuracy in measuring speed changes during acceleration and deceleration. Furthermore, we did not find any critical changes to the performance SoG radar in this test.

6.3.2. Elevated Bars (Test-scenario 2)

The second test-scenario was performed on a concrete road with elevated bars that stimulates strong vibrations to the test vehicle when traversing on it. The performance of the estimated speed is presented in Figure 6.14. For comparison purpose, the test vehicle was also driven about the same speed on a concrete road with no elevated bars. The performance of this test is presented in Figure 6.15.

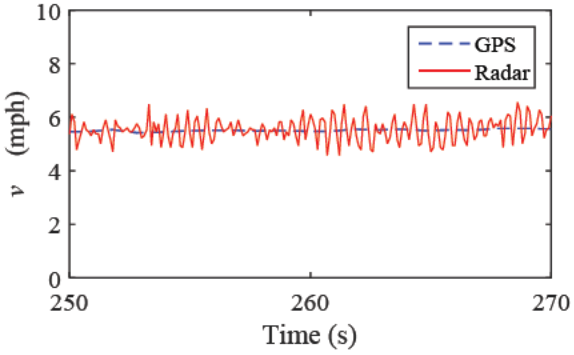

(a)

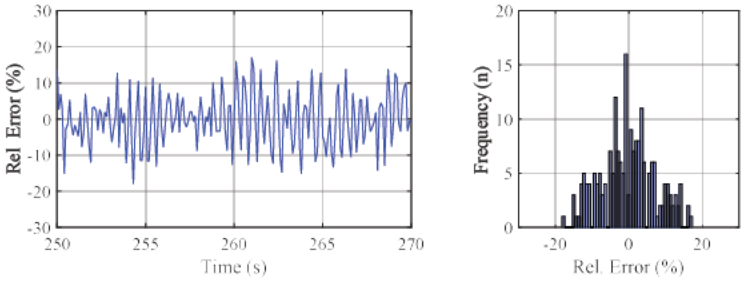

(b)

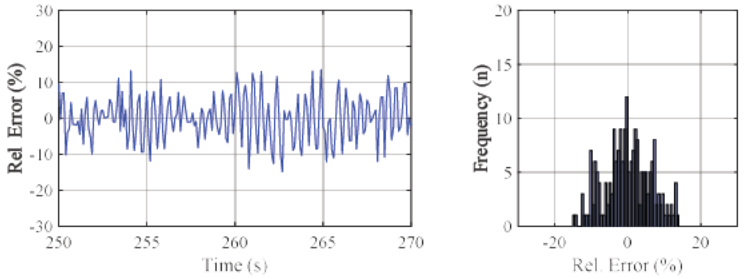

(c)

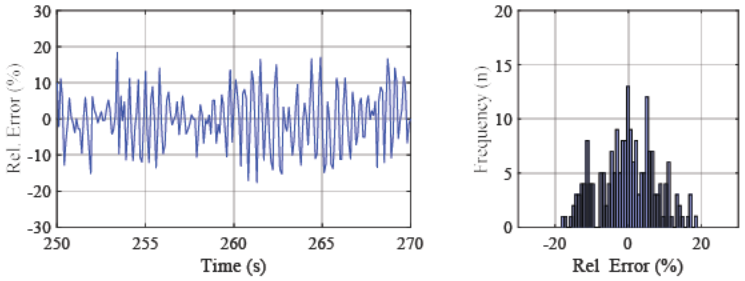

(d)

Figure 6.14 Results for bumps. (a) Radar vs. GPS. Plot of relative error and histogram for each algorithm, (b) CMA-AT (c) CMA-ST (d) XCA

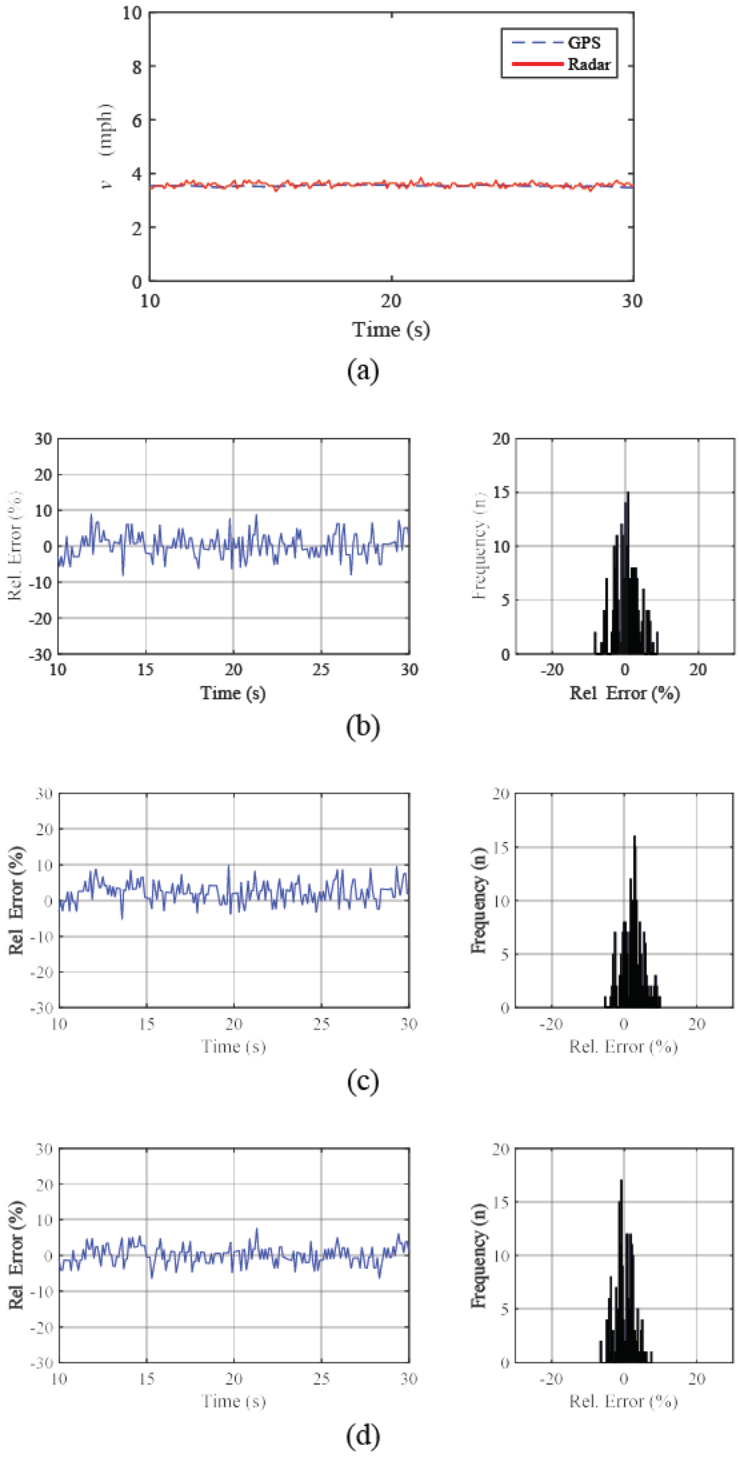

Figure 6.15 Results for a smooth surface. (a) Radar vs. GPS. Plot of relative error and histogram for each algorithm, (b) CMA-AT (c) CMA-ST (d) XCA

The statistical parameters from both tests are presented in Table 6.3(a) – (b)

Table 6.3 The statistical results obtained from Figure 6.14 and Figure 6.15

(a) Road with elevated bars

	$\bar{v}$ (mph)	σ_v (mph)	Avg. δ_v (%)	Max. δ_v (%)	in 3% of v_{GPS} (%)
GPS (*Reference*)	5.48	0.04			
CMA-AT	5.46	0.42	5.46	20.9	30.54
CMA-ST	5.47	0.37	5.46	19.6	32.05
XCA	5.46	0.45	6.58	21.8	40.29

(b) Smooth road

	$\bar{v}$ (mph)	σ_v (mph)	Avg. δ_v (%)	Max. δ_v (%)	in 3% of v_{GPS} (%)
GPS (*Reference*)	3.54	0.03	0.00	0.00	
CMA-AT	3.55	0.12	3.02	8.97	66.67
CMA-ST	3.63	0.10	3.02	9.98	58.50
XCA	3.55	0.09	2.08	7.63	75.62

Comparison between Table 6.3(a) and Table 6.3(b) reveals three changes in the quality of the estimates associated with the vehicle vibration. We find an increase in average and maximum relative error between 2% and 3%, and between 10% and 13% respectively. Secondly, the number of estimate that falls within 3% of reference speed also decreases by 20-30%. In this evaluation, we observed that the performance of the XCA algorithm is about the same accuracy to the CMA methods.

This evaluation shows that vehicle vibration can reduce the performance of the SoG system. Despite having 4-beam radars in Janus configuration, the pitch and roll or the combinations of it cannot be entirely suppressed in the estimates of speed. This is because the principle of Janus itself, which requires accurate determination of beam centroids of the two opposing beams. However, this may be difficult to achieve in this work since each algorithm will produce some

bias in the estimate of beam centroids. In most cases, vibrations from the ground surface are absorbed by the car suspension system, which reduces the effect of vibration on the SoG radar system. Based on the theoretical analysis in Section 3.2.1, the 2 to 3% increase in average relative error corresponds to the angle between 1° and 2° of pitch and roll angles which is possible when the test vehicle traversed the elevated bars in this test. One solution to this problem is to use stabiliser to the radar which reduces the impact of vehicle vibrations.

6.3.3. Off-Road Surfaces (Test-scenarios 3-6)

The performance of the SOG system was evaluated under off-road conditions. The test vehicle was driven on four different types of surfaces which we called grass, bumpy dirt, wet dirt, and water. The vehicle speed was not maintained at a constant speed but varied within ±2 mph of the target speed of 5 mph. One aspect of this evaluation that is different from the previous evaluation is the percentage of speed which falling close to the GPS speed is specified at 5%. This value was chosen since the vehicle is driven at low speed (below 10 mph). A 5% error at low speed is small, for example, if the speed is 5 mph, the equivalent 5% in absolute error is 0.25 mph. The results of estimated speed by radar for grass, bumpy dirt and wet dirt are shown in Figure 6.16 through Figure 6.18 respectively.

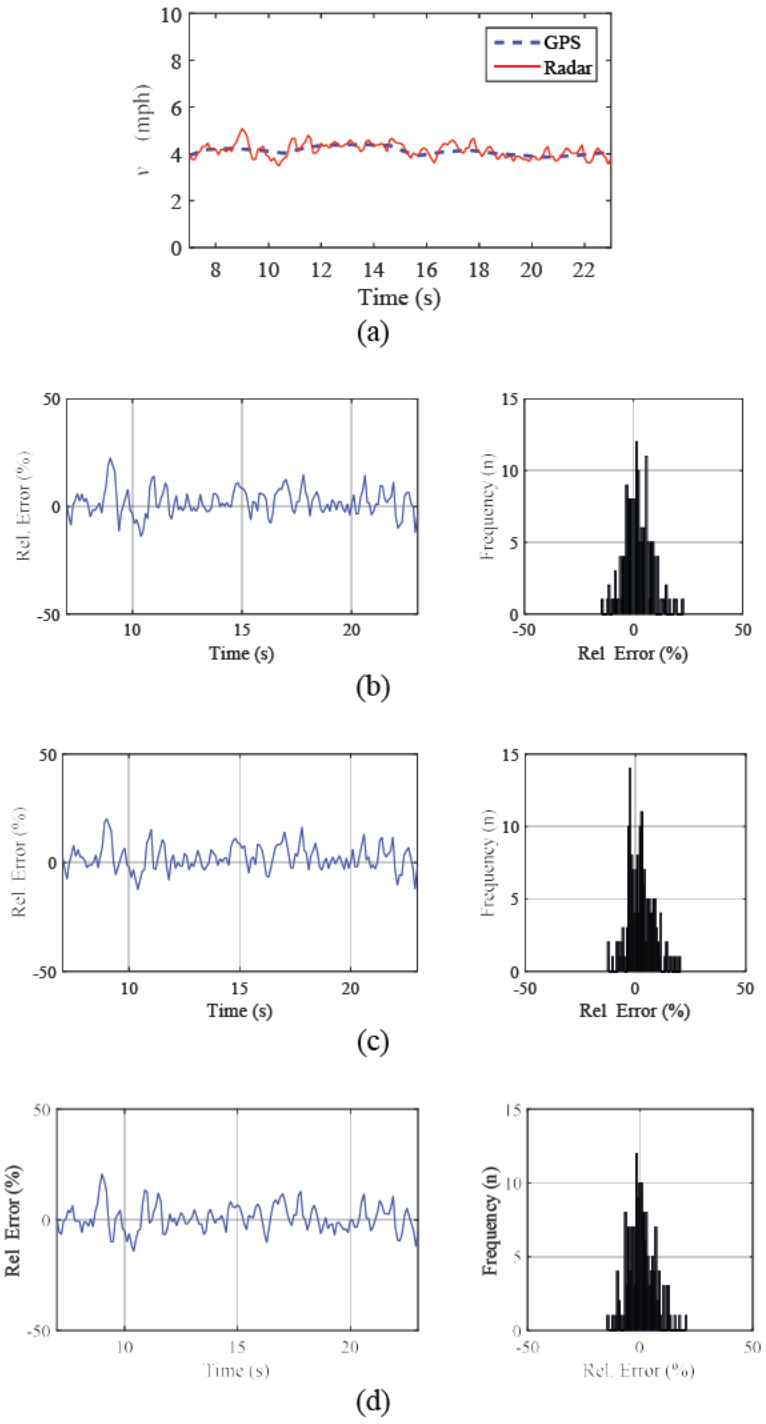

Figure 6.16 Results for Grass. (a) Radar vs. GPS. Plot of relative error and histogram for each algorithm, (b) CMA-AT (c) CMA-ST (d) XCA

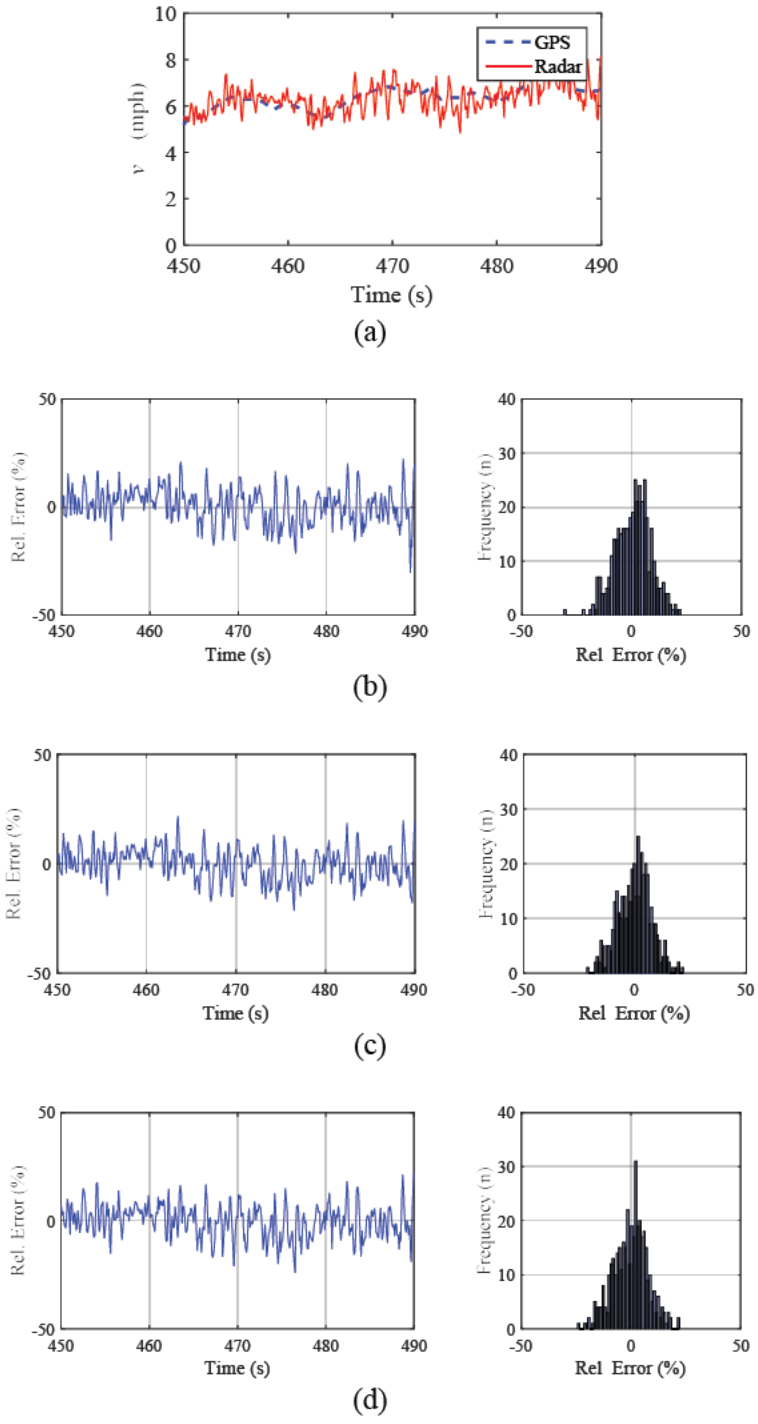

Figure 6.17 Results for Bumpy dirt. (a) Radar vs. GPS. Plot of relative error and histogram for each algorithm, (b) CMA-AT (c) CMA-ST (d) XCA

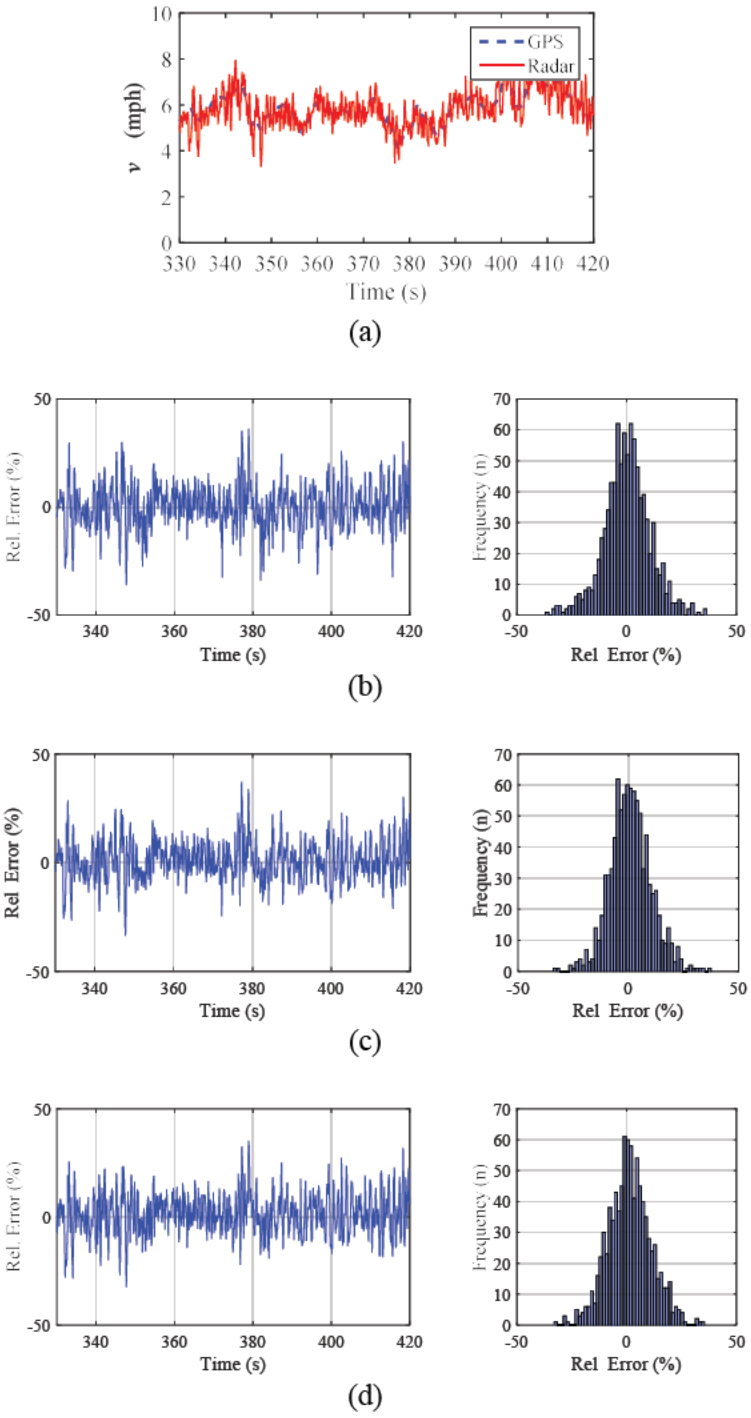

Figure 6.18 Results for Wet dirt. (a) Radar vs. GPS. Plot of relative error and histogram for each algorithm, (b) CMA-AT (c) CMA-ST (d) XCA

From the plots of radar versus GPS speed, the speed estimate by radar follows the GPS speed. However, we observed small and inconsistent bias throughout the test. Such example can be seen in Figure 6.16(a). The dissimilarity from the GPS speed is apparent although calibration has been performed. One can assume the difference is due to the vibration of the vehicle during the test. However, it has been shown in Section 6.3.2 (test-scenario 2) that vehicle vibrations do not increase the bias in the estimates of speed. This suggests that the inconsistent difference between radar and GPS speed is because of the ground characteristics. Video recording from these surfaces reveals that the bumpy dirt and wet dirt surfaces were wet, and many potholes are entirely covered by rainwater. As discussed in Chapter 2, the smooth surface of water can generate a skewed Doppler spectrum and significantly reduces its amplitude. Hence, some small bias is observed in the estimated speed.

The statistical results in Figure 6.16 through Figure 6.18 is presented in Table 6.4(a) to (c).

Table 6.4 The statistical results obtained from Figure 6.16 to Figure 6.18

(a) Grass

	$\bar{v}$ (mph)	σ_v (mph)	Avg. δ_v (%)	Max. δ_v (%)	in 5% of v_{GPS} (%)
GPS (Reference)	4.11	0.17			
CMA-AT	4.22	0.31	4.91	22.4	59.6
CMA-ST	4.16	0.36	4.70	20.2	63.2
XCA	4.13	0.31	4.64	20.7	60.9

(b) Bumpy dirt

	$\bar{v}$ (mph)	σ_v (mph)	Avg. δ_v (%)	Max. δ_v (%)	in 5% of v_{GPS} (%)
GPS (Reference)	6.26	0.51			
CMA-AT	6.39	0.89	6.52	30.2	45.3
CMA-ST	6.17	0.85	6.00	21.62	47.9
XCA	6.19	0.85	6.13	24.4	48.8

(c) Wet dirt

	$\bar{v}$ (mph)	σ_v (mph)	Avg. δ_v (%)	Max. δ_v (%)	in 5% of v_{GPS} (%)
GPS (Reference)	4.78	0.82			
CMA-AT	5.12	1.09	8.12	38.9	38.7
CMA-ST	5.18	1.16	7.48	38.6	42.5
XCA	5.03	1.05	7.63	34.2	42.6

From Table 6.4(a) to (c), the main difference between these statistics and the ones recorded from the asphalt road is that the relative error is higher. The maximum relative error is between 20% to 40% with wet dirt giving the highest error. Also, variation in the estimate of speed is also higher than measurement performed on asphalt road. The standard deviation is between 0.1 and 1.2 mph for an average speed of 5.4 mph. These results show the off-road surfaces increases the error in speed measurement. Nonetheless, the average relative error for the three algorithms is between 4% to 8% which we found adequate for low-speed measurements. It can be said that the SoG system performs reasonably good on the off-road surfaces except on the water surface.

Water surface (Test scenario 6)

The fourth test of the off-road environments was performed by driving the test vehicle on a long pothole that was filled with rainwater. The vehicle was driven at a speed between 3 to 5 mph. Figure 6.19(a) shows the plot of power versus time measured by a radar traveling from wet dirt to the long pothole. The vehicle travelled on the wet dirt between the 35th and 55th seconds and crossed the water surface between 55th and 75th seconds. The return power from the water surface is 10 to 20 dB lower than the one from the wet dirt. Besides, we observed that when the water is at calmest state, the received power further reduces to approximately -30 dB.

Figure 6.19(b) to (d) shows the plot of speed estimated by CMA-AT and CMA-ST and XCA algorithm respectively. Comparison between these three plots shows a significant difference. Both CMA algorithms produce many speed drops to 0 mph. While the XCA algorithm has only a few speed drops to 0 mph. These speed drops were designed in the algorithm to indicate that the main lobe of the Doppler spectrum is not found.

This result suggests that the XCA algorithm can estimate speed from the water surface. However, we observed a small bias of -0.4 mph in the speed estimate which is likely caused by the 'terrain bias' due to the smooth surface of the water as explained in Chapter 2. This result also agrees with the simulation result in Chapter 4 which shows that only the XCA algorithm can work well under low SNR condition (SNR = 10 dB). The few speed drops to 0 mph in XCA algorithms is associated with the calmest state of the water surface. This results also suggest that no algorithm will work under severe SNR conditions.

Working in limited SNR condition is essential to the operation of a SoG radar system. Hence, it is important to know the minimum level of SNR which the system can work properly. In this work, it has been shown that the XCA algorithm can work at low SNR condition. This result agrees well with the simulation results in Chapter 4. One advantage of the XCA method is that cross-correlation works by fitting a template to the measured spectra. This fitting process is independent of amplitude threshold such as found in the CMA methods.

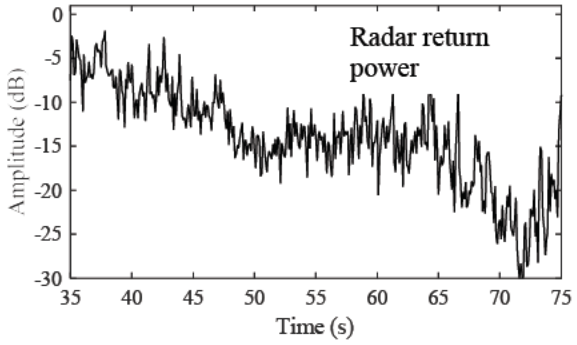

(a)

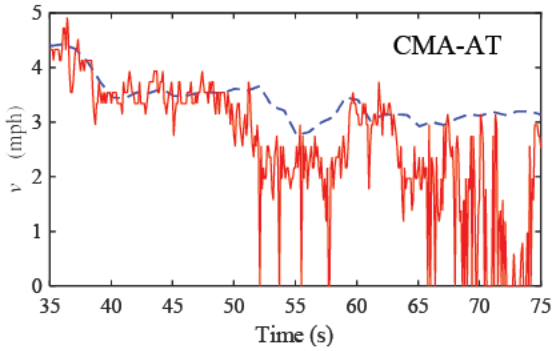

(b)

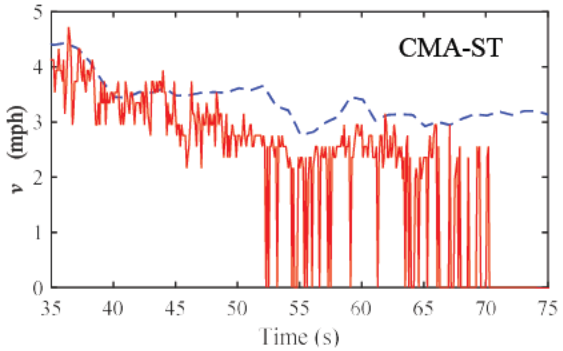

(c)

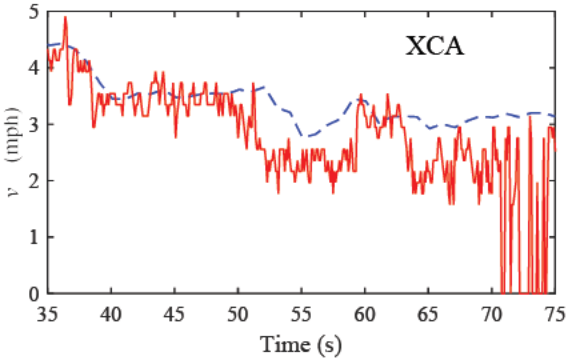

(d)

Figure 6.19 Water measurements. (a) Radar return power. Plot of radar versus GPS speed estimated by algorithm (a) CMA-AT. (b) CMA-ST and (c) XCA

The relationship between surface and measurement error for off-road surfaces.

Figure 6.20(a) to (c) shows the plots of average relative error, maximum relative error and the percentage of the estimate that fell under 5% of GPS speed for the four types of off-road surfaces. There are two points to note from these plots. Firstly, the average relative error is different for each type of surface but tend to rise with the complexity and wetness of the surface. The lowest average-error is given by the grass surface which is relatively flat and has no water potholes while the largest average-error excluding water surface is given by the wet dirt which has many potholes of water. Secondly, we observed no algorithm that performs consistently better than others. Although the XCA algorithm shows better performance than the CMA algorithms on the asphalt road, we found did not found such a trend on the off-road test. This result suggests that the characteristics of the off-road surface may slightly change the shape of Doppler spectra; such changes in shape can reduce the effectiveness of cross-correlation between the Gaussian curve and the spectra.

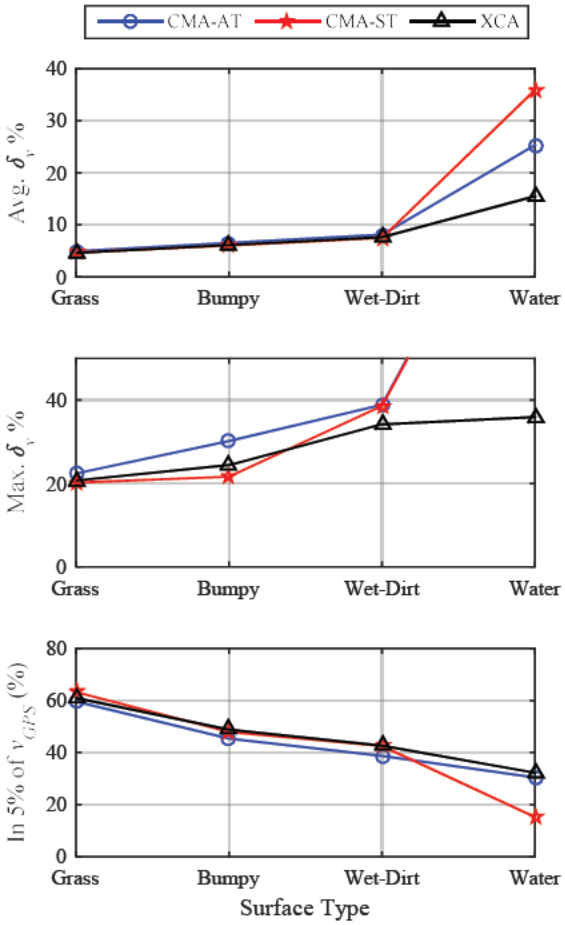

Figure 6.20 The trends of error across four types of off-road surface

6.4. Circle Trajectory

Our primary objective here is to analyse the performance of the SoG radar system in sensing speeds under circular motion. For this purpose, only the XCA algorithm is used to estimate the vehicle speed.

6.4.1. Asphalt Road (Test-scenario 7)

Measurements were performed by driving the test vehicle in a circular track as in test-scenario 7. Two runs were conducted at a speed of v = 5 and v =15 mph. For each run, the vehicle was driven on the test track in a clockwise direction for three complete rotations. The performance of the estimated speed is presented in Figure 6.21 and Figure 6.22. The statistical data from the figures are tabulated in Table 6.5(a) and (b).

As can be seen from Figure 6.21 and Figure 6.22, the radar speed follows the GPS speed closely. The relative error is comparable to the one found in the straight-line trajectory. Furthermore, the standard deviation of the estimate is also small which indicates the accuracy of the SoG system in estimating speed under circular motion.

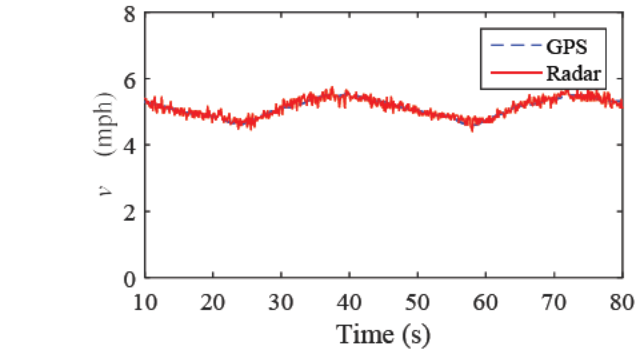

(a)

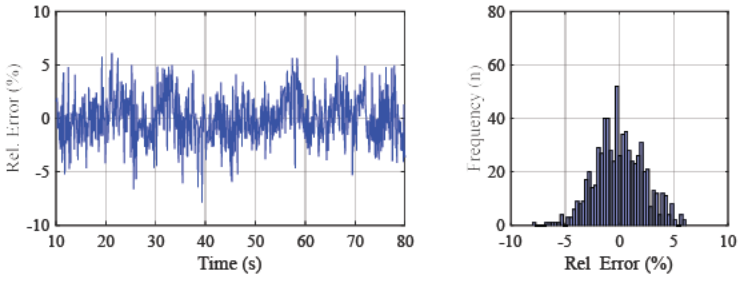

(b)

Figure 6.21 Results for asphalt road (v = 5 mph). (a) Radar vs. GPS. (b) Plot of relative error and histogram

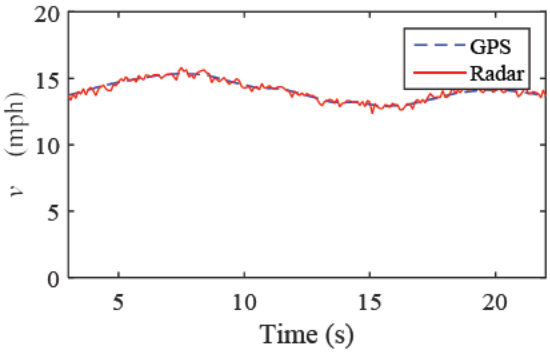

(a)

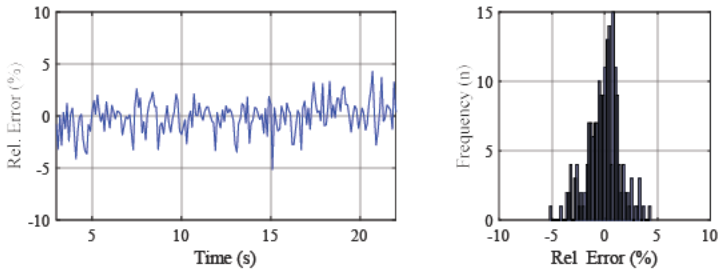

(b)

Figure 6.22 Results for asphalt road (v = 15 mph). (a) Radar vs. GPS. (b) Plot of relative error and histogram

The statistical parameters for both run (v = 5 and 15) mph are presented in Table 6.5(a) – (b)

Table 6.5 The statistical results obtained from Figure 6.22

(a)

	$\bar{v}$ (mph)	σ_v (mph)	Avg. δ_v (%)	Max. δ_v (%)	in 5% of v_{GPS} (%)
GPS (*Reference*)	5.12	0.27			
XCA	5.12	0.28	1.81	7.85	81.31

(b)

	$\bar{v}$ (mph)	σ_v (mph)	Avg. δ_v (%)	Max. δ_v (%)	in 5% of v_{GPS} (%)
GPS (*Reference*)	14.09	0.73			
XCA	14.08	0.76	1.19	5.19	91.61

6.4.2. Off-Roads (Test-scenario 8)

For the off-road circular trajectory test, we do not find any suitable location to perform a complete circular trajectory like the one on the asphalt surface. Therefore, the test vehicle was driven around a curve on a wet dirt surface. Figure 6.23 shows the performance of the estimated speed and Table 6.6 tabulate the statistics from the estimate of speed.

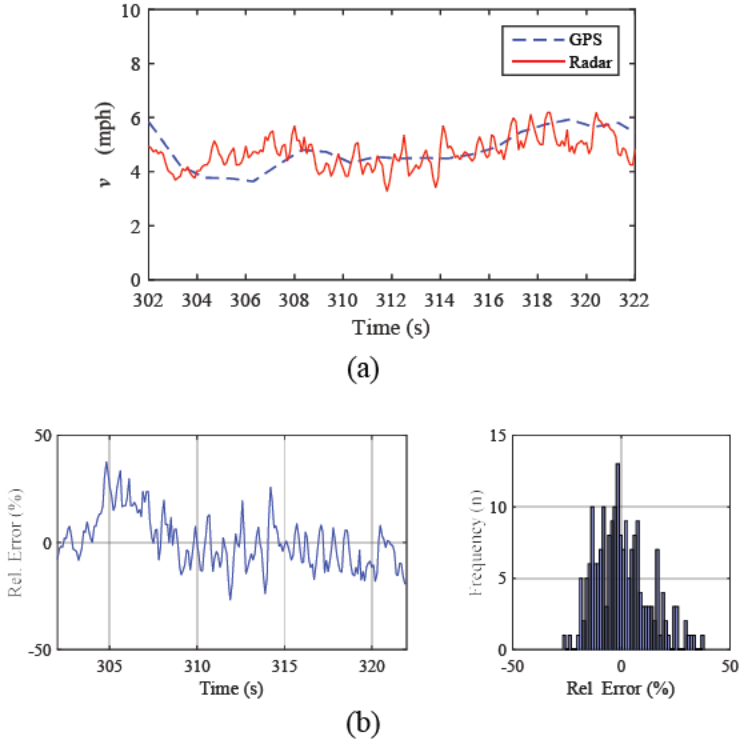

Figure 6.23 Results for Wet dirt. (a) Radar vs. GPS. (b) The measurement of relative error

The statistical parameters obtained in this test is presented in Table 6.6

Table 6.6 The statistical results obtained from Figure 6.23

	$\bar{v}$ (mph)	σ_v (mph)	Avg. δ_v (%)	Max. δ_v (%)	in 5% of v_{GPS} (%)
GPS (*Reference*)	4.75	0.66			
XCA	4.73	0.59	9.77	37.79	21.40

The above results show that cornering on off-road surface produces larger errors than on asphalt road. The average and maximum relative error found here are comparable to the result obtained on the straight-line trajectory moving on a wet dirt surface. This result suggests that the performance is highly influenced by the type of surface and not by the pattern of motions (straight or circular or cornering). Nonetheless, this test shows that the SoG radar system can provide satisfactory results for circular trajectory on the wet dirt surface.

6.5. Vehicle Sideslip Angle Measurement

This section describes the results of vehicle sideslip measurement estimated using the developed SoG system. When a vehicle is driven on a flat surface and in a straight line, the vehicle velocity is parallel to the longitudinal axis of the vehicle. However, when the vehicle turns, the vehicle exhibits a transverse velocity component. A non-zero transverse velocity means that the direction of travel is no longer in the course of the longitudinal axis. The angle between the direction of travel and the orientation of the vehicle is defined as the sideslip angle, Γ . Figure 6.24. depicts the sideslip angle,

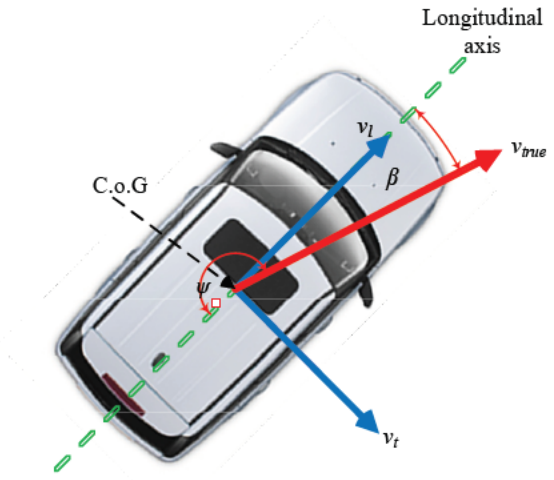

Figure 6.24 The velocity component and the side slip of a vehicle

The sideslip angle, Γ is given by

$$\Gamma = \tan^{-1}\left(\frac{v_l}{v_t}\right) \tag{6.1}$$

where v_l vl and v_t are the longitudinal and lateral speed of the vehicle.

Sideslip angle has a strong association with the stability of a vehicle. Despite its importance, there are no sensors equipped on production cars to measure the sideslip angle. A large amount of research has been dedicated to sideslip measurement sensors. Some researchers have proposed the used of the optical sensor [90], but this method is expensive. Another approach is using algorithms that analyses the speed of vehicle wheels. However, this method is complicated because the dynamic behaviours of the passenger car is non-linear [90].

In work this, we present the first experimental results of sideslip angle estimation using SoG radar. Several sideslip measurements were performed by driving the test vehicle on two circle test-tracks as shown in Figure 6.25. The track is painted in white, and the red line represents the trajectory of the test vehicle during the test. The speed of the vehicle was kept constant while driving in the two circles. The vehicle was driven in a clockwise direction for three full circular motions on the first track and another three complete circular motions on the second track but in an anti-clockwise direction.

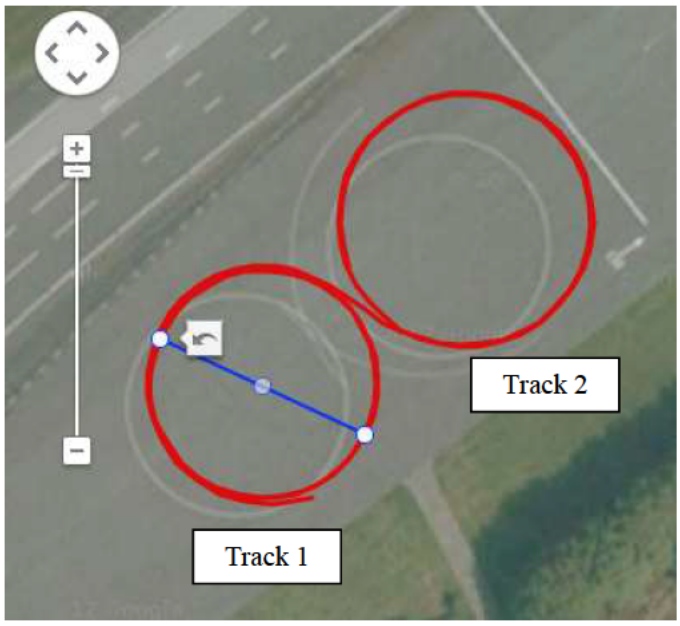

Figure 6.25 The circular track in JLR Gaydon.

Data from test-scenario 7 was used to estimate the sideslip angle of the test vehicle. Figure 6.26(a) to (c) show the estimated v_l, $v_{t,}$ and Γ respectively. The red line indicates the average sideslip (sample averaging size, n = 5). From the plots, the measured side-slip on the counterclockwise direction is about 4°. On the other hand, when the vehicle is moving in the counter-clockwise direction the measured sideslip angle changes to about -4°. The changes from 4° to 4° is due to the vehicle leaving track 1 and entering track 2.

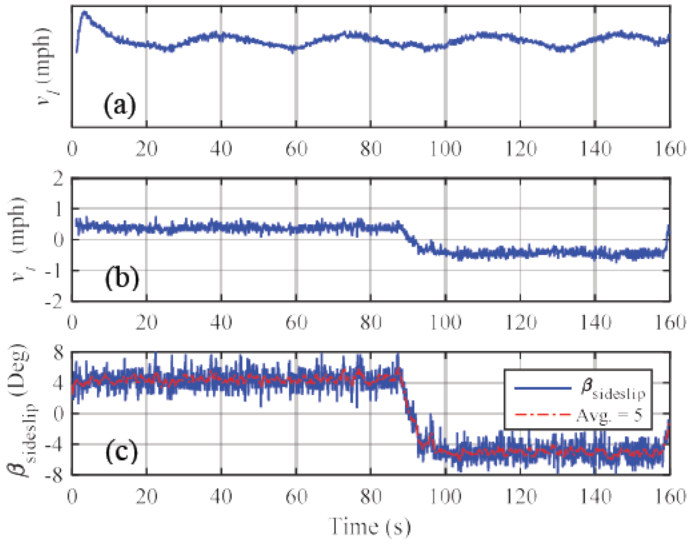

Figure 6.26 The sideslip angle measurement at v = 5 mph (a) Estimated longitudinal speed, v_l (b) Estimated transverse speed v_t and (c) Estimated sideslip angle

Similarly, Figure 6.27(a) – (c) shows the sideslip angle measurement when the vehicle was driven with v = 15 mph on the two circular tracks.

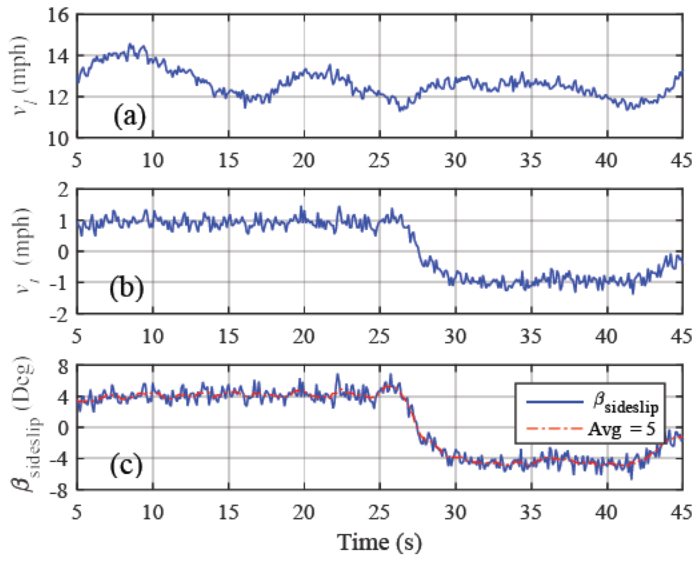

Figure 6.27 The sideslip measurement at v = 15 mph (a) Estimated longitudinal speed, v_l (b) Estimated transverse speed v_t and (c) Estimated sideslip angle

Measurements from both $v = 5$ and $v = 15$ mph show that the variation of the estimated sideslip angle is considerably large, approximately between 0.6° and 1.0° for $v = 5$ and $v = 15$ mph respectively. However, a clear pattern of sideslip can be seen.

The standard set by ISO (ISO 15037-1:2006 Vehicle dynamics test methods) recommended that the maximum error of side-slip measurement must be less than 0.5° [91]. Although the results presented here is less feasible than the standard set by ISO, several methods can be used to reduce the variations in the measurement. These include using smaller antenna beamwidth as in [92] or using signal processing technique such as Kalman Filtering [93]. However, this problem is not focused of this thesis.

6.6. Summary

In this chapter, the performance of the developed SoG radar system was tested under real-world conditions. Evaluation on the three proposed algorithms shows that all algorithms can provide excellent accuracy on an asphalt road with more than 90% of speed measured are within the 3% of relative error. Particularly for asphalt road, the XCA algorithm performed better the CMA methods. However, the measurement accuracies were found less under off-road conditions. Only 30% to 60% of measurement fall under the 5% of relative error. The analysis reveals that the vibrations of vehicle and ground surface characteristics such as water potholes increase the measurement error. In additions, no algorithm performs better than another. Despite the lower accuracy on off-road conditions, the average relative error was found between 4% to 8% which is considered satisfactory for low-speed measurements when operating under off-road conditions. This chapter also demonstrated the capability of the 4-beam SoG radar to estimate vehicle sideslip angle. Analysis of flat asphalt surface shows that

the radar system can provide satisfactory results. However, more research is needed in this area.

Chapter 7. Conclusion and Future Works

7.1. Summary

In this thesis, a vehicle SoG radar system has been developed for accurate vehicle velocity measurement. Several aspects of SOG radar has been investigated which aim to improve the performance of SoG radar during my four years of study. The results of the investigation have been presented in this thesis in the following structured way.

After the introductory project remark in Chapter1, Chapter 2 starts with the general overview of radar. The principles operation of radar including the radar power equation, radar cross section and the principle of Doppler effect are introduced. Next, the theory of SoG radar is described in the second part of Chapter 2. The SoG radar measures speed which is based on the Doppler principle. In specific, the received signal is obtained through the illumination of the road surface. Consequently, the measurement accuracy of SoG radar is affected by few limitations such as finite antenna beamwidth, the vibration of the moving platform and slow signal processing. A survey of literature shows lack of research mitigating the impact of vehicle vibrations to the accuracy of speed estimation. Additionally, literature survey concerning the signal processing shows that frequency-domain based signal processing can be implemented to reduce the effect of noise in the Doppler signal. To summarise, this chapter covers the introduction of radar and the theory of SoG radar necessary for the work in the following chapters of this thesis.

Chapter 3 is dedicated to understanding the impact of the physical configuration of radar parameters on the accuracy of a SOG radar based on a theoretical approach. It is essential to understand the effect of the radar parameters such as antenna beamwidth, viewing angle and

radar height to the accuracy of speed estimation so that best parameters can be selected and used for the experimental setup in Chapter 5. Thus, part of this thesis has been invested in the examination of radar parameters to the accuracy and operation of SoG radar. To complete the task, a mathematical relationship between radar beam geometry and sources of error; pitch and roll motions are developed. Analytical results from the derivation show that the proposed 4-beam radar can provide velocity measurement with higher accuracy than the conventional single-beam radar. Concurrently, several simulations have been performed to develop an understanding of the measurement accuracy and characteristics of the return Doppler signal. The effect of radar parameter to characteristics of radar footprint are also studied. The suitable viewing angle to produce narrow peak Doppler beamwidth and small radar footprint size (< 1 m^2) was determined to be 45° on depression and azimuth angle at the height of 0.5 m from the ground surface. In summary, the work in this chapter provides useful knowledge on the proper selection of radar parameters for SoG operations.

Chapter 4 focused on the speed estimation algorithm of SoG radar. Previous research shows that there is a need to improve the accuracy and reliability of the speed estimation algorithm. Therefore, in this chapter, three new speed estimation methods are proposed. Methods based on CMA methods are called CMA-AT and CMA-ST, and they differ in term of the CMA pre-processing. The method based on cross-correlation is called XCA. For each algorithm, the detail operations are explained. The evaluation of the algorithms is described in the second part of this chapter. The assessment was performed using a reasonably large data sets of 100,000 simulated Doppler signals with different SNR and frequency resolution. The simulation results from this chapter show that the three proposed algorithms can estimate speed with low bias and standard deviation when SNR is high (SNR > 30 dB). In particular, the XCA algorithm gives the lowest bias and standard deviation and can work well at low SNR (SNR = 10 dB). However, the disadvantage of XCA is also identified. First, the antenna pattern must have a

shape of the normal distribution, and the computational complexity is higher than the CMA methods. In summary, these results demonstrate that the proposed algorithms are suitable for real-time and accurate speed estimation.

The development of a SoG radar system is described in Chapter 5. For the first time, SoG radar is realised using four radars with Janus configuration. Despite its complexity, such arrangement allows the measurement of velocity components of the vehicle in 3-dimension. The 4-beam SoG radar is developed using 24 GHz off-the-self radar modules to capture Doppler signal from the ground surface. Furthermore, the radar viewing angles are arranged based on the theory learned in Chapter 3. A GPS receiver was also installed to record the vehicle speed based on GPS data to allow speed accuracy comparison. The performance of the SoG radar is evaluated in practical conditions where the test vehicle can move in straight and circular trajectory at different speeds and moving on many types of surfaces namely asphalt, and off-road surfaces; including grass, dirt and water surface. A total of eight test-scenarios has been considered to develop an understanding of measurement accuracy.

In Chapter 6, the evaluation of the SoG radar system was performed to confirm its performance in actual road condition. The performance of the proposed algorithms is assessed by comparing the speed estimated by each algorithm to the speed derived from GPS-receiver. Several performance metrics including average relative error, maximum relative error, standard deviation and percentage of the estimate that fall within a small percentage of relative error are used to provide the statistical measure of the system performance. The summary of the SoG performance is given in Table 7.1.

The assessments in this chapter proof that the SoG radar system can estimate the vehicle speed accurately, either on low (10 mph) or high speeds (70 mph) in the situation where the ground surface is relatively flat. In these situations, the SoG radar system maintains a stable and

accurate speed measurement. In particular, the XCA algorithm shown to provide better accuracy than the CMA algorithms. This result supports the finding in Chapter 4.

The performance of the SoG radar system is also good on off-road tracks, provided that the ground surface is a not calm water surface. In that case, the proposed algorithms cannot work correctly. Unlike on asphalt road, the XCA algorithms do not produce more accurate results than the CMA methods under off-road conditions. This result was expected since the characteristics of the ground surface do not provide a return Doppler signal that is similar to a normal distribution.

The feasibility of the SoG radar system to estimate vehicle side slip was also shown in this chapter. The SoG radar system is shown to provide good accuracy in measuring side slip estimation where the accuracy of longitudinal and transverse velocity is needed. To summarise, the results given in this chapter shows that the proposed SoG radar can estimate vehicle velocity with good accuracy. The proposed system can provide a sufficiently accurate estimate of velocity for on-road and off-road conditions.

Table 7.1: Comparison of different mean frequency estimation algorithm during a straight trajectory

Surface & speed	CMA-AT	CMA-ST	XCA
On-road	Percentage of measurements that fall under 3% of reference GPS speed (%)		
Asphalt; 10, 20, 30, 40 & 70 mph	93.5, 97.6, 99.0, 98.1, 99.4	92.8, 98.5, 99.1, 99.0, 99.5	94.9, 99.2, 99.9, 100.0, 100.0
Asphalt; 20 to 70 mph (acceleration)	92.7	94.6	98.2
Asphalt: 70 to 20 mph (deceleration)	96.9	98.8	99.4
Concrete; 5 mph	66.67	58.50	75.62
Concrete with elevated bars; 5 mph	30.5	32.0	40.3
Off-road	Percentage of measurements that fall under 5% of reference GPS speed (%)		
Grass; 5 mph	59.6	63.2	60.9
Bumpy dirt; 5 mph	45.3	47.9	48.8
Wet dirt; 5 mph	38.7	42.5	42.6
Water Surface; 5 mph	27.2	25.3	43.1

7.2. Conclusion

This thesis presented contributions towards accurate velocity estimation for vehicles operating on-road and off-road conditions using radar. The limitation of measurement accuracy with the conventional wheel speed sensor method has been identified as the results of:

- Wheel-slip or lock caused by a vehicle moving on wet or slippery roads.
- Change in the dimension of wheels. Wheel-based speedometer system assumes that the dimension of the wheel is fixed whereas, in practice, the wheel size can change.

The above factors reduce the effectiveness of vehicle safety system such as ABS which heavily depends on accurate velocity information. Therefore, a key solution to this problem is to use contactless speed sensor that is independent of the wheel rotation and also can work regardless of weather conditions. The only contactless sensor that can work in all weather conditions is radar.

When this research commenced, there was no commercially available radar for vehicle speed estimation. Existing SoG radar in literature uses a single or dual beam that can estimate speed but cannot estimate the velocity of the vehicle. Furthermore, the speed estimation algorithms are not suitable for practical operation. Therefore, the challenges of accurate velocity estimation using radar are identified, and I have worked several analysis and development aiming to improve the accuracy of velocity measurement of a SoG radar. The points below are the contribution of this thesis

- An analysis of 4-beam radar speed estimation accuracy under the influence of vehicle motions. In this work, the relationship between speed estimation accuracy and dynamic vehicle motions are established. It demonstrates how accurate a 4-beam radar system in measuring speed when moving on uneven surfaces.

- Examination of radar parameters impact on the operations of SoG. Two examinations are presented. The first one examines the effects of radar parameters to the shape and size of the radar footprint. The second one considers the effects of radar parameters on the shape of the Doppler spectrum. Radar parameters such as antenna beam, viewing angle, radar height, and transmitter frequency are considered. Both these examinations provide information on the suitable radar parameters for effective SoG operation.

- The development of new speed estimation methods. Traditional speed estimation methods based on time-domain performs poorly in applications with low SNR and high amplitude noises. This thesis introduces three new speed estimation algorithms based on frequency-domain. Two methods based on centre-of-mass and an approach based on cross-correlation were used to provide a relatively low complexity way minimise the impact of noise using simple signal processing.
- Performance analysis of the developed speed estimation algorithms. The developed algorithms are analysed in terms of their bias and variance and the suitability for real-time speed estimation. The limitation of the algorithms in terms of accuracy was also shown.
- Performance analysis of SoG radar on real measurement based on real-world scenarios. A 4-beam SoG radar system was developed in the University of Birmingham and have been tested under different road surfaces. We demonstrated that the proposed algorithms could be used to estimate vehicle speed for on-road and off-road surfaces with high accuracy. Furthermore, we showed that the 4-beam radar can measure the vehicle velocity components in longitudinal and transverse directions.

7.3. Future Works

For the continuation of this work, the author suggests four works that can be investigated to further explore the potential of the SoG system.

Further investigation of antenna parameters, with the use of 77 GHz and narrower antenna beam

77 GHz is the future frequency band for vehicular radar. The European Conference of Postal and Telecommunications Administrations (CEPT) mandates that 24 GHz radar as an interim solution for automotive radars. The decision is to discontinue the use of 24 GHz frequency band after the year 2013. However, due to delay in the commercialisation of 77 GHz radars. The use of the 24 GHz frequency band is permitted until January 2018 [28]. When this work started in 2014, a suitable radar operating at 77 GHz radar as not readily available in the market. Hence, to cope with the changes in the regulation, it would be recommended to investigate the performance of SoG radar at this frequency band.

The use of Kalman Filtering to smooth the estimated speed by the algorithm. The speed obtained from the estimates of all algorithms has a finite standard deviation. For practical application, smoothing must be performed to reduce the fluctuation. Due to the nature of vehicle speed which can rapidly change in a short period, a simple filter like moving-average may not produce the best estimates of smoothing. Hence, a more complex filter such as Kalman filter can be explored to improve the output of the algorithms.

The parametric approach to frequency estimation. The current approach of using FFT limits the signal resolution when short-time samples are used. Another approach is to use the parametric approach such as auto-regressive (AR) and moving average (MA) to estimate the

spectral distribution of the Doppler signal at higher frequency resolution. This approach may improve the fluctuation error in the estimate of speeds.

More extensive field testing. In this work, the proposed system is evaluated with Doppler signal collected from asphalt and few off-road conditions. Although these surfaces represent the typical conditions for vehicle operation, field test can be extended to surfaces such as gravel, snow, ice, and desert-like surfaces. Hence, the knowledge of reliability and accuracy of the system is further known.

References

[1] M. Tanelli, S. M. Savaresi, and C. Cantoni, "Longitudinal vehicle speed estimation for traction and braking control systems," in *2006 IEEE Conference on Computer Aided Control System Design, 2006 IEEE International Conference on Control Applications, 2006 IEEE International Symposium on Intelligent Control*, 2006, pp. 2790–2795.

[2] C. H. Goddard and D. Price, "Speedometers and Collision Reconstruction," 2017.

[3] M. Imamura, K. Kobayashi, and K. Watanabe, "Real time positioning by fusing differential-GPS and local vehicle sensors," in *SICE 2003 Annual Conference (IEEE Cat. No.03TH8734)*, 2003, vol. 1, pp. 778-781 Vol.1.

[4] K. Kobayashi, K. Watanabe, and F. Munekata, "Accurate navigation via sensor fusion of differential GPS and rate-gyro," in *Conference Proceedings. 10th Anniversary. IMTC/94. Advanced Technologies in I & M. 1994 IEEE Instrumentation and Measurement Technolgy Conference (Cat. No.94CH3424-9)*, 1994, pp. 556–559 vol.2.

[5] A. Day, *Braking of Road Vehicles*. Elsevier Science & Technology Books, 2014.

[6] L. Vlacic, M. Parent, and F. Harashima, *Intelligent Vehicle Technologies: Theory and Applications*. Butterworth-Heinemann, 2001.

[7] M. Shanshan, "A vehicle laser Doppler velocimeter configured with three transmitting beams," in *2013 International Conference on Optoelectronics and Microelectronics (ICOM)*, 2013, pp. 170–173.

[8] C. Xu, L. Daniel, E. Hoare, V. Sizov, and M. Cherniakov, "Comparison of speed over ground estimation using acoustic and radar Doppler sensors," in *European Radar Conference (EuRAD), 2014 11th*, 2014, pp. 189–192.

[9] T. O'Kane and J. V. Ringwood, "Vehicle speed estimation using GPS/RISS (Reduced Inertial Sensor System)," in *Signals and Systems Conference (ISSC 2013), 24th IET Irish*, 2013, pp. 1–6.

[10] K. Imou, M. Ishida, T. Okamoto, Y. Kaizu, A. Sawamura, and N. Sumida, "Ultrasonic Doppler Sensor for Measuring Vehicle Speed in Forward and Reverse Motions Including Low Speed Motions," *Agric. Eng. Int. CIGR J. Sci. Res. Dev.*, vol. III, no. PM 01 007, Oct. 2001.

[11] J. G. McNeff, "The global positioning system," *IEEE Trans. Microw. Theory Tech.*, vol. 50, no. 3, pp. 645–652, Mar. 2002.

[12] R. H. Rasshofer and K. Gresser, "Automotive Radar and Lidar Systems for Next Generation Driver Assistance Functions," *Adv Radio Sci*, vol. 3, pp. 205–209, May 2005.

[13] J. Borenstein and Y. Koren, "Noise rejection for ultrasonic sensors in mobile robot applications," in *, 1992 IEEE International Conference on Robotics and Automation, 1992. Proceedings*, 1992, pp. 1727–1732 vol.2.

[14] W. J. Fleming, "New Automotive Sensors-A Review," *IEEE Sens. J.*, vol. 8, no. 11, pp. 1900–1921, Nov. 2008.

[15] H. H. Meinel, "Commercial applications of millimeterwaves: history, present status, and future trends," *IEEE Trans. Microw. Theory Tech.*, vol. 43, no. 7, pp. 1639–1653, Jul. 1995.

[16] R. Dixit, "Microwave and millimeter-wave applications in automotive electronics," in *Microwave Symposium Digest, 1996., IEEE MTT-S International*, 1996, vol. 1, pp. 31–33 vol.1.

[17] M. E. Russell, C. A. Drubin, A. S. Marinilli, W. G. Woodington, and M. J. D. Checcolo, "Integrated automotive sensors," *IEEE Trans. Microw. Theory Tech.*, vol. 50, no. 3, pp. 674–677, Mar. 2002.

[18] P. D. L. Beasley, “Doppler radar speed sensor,” US5204682 A, 20-Apr-1993.
[19] D. D. Carpenter and R. L. Lanning, “Doppler speed sensing apparatus,” US4414548 A, 08-Nov-1983.
[20] A. R. E and A. C. F, “Doppler radar for land vehicles,” US3859660 A, 07-Jan-1975.
[21] A. Egawa, “Speed detecting device employing a Doppler radar,” US4608568 A, 26-Aug-1986.
[22] P. C. Brownrigg, D. B. Chang, and V. Vali, “True ground speed sensor,” US5100230 A, 31-Mar-1992.
[23] K. M. Strohm, H. L. Bloecher, R. Schneider, and J. Wenger, “Development of future short range radar technology,” in *European Radar Conference, 2005. EURAD 2005.*, 2005, pp. 165–168.
[24] I. Gresham *et al.*, “Ultra-wideband radar sensors for short-range vehicular applications,” *IEEE Trans. Microw. Theory Tech.*, vol. 52, no. 9, pp. 2105–2122, Sep. 2004.
[25] J. Wenger, “Automotive radar - status and perspectives,” in *IEEE Compound Semiconductor Integrated Circuit Symposium, 2005. CSIC ’05.*, 2005, pp. 21–24.
[26] H. H. Meinel, “Evolving automotive radar - From the very beginnings into the future,” in *The 8th European Conference on Antennas and Propagation (EuCAP 2014)*, 2014, pp. 3107–3114.
[27] T. M. Hyltin, T. D. Fuchser, H. B. Tyson, and W. R. Regueiro, “Vehicular Radar Speedometer,” SAE International, Warrendale, PA, SAE Technical Paper 730125, Feb. 1973.
[28] W. Kleinhempel, D. Bergmann, and W. Stammler, “Speed measure of vehicles with on-board Doppler radar,” in *Radar 92. International Conference*, 1992, pp. 284–287.
[29] J. Crestel, M. Guitton, and H. Chuberre, “An enhanced method for the estimation of a Doppler frequency,” in *European Signal Processing Conference, 1996. EUSIPCO 1996. 8th*, 1996, pp. 1–4.
[30] M. I. Skolnik, *Radar Handbook, Third Edition*, 3 edition. New York: McGraw-Hill Education, 2008.
[31] F. Santi, M. Bucciarelli, D. Pastina, and M. Antoniou, “CLEAN technique for passive bistatic and multistatic SAR with GNSS transmitters,” in *2015 IEEE Radar Conference (RadarCon)*, 2015, pp. 1228–1233.
[32] A. V. Borisenkov, O. V. Goriachkin, V. N. Dolgopolov, and B. G. Zhengurov, “Bistatic SAR Based on TV-signal,” in *EUSAR 2014; 10th European Conference on Synthetic Aperture Radar*, 2014, pp. 1–4.
[33] G. S. N. Raju, *Radar Engineering*. I. K. International Pvt Ltd, 2010.
[34] E. F. Knott, J. F. Schaeffer, and M. T. Tulley, *Radar Cross Section*. SciTech Publishing, 2004.
[35] D. K. Barton, *Radar Technology Encyclopedia*. Artech House Publishers, 1997.
[36] S. Kingsley and S. Quegan, *Understanding Radar Systems*. SciTech Publishing, 1999.
[37] M. Schiementz, *Postprocessing Architecture for an Automotive Radar Network*. Cuvillier Verlag, 2005.
[38] I. H. Woodhouse, *Introduction to Microwave Remote Sensing*. CRC Press, 2005.
[39] F. B. Berger, “The Nature of Doppler Velocity Measurement,” *IRE Trans. Aeronaut. Navig. Electron.*, vol. ANE-4, no. 3, pp. 103–112, Sep. 1957.
[40] G. Wang and Q. Weng, *Remote Sensing of Natural Resources*. CRC Press, 2013.
[41] Y. Oh and Y. C. Kay, “Condition for precise measurement of soil surface roughness,” *IEEE Trans. Geosci. Remote Sens.*, vol. 36, no. 2, pp. 691–695, Mar. 1998.
[42] W. G. Rees, *Physical Principles of Remote Sensing*. Cambridge University Press, 2013.

[43] F. T. Ulaby, P. P. Batlivala, and M. C. Dobson, “Microwave Backscatter Dependence on Surface Roughness, Soil Moisture, and Soil Texture: Part I-Bare Soil,” *IEEE Trans. Geosci. Electron.*, vol. 16, no. 4, pp. 286–295, Oct. 1978.
[44] M. W. J. Davidson *et al.*, “Joint statistical properties of RMS height and correlation length derived from multisite 1-m roughness measurements,” *IEEE Trans. Geosci. Remote Sens.*, vol. 41, no. 7, pp. 1651–1658, Jul. 2003.
[45] G. P. Kulemin, *Millimeter-Wave Radar Targets and Clutter*. Boston: Artech House Publishers, 2003.
[46] S. S. Stuchly, A. Thansandote, J. Mladek, and J. S. Townsend, “A Doppler radar velocity meter for agricultural tractors,” *IEEE Trans. Veh. Technol.*, vol. 27, no. 1, pp. 24–30, Feb. 1978.
[47] T. M. Hyltin, T. D. Fuchser, H. B. Tyson, and W. R. Regueiro, “Vehicular Radar Speedometer,” 1973.
[48] F. B. Berger, “The Design of Airborne Doppler Velocity Measuring Systems,” *IRE Trans. Aeronaut. Navig. Electron.*, vol. ANE-4, no. 4, pp. 157–175, Dec. 1957.
[49] N. Kees, M. Weinberger, and J. Detlefsen, “Doppler measurement of lateral and longitudinal velocity for automobiles at millimeter waves,” in *Microwave Symposium Digest, 1993., IEEE MTT-S International*, 1993, pp. 805–808 vol.2.
[50] M. S. Sohel and H. S. Hayre, “Doppler Radar Return from Two-Dimensional Random Rough Surfaces,” *IEEE Trans. Geosci. Electron.*, vol. 10, no. 1, pp. 33–47, Jan. 1972.
[51] R. F. Broderick and H. S. Hayre, “Doppler Return from a Random Rough Surface,” *IEEE Trans. Aerosp. Electron. Syst.*, vol. AES-5, no. 3, pp. 441–449, May 1969.
[52] B. Boashash, “Estimating and interpreting the instantaneous frequency of a signal. II. Algorithms and applications,” *Proc. IEEE*, vol. 80, no. 4, pp. 540–568, Apr. 1992.
[53] P. S. Els, “The applicability of ride comfort standards to off-road vehicles,” *J. Terramechanics*, vol. 42, no. 1, pp. 47–64, Jan. 2005.
[54] J. Kehrbeck and W. Wiesbeck, “Dual channel microwave front-end at 24 GHz for true ground speed measurement,” in *Proceedings of IEEE Vehicular Technology Conference (VTC)*, 1994, pp. 1316–1320 vol.2.
[55] M. Kayton and W. R. Fried, *Avionics Navigation Systems*, 2nd Revised edition edition. New York: John Wiley & Sons, 1997.
[56] J. H. Bryant and S. M. Schultz, “True ground speed sensor,” US4517566 A, 14-May-1985.
[57] B. Boashash, “Estimating and interpreting the instantaneous frequency of a signal. I. Fundamentals,” *Proc. IEEE*, vol. 80, no. 4, pp. 520–538, Apr. 1992.
[58] G.-C. Hsieh and J. C. Hung, “Phase-locked loop techniques. A survey,” *IEEE Trans. Ind. Electron.*, vol. 43, no. 6, pp. 609–615, Dec. 1996.
[59] J. Dybedal, *Doppler Radar Speed Measurement Based On A 24 GHz Radar Sensor*. Institutt for elektronikk og telekommunikasjon, 2013.
[60] M. Corinthios, *Signals, Systems, Transforms, and Digital Signal Processing with MATLAB*. CRC Press, 2009.
[61] M. Weeks, *Digital Signal Processing Using MATLAB & Wavelets*. Jones & Bartlett Learning, 2010.
[62] W. B. Heard, *Rigid Body Mechanics: Mathematics, Physics and Applications*. John Wiley & Sons, 2008.
[63] W. R. Fried, “Principles and Performance Analysis of Doppler Navigation Systems,” *IRE Trans. Aeronaut. Navig. Electron.*, vol. ANE-4, no. 4, pp. 176–196, Dec. 1957.
[64] A. Nekrasov, “Measuring the sea surface wind vector by the Doppler navigation system of flying apparatus having the track-stabilized four-beam antenna,” in *2005 Asia-Pacific Microwave Conference Proceedings*, 2005, vol. 1, pp. 3-4.

[65] K. V. Jorgensen, B. L. Grose, and F. A. Crandall, “Doppler sonar applied to precision underwater navigation,” in *OCEANS ’93. Engineering in Harmony with Ocean. Proceedings*, 1993, pp. II469-II474 vol.2.
[66] F. De Serio and M. Mossa, “Analysis of mean velocity and turbulence measurements with ADCPs,” *Adv. Water Resour.*, vol. 81, pp. 172–185, Jul. 2015.
[67] B. L. Stevens, F. L. Lewis, and E. N. Johnson, *Aircraft Control and Simulation: Dynamics, Controls Design, and Autonomous Systems*, 3rd Revised edition edition. Hoboken, N.J: John Wiley & Sons, 2016.
[68] W. J. Fleming and A. K. Hundiwal, “Radar ground speed sensors,” in *35th IEEE Vehicular Technology Conference, 1985*, 1985, vol. 35, pp. 262–272.
[69] P. Zetterlund, “Measuring traveled distance using doppler radar sensors.,” Linkoping University, 2004.
[70] F. Feng, “Doppler radar speed measurement on board - digital signal processing,” 2013.
[71] P. D. L. Beasley, I. M. Simmons, and A. G. Stove, “High accuracy radar speedometer,” in *IEE Colloquium on Automotive Sensors*, 1992, pp. 8/1-8/5.
[72] Céline Corbrion, Thierry Ditchi, Stephane Holé, Eric Carreel, and Jacques Lewiner, “A broad beam Doppler speed sensor for automotive applications,” *Sens. Rev.*, vol. 21, no. 1, pp. 28–32, Mar. 2001.
[73] W. Kleinhempel, “Automobile Doppler speedometer,” in*, Proceedings of the IEEE-IEE Vehicle Navigation and Information Systems Conference, 1993*, 1993, pp. 509–512.
[74] S. Boll, “Suppression of acoustic noise in speech using spectral subtraction,” *IEEE Trans. Acoust. Speech Signal Process.*, vol. 27, no. 2, pp. 113–120, Apr. 1979.
[75] S. V. Vaseghi, *Advanced Digital Signal Processing and Noise Reduction*. John Wiley & Sons, 2008.
[76] J. Crestel, B. Emile, M. Guitton, and D. Menard, “A Doppler frequency estimate using the instantaneous frequency,” in*, 1997 13th International Conference on Digital Signal Processing Proceedings, 1997. DSP 97*, 1997, vol. 2, pp. 777–780 vol.2.
[77] P. Castagliola and P. E. Maravelakis, “A CUSUM control chart for monitoring the variance when parameters are estimated,” *J. Stat. Plan. Inference*, vol. 141, no. 4, pp. 1463–1478, Apr. 2011.
[78] W. J. Riley, “Algorithms for frequency jump detection,” *Metrologia*, vol. 45, no. 6, p. S154, 2008.
[79] G. Reina, J. Underwood, G. Brooker, and H. Durrant-Whyte, “Radar-based Perception for Autonomous Outdoor Vehicles,” *J Field Robot*, vol. 28, no. 6, pp. 894–913, Nov. 2011.
[80] B. A. Walther and J. L. Moore, “The concepts of bias, precision and accuracy, and their use in testing the performance of species richness estimators, with a literature review of estimator performance,” *Ecography*, vol. 28, no. 6, pp. 815–829, Dec. 2005.
[81] K. K. M. Shariff, E. Hoare, L. Daniel, M. Antoniou, and M. Cherniakov, “Comparison of Adaptive Spectral Estimation for Vehicle Speed Measurement with Radar Sensors,” *Sensors*, vol. 17, no. 4, p. 751, Apr. 2017.
[82] P. Dutta and P. M. Horn, “Low-frequency fluctuations in solids: 1/f noise,” *Rev. Mod. Phys.*, vol. 53, pp. 497–516, Jul. 1981.
[83] T. Nagasaku *et al.*, “77GHz Low-Cost Single-Chip Radar Sensor for Automotive Ground Speed Detection,” in *2008 IEEE Compound Semiconductor Integrated Circuits Symposium*, 2008, pp. 1–4.
[84] A. Daiss and U. Kiencke, “Estimation of vehicle speed fuzzy-estimation in comparison with Kalman-filtering,” in *Proceedings of International Conference on Control Applications*, 1995, pp. 281–284.

[85] M. E. Hines and S. A. Zelubowski, “Conditions affecting the accuracy of speed measurements by low power MM-wave CW Doppler radar,” in *Vehicular Technology Conference, 1992, IEEE 42nd*, 1992, pp. 1046–1050 vol.2.
[86] S. M. Kuo, B. H. Lee, and W. Tian, *Real-Time Digital Signal Processing: Fundamentals, Implementations and Applications*, 3rd Revised edition edition. Chichester, West Sussex: Wiley-Blackwell, 2013.
[87] D. S. Zrnić, “Simulation of Weatherlike Doppler Spectra and Signals,” *J. Appl. Meteorol.*, vol. 14, no. 4, pp. 619–620, Jun. 1975.
[88] M. K. Simon, *Probability Distributions Involving Gaussian Random Variables: A Handbook for Engineers and Scientists*. Springer Science & Business Media, 2007.
[89] I. Zelinka, G. Chen, O. E. Rössler, V. Snasel, and A. Abraham, *Nostradamus 2013: Prediction, Modeling and Analysis of Complex Systems*. Springer Science & Business Media, 2013.
[90] J. Ryu, F. Nardi, and N. Moshchuk, “Vehicle Sideslip Angle Estimation and Experimental Validation,” p. V04AT04A052, Nov. 2013.
[91] “ISO 15037-1:2006 - Road vehicles -- Vehicle dynamics test methods -- Part 1: General conditions for passenger cars.” [Online]. Available: https://www.iso.org/standard/38887.html. [Accessed: 30-Apr-2017].
[92] A. Hantsch and W. Menzel, “A 76 GHz Folded Reflector Antenna for True Ground Speed Measurement,” presented at the Proceedings of the German Microwave Conference, Karlsruhe, Germany.
[93] G. Morrison and D. Cebon, “Sideslip estimation for articulated heavy vehicles at the limits of adhesion,” *Veh. Syst. Dyn.*, vol. 54, no. 11, pp. 1601–1628, Nov. 2016.
[94] M. Matosevic, Z. Salcic, and S. Berber, “A Comparison of Accuracy Using a GPS and a Low-Cost DGPS,” *IEEE Trans. Instrum. Meas.*, vol. 55, no. 5, pp. 1677–1683, Oct. 2006.
[95] T. H. Witte and A. M. Wilson, “Accuracy of non-differential GPS for the determination of speed over ground,” *J. Biomech.*, vol. 37, no. 12, pp. 1891–1898, Dec. 2004.

Appendix A: Description of radar beam in space

This appendix is used to ease the understanding of radar beam geometry in Section 3.1. The direction cosines in Figure 3.1 are given as $d_1 = \cos\alpha\cos\beta$, $d_2 = \sin\beta$ and $d_3 = -\sin\alpha\cos\beta$. These quantities are geometrically shown here for better clarification of the relationships.

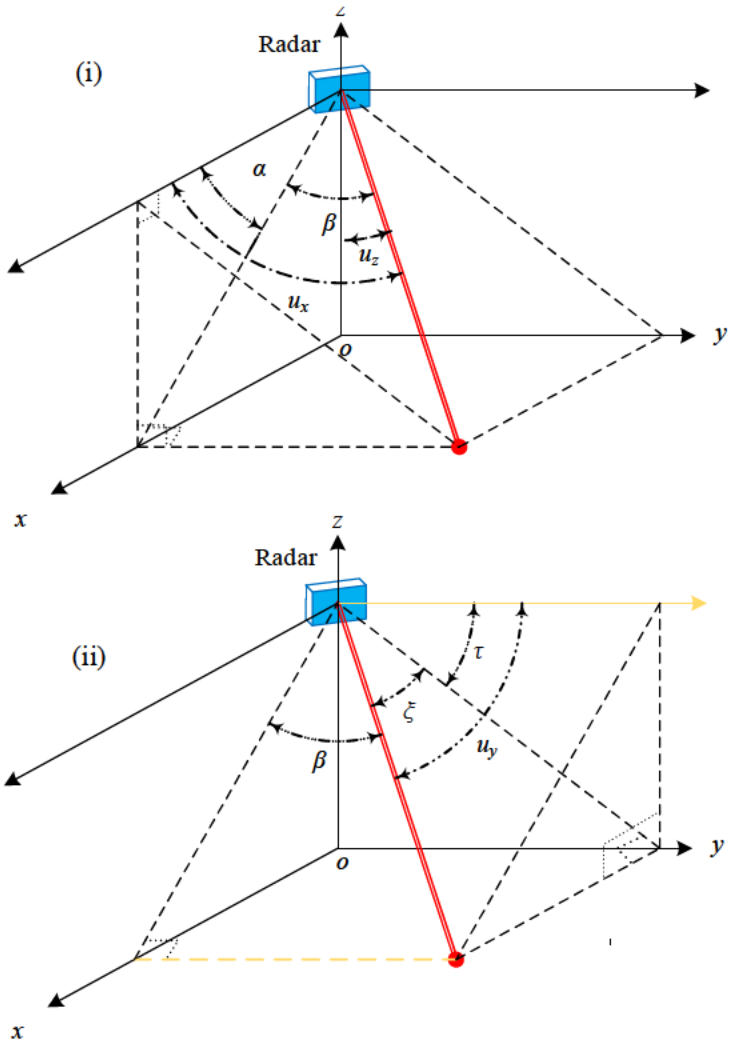

Figure A

From Figure A(i), it can be shown that $\cos u_x = \cos\alpha\cos\beta$ and $\cos u_z = -\sin\alpha\cos\beta$. And, from Figure A(ii), it can be shown that $\cos u_y = \cos\xi\cos\tau = \sin\beta$.

Appendix B: SoG radar System Characteristics During No Motion

Introduction

This test aims to verify the experimental SoG radar system from any unwanted noise. Therefore, any uncertainty in the system can be known earlier and hence removed. Otherwise, it may cause unexplainable experimental results.

System Characteristics During No Motion

We examined the frequency spectrum of the Nyquist sampling bandwidth to make sure there is no high amplitude noise due to the data acquisition system and test vehicle. Doppler measurements were made when the vehicle was stationary. Data were collected during both engines off and on. The Doppler signal outputs were sampled at f_s = 25 kHz. Figure 5.15(a) and (b) show the Doppler measurements of four radars during the engine off and on respectively. The integration time for the spectra is 1 s.

During engine off, the noise floor for all radar spectrum is approximate to -60 dB. However, when the engine is turned on, the noise floor on Radar 1 and Radar 4 increases to about -90 dB and -80 dB respectively. An explanation of this is because of the 'rapid sleep wakeup' function of the radar. However, this effect is not detected on Radar 2 and Radar 3. Both of their noise floors remain at -60 dB. This is likely that they experienced insignificant engine vibration and hence the radar is not waking up. In summary, all radar shows uncorrelated noise with time. However, there were random peak noises below 50 Hz during both states of the engine off and on. In signal processing, this 50 Hz peak noise is suppressed using HPF in MATLAB. Some noise spikes existed across the spectrum, but the amplitude is insignificant

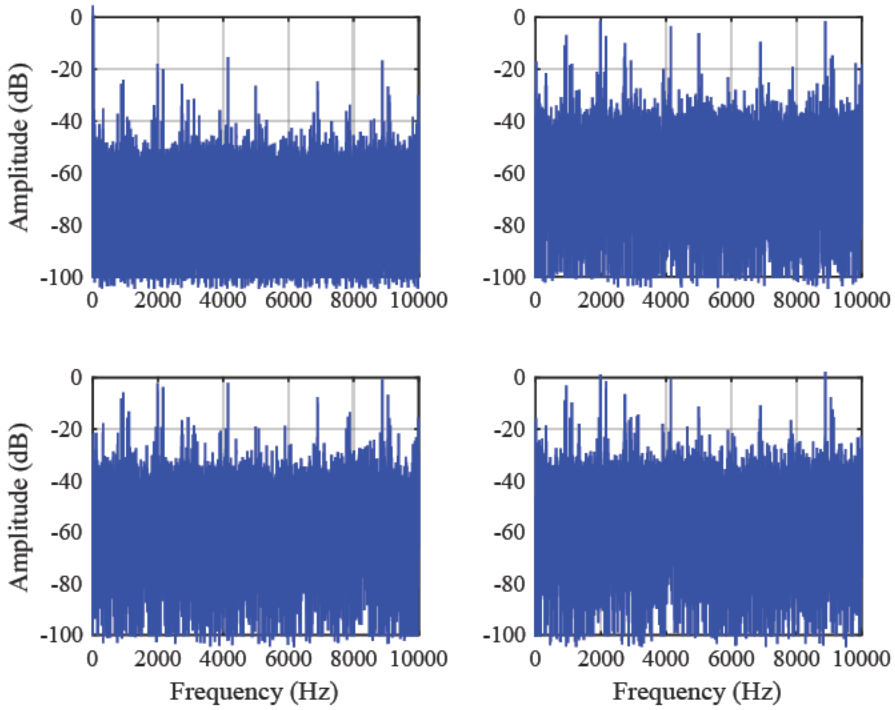

(i)

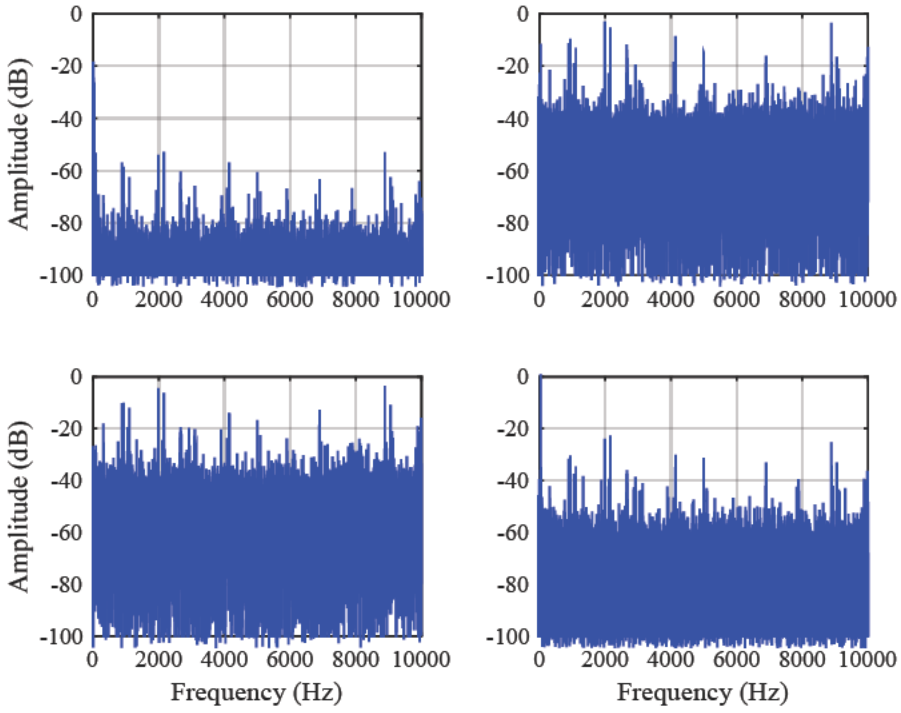

(ii)

Figure B The observed spectrum for the static test vehicle (a) Engine off (b) Engine ON

Appendix C: Comparison between low-cost GPS and differential GPS

The GPS in this work functions as a speed reference. In the experimental design stage, we proposed to use a Differential GPS (DPGS) system which is known to have superior accuracy in both measurements of speed and location compared to low-cost GPS [94], [95]. However, because of technical issues, the Differential GPS (DPGS) system was not integrated into the experimental data collection setup. Instead, we used an off-the-shelf, low-cost GPS receiver.

A literature review regarding the comparison between these two devices in terms of accuracy in measuring vehicle speed on the actual road is limited. Because of this reason, we have performed a simple experiment to compare their accuracy performance.

The DGPS system used in this experiment is Topcon NET-G5, and the antenna model number used is CR-G5-C. This system produces GPS NMEA strings at speed up to 100 Hz. This system can records GPS data without the need of a computer. Figure C.1 shows the image of the setup. Both GPS antenna was mounted on the front bonnet of the test vehicle to provide the view of the sky always.

The test was performed by driving the test vehicle at variable speed along the ring road of the University of Birmingham. Both GPS records data at a rate of 1 Hz. A total of 100 seconds long of speed data was recorded. Note that, due to the limitation of the test setup, the speed recorded by the low-cost GPS was slightly lagging the speed measured using DPGS. This lag is minimised by interpolating the recorded speed to a smaller interval of 0.1 seconds and finding the lag between the two measurements via cross-correlation. Figure C.2 shows the comparison of speed obtained using both GPS. As can be seen, the curve of low-cost GPS follows the curve of DPGS very closely with the exception at some points. From the plots, the measured average and maximum absolute error are 0.1 and 1 mph respectively. From this

experiment, it can be said that the low-cost GPS can provide enough accuracy as a reference system in this work.

Figure C.1 The installation of antennas for low-cost GPS and DPGS system on the test vehicle

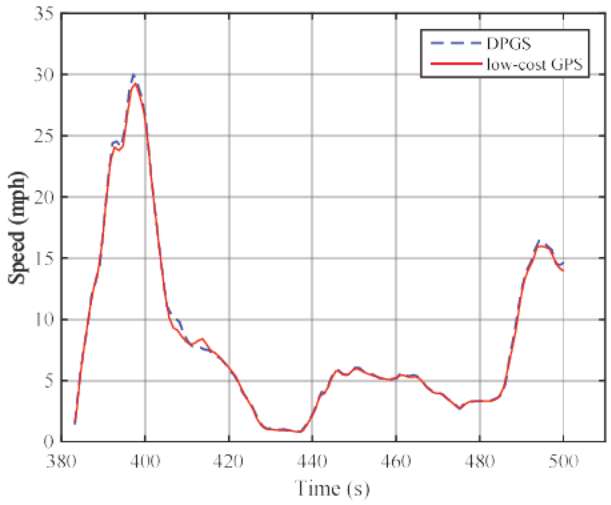

Figure C.2 Comparison of speed obtained using low-cost GPS and DGPS systems.

Appendix D: Specification of Radar

RFbeam Microwave GmbH

K-MC1 RADAR TRANSCEIVER Datasheet

Features

- 24 GHz short range transceiver
- 180 MHz sweep FM input
- High sensitivity, with integrated RF/IF amplifier
- Dual 30 patch antenna
- Buffered I/Q IF outputs
- Additional DC IF outputs
- Beam aperture 25°/12°
- RSW Rapid Sleep Wakeup
- Slim 6mm thickness construction

Applications

- Traffic supervision
- Object speed measurement systems
- Ranging and distance detection
- Industrial sensors

Description

K-MC1 is a 60 patch doppler module with an asymmetrical narrow beam for long distance sensors. It is ideally suited for traffic supervision.
This module includes a RF low noise amplifier and two 47dB IF preamplifiers for both I and Q channels. The need for external analogue electronics will be significantly reduced by this feature. For special signal condition applications, an additional buffered Mixer DC output is provided. This greatly improves flexibility in FSK ranging applications.

The unique "RSW" *R*apid *S*leep *W*akeup function with <4us wakeup time makes this module ideal for battery operated equipment. Typical duty cycle in RWS mode may be < 1% with full movement detection capability by sampling the IF signals.
An extremely slim construction with only 6mm depth gives you maximum flexibility in your equipment design.
Powerful starter kits with signal conditioning and visualization are available.

Blockdiagram

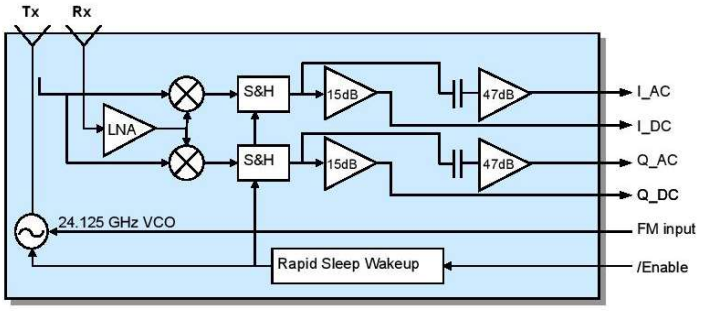

Fig. 1: K-MC1 Blockdiagram

Characteristics

Parameter	Conditions / Notes	Symbol	Min	Typ	Max	Unit
Operating conditions						
Supply voltage		V_{cc}	4.75	5.0	5.25	V
Supply current	Module enabled (Pin 1 = V_{IL})	I_{cc}		70	100	mA
	Module RSW mode (Pin 1 = V_{IH})			7	10	mA
VCO input voltage		U_{vco}	1		10	V
VCO pin resistance	Internal pulldown 10k	R_{vco}		10k		Ω
Operating temperature		T_{op}	-20		+80	°C
Storage temperature		T_{st}	-20		+80	°C
Power down/Enable						
Module power down	Input tied high with pullup 10k	V_{IH}	V_{cc}-0.7		V_{cc}+ 0.3	V
Module enable		V_{IL}	-0.2		2	V
Minimum enable time	Sample&Hold capacitor charged	t_{on}	4			µs
Maximum hold time	S&H error <10%	t_{off}			2	ms
Hold Step	Charge injection visible at DC output	V_{step}		6		mV
Transmitter						
Transmitter frequency	U_{VCO}= 5V, T_{amb}=-20°C .. +60°C	f_{TX}	24.050	24.150	24.250	GHz
Frequency drift vs temp.	V_{cc}=5.0V, -20°C .. +60°C Note 1	Δf_{TX}		-1.0		MHz/°C
Frequency tuning range		Δf_{vco}		180		MHz
VCO sensitivity		S_{vco}		18		MHz/V
VCO Modulation Bandwidth	Δf=20MHz	B_{VCO}		3		MHz
Output power	EIRP	P_{TX}	+16	+18	+20	dBm
Output power deviation	Full VCO tuning range	ΔP_{TX}		+/- 1		dBm
Spurious emission	According to ETSI 300 440	P_{spur}			-30	dBm
Receiver						
Antenna gain	F_{TX}=24.125GHz Note 2	G_{Ant}		18.5		dBi
LNA gain	F_{RX}=24.125GHz	G_{LNA}		16		dB
Mixer Conversion loss	f_{IF} =500Hz	D_{mixer}		-6		dB
Receiver sensitivity	f_{IF} =500Hz, B=1kHz, S/N=6dB	P_{RX}		-123		dBm
Overall sensitivity	f_{IF} =500Hz, B=1kHz, S/N=6dB	D_{system}		-141		dBc
IF output						
IF output impedance	_AC outputs	R_{IF_AC}		100		Ω
	_DC outputs	R_{IF_DC}		100		Ω
IF Amplifier gain	_AC outputs	G_{IF_AC}		47		dB
	_DC outputs	G_{IF_DC}		15		dB
I/Q amplitude balance	f_{IF} =500Hz, U_{IF}=100mV_{pp} (_AC outputs)	ΔU_{IF}		3		dB
I/Q phase shift	f_{IF} =500Hz, U_{IF}=100mV_{pp} (_AC outputs)	φ	80	90	100	°
IF frequency range	-3dB Bandwidth (_AC outputs)	f_{IF_AC}	40		15k	Hz
	-3dB Bandwidth (_DC outputs)	f_{IF_DC}	0		500	kHz
Spurious signals	Internal regulator @100kHz at DC output	V_{so}			0.1	mVrms

Parameter	Conditions / Notes	Symbol	Min	Typ	Max	Unit
IF output (continued)						
IF noise voltage	f_{IF} =500Hz	$U_{IFnoise}$		22		µV/√Hz
	f_{IF} =500Hz	$U_{IFnoise}$		-93		dBV/Hz
IF output offset voltage	V_{cc} = 5V, _AC outputs	U_{os_AC}	2.0	2.5	3.0	V
	no object in range,VCO pin open,_DC outputs	U_{os_DC}	0.5	2.5	4.5	V
Supply rejection	Rejection supply pins to _AC outputs, 500Hz	D_{supply}		-24		dB
Antenna						
Horizontal -3dB beamwidth	E-Plane	W_ϕ		12		°
Vertical -3dB beamwidth	H-Plane	W_θ		25		°
Horiz. sidelobe suppression		D_ϕ		-20		dB
Vert. sidelobe suppression		D_θ		-18		dB
Body						
Outline Dimensions	connector left unconnected			65*65*6		mm^3
Weight				50		g
Connector	Module side: AMP X-338069-8			8		pins

Note 1 Transmit frequency stays within 24.050 to 24.250GHz over the specified temperature range when the VCO pin is left open

Note 2 Theoretical value, given by Design

Antenna System Diagram

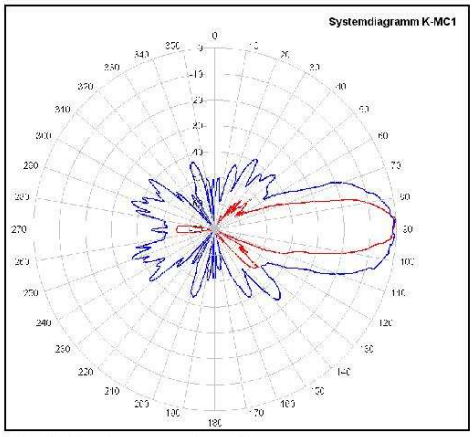

This diagram shows module sensitivity in both azimuth and elevation directions. It incorporates therefore the transmitter and receiver antenna characteristics.

Fig. 2: Anntenna system diagram

QUECTEL®

Build a Smarter World

Quectel L80

Compact GPS Module Integrated with Patch Antenna

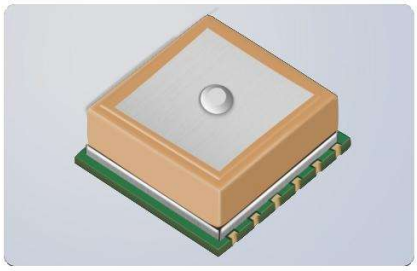

L80 is an ultra compact GPS POT (Patch on Top) module with an embedded 15.0mm × 15.0mm × 4.0mm patch antenna. This space-saving design makes L80 the perfect module for the miniature devices. Adopted by LCC package and integrated with patch antenna, L80 has exceptional performance both in acquisition and tracking.

Combining advanced AGPS called EASY™ (Embedded Assist System) and proven AlwaysLocate™ technology, L80 achieves the highest performance and fully meets the industrial standard. EASY™ technology ensures L80 can calculate and predict orbits automatically using the ephemeris data (up to 3 days) stored in internal RAM memory, so L80 can fix position quickly even at indoor signal levels with low power consumption. With AlwaysLocate™ technology, L80 can adaptively adjust the on/off time to achieve balance between positioning accuracy and power consumption according to the environmental and motion conditions.

L80 supports automatic antenna switching function. It can achieve the switching between internal patch antenna and external active antenna. Moreover, it keeps positioning during the switching process.

The Fitness Low Power (FLP) feature provides low power GPS solution for fitness application. It is an optimized solution for wearable, fitness and tracking devices and only costs about 50% power consumption of normal mode.

With its compact design, high precision and sensitivity, L80 is perfectly suitable for a broad range of M2M applications such as portable device, automotive, personal tracking, security and industrial PDA, especially suitable for special applications, like GPS mouse and OBD.

Key Benefits

- Embedded patch antenna: 15.0mm × 15.0mm × 4.0mm
- Extremely compact size: 16.0mm × 16.0mm × 6.45mm
- Automatic antenna switching function
- Support short circuit protection and antenna detection
- Built-in LNA for better sensitivity
- EASY™, an advanced AGPS technology without external memory
- Ultra low power consumption in tracking mode, 20mA
- AlwaysLocate™, an intelligent controller of periodic mode
- LOCUS, an embedded logger solution with no need of host and external flash
- High sensitivity, -165dBm @Tracking, -148dBm @Acquisition
- 66 acquisition channels, 22 tracking channels
- FLP mode, about 50% power consumption of normal mode
- Balloon mode, for high altitude up to 80km
- Support DGPS, SBAS (WAAS/EGNOS/MSAS/GAGAN)
- Anti-Jamming, Multi-tone Active Interference Canceller
- PPS VS. NMEA can be used for time service
- Support SDK command developed by Quectel

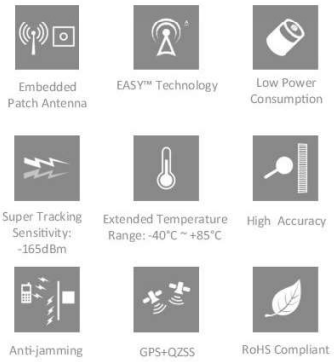

EMAIL US: info@quectel.com

VISIT US: www.quectel.com

Quectel L80

Compact GPS Module Integrated with Patch Antenna

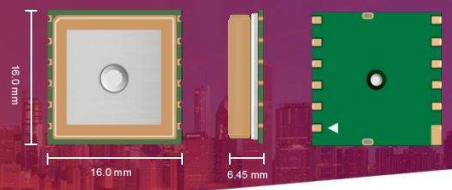

GPS Features

L1 Band Receiver (1575.42MHz):

Channel: 22 (Tracking)/ 66 (Acquisition)

C/A Code

SBAS: WAAS, EGNOS, MSAS, GAGAN

Horizontal Position Accuracy:

Autonomous: <2.5m CEP

Velocity Accuracy:

Without Aid: <0.1m/s

Acceleration Accuracy:

Without Aid: <0.1m/s²

Timing Accuracy:

1PPS Out: 10ns

Reacquisition Time: <1s

TTFF @-130dBm with EASY™:

Cold Start: <15s

Warm Start: <5s

Hot Start: <1s

TTFF @-130dBm without EASY™:

Cold Start: <35s

Warm Start: <30s

Hot Start: <1s

Sensitivity:

Acquisition: -148dBm

Tracking: -165dBm

Reacquisition: -160dBm

Dynamic Performance:

Maximum Altitude: Max. 18000m

Maximum Velocity: Max. 515m/s

Maximum Acceleration: 4G

Interfaces

Serial Interface:

UART: Adjustable 4800bps~115200bps

Default: 9600bps

Update Rate:

1Hz (Default), up to 10Hz

I/O Voltage:

2.7V~2.9V

Protocols:

NMEA 0183

PMTK

General Features

Temperature Range:

-40°C ~ +85°C

Dimensions:

16.0mm × 16.0mm × 6.45mm

Weight:

Approx. 6.0g

Power Management

Power Supply:

3.0V~4.3V

Power Acquisition:

25mA

Power Tracking:

20mA

Power Saving:

3mA @AlwaysLocate™ (Note1)

7uA @Backup Mode

1mA @Standby Mode

11mA @FLP Mode

Periodic Mode

Note1: Measured in GPS System under Outdoor Static Mode.

HQ address: 7th Floor, Hongye Building, No.1801 Hongmei Road, Xuhui District, Shanghai 200233, China
Tel: +86 21 51086236 Fax: +86 21 54453668 Email: info@quectel.com

Appendix F: Explanation of Software

This appendix is intended to give the detail processing steps for estimating vehicle speed from the Doppler signal. The processing is implemented using MATLAB software. The following points are the provided codes in this appendix:

I. Main processing
II. CMA-AT
III. CMA-ST
IV. XCA
V. Statistical processing

Main processing

This main processing code functions to estimate vehicle speed for a given Doppler signal. This code is the implementation of signal processing steps explained in Section 5.3. The following points are the processing performed in this code

- Combining in-phase and quadrature Doppler signals.
- Windowing of Doppler signal
- DC removal and I/Q signal balancing
- Fourier transformation
- Mean frequency estimation via SoG algorithms
- Computation of velocity from the estimated Doppler shift.

The main processing software also provides several statistical measurements including mean average error, maximum error, and percentage of speed that fall under the band of limits.

```
%%%%%%%%%%%%%%%%%%%%%%%%%%%%%%%%%%%%%%%%%%%%%%%%%%%%%%%%%%%%%%%%%%%%%%%%%%%%%%%
% MAIN PROCESSING
% 1. Read radar I/Q, Sampling rate and GPS data
% 2. Quadrature data generation
% 3. Data portioning
% 4. Main loop. incl. Data conditioning, Fourier transform, fd estimation
% and store in a matrix
% 5. Speed-vector computation
% 6. Radar-GPS speed Performance measurement
%%%%%%%%%%%%%%%%%%%%%%%%%%%%%%%%%%%%%%%%%%%%%%%%%%%%%%%%%%%%%%%%%%%%%%%%%%%%%%%

close all; clear all; clc

%% RADAR CONSTANTS
beta = 45; alpha = 45;
txfreq = 24.125e9;
lamda = 3e8/txfreq;

%% READ RADAR AND GPS DATA
daqfile = 'test15_daq';
GPSfile = 'test15_gps';
[data, tData, ~, ~, info] = daqread([daqfile '.daq']);
phy_sRate0 = info.ObjInfo.SampleRate;
phy_srate = phy_sRate0;

frameRate = 0.1;
srate = ceil(phy_srate*frameRate);

%% GENERATE COMPLEX DATA
radardata = [data(:,1)+j*data(:,2) data(:,5)+j*data(:,6) data(:,9)+j*data(:,10)...
    data(:,13)+j*data(:,14)];
clear data
radardatalength = size(radardata,1);

%% FILTRERING  - LPF
fstop = 10; fpass = 400; astop = 65; apass = 0.5; filterfs = 15e3;
LPF =   designfilt('highpassfir','StopbandFrequency',fstop, ...
        'PassbandFrequency',fpass,'StopbandAttenuation',astop, ...
        'PassbandRipple',apass,'SampleRate',filterfs,'DesignMethod','equiripple');
% Illustrate the filter
% fvtool(d) % show designed filter response

%% PROCESSING DEFINITIONS
fftlength = srate;
rdrdata_length = floor(radardatalength/srate);
vlongconst = lamda/(2*cosd(beta)*cosd(alpha));       % the constants for Sensors
forward speed (FS) estimation
vtransconst = lamda/(2*cosd(alpha)*sind(beta));      % the constants for Sensors
transverse speed (TS) estimation
knots2m = 0.51444;  % knots to m/s
%% ALGORITHMS CONSTANTS
smoothfactor = 10;              %XCA
theta_bw = [25 25 25 25] ;      %XCA
%theta_bw = [30 30 30 30] ;

th1 = [10 10 10 4];    % (u + 3sigma)
th2 = [10 10 10 10 10];

%% MAIN LOOP
h = waitbar(0,'Please wait...');
for radar = 1:4
```

```
    for t = 1: rdrdata_length

        step_percentage = ((radar-1)*rdrdata_length+t)/4/rdrdata_length;
        waitbar(step_percentage,h,sprintf('completed%3.0f%%',step_percentage*100));

        % Segmenting the data
        block = (t-1)*srate+1:t*srate;
        IQblock = radardata(block,radar);

        % Filter
        IQblock = filter(LPF,IQblock);

        % Remove the DC from Sensor's data
        IQblock = detrend(IQblock,'constant');

        % Balance the I/Q gain
        Gain = var(real(IQblock))/var(imag(IQblock));
        IQblock = real(IQblock) + j*imag(IQblock)*sqrt(Gain);

        %Fourier Transformation
        cmplxfft = fftshift(fft(IQblock,fftlength));
        absfft = abs(cmplxfft);

        % [view spectral data] OPTIONAL
        if radar == 5

                  if  t>400 && t<800

                      plot(-srate/2:srate/2-1,absfft);
                      title(sprintf('Spectrum 10 mph',radar));ylim([0 60]);
                    %xlim([-200 200]);
                      xlabel('Frequency (Hz)');ylabel('Magnitude');grid on;pause;
                  end
        end

        % Estimatte mean frequency from fourier data
        % CMA-AT
        arrayfd(t,radar) = CMA_AT(absfft,radar,th1(radar),th2);

        % CALL CMA-ST
        %DopplerShift(t,Sensor) = CMA_ST(AbsFFT,Sensor,SamplingRate,Phy_sRate);

        % CALL XCA
        %DopplerShift(t,Sensor) =
XCA(AbsFFT,Sensor,RadarBeamwidth(Sensor),Lamda,SamplingRate,SmoothFactor,AzimuthAng
le,DepressAngle,PM_threshold);

    end
end
close(h);

%% COMPUTE SPEED VECTOR
arrayvlong = (arrayfd - floor(srate/2)-1)*phy_srate/srate*vlongconst;
arrayvtrans = (arrayfd - floor(srate/2)-1)*phy_srate/srate*vtransconst;

% compute longitudinal and transverse speed
vlong = (((arrayvlong(:,1) + arrayvlong(:,4))-(arrayvlong(:,2) +
arrayvlong(:,3)))/4)';
vtrans = ((arrayvtrans(:,1) + arrayvtrans(:,2))-(arrayvtrans(:,3) +
arrayvtrans(:,4)))/4;

%% READ GPS SPEED
```

```
k = fopen([GPSfile '.txt']);
vgps = textscan(k,'%u16 %u8 %u8 %u8 %u8 %f %s %f %s %f %s %f %s %f %f %f %f %s
%s');
vgps = vgps{14}*knots2m;  % Speed in m/s.
tgps = (1:length(vgps));

%% INTERPOLATE vRADAR DATA AND MINIMISE LAG BETWEEN vGPS and vRADAR

xq = (1:frameRate:tgps(end))';
vgps = interp1(tgps,vgps,xq);
tgps = 1:rdrdata_length(end);
trdr = 1:rdrdata_length(end);
vgps = Fixlag(vgps,vlong);
arrayvlong = arrayvlong';

%% SYNCHRONISE DATA LENGTH
sets =
{vgps,tgps,trdr,vlong,arrayvlong(1,:),arrayvlong(2,:),arrayvlong(3,:),arrayvlong(4,
:)};
array0 = cellfun(@(x)size(x,2), sets);
% Get all array length
minLength = min(array0);
% Find the shortest array
vect0 = cell2mat(cellfun(@(x)x(1:minLength), sets, 'uniformoutput', false));
% Amputate the longer array than min
for j = 1:8
    k = (j-1)*minLength+1:j*minLength;
    l(:,j) = vect0(k);
end

vgps = l(:,1); tgps = l(:,2);
trdr = l(:,3);
vlong = l(:,4);
vSen1 = l(:,5); vSen2 = l(:,6); vSen3 = l(:,7); vSen4 = l(:,8);
tgps = tgps*(srate/phy_srate);
trdr = trdr*(srate/phy_srate);

%% [PLOTTING RESULTS]

% Figure 1 - vRADAR vs vGPS PLOT (whole)
f = figure(1);
movegui(f,'southwest'); plot(tgps,vgps,'k',trdr,vlong,'b');
title('Forward Speed (Whole Data)'); legend('GPS','24 GHz Radar');
xlabel('Time (s)'); ylabel('Speed (m/s)');
ylim([0 20]); grid on;

% Make plots within the interested region
iregion = 30:120; % in seconds

% Figure 2 - vRADAR vs vGPS PLOT (Interested region)
f = figure(2); movegui(f,'northwest')
plot(tgps,vgps,'k',trdr,vlong,'b');
title('Forward Speed (Statistic Area): Radar vs GPS');
legend('GPS','24 GHz Radar');
xlabel('Time (s)');ylabel('Speed (m/s)');grid on;
xlim([iregion(1) iregion(end)]); ylim([0 20]);

% Figure 3 - vRADAR vs vGPS PLOT (interested region - indiv. radar plot)
f = figure(3);
movegui(f,'southeast')
plot(tgps,vgps,'k',trdr,vSen1,trdr,-1*vSen2,trdr,-1*vSen3,trdr,vSen4);
title('Forward Speed: Individual Sensor vs GPS');
legend('GPS','Radar 1','Radar 2','Radar 3','Radar 4');xlabel('Time
(s)');ylabel('Speed (m/s)');grid on;
```

```
xlim([iregion(1) iregion(end)]); ylim([0 20]);

%% SCALE vRADAR to vGPS
df = iregion*10;
scale_vrdr1 = fminunc(@(c) SqrError(c,tgps(df), vgps(df), trdr(df),
vSen1(df)),[1;1])
scale_vrdr2 = fminunc(@(c) SqrError(c,tgps(df), vgps(df), trdr(df),
vSen2(df)),[1;1])
scale_vrdr3 = fminunc(@(c) SqrError(c,tgps(df), vgps(df), trdr(df),
vSen3(df)),[1;1])
scale_vrdr4 = fminunc(@(c) SqrError(c,tgps(df), vgps(df), trdr(df),
vSen4(df)),[1;1])
allscale = [scale_vrdr1(2) scale_vrdr2(2) scale_vrdr3(2) scale_vrdr4(2)]
scale_vfwd = fminunc(@(c) SqrError(c,tgps(df), vgps(df), trdr(df),
vlong(df)),[1;1])



%% MEASUREMENT OF RELATIVE ERROR
%analyselag = 0;        %skip
analyselag = 1;         %analyse the lag
delta = 0;
[vgps_mean,vgps_sigma,vrdr_mean,vrdr_sigma,avgrdr_e,maxrdr_e,stdrdr_er...
    ,vcal,optimalscale,histdata,RMSE,errabs] = Error_est...
    (iregion,vlong,vgps,delta,frameRate,analyselag,srate,phy_srate);

f = figure(4);
movegui(f,'northeast')
plot(tgps,vgps,'k',trdr + analyselag ,vcal,'b');
title('Forward Speed: Radar vs GPS');
legend('GPS','24 GHz Radar');xlabel('Time (s)');ylabel('Speed (m/s)');grid on;
xlim([iregion(1) iregion(end)]);

% Print results of relative error
% note for not to forget
% \t\t\t - 3 tabs
% \n - new line
% %3.2f formatting string for input
sprintf('\t\t\t\t  Mean\t\t  Std Dev\nGPS:\t\t\t\t%3.2fm/s\t\t%3.2f\n24 GHZ
Radar:\t\t\t%3.2fm/s\t\t%3.2f',...
vgps_mean,vgps_sigma,vrdr_mean,vrdr_sigma)
sprintf('\t\t\t\t Avg Rel Error   Max Rel Error   Mean Std Error\n24 GHz
Radar:\t\t\t%3.2f%%\t\t\t%3.2f%%\t\t\t%3.2f%%',...
avgrdr_e,maxrdr_e,stdrdr_er)

%% [PLOTS OF DISTRIBUTION OF ERROR]
figure(5)
histogram(histdata,50)
grid on; ylim([0 150]);
xlabel('Relative Error (%)'); ylabel('No. of Data');
xlim([-10 10]); title('Dist. of Rel. Error (%)')
%xlim([-10 10]); title('Rel. Error Dist. Adaptive Mass Center')
set(gca,'fontsize',16)
x2 = 1.5;,y2 = 35;
% txt2 = 'Level = -30dB';
% text(x2,y2,txt2,'fontsize',16)

figure(6)
histogram(errabs,50)
set(get(gca,'child'),'FaceColor','bl','EdgeColor','bl');
grid on; ylim([0 150]);
xlabel('Speed (m/s)'); ylabel('No. of Data');
xlim([-1.5 1.5]); title('Dist. of Rel. Error (absolute)')
%xlim([-0.5 0.5]); title('Error in m/s Adaptive Mass Center')
set(gca,'fontsize',16)
x2 = 1.5;,y2 = 35;
```

```
% txt2 = 'Level = -30dB';
% text(x2,y2,txt2,'fontsize',16)

% RMSE -  represents the standard deviation of the differences between
% radar and and gps, scale dependant
Sqrt_Root_mean_Error = RMSE

% Measure % of error under a limit of error
binranges1 = -1:1;
[bincounts1] = histc(histdata,binranges1);
under2 = sum(bincounts1);
percentUnder2 = under2/length(histdata)*100
```

CMA-AT

CMA-ST is proposed algorithm based on centre-of-mass. This algorithm is implemented as a sub-function of the main processing code. The following describes the processing implemented in the code

```
function [estmeanfreq,fmin,fmax,thres2] = CMA_AT(mat,rdr,sig,thres1);
%%%%%%%%%%%%%%%%%%%%%%%%%%%%%%%%%%%%%%%%%%%%%%%%%%%%%%%%%%%%%%%%%%%%%%%%%%%%%%%
% Centre-of-mass method: Amplitude-Threshold
% 1. Measure noise at the end of freq. spectrum to sample noise character
% 2. Find bins above the threshold - TH1
% 3. Find a width, w with a value above the threshold - TH2, do for fmin and fmax
% 4. Compute half-mass of the spectrum
% 5. Find the mean frequency using centroid method
% 6. Return the fmean
%%%%%%%%%%%%%%%%%%%%%%%%%%%%%%%%%%%%%%%%%%%%%%%%%%%%%%%%%%%%%%%%%%%%%%%%%%%%%%%

if rdr==2 || rdr==3
    mat = mat(end:-1:1);
end

n = length(mat);
mat(1:5) = 0;
%Noise selector
%noise = temp_abs(54000:55000); % T = 1
%noise = temp_abs(2700:28000); % T = 0.5
%noise = temp_abs(1000:11000); % T = 0.5
noise = mat(400:500); % T = 0.5

thres2 = mean(noise)*sig; % level_1(30 dB) = 0.45

temp_bin = zeros(size(mat));
temp_bin(find(mat>=thres2)) = 1;

fmin = 0;
for i=n/2:n
    if temp_bin(i)==1
        tempx = temp_bin(i:i+10);
        if sum(tempx)>thres1
            fmin = i;
            break;
```

```
        end
    end
end

fmax = 0;
for i = n:-1:ceil(n/2)
    if temp_bin(i)==1
        tempx = temp_bin(i:-1:i-10);
        if sum(tempx)>thres1
            fmax = i;
            break;
        end
    end
end

if fmin==0 || fmax == 0
    estmeanfreq = ceil(n/2);
    return;
end


% CMA
halfmass = sum(mat(fmin:fmax))/2;
area = 0;
i = fmin;
while area<=halfmass
    area = area + mat(i);
    i = i+1;
end

if rdr==2 || rdr==3
    estmeanfreq = n-i;
    mat = fmin;
    fmin = n-fmax;
    fmax = n-mat;
else
    estmeanfreq = i;
end

end
```

CMA-ST

CMA-ST is proposed algorithm based on centre-of-mass. This algorithm is implemented as a sub-function of the main processing code. The following describes its implementation in MATLAB

```
function [estmeanfreq] = CMA_ST(mat,rdr,srate,actrate)
%%%%%%%%%%%%%%%%%%%%%%%%%%%%%%%%%%%%%%%%%%%%%%%%%%%%%%%%%%%%%%%%%%%%%%%%%%%%%%%%
% Centre-of-mass method: Slope-threshold
% 1. Measure nmean and std of noise at end of the spectrum
% 2. Compute CUSUM (begin from left of data)
% 3. Compute CUSUM (begin from right of data)
% 4. Compute slope for l2r and r2l CUSUM data
% 5. Find slope which is above the threshold to determine fmin and fmax
```

```
% 6. Find the half-mass of the spectrum
% 7. Find the fmean
% 8. Return the value of fmean
%%%%%%%%%%%%%%%%%%%%%%%%%%%%%%%%%%%%%%%%%%%%%%%%%%%%%%%%%%%%%%%%%%%%%%%%%%%%%%%%

if rdr==2 || rdr==3
    mat = mat(end:-1:1);
end

N = srate/2:srate-1;

matabs = mat(N);
matabs(1:5) = 0;
L = round(4000*srate/actrate);
H = round(5000*srate/actrate);

u0 = mean(matabs(L:H));
stddev0 = std(matabs(L:H));

mszU = 5; % five sigma away
mszH = 5;

kU = mszU*stddev0/2;
kH = mszU*stddev0/2;
dp = 5;
H = dp*stddev0;

r2ldata = matabs(end:-1:1);
r2lcusum = zeros(1,length(r2ldata));

for jj = 1: length(r2ldata)

    r2lcusum(jj) = max([0, r2ldata(jj) - (u0 + kU) + r2lcusum]);

end

l2rdata = matabs;
l2rcusum = zeros(1,length(l2rdata));

for jj = 1: length(l2rdata)

    l2rcusum(jj) = max([0, l2rdata(jj) - (u0 + kU) + l2rcusum]);

end

delta = abs(r2lcusum(end:-1:1) - l2rcusum);


[mg,indx] =  min(delta);

coef = 5;
r2lcusum = r2lcusum(end:-1:1);

slopeRIGHT = (l2rcusum(indx) - l2rcusum(indx-coef))/(indx-(indx-coef));
C1 =  l2rcusum(indx) - slopeRIGHT*indx ;
B_Low = max([1,ceil(-C1/slopeRIGHT)]);

slopeLEFT = (r2lcusum(indx) - r2lcusum(indx-coef))/(indx-(indx-coef));
C1 =  r2lcusum(indx) - slopeLEFT*indx  ;
B_High = ceil(-C1/slopeLEFT) ;
```

```
if B_High > srate/2 || B_High < B_Low

    estmeanfreq = round(srate/2);  % false detection

else

    half_area = sum(matabs(B_Low:B_High))/2;
    area = 0;
    i = B_Low;
    while area<=half_area

        area = area + matabs(i);
        i = i+1;
    end

    if rdr==2 || rdr==3

        estmeanfreq = round(srate/2)-i;

    else

        estmeanfreq = i + round(srate/2);
    end

end


end
```

XCA

XCA is proposed algorithm based on cross-correlation. This algorithm is implemented as a sub-function of the main processing code. The following describes its implementation in MATLAB

```
function [vel_center] =
XCA(spectm,iSen,bmWidth,lamda,sRate,smFactor,aziAng,depAng,SNR)
%%%%%%%%%%%%%%%%%%%%%%%%%%%%%%%%%%%%%%%%%%%%%%%%%%%%%%%%%%%%%%%%%%%%%%%%%%%%%%%
% Cross-correlation method
% 1. Smooth the spectral data and measure the frequecy of peak amplitude
% 2. Estimate v based on the frequency of peak amplitude
% 3. Estimate std of Gaussian function
% 4. Generate Gaussian Function
% 5. Cross-correlate the generatedGaussian function to the spectral data
% 6. Determine the coefficient of correlation with max amplitude
% 7. Determine the fmean based on the position of max coeff value
% 8. Return the fmean
%%%%%%%%%%%%%%%%%%%%%%%%%%%%%%%%%%%%%%%%%%%%%%%%%%%%%%%%%%%%%%%%%%%%%%%%%%%%%%%
```

```
if iSen==2 || iSen==3
    spectm = spectm(end:-1:1);
end

L = 1:sRate/2;
L0 = 2*length(L);
N = sRate/2:sRate-1;
spectReal = spectm(N);


%% Disting noise and useful signal

spectReal = spectm(N);
spectReal(1:5) = 0;
rdrCurve = smooth(spectReal,smFactor);

%% Main Spectral shift finding method

        % STEP 1: Generate a ref curve and find its maximum ampltidue and location
        rdrCurve = smooth(spectReal,smFactor);
        [mMax,fMax] = max(rdrCurve);

        % STEP 2: Generate and build a Gaussian curve
        % a) find the speed for 1st freq. guess.
        vEst = (fMax*(lamda))/(2*cosd(aziAng));

        % b) find the std deviation for radar gaussian curve
        sigma = vEst*bmWidth*pi/180*sind(depAng)/lamda;

        % c) build curve
        k = -((L-fMax).^2)/(2*sigma.^2);
        gsCurve = (mMax.*exp(k));

        % STEP 3: move the curve to left and right and find the best
        % prepare the -lag & +lag for xcorrelation
%         Po = mMax/(10^(SNR/20));
%         gsCurve(gsCurve <Po) = 0;
%         rdrCurve(rdrCurve <= Po) = 0;


        %xcorr(A,B)
        [acor,lag] = xcorr(gsCurve,rdrCurve);
        [esamp,I] = max(acor);

        if esamp > 0.1;

        % validation gauss plot (for test only)
        fDiff0 = sRate/2 - I;
        k = -((L-(fMax+fDiff0)).^2)/(2*sigma.^2);
        gsCurveCal = (mMax.*exp(k));

        % ESTIMATED fd
        [~,c] = max(gsCurveCal);

                if  iSen==2 || iSen==3

                    vel_center = L0-(sRate/2+c);

                else
                    vel_center = sRate/2+c;
```

```
            end
        else

            vel_center = 0;

        end

 end
```

Statistical processing

The statistical processing is a sub-function that computes the mean, standard deviation, average and maximum relative error from the speed estimates. The following code describes the implementation.

```
function
[vGPSmean,vGPSsigma,MethodMean,MethodSigma,methodAvgRelErr,methodMaxRelErr,MeanStdE
r,MethodCal,scaleX,Rel_ErrorPercentage,RMSE,Error_in_mph]= ...
    Error_est(analySeg,Method,vGPS,diff,span,ana,SamplingRate,Phy_sRate)

% Set statistics interval for GPS and Method

analySeg0 =
ceil(analySeg(1)/(SamplingRate/Phy_sRate)):ceil(analySeg(end)/(SamplingRate/Phy_sRa
te)) ;%./round(span);
Method_ori = Method;
% give controls to allign GPS speed and radar speed
controls = 0;
indRng = analySeg0 + controls;
vGPS = vGPS(indRng);

MethodIndex = indRng - round(diff);
MethodMean = mean(Method(MethodIndex));

% Calibrate the method speed to GPS speed removing bias error
vGPSmean = mean(vGPS);
vGPSsigma =std(vGPS);
Method = Method*vGPSmean/MethodMean;
MethodCal = Method;

  if  ana == 1

      figure('units','normalized','outerposition',[0 0 1 1])
      plot(MethodCal(MethodIndex));
      hold on
      plot(vGPS)
      hold off; grid on; title('Forward Speed (Whole Data)'); legend('GPS','24 GHz
Radar'); xlabel('Time (s)'); ylabel('Speed (m/s)');

 end
```

```
% Measure the mean standard error for Method
MethodSigma = std(Method(MethodIndex));
MeanStdEr = MethodSigma/vGPSmean*100;

% Measure the relative error
methodAvgRelErr = mean(abs(Method(MethodIndex)-vGPS)./vGPS)*100;
methodMaxRelErr = max(abs(Method(MethodIndex)-vGPS)./vGPS)*100;

scaleX = fminbnd(@(scale) norm(scale*Method_ori(MethodIndex)-vGPS, 2), .1, 10);
Rel_ErrorPercentage = 100*(Method(MethodIndex)-vGPS)./vGPS;
Error_in_mph = Method(MethodIndex) - vGPS;
% RMSE
RMSE = sqrt(mean(( Method(MethodIndex)-vGPS).^2));

end
```

Appendix G: Publication

1. Shariff, K.K.M.; Hoare, E.; Daniel, L.; Antoniou, M.; Cherniakov, M. Comparison of Adaptive Spectral Estimation for Vehicle Speed Measurement with Radar Sensors. Sensors 2017, 17, 751.